Simulation-based Innovation and Discovery

Energetics Applications

Simulation-based Innovation and Discovery

Energetics Applications

Edited by

Davinder K. Anand
Satyandra K. Gupta
Robert A. Kavetsky

Center for Energetic Concepts Development Series

CALCE
EPSC Press

University of Maryland, College Park, Maryland

Cover design by Ania Picard

Peregrine falcon photograph taken by and used with the permission of Michael “Mike” L. Baird

Library of Congress Control Number: 2011932909

Direct all inquiries to:

CECD
Department of Mechanical Engineering
2140 Glenn L. Martin Hall
University of Maryland
College Park, MD 20742
Ph.: (301) 405-5205
http://www.cecd.umd.edu

International Standard Book Number 978-0-9846274-2-4

Printed in the United States of America

Printed in Southern Maryland

Preface

Simulation-based virtual prototyping systems have allowed companies in many sectors to dramatically cut product development time, reduce costs, and enhance product quality. However, the timeline to move a new energetic material from research to application is usually measured in decades. The most recent example of this timeline is the development of CL-20, which was discovered in 1987, and is just now making its way into actual usage. Since conducting extensive physical experiments is very expensive and time consuming, due to safety and environmental considerations for energetics applications, the idea of "computational energetics" has been gaining traction in recent years. There is now an opportunity to shrink this "transition-to-use" time by using simulation tools for validating the entire development/production cycle from chemistry to manufacturing and testing.

In addition, there is another important driver for increasing the use of simulation in energetic materials development, and that has to do with moving beyond the traditional Carbon–Hydrogen–Nitrogen–Oxygen (CHNO)-based chemistry that forms the basis of today's conventional energetic materials, to whole new classes of materials, where understanding the underlying physics of the material is just as important as understanding material chemistry. Linked to this need to move beyond CHNO is the need to develop new methods of energetic material production, as many of the limitations energetic material developers have encountered in the last 50 years are a result of the energetic community's reliance on basically one method of producing material, and that is the batch processing approach. Batch processing by definition limits the range of formulations that can be evaluated, mainly due to dwell time issues in the batch mixer. In order to address these challenges, simulation can play a valuable and cost-effective role, in exploring new materials, and equally important, new material production methods, without having to manufacture either trial compounds, or building expensive manufacturing facilities, until one is convinced that a reasonable material or new production process is at hand. The goal for the energetics community should be to achieve what the aircraft industry has attained, and that is the ability to fully design a new system in the virtual world, without having to do expensive prototyping at every stage. To do so would require a fundamental paradigm shift in the energetics community.

Representative tasks that benefit from the use of simulation in the field of energetics applications include functionality evaluation, manufacturing process evaluation, ergonomic analysis and optimization. A wide variety of simulation tools are currently available. Popular tools include structural and thermal finite element analysis, computational fluid dynamics, multi-body dynamics, electromagnetic field propagations, and ergonomic analysis. Emerging simulation tools include molecular dynamics simulations for evaluating and discovering new materials.

The simplest and most common use of the simulation in the innovation process is to use it as an evaluation tool to investigate a proposed new design and assess its feasibility. Simulations can also be used to identify trends in the design space or design rules that can then be used by the designers to guide the design process and conduct optimization studies to select the best set of the product or process parameters. Recent advances in high fidelity simulations enable us to do a more accurate analysis of proposed solutions. The advent of low-cost, high-performance computing architecture enables us to explore a very large number of solutions in a short period of time. A number of computational advances were needed to effectively exploit simulation during the innovation process. Some of the key advances were: meta modeling, hybrid representations, human-computer interactions, methods for exploration of large search spaces and reasoning algorithms in the presence of uncertainties.

This book discusses nine representative and important applications in energetics research, development, and manufacturing. These include the use of classical molecular dynamics simulations to simulate the mechanochemical behavior of small oxide coated aluminum nanoparticles, a study focused on the design and implementation of an energetic material, an approach for simulation-based design of materials, an approach that uses small scale testing to predict full scale explosion effects, the development of new modeling capabilities for multiphase explosions containing a dispersed particle phase, a review of different models and approaches to study blast wave interactions with soft-tissue matter, a simulation-based approach to the design of drive mechanisms for flapping wing miniature air vehicles, and finally an investigation of the problem of task space synchronization and trajectory tracking for heterogeneous robots under dynamic uncertainties.

Our objective here is to emphasize that simulation presents a fundamentally new way of discovering trends and insights that can be used by designers to create new products and policies associated with the development of advanced energetics capabilities, including the development of new production methods.

Some experts hold the view that all the benefit of advancements in energetic materials has been obtained, and that the opportunity for new capabilities built on energetics is behind us. We hope to provide a cogent view that in fact a new era in energetics is upon us, wherein the use of modeling and simulation will enable entirely new capabilities to be developed from first principles that will enable exciting new advancements which were only ideas in the past.

We would like to acknowledge the support of LWI Inc, under Contract W 911NF-07-2-0062 and sub award LWI-391-001, and EHS Inc, under Contract N00178-05-D-4309 FG 03, for some material presented in parts of this book. Also, Eric Hazell copy edited the book and as usual Ania Picard prepared the entire manuscript for publication.

College Park, MD

Author Biographies

Davinder K. Anand is Professor of Mechanical Engineering and Director of the Center for Energetic Concepts Development, both at the University of Maryland, College Park. He received his doctorate from George Washington University in 1965. Dr. Anand was Senior Staff at The Applied Physics Laboratory of the Johns Hopkins University from 1965-1974. From 1991-2002, he chaired the Department of Mechanical Engineering at College Park. He has served as a Director of the Mechanical Systems Program at the National Science Foundation, and his research has been supported by NIH, NASA, DOE, DOD, and industry. He has lectured internationally, founded two high technology research companies (most recently Iktara and Associates, LLC), published three books and over one hundred and seventy papers, and has one patent. He is a Distinguished Alumnus of George Washington University and was awarded the Outstanding and Superior Performance Award by the National Science Foundation. Dr. Anand is a Fellow of ASME and is listed in Who's Who in Engineering.

Arvind Ananthanarayanan is a post doctoral researcher at the University of Maryland, College Park. He specializes in the areas of bio-inspired and medical robotics, design for manufacturing, and computational modeling of manufacturing processes. He received his Bachelor of Technology (B. Tech.) in Mechanical Engineering and Master of Technology (M. Tech.) in Computer Integrated Manufacturing from the Indian Institute of Technology, Bombay, in 2005. Subsequently he received his Ph.D. in Mechanical Engineering from the University of Maryland at College Park in 2009. He is a member of Society of Manufacturing Engineers (SME) and American Society of Mechanical Engineers (ASME). He has authored and co-authored over twelve articles in journals and conference proceedings.

Balakumar Balachandran is a Professor of Mechanical Engineering at the University of Maryland, where he has been since 1993. His research interests include nonlinear phenomena, dynamics and vibrations, and control. His publications include a Wiley textbook entitled *Applied Nonlinear Dynamics: Analytical, Computational, and Experimental Methods* (1995, 2006), a Cengage textbook entitled *Vibrations* (2004,

2009), and an edited Springer book entitled *Delay Differential Equations: Recent Advances and New Directions* (2009). He serves on the editorial board of the Journal of Vibration and Control, is a Deputy Editor of the AIAA Journal, and is an Associate Editor of the ASME Journal of Computational and Nonlinear Dynamics. He is a Fellow of ASME and AIAA.

Wojciech Bejgerowski is a Graduate Research Assistant in the Department of Mechanical Engineering at the University of Maryland. He received a Master of Science (M.S.) degree in Mechanical Engineering from the Poznan University of Technology in 2003. His research interest is broadly in the area of manufacturing technology. Currently, he is working on developing in-mold assembly processes to create multi-material multi-functional polymer structures. He has experience in many different manufacturing domains, including mechanical assembly, machining, injection molding, in-mold assembly, and cold roll forming.

Hugh A. Bruck received his B.S. and M.S. in Mechanical Engineering in 1988 and 1989 respectively, developing the experimental mechanical characterization technique known as Digital Image Correlation (used, for example, to characterize multi-mode fracture in aluminum alloys), and his Ph.D. in Materials Science from Caltech in 1995, where he worked on the development of Bulk Metallic Glasses (aka, Liquidmetal). After working at Idaho National Engineering Laboratories on processing, characterization, and modeling of residual stresses and stress wave propagation in Functionally Graded Materials (including a patent on Graded Aluminum-Alumina Armor), he came to the Department of Mechanical of Engineering at the University of Maryland as an Assistant Professor in 1998 and is currently Professor and Director of Graduate Studies. His current research has led to the development of a new combinatorial technique for formulating polymer nanocomposites and highly filled polymers, new processing-structure-property models for multifunctional polymer nanocomposites, new label-free biosensors based on electrical percolation and enhanced chemiluminescence in bio-nanocomposites, and new multiscale characterization approaches for hierarchically-structured polymer composites and biological materials. He has authored or co-authored 7 book chapters, 67 journal papers, and 70 conference papers. His work has been recognized with many honors and awards, including the ONR Young Investigator Program Award, A.J. Durelli Award, and Fulbright Scholar Award. He was an Associate Editor of the journal Experimental Mechanics for 9 years, serves on the

Executive Board of the Society for Experimental Mechanics, and is a fellow of ASME.

Nikhil Chopra received the B. Tech. in Mechanical Engineering from Indian Institute of Technology, Kharagpur, India, 2001, and the M.S. and Ph.D. degrees from General Engineering in 2003 and Systems and Entrepreneurial Engineering in 2006, respectively. From 2006 to 2007, he was a Postdoctoral Research Associate with the Coordinated Science Laboratory, University of Illinois, Urbana-Champaign. Since 2007, he has been an Assistant Professor with the Department of Mechanical Engineering and the Institute for Systems Research, University of Maryland, College Park. His research interests include control of semi-autonomous systems, control of dynamical systems over unreliable networks, synchronization of dynamical systems, and bilateral teleoperation over unreliable communication networks.

William Fourney is Keystone Professor and Associate Dean of Engineering at the University of Maryland. He holds a joint appointment in the Mechanical Engineering Department and the Aerospace Engineering Department. He received his B.S. in Aerospace Engineering and his M.S. in Theoretical and Applied Mechanics from West Virginia University. His Ph.D. in Theoretical and Applied Mechanics was received from the University of Illinois in 1966. His areas of research interest are in experimental mechanics and fracture mechanics - primarily from a dynamic aspect. He has published approximately 220 articles describing the results of his research in dynamic fracture and crack arrest, including approximately 50 reports to the sponsors of his research. His research has been sponsored by NSF, AFOSR, ONR, NRC, DOE, NSWC, ARL, Oak Ridge National Labs, Los Alamos National Labs, and the US Bureau of Mines.

John Gerdes is a mechanical engineer at the Army Research Laboratory (Aberdeen) in the Vehicle Technology Directorate. His research interests are in microsystem mechanics, experimental design, unmanned engines, and vehicle applied research. John received his Bachelor’s degree in Mechanical Engineering in 2007, and his Master’s degree in Mechanical Engineering in 2010, both from the University of Maryland. He is a member of American Society of Mechanical Engineers (ASME).

Satyandra K. Gupta is a Professor in the Department of Mechanical Engineering and the Institute for Systems Research at the University of Maryland. He is also the director of the Maryland Robotics Center and a member of the Center for Energetics Concepts Development. He

received a Bachelor of Engineering (B.E.) degree in Mechanical Engineering from the University of Roorkee (presently known as the Indian Institute of Technology, Roorkee) in 1988. He received a Master of Technology (M. Tech.) in Production Engineering from the Indian Institute of Technology, Delhi, in 1989. He received a Ph.D. in Mechanical Engineering from the University of Maryland at College Park in 1994. He is a fellow of American Society of Mechanical Engineers (ASME) and has authored or co-authored more than two hundred articles in journals, conference proceedings, and book chapters.

Brian Henz received his Ph.D. in Mechanical Engineering from the University of Maryland, College Park in 2009. Since 2001 he has been employed as a Research Engineer at the U.S. Army Research Laboratory in the Computational and Information Sciences Directorate. He has authored/co-authored 12 journal publications and his work appears in numerous conference proceedings. His research interests include the atomistic simulation of nanoparticle materiel systems, the application of advanced computing techniques to physics-based simulations, battlefield applications, and mobile ad-hoc network emulation.

Gregory S. Jackson is a faculty member in the Department of Mechanical Engineering at the University of Maryland, where he has been leading research on reacting flows and fuel cell systems since 1997. Dr. Jackson received his Ph.D. from Cornell University in 1994 and worked at Precision Combustion, Inc. on advanced catalytic combustion technology for four years before joining the faculty at Maryland. While at Maryland, he has led numerous research projects on combustion, solid oxide fuel cells, and high-temperature catalysis for energy conversion. From 2007-2009, Dr. Jackson served as the acting director for the campus-wide University of Maryland Energy Research Center.

Robert A. Kavetsky is the Executive Director of the Energetics Technology Center, where he leads a Policy Development Group for a number of Department of Defense clients. He was the founder of the N-STAR(Naval Research – Science and Technology for America's Readiness) initiative at the Office of Naval Research, a Navy-wide effort aimed at reinvigorating the science and technology community within the Navy's Warfare Centers. He received a Bachelor of Science Mechanical Engineering in 1975, a Master of Science Mechanical Engineering in 1977, and a Master of Science Engineering Administration in 1978, all from Catholic University. He was head of the Explosion Damage Branch, Program Manager for the Undersea Warheads Program, and Program Manager for Undersea Weapons at the

Naval Surface Warfare Center. At the Pentagon, he helped develop science and technology programs for organic mine countermeasures and expeditionary logistics, and then at Naval Surface Warfare Center Indian Head created "Workforce 2010," a government, industry, and academic consortium focused on developing Indian Head's next generation workforce. He has authored a number of technical and workforce policy and program publications for the American Society for Engineering Education, the American Society of Mechanical Engineers, the American Institute of Aeronautics and Astronautics, and other forums.

Thomas M. Klapötke received his Ph.D. in 1986 (TU Berlin), post-doc in Fredericton, New Brunswick, habilitation in 1990 (TU Berlin). From 1995 until 1997 Klapötke was Ramsay Professor of Chemistry at the University of Glasgow in Scotland. Since 1997 he has held the Chair of Inorganic Chemistry at LMU Munich. In 2009 Klapötke was appointed a visiting Professor at the CECD, University of Maryland. Klapötke is a Fellow of the RSC (C.Sci., C.Chem. F.R.S.C.), a member of the ACS and the Fluorine Division of the ACS, a member of the GDCh, and a Life Member of both the IPS and the National Defense Industrial Association. Most of Klapötke's scientific collaborations are between LMU and ARL in Aberdeen, MD and ARDEC in Picatinny, NJ. Klapötke also collaborates with ERDC in Champaign, IL. He is the executive editor of *Zeitschrift für Anorganische und Allgemeine Chemie* and an editorial board member of *Propellants, Explosives and Pyrotechnics*, *Journal of Energetic Materials*, *Central European Journal of Energetic Materials*, and the *International Journal of Energetic Materials and Chemical Propulsion*. Klapötke has published over 500 papers, 23 book chapters and five books.

Hans Ulrich Leiste is the laboratory manager of the Dynamic Effects Laboratory, pursuing doctoral studies in Mechanical Engineering at the University of Maryland. He joined the University of Maryland in 2003. Prior to that, he completed his Master's in power engineering at the Technical University of Berlin, Germany. His areas of interest include hyper-acceleration of targets due to explosive loading, pressure distributions close to buried mines, and impulse mitigation explosively loaded platforms. He has published numerous articles about the research conducted in these areas.

Yen-Chen Liu received the B.S. and M.S. degrees from the Department of Mechanical Engineering, National Chiao Tung University, HsinChu, Taiwan in 2003 and 2005, respectively. He is currently working toward his Ph.D. at the University of Maryland, College Park. His research

interests include synchronization of networked robotic systems, collaboration between wireless sensor network and multi-robot systems, and control of robotic systems under unreliable networks.

Thomas P. McGrath II is the Senior Energetics Modeling and Simulation Developer for the Indian Head Division, Naval Surface Warfare Center. He serves as the principal investigator for several energetics modeling and simulation programs, and is a lead developer for the DYSMAS program. He is an expert in the fields of code development, energetic technology, multiphase physics, detonation physics, and warhead concept development. Dr. McGrath earned his PhD in Mechanical Engineering from the University of Maryland for his research on compressible multiphase flows.

Dominik Mueller is a Mechanical Engineer in the Department of Nuclear Pump Research and Development at the KSB AG Headquarters, Frankenthal (Germany). He received a Diploma degree in Mechanical Engineering from the University of Applied Sciences Hochschule Mannheim (Germany). His Diploma thesis was titled “Analysis and Optimization of the Wings and Mechanism Structure of a Flapping Wing Miniature Air Vehicle.” He received a Master of Science (M.Sc.) in Mechanical Engineering from the University of Applied Sciences Hochschule Mannheim (Germany) in 2010.

Maxim Schwartz is principal software engineer for the Energetics Technology Center. Prior to joining the ETC, he was a software engineer at the Department of Mechanical Engineering’s Center for Energetic Concepts Development (CECD), where he was an integral part of the virtual reality design team. Mr. Schwartz’s main expertise is in development of geometric algorithms for virtual environments. He is currently spearheading the development of the virtual reality laboratory at the ETC, one of the few private sector labs in the country. His latest work involves building virtual environment-based simulators for unmanned vehicles. His experience includes 3D visualization development, parallel computing, networking, and building applications for desktop PCs.

Jörg Stierstorfer studied chemistry at the Ludwig-Maximilian University in Munich, Germany. He received his diploma degree in 2005, investigating the “Chemistry of BTA.” He worked on his Ph.D. as a co-worker in the research group of Dr. Thomas Klapötke. He has gained expertise in energetic materials research in close collaborations with US and German institutions. His scientific interests include

synthesis, characterization, and scale-up, as well as performance and safety testing of new energetic materials. Stierstorfer received his Ph.D. with honors in March 2009. Since then he has worked as a research director in the Klapötke group. Stierstorfer has published more than 40 scientific papers, and in 2007, he was awarded the Römer Prize of the University of Munich for his scientific achievements.

Petr Svec is a Postdoctoral Research Associate at the University of Maryland, College Park. His research interests are in Robotics, Machine Learning, Motion Planning, Computational Geometry, and Graph Theory. Prior to joining the University of Maryland, he was a Graduate Research Assistant in Mechanical Engineering, Brno University of Technology in the Czech Republic. Dr. Svec received a Master's degree in Computer Science from Institute of Automation and Computer Science, Faculty of Mechanical Engineering at Brno University of Technology in 2003. Due to his simultaneous studies of Computer Science and Mechanical Engineering at two universities, he received a Bachelor's degree in Computer Science from the Faculty of Informatics, Masaryk University in 2004, and a second Master's degree in 2006 from the same institute. Dr. Svec received a Ph.D. in Robotics (Machines and Equipments program, Design and Process Engineering branch) from the Brno University of Technology, in 2007.

Leslie C. Taylor has been a Faculty Research Assistant in the Department of Aerospace Engineering at the University of Maryland since 1995. His research interests include the effect of burial on the output and damage capability of explosives. He received a Bachelor of Mechanical Engineering (B.M.E) degree from Cornell University in 1959, a Master of Science (M.S.) degree in Mechanical Engineering from the University of Maryland in 1966 and a Diploma from the US Naval War College in 1985. Prior to coming to the University of Maryland, he worked for 45 years at the US Naval Ordnance Laboratory and successor organizations, where he focused on the design and development of underwater weapons and on the effects of explosions in shallow water. This time includes two years working in the United Kingdom Ministry of Defence as an exchange engineer. He has chaired several international collaborative efforts. He has received two Meritorious Civilian Service Awards and has authored 25 papers and 30 classified and unclassified company and agency reports. He is a member of NDIA.

Atul Thakur is a Ph.D. candidate in the Department of Mechanical Engineering at the University of Maryland. He received Bachelor of

Engineering (B.E.) degree in Production Engineering from the University of Mumbai in 2003. He received a Master of Technology (M. Tech.) in Manufacturing Engineering from the Indian Institute of Technology, Bombay, in 2003. He is a member of American Society of Mechanical Engineers (ASME).

Marcelo Valdez is a graduate student pursuing doctoral studies in Mechanical Engineering at the University of Maryland. He joined the University of Maryland in 2008. Prior to that, in 2006, he completed a five-year engineering program in Aeronautical Engineering at the University of Cordoba, Argentina. His areas of interest include computational fluid-structure interactions, nonlinear dynamics, and wave mechanics. He has published articles on flapping wing systems and blast wave interactions with soft tissue.

Stephen Wilkerson is a researcher at the Army Research Laboratory (Aberdeen) and Associate Director for Special Programs in the Vehicles Technology Directorate. His focus areas include Microsystems, Unmanned Air and Ground Vehicles Research, and Autonomous Control. Dr. Wilkerson received his Doctorate from the Johns Hopkins University in 1990. Since then he has been an exchange scientist to Germany, taught at the United States Military Academy West Point and continues teaching math part time at Towson University and Harford Community College. He has authored approximately 60 publications on a variety of subject matters and holds 2 patents.

Michael Zachariah is a Professor in the departments of Mechanical Engineering and Chemistry and Biochemistry at the University of Maryland, and holds a joint appointment at the National Institute of Standards and Technology. His primary research interests are in nanoenergetic materials and their reaction dynamics, nanoparticle metrology, and atomistic simulation. He has authored over 200 refereed publications, and he has served as associate editor of the *Journal of Nanoparticle Research*, and on the editorial boards of *Aerosol Science and Technology*, the *International Journal of Chemical Kinetics* and *Combustion Theory and Modeling.*

Contents

Chapter 1

Computational Foundations for Simulation-based Innovation and Discovery in Energetics Applications

Satyandra K. Gupta, Davinder K. Anand, and Robert Kavetsky

1.1 Introduction

Computer simulations play an extremely important role in the modern product development process. Simulation-based virtual prototyping systems have allowed companies to dramatically cut product development time, reduce costs, and enhance product quality. For example, a new cell phone can now be developed in less than six months as opposed to two years. A mold for a limited production run now only costs a few thousand dollars as opposed to tens of thousands. The first Boeing 777 that came out of the assembly line flew flawlessly in its maiden flight.

Historically the field of energetic materials development has relied on an empirical approach to creating new materials. This has resulted in the timeline to move a new energetic material from research to application (or molecule to munition in DoD parlance) that is usually measured in decades. The most recent example of this timeline is the development of CL-20, which was discovered by Dr. Arnold Nielson in 1987, and is just now making its way into actual usage. The problem with this timeline is that it is inherently out of synch with "new product" development timelines in the military – or in industry for that matter – which are measured in 5 to 7 year increments. Thus, the opportunity to insert new energetic materials for consideration into a new system will not happen, unless there is an urgent need for a new capability that relies solely on the enhanced properties of the material. The result has been

that in the last 20 years, there have been very few new energetic materials incorporated into modern defense systems. That paradigm needs to change and take advantage of advances in the modeling and simulation arena in the last 20 years to fully embrace the idea of "computational energetics." The development of new energetic materials and energetic systems needs to move more aggressively into using well validated and computationally effective modeling and simulation tools.

There is another important driver for increasing the use of simulation in energetic materials development, and that has to do with moving beyond the traditional Carbon–Hydrogen–Nitrogen–Oxygen(CHNO)-based chemistry that forms the basis of today's conventional energetic materials, to whole new classes of materials, where understanding the underlying physics of the material is just as important as understanding material chemistry. Linked to this need to move beyond CHNO is the need to develop new methods of energetic material production, as many of the limitations energetic material developers have encountered in the last 50 years are a result of the energetic community's reliance on basically one method of producing material, and that is in batch processing. Batch processing by definition limits the range of formulations that can be evaluated, mainly due to dwell time issues in the batch mixer. In addressing these challenges, simulation can play a valuable and cost effective role, both in exploring new materials, and equally important, in developing new material production methods, without having to manufacture either trial compounds or building expensive manufacturing facilities, until one is convinced that a reasonable material or new production process is at hand. The goal for the energetics community should be to achieve what the aircraft industry has attained, and that is the ability to fully design a new material/product in the virtual world, without having to do expensive prototyping at every stage.

Representative tasks that benefit from the use of simulations in the field of energetics applications include the following:

- *Functionality Evaluation*: Simulations can be used to evaluate a proposed design and assess its ability to meet functional specifications. For example, finite element simulations can be used to assess if the proposed housing in a cartridge activated device is strong enough to withstand the stresses introduced during the ejection process. This would enable more rapid and less expensive prototyping of energetic system designs prior to building a physical prototype.
- *Manufacturing Process Evaluation*: Simulations can be used to evaluate a proposed manufacturing process sequence, assess its

feasibility and estimate its cost. For example, assembly simulations can be used to ensure that a proposed step in the assembly of a cartridge activated device is feasible from the accessibility point of view. Additionally, there are new classes of energetic materials currently not being pursued, due to inherent limitations in the industry standard batch processing approach. High fidelity manufacturing process simulations would allow for evaluation of new energetic manufacturing processing techniques that would open up the energetic molecule design envelope for the synthesis chemists pursuing new energetic materials.

- *Ergonomic Analysis*: Simulations can be used to evaluate the ease of use for a proposed design from the human user's perspective. These scenarios include operation as well as maintenance and service tasks. For example, ergonomic analysis can be used to determine the level of difficulty in replacing an expired cartridge activated device from an ejection seat on an aircraft.
- *Optimization*: Increasingly, simulations are being used during the product optimization stages. For example, the wall thickness for housing on a cartridge activated device can be selected to minimize its weight while satisfying the strength constraints. Optimization will be especially critical for the next generation energetics-based systems, where the ability to fully integrate the energetic material with the delivery platform will be especially challenging.

The use of simulations during the product development process often leads to the following benefits:

- *Reduced Product Development Cost*: The use of simulations often leads to reduction in physical prototyping and the associated costs. It also enables detecting design errors early during the product development cycle. Correcting these errors early is much cheaper than discovering them during the production phase and then correcting them.
- *Reduced Time to Market*: The reduction in the physical prototyping also leads to speeding up of the product development process and bringing products to market quickly. This also eliminates many time consuming design iterations. As noted earlier, this is an especially critical issue in the development of new energetics-based systems.
- *Improved Product Quality*: Simulation enables the design team to evaluate many more design options and hence allows them to do a better job in optimizing the products. Simulation also enables design teams to evaluate the product from a wide variety of life cycle

considerations. This reduces the possibility for encountering unexpected problems after the product launch.

A wide variety of simulation tools are currently available. Popular tools include structural and thermal finite element analysis, computational fluid dynamics, multi-body dynamics, electromagnetic field propagations, and ergonomic analysis. Emerging simulation tools include molecular dynamics simulations for evaluating and discovering new materials.

Recent advances in simulation have led to the development of multi-physics simulations that can concurrently account for multiple phenomena (e.g., structural and thermal). Simulation tools can also be configured to run in multi-scale mode to utilize relevant scale-dependent physics. At the macroscale, traditional continuum mechanics models can be used, while at the small scale atomistic and molecular dynamics models can be used. These recent advances have made simulation tools suitable for exploring complex phenomena and designing complex products.

In order to determine the next frontier in simulations in the product development area, let us examine the changes taking place in the engineered products and systems. The following two trends are expected to significantly affect tomorrow's products and systems.

- Recent advances in manufacturing processes such as composites manufacturing and solid freeform fabrication are enabling manufacturing of multi-functional structures of high complexity. As we begin to exploit micro and nano manufacturing technologies, we are seeing highly complex designs that are fault tolerant and robust with respect to manufacturing defects. In most designs, basic elements in an array need not be identical to each other, thereby resulting in significant complexity.
- From exercise equipment to hearing aids, people are beginning to demand customized products and systems that fit their individual forms, needs, and tastes. Recent advances in manufacturing technology are bringing mass customization a step closer to reality. The desire to create highly customized designs leads to new challenges in the product development process.

Both of the above described trends are leading us to exploit the computing technology to truly revolutionize the innovation and discovery process in the context of energetics applications. The ability to rapidly develop energetics products that meet a wide range of constantly changing performance requirements will have significant economic

impact associated with ensuring national security. Over the last two decades, information technology has influenced all facets of the engineering practice. So a natural question is – what role can computers play in the innovation and discovery process? This book attempts to answer this question in the context of energetics applications.

1.2 Simulation Driven Innovation and Discovery

The simplest and most common use of the simulation in the innovation process is to use it as an evaluation tool to investigate a proposed new design and assess its feasibility. This is specially relevant and useful in energetics applications due to the inherently high cost associated with safely assessing and evaluating novel energetic materials. Unless a new material formulation appears promising, there is no point in conducting expensive physical feasibility tests. So in this case simulation serves as a screening tool to eliminate unpromising solutions. Figure 1.1 illustrates the basic concept behind using simulations as an innovation screening tool.

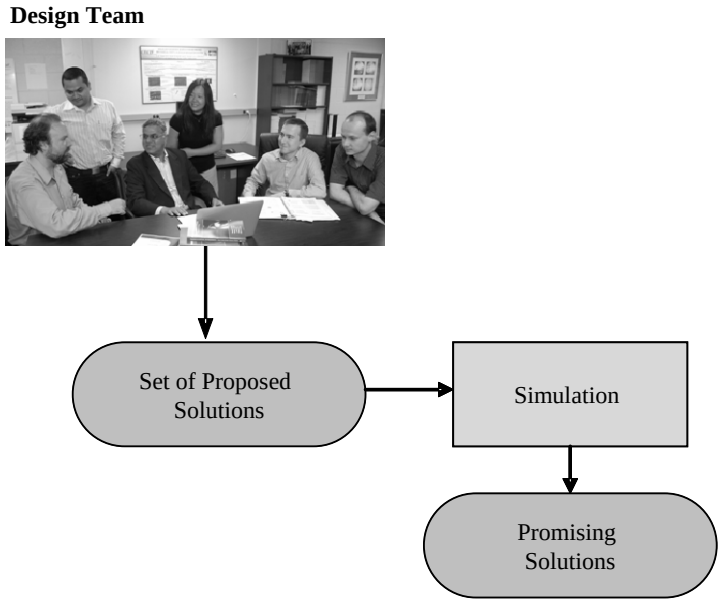

Figure 1.1: Simulation as innovation screening tool.

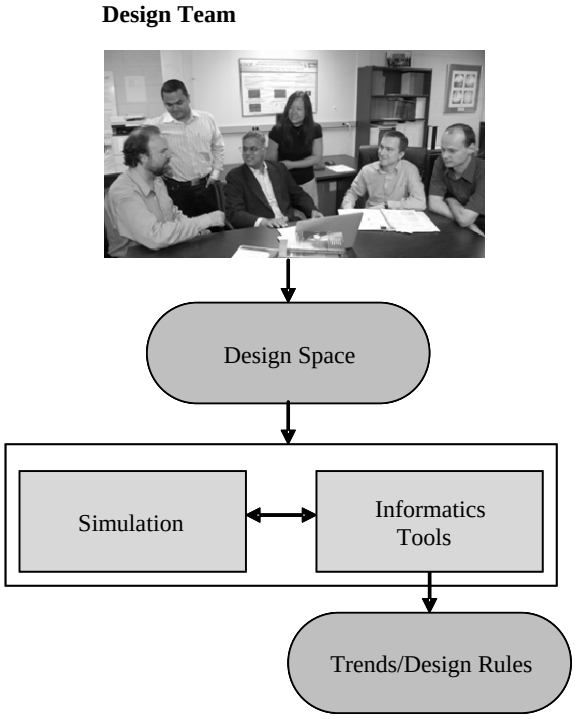

Figure 1.2: Use of simulation in discovering design rules.

Simulations can be used to identify trends in the design space or design rules that can then be used to guide the design process. This usually requires using simulation in conjunction with informatics technologies to conduct many virtual experiments and analyze results of those experiments to develop new insights. For example, simulations can be used to obtain new insights to develop safety guidelines in shipping and storing explosives. Informatics tools can be used to extract relevant information from simulations and present it in a useful format. Figure 1.2 illustrates the basic concept behind using simulations during the discovery process to gain new insight or develop a design guideline.

Simulations can be used during the optimization process to select the best set of the product or process parameters. The most commonly used simulation-based optimization approaches use either gradient-based or stochastic search techniques to find the optimal solutions. Usually, optimization routines control the simulation process to perform the evaluation at appropriate places in the search space. In some cases, the optimization routine uses response surfaces. These surfaces are constructed by fitting appropriate curves to the data generated by

conducting offline simulations. Figure 1.3 illustrates the basic idea behind using simulations in the optimization loop.

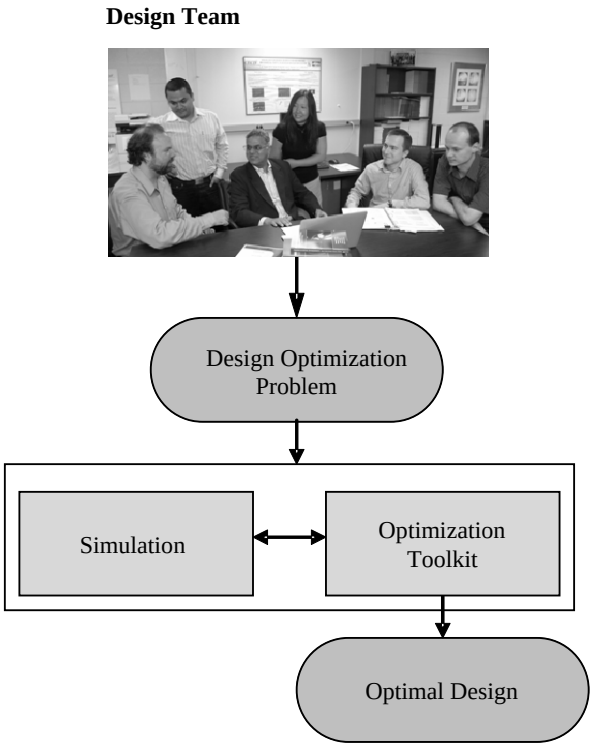

Figure 1.3: Simulation-based design optimization.

Recent advances in the high fidelity simulations enable us to do an accurate analysis of proposed solutions. The advent of low-cost, high-performance computing architecture enables us to explore a very large number of solutions in a short period of time. Advances in procedural representations enable us to automatically generate complex candidate solutions. Hence, high fidelity simulations are now poised to play a bigger role in the innovation process.

Increasing simulations are being used in the computational synthesis process. In this process, solutions are automatically synthesized and then evaluated by simulation tools. Synthesis techniques range from simple graph grammar-based techniques to sophisticated evolutionary techniques such as genetic programming. Sometimes, case-based reasoning techniques are utilized to find a solution for a similar problem

and then modify it. Figure 1.4 illustrates the basic idea behind simulation-driven computational synthesis.

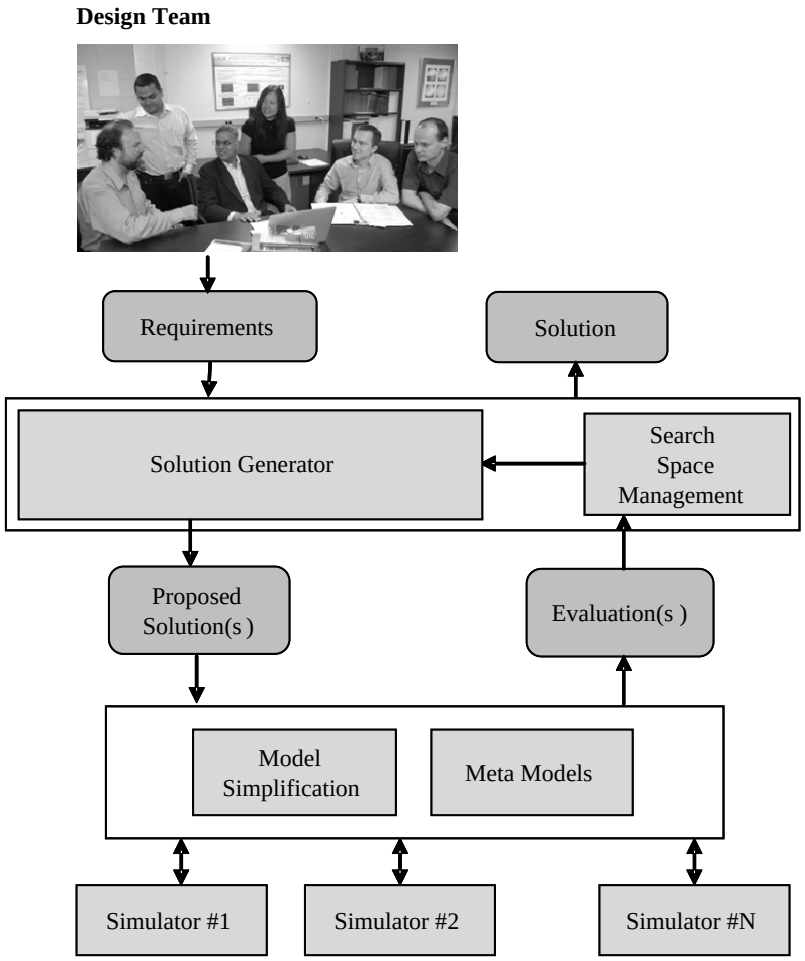

Figure 1.4: Simulation-driven computational synthesis.

A number of computational advances were needed to effectively exploit simulation during the innovation process. The following list mentions a few key advances:

- *Meta Modeling and Modeling Simplifications*: In order to use simulations as the main driver of the innovation process, a very large

number of alternatives need to be evaluated. High fidelity simulations tend to be quite slow. So using them directly is not practical. Hence we need to find a way to speed up the simulation process. Two different techniques have emerged as possible solutions. The first is called meta-modeling. In this technique, simulations are run offline over the desired design space. During the actual design exploration stage, archived results from the offline simulations are used. Often interpolations techniques are used to estimate results from the archived data points that are close to the current context. The second technique is called model simplification. This technique requires simplification of either the physics or the geometry involved so that the computational burden can be significantly reduced without overly compromising accuracy.

- *Hybrid Representations*: The success of simulation tools in design applications depends on finding the right representation. The choice of representation becomes very important when dealing with complex designs. Purely procedural representations do not result in acceptable performance for the reasoning needed for the design process. On the other hand, purely descriptive representations can be extremely large for complex designs, and hence the synthesis process may become impractical. Most complex products have hierarchical structures, and this characteristic can be exploited to find the right combination of declarative and procedural elements in the representation. Most modern 3D CAD systems use feature-based representations that are built on the concept of hybrid representations. These representations can be tailored to specific needs by utilizing user-defined features.
- *Human-Computer Interactions*: Human designers play a very crucial role in the simulation-based innovation and discovery process. An important issue is to determine the best roles for both humans and computers so that they can be utilized for the tasks that they do the best. Specifically, when the computer program is trying various options, the human designer should be able to visualize the search process and steer it in the right direction. Human designers should also have the ability to edit the solution being generated during and after the synthesis process. Furthermore, human designers should be able to define the relevant constraints and objective function and to iteratively adjust them during the course of synthesis process. The recent work in the area of human-computer interfaces in data mining provides a useful foundation for human-computer interfaces in simulation-driven innovation and discovery.

- *Methods for Exploration of Large Search Spaces*: An important reason behind the success of human designers in the synthesis step is that they construct problem-solving strategies specific to the particular problem instance being tackled. These instance-specific strategies are devised based on limited exploration of the search space of a given problem. For example, if human designers generate a solution and find it infeasible, then they avoid generating similar infeasible solutions and prune the search space appropriately. Application-specific knowledge is expected to play a very important role in generating innovative solutions by keeping the search focused. Methods to capture the application-specific knowledge and integrate it with the synthesis process are expected to provide the foundations for efficiently exploring large search spaces.
- *Reasoning Algorithms in the Presence of Uncertainties*: Simulation-based evaluation introduces inherent uncertainties in the evaluation process due to the limitations of the simulation. Moreover, several applications such as nano-particle-based energetics applications force us to work with entities that have inherent uncertainties. Hence it is very important to account for these uncertainties during the selection process. This requires developing representations to model uncertainties and reasoning algorithms that can cope with uncertainties in a rigorous way.

1.3 Organization of Book

Chapter 2 discusses the use of classical molecular dynamics simulations to simulate the mechanochemical behavior of small oxide coated aluminum nanoparticles. Much of the interest in nanoparticles is derived from an appreciation that chemical/physical properties often vary from those of the bulk material. Some of these properties, including increased reactivity, can simply be attributed to the high surface area to volume ratio of nanoparticles. Aluminum nanoparticles with a core diameter of approximately 5nm and 8nm are simulated with 1nm and 2nm thick oxide coatings or shells. Computed results include the diffusion coefficients of aluminum cations for each shell configuration and at various temperatures. The observed results are discussed and compared with the oxidation mechanisms reported in the literature. This study reports that the oxidation process for nanometer sized oxide coated aluminum particles is the result of an enhanced diffusion rate due to an electric field induced by the oxide shell.

Chapter 3 reports a study focused on the design and implementation of the energetic material triaminoguanidinium 1-methyl-5-nitrimino tetrazolate, which is a promising alternative to the secondary explosive

RDX. This study involves prediction of molecular and thermodynamic properties using *ab initio* methods that use high level, quantum chemical computations. This study also involved simulation of the long-term thermal stability of the compound. In these computational experiments, the compatibility of TAG-1MeAtNO_2 towards various other ingredients (nitroguanidine and methylammonium nitrate) in energetic formulations was investigated via simulations.

Chapter 4 presents an approach for simulation-based design of materials. The main focus of this study is on creating energetic materials using functionally graded materials concepts. This approach uses a process, known as twin screw extrusion, for continuous manufacturing of energetic polymer composites. It takes advantage of the continuous nature and superior mixing characteristics of the twin screw extrusion process to produce functionally graded energetic materials, a relatively new concept for propellants and explosives. One of the key attributes of this new approach is the ability to tailor the characteristics of the energetic material in several dimensions, depending on the desired system performance. This process holds the promise of developing an entirely new energetic material manufacturing approach, which would enable whole new classes of materials to be considered for development: materials previously ignored due to limitations of the entrenched batch processing approach historically used in energetics manufacturing.

Chapter 5 presents an approach that uses small scale testing to predict full scale explosion effects. This approach has been successfully used in underwater cratering and channeling, the loading on military vehicles due to the detonation of buried mines, the positive effects of bottom shaping for military vehicles to reduce this loading, and the movement of obstacles underwater by explosive charges. This study shows that small scale testing is cost efficient, more easily observed, and more easily instrumented. Small scale testing has been successfully used to predict full scale results in underwater cratering and channeling, the loading (both pressures and impulse) on military vehicles due to the detonation of buried mines, the positive effects of bottom shaping for military vehicles to reduce this loading, and the movement of obstacles underwater by explosive charges. These results have been supplied to code developers within the DOD to hone their computer simulations, and they have been used to develop scaling laws that would be applicable to full scale situations.

Chapter 6 discusses the development of new modeling capabilities for multiphase explosions containing a dispersed particle phase. Understanding the behavior of such multiphase explosions is critical for many applications, including hazard/risk assessment, energetic material

development, and propulsion. For hazard/risk assessment, events related to improvised explosive devices (IEDs), coal dust explosions, and gas-phase explosions with particulate debris are of concern. This work provides a basis of assessing both the dispersion of particles by high energy shock waves generated from energetic devices and the effect of particle dispersion and reaction on energetic performance. The approach is illustrated using the following three examples: (1) a nitromethane explosive with interspersed steel particles, (2) a PETN explosive with interspersed glass particles, and (3) aluminum combustion in post-explosion detonation wave propagation. Many advanced propulsion technologies for underwater or other applications may depend on multiphase energetic materials. Design optimization of such technology requires detailed models that can predict the behavior of such events within the context of the propulsion system.

Chapter 7 presents a review of different models and approaches to study blast wave interactions with soft-tissue matter. An increased focus has been place on understanding blast-related traumatic brain injury (BTBI) particularly in war related environments, as there is confirmed evidence that traumatic brain injury can be developed after exposure to blast originating from an explosion. Although brain injury mechanisms during direct (collision) and indirect (sudden acceleration/deceleration) impact have been widely studied, little is known about the inherent injury mechanism of blast-induced brain injury. A nonlinear visco-elastic model is incorporated into a system for studying interactions between blast waves and rigid structures supported by a visco-elastic material. This model is used to characterize brain tissue behavior by using experimental data. Another component includes a reduced-order model of a brain fiber bundle that is used to study wave propagation along such bundles. It can help us understand the role of a protective shell or rigid structure. The results show that lighter rigid structures are better for blast protection than the heavier ones. The development of finite element models is unavoidable for further research in this area, as a complete brain model, containing the network of brain fibers, should be developed in order to observe the real energy pathways inside the brain. This will help confirm or refute the hypothesis that stress waves travel through the brain fibers and stress localization along them leads to injury. Finite element models that incorporate explosions in air, the skull/brain system and fluid-structure interactions need to be developed to study systematically the phenomenon of blast related brain injury.

Modeling and simulation is playing a major role in the development of autonomous systems. A reasonable argument can be made that the nation that first masters autonomy will be in an economically advantageous position with respect to the global marketplace, and will

have enhanced security. Chapter 8 describes a new approach for automated development of planning logic using simulation-based synthesis. The planning logic is represented as a decision tree, which consists of high-level controllers as building blocks, conditionals and other program constructs. Strongly-typed genetic programming-based evolutionary framework is used for automatic generation of planning logic for blocking the advancement of a computer-driven intruder boat toward a valuable target. The results reported in this chapter show that the automatically generated planning logic was able to find and exploit repetitive motion patterns in the intruder's behavior for effective blocking.

Chapter 9 presents a simulation-based approach to the design of drive mechanisms for flapping wing miniature air vehicles. In order to ensure that the payload capacity of the miniature air vehicles is maximized for a given wing area and flapping frequency, the drive mechanism must be carefully designed to reduce its mass and ensure that it meets the intended functional requirements. The overall design approach described in this chapter incorporates the advances in modeling and simulation methods in kinematic and dynamic analysis, finite element analysis, and manufacturability analysis. The applicability of this design approach is demonstrated using two case studies.

Chapter 10 investigates the problem of task space synchronization and trajectory tracking for heterogeneous robots under dynamic uncertainties. Task space manipulation of multiple robotic manipulators by a single human operator is a challenging task. Synchronization has emerged as an important mechanism to achieve the desired cooperative behavior in the semi-autonomous robotic system. However, the focus of the current synchronization schemes has primarily been on joint-space control, and, in the absence of communication, unreliabilities between the agents. Exploiting passivity-based synchronization results developed previously, this chapter presents a new control algorithm to guarantee task space synchronization for a group of robotic manipulators. Both non-redundant and redundant robots are considered and the proposed scheme is validated by a numerical example and experiments.

1.4 Conclusions

Simulations are playing a very important role in the innovation and discovery process in the world of energetic systems applications. On one end of the spectrum, simulations present a fundamentally new way of discovering trends and insights that can be used by the designers to create new products and policies associated with the energetics applications. At the other end of the spectrum, simulations can directly

be used during the computational synthesis process to automatically design behaviors, policies, and structures. This book describes the following applications of simulations in the energetics application area:

- Discovery of new energetic materials
- Determining the right process conditions to manufacture high performance energetic materials using a novel manufacturing process
- Design of structures that are resistant to explosions and can protect human users
- Development of safety policies to cope with emergency situations associated with energetic materials
- Discovery of new control algorithms and planning logic to support robotics platforms used in energetic applications
- Design of unmanned vehicles used in energetic applications.

Chapter 2

Molecular Dynamics Simulation of Energetic Nanoparticles

Brian J. Henz and Michael R. Zachariah

Nanoparticles as ingredients in energetic materials are of increased interest due to the higher reactivity as compared to their micron sized counterpart and the higher energy density compared to traditional CHNO based energetics. However the basic mechanisms related to how these materials react and their inherent stability have hardly been explored. This chapter discusses the use of classical molecular dynamics simulations to simulate the mechanochemical behavior of small (i.e. core diameter < 10nm) oxide coated aluminum nanoparticles. Aluminum nanoparticles with a core diameter of approximately 5nm and 8nm are simulated with 1nm and 2nm thick oxide coatings or shells. In addition to thickness the shells are parameterized by varying degrees of crystallinity, density, and atomic ratios in order to study their effect on nanoparticle oxidation. The oxide shell is also parameterized to consider oxide coatings with the defects that commonly occur during the formation of an oxide layer and for comparison with a defect free crystalline oxide shell. Computed results include the diffusion coefficients of aluminum cations for each shell configuration and at various temperatures. The coated nanoparticles are heated from room temperature to temperatures above the melting point of the aluminum core and subsequently above the melting point of the oxide shell. The observed results are discussed and compared with the oxidation mechanisms reported in the literature. From this effort we have found that the oxidation process for nanometer sized oxide coated aluminum particles is the result of an enhanced diffusion rate due to an electric field induced by the oxide shell. This is in disagreement with some of the

current literature, which is based on the assumption that the oxidation process is initiated by mechanical failure of the oxide shell.

2.1 Introduction

The high enthalpy of combustion from the oxidation of metal nanoparticles has prompted the addition of metal nanoparticles into propellants and explosives. It is likewise because of this high enthalpy of combustion that these materials also form an oxide layer during manufacture or after exposure to the atmosphere. It is therefore important to understand not only the combustive reaction of the bare nanoparticle but also how the oxide layer affects further oxidation.

Much of the interest in nanoparticles is derived from an appreciation that chemical/physical properties often vary from those of the bulk material. Some of these properties, including increased reactivity [1], can simply be attributed to the high surface area to volume ratio of nanoparticles. However, it is known that catalytic activity can be significantly changed from that of the corresponding bulk [23,24]. It is also well known that metal nanoparticles are pyrophoric and have enhanced energy release rates, which make them attractive in propulsion [2].

One material with widespread use as an energetic material is aluminum, which has been extensively analyzed and modeled. Many numerical models have been developed in an attempt to understand the combustion of aluminum particles. The primary disadvantage of these models is that they may work for micron sized particles where the mean free path is much shorter than the size of the particles, but this is not the case for nanoparticles, which by definition are less than 100nm in diameter. For the burning of aluminum nanoparticles, it is not possible to make continuum assumptions. Even with these complexities, aluminum nanoparticles are interesting because they have been found to enhance the burning of propellants by a factor of 5 to 10 over micron size particles.

Virtually all metal nanoparticles will nominally have a native oxide shell, which for aluminum is ~ 2-3 nm thick. Thus any oxidative reaction or vigorous combustion must proceed by transport of either the aluminum or oxidizer though the oxide shell. The oxidation reaction of oxide coated aluminum nanoparticles has been observed to occur at a lower temperature and a faster rate than that of micron sized particles, suggesting to some a different oxidation mechanism than observed in larger particles. In fact, nanoparticles have been experimentally shown to react at or near the melting point of bulk aluminum ~933K [2], whereas larger particles react closer to the melting point of the oxide shell, namely 2327K. The closeness of the reaction temperature to the melting

point of pure aluminum indicates that the melting of the aluminum core is the possible initiator of this reaction for nanoparticles.

The current body of literature for oxidation of oxide coated aluminum nanoparticles focuses on melting or mechanical failure (cracking) of the oxide shell as the initiator of the reaction mechanism. Examples of these theories are the melt dispersion mechanism presented by Levitas et al. [3,4], and the cracking and reduced temperature melting of the oxide shell presented by Puri and Yang[5]. In the reaction described by Levitas et al., the oxide shell ruptures from the internal pressure exerted on it due to the expansion of the aluminum core upon melting. This scenario, the so-called melt dispersion mechanism, assumes some property values, in particular that the diffusion coefficient of the aluminum cations must be below 10-5 cm2/s [3], or more specifically around 10-18 cm2/s for the melt dispersion mechanism to occur. In Levitas et al. [3,4], the author also finds that for rupture to occur the ratio of the oxide shell thickness to the nanoparticle radius must be larger than 5 for an assumed shell strength of about 1/3 of the theoretical strength for Al2O3. This equates to a core/shell ratio of over 20 for shells approaching the theoretical strength of Al2O3. This maximum nanoparticle size falls outside of the range of nanoparticles analyzed in this work and will be considered in a future effort. In this work we have investigated core radius to shell thickness ratios of between 1.3 and 5.3, and comment on the trends observed. Another possible oxidation ignition process for nanoparticles in the size range considered here is put forward by Puri and Yang [5]. In [5] the oxidation process does not ignite until the oxide shell melts and the core aluminum is exposed to oxygen in the surrounding environment. Since the melting temperature of the oxide shell is lowered by the small size of the particle, the shell is predicted to melt at around 1100K [5], a much lower temperature than that observed in melting of bulk Al_2O_3, namely 2327K, but it is relatively close to the melting temperature of bulk aluminum.

Molecular dynamics (MD) simulations performed here show another possible mechanism for ignition of the oxidation process for oxide coated aluminum nanoparticles, namely rapid diffusion driven by an induced electric field. [18] The flux of aluminum cations driven by this electric field through the oxide shell limits the internal pressure buildup during heating and melting of the aluminum core by driving atoms from the core into the shell. Experimentally produced hollow aluminum oxide nanoparticles provide support for this rapid diffusion hypothesis [9,10] by illustrating that it is possible to produce undamaged hollow oxide shells as a result of the oxidation process. Additionally, it has been observed that ignition delays can be varied by deliberate thickening of the oxide shell and that these delay times are consistent with a diffusion

mechanism [37,38]. The primary discrepancy between the aforementioned experimental work and the computer simulations performed here is that the temperatures considered in the experiments were below the melting point of the aluminum core. Additional support for this transport mechanism comes from other numerical [11,12] and experimental studies [13,14].

This work explores the pressure generated in the core and oxide shell during melting of the aluminum core and compares results for three sizes of aluminum cores, namely 5.6nm, 8.2nm, and 21nm. The oxide shell thicknesses considered are 1nm and 2nm, with various configurations from amorphous to crystalline. The results of these simulations are used to compare with the oxidation mechanisms reported elsewhere [6-8]. We will also comment on expected size dependent trends, providing some thoughts as to the mechanisms expected in nanoparticles larger than those explicitly simulated here. It has previously been assumed that either the sudden decrease in density of the aluminum upon melting [3,4] or the lower melting temperature of the nanometer sized oxide shell [5] is the key to initiation of the oxidation process. However, in this paper we explore the possibility that built-in electric fields, as opposed to Fickian diffusion, drive aluminum cations through the oxide shell to the nanoparticle surface where it is possible for the oxidation process to proceed. Experimentally produced hollow aluminum oxide nanoparticles provide support for this rapid diffusion hypothesis [9,29]. These hollow oxide shells illustrate that the predicted result of this diffusion oxidation process is experimentally observable. We will show that field mediated ion-transport is much faster than Fickian diffusion, and will be the dominant transport process in the oxidation of nanoaluminum. Anecdotal support for this mechanism comes from numerous numerical [10,20] and experimental studies [21,22].

2.2 Simulation Approach

Molecular Dynamics (MD) simulations are used in this work to compute the equilibrium and transport properties of classical many-body systems. The MD algorithm defines atoms or molecules to be treated as particles that obey the laws of classical mechanics. With this treatment the particle positions are calculated using Newton's equations of motion. The Verlet algorithm is used to integrate these equations of motion and to calculate the positions of the simulated particles at all times using equation 2.1.

$$\vec{x}(t+\Delta t) = 2\vec{x}(t) - \vec{x}(t-\Delta t) + \frac{\vec{f}(t)}{m}\Delta t^2 \tag{1}$$

In equation 1, $\vec{x}$ is the position of a particle, $\vec{f}$ is the force acting on the particle computed from interaction potentials with other particles, m is the particle mass, and t+Δt is the time at which the particle positions are computed.

The study of oxide coated aluminum poses several challenges to a molecular simulation. In particular the choice of interatomic potential is critical due to charge transfer between Al and O and its evolution of the Al/O ratio during oxidation. This has numerical complexities beyond a simple multibody interaction. This work uses the ReaxFF potential, which has been demonstrated to accurately simulate the material system of interest, namely aluminum oxide [6,7].

The ReaxFF potential contains many more terms and is much more computationally complex than any of the previously discussed potentials. As an illustration, all of the energy terms that may be provided for a material system are given in equation 2:

$$E_{system} = E_{bond} + E_{over} + E_{under} + E_{lp} + E_{val} + E_{pen} + E_{tors} + E_{conj} + E_{vdWaals} + E_{Coulomb} \quad (2)$$

The terms in equation 2 are bond energies (Ebond), under-coordination penalty energies (Eunder), lone-pairs energies (Elp), over-coordination penalty energies (Eover), valence angles energies (Eval), energy penalty for handling atoms with two double bonds (Epen), torsion angles energies (Etors), conjugated bonds energies (Econj) and terms to handle non-bonded interactions, namely van der Waals (EvdWaals) and Coulomb (ECoulomb) interactions. The potential terms required for the aluminum oxide material system are ECoulomb, Ebond, Eover, and EvdWaals.

The Al-O potential parameter set used in this work comes from a previous effort that considered the sliding of Al2O3 coatings against Al and Al2O3 [7]. The computational requirement of this software is high, with the largest system here containing nearly 100,000 atoms, and is simulated efficiently with 96 Intel Woodcrest processor cores running at 3.0 GHz.

2.3 Model Description

Several core sizes are considered here. The smaller of these consists of a 5.6nm diameter core of aluminum with either a 1nm or 2nm thick shell of Alumina (Al2O3) as illustrated by the example systems in Figure

2.1. Dark spheres represent oxygen atoms and light spheres denote aluminum atoms.

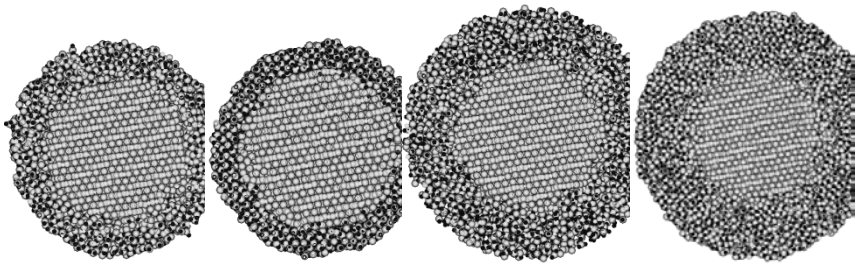

(a) (b) (c) (d)

Figure 2.1: Cross sections of some of the oxide coated aluminum nanoparticle models used in this work. a) 1nm thick, dense oxide shell. b) 1nm thick, crystalline oxide shell. c) 2nm thick, amorphous oxide shell. d) 2nm thick, dense oxide shell with 2:2.7 Al:O ratio.

The larger particles used in this effort include an 8.2nm aluminum core and a 21nm aluminum core with a 2nm thick crystalline oxide shell, as shown in Figure 2.2. Light denotes aluminum atoms and oxygen atoms are dark.

There are four shell configurations considered for each oxide shell thickness:

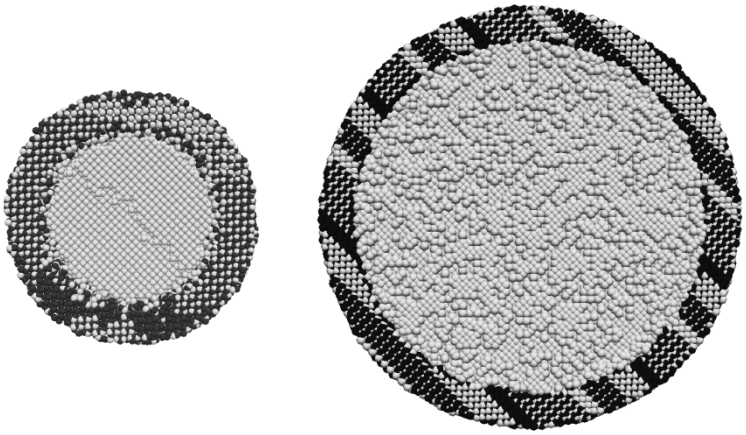

Figure 2.2: Configuration of atoms for larger (8.2nm, left) and (21.0nm, right) nanoparticle cores

A defect free crystalline shell that may result from extremely slow or high temperature formation. This shell is modeled by coating a bare aluminum nanoparticle with a crystalline shell made up of α-Al2O3. The alpha form is used as a representative crystalline shell configuration.

A dense amorphous shell that has an atomic ratio of 2:3 aluminum to oxygen atoms (i.e. Al2O3). This shell is formed by heating the oxide shell above its melting temperature while holding the aluminum core atom positions fixed. In this way the oxide layer melts and then is rapidly cooled and trimmed in order to obtain a slightly amorphous oxide layer with the desired thickness.

A dense amorphous shell 10% deficient in oxygen atoms, Al/O = 2:2.7. This shell may form during a faster rate of formation or if the environment during formation was oxygen lean. In the computer simulation this shell is formed by removing 10% of the oxygen from the previous dense oxide shell that is at the stoichiometric ratio of 2:3 aluminum to oxygen atoms.

Lastly, a porous amorphous shell with an atomic ratio of 2:3 aluminum to oxygen atoms. This shell has approximately one half of the density of the previously described dense shell with the same atomic ratio. This more porous amorphous shell represents oxide formation that *may occur at a very fast rate with a sufficient presence of oxygen.* This oxide shell is formed in the computer simulation similarly to the process used for the dense shell, except that the shell is repeatedly heated to a higher temperature and rapidly cooled until a much more amorphous configuration is achieved.

Following the creation and equilibration of the oxide shell, the model systems were heated at rates of 1011K/s, 1012K/s, and 1013K/s in order to determine any rate dependencies. We found, similarly to Levitas et al. [3,4], that at rates below 1012K/s the heating rate appears to have little effect on the simulation results. This is important, as lower heating rates would increase the number of MD simulation time steps, which for this work was ~ 1fs to maintain energy conservation, to a level that would be unreasonable with current computing capacities. The temperature of the model systems was raised from 300K to 1000K and eventually up to 3000K, which is much higher than the melting point of the oxide layer. From experimental data available in the literature [2], it is expected that some reaction should be observed near the melting point of the aluminum core. At the melting point of the core the aluminum density decreases from 2.7g/cm3 to 2.4g/cm3, resulting in a volumetric expansion of about 12%. Melting of the oxide shell requires heating the nanoparticle to above the melting point of the oxide, which is 2327K for the bulk material or somewhat less for a nanoparticle shell because of the

size affect. The results of each of these efforts are detailed in the following sections.

2.4 Results of Rapid Heating Simulations

The simulations in this section were carried out in a vacuum so that as Al cations move radially outward towards the oxide surface there are no oxygen molecules available for oxidation reactions. In simulations discussed later we have found the diffusivity of Al through the oxide layer to be more important than oxygen diffusion towards the core. For this reason we are primarily concerned in this work with the mechanism by which Al cations reach the surface of the nanoparticle. Initially, the nanoparticles were heated from 300K to about 1000K, which is above the core melting point but below the size dependent oxide melting point reported by Puri and Yang [5]. At around 900K, or slightly below the bulk melting temperature of the aluminum core, a rapid volumetric expansion of the core is observed, indicating that the aluminum core has begun to melt. At 1000K the oxide shell still remains intact, with no cracking, even when maintained at that temperature for 100ps. We do see however, as illustrated in Figure 2.3, the initiation of aluminum cation diffusion to the particle surface.

The results in Figure 2.3 show a slightly inhomogeneous melting of the aluminum core, which is evident in the “1000K, +0ps” plot. Some of the less dense faces of the core begin to melt while the top and bottom remain crystalline, giving the nanoparticle a slightly elongated appearance. The plots in Figure 2.3 also show the mechanism by which oxidation will proceed at elevated temperatures. The first observation is that the oxide shell does not crack as one might expect, if diffusion were extremely limited or the shell were brittle. This suggests that the shell is more elastic at this scale, or the expansion of the aluminum is insufficient to cause failure in the shell, even at these elevated temperatures. One possible reason for the enhanced elasticity is the lower coordination of the atoms in the oxide shell as compared to the bulk material [14], which is incidentally also a contributing factor to the size dependent melting temperature observed in nanoparticles. In addition, we observe significant diffusion of the core atoms through the oxide shell, thus relieving the potentially high internal pressures. The primary mechanism driving this diffusion is discussed in the following sections.

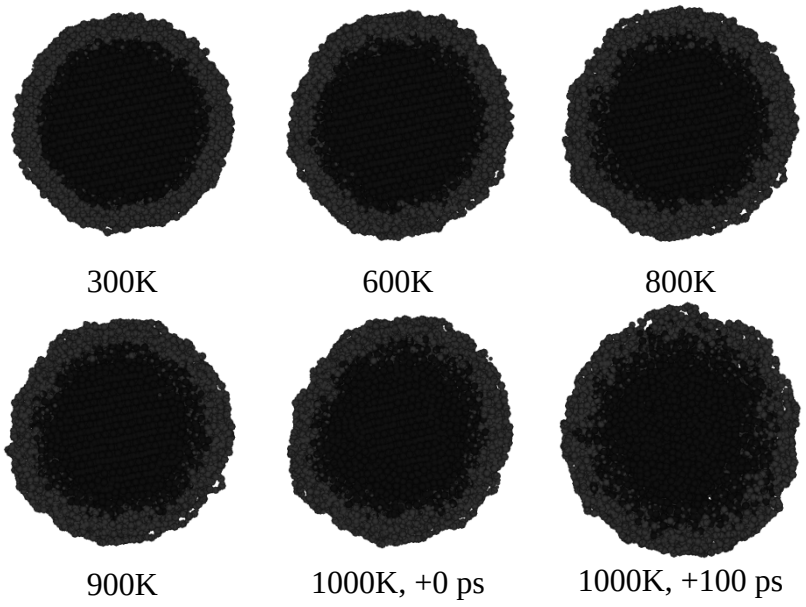

Figure 2.3: Plot showing diffusion of aluminum cations (darker) through the 1nm thick oxide shell (lighter) as the temperature increases from 300K to 1000K and held for 100 ps.

2.5 Aluminum Cation Diffusion through the Oxide Shell

As observed by us and by others [5], at temperatures below the melting point of the oxide shell there is significant diffusion of aluminum cations through the oxide shell. Computation of the diffusivity from the mean square displacement (MSD) of the aluminum cations yields values typically found for liquids. This was unexpected because these measurements were taken at 600K, somewhat below the melting temperature of the relatively small 5.6nm aluminum nanoparticle core. Although the MSD data is somewhat noisy because of the limited simulation time and small nanoparticle sizes, there is an obvious trend of proportionally increasing diffusion rates radially through the shell with increased temperature. To support this observation the radial diffusivity is compared to the overall diffusivity in Table 2.1.

Table 2.1: Diffusion coefficients for core aluminum atoms with various oxide shell configurations. The diffusion coefficients are for general diffusion (D) and radial diffusion (D_{radial}).

Shell Thickness	Type	Temperature	D (cm^2/s)	D_{radial} (cm^2/s)
1nm	Amorphous	600K	$5.3 \cdot 10^{-6}$	$5.9 \cdot 10^{-7}$
1nm	Amorphous	1000K	$4.2 \cdot 10^{-5}$	$3.0 \cdot 10^{-5}$
1nm	Amorphous	2000K	$7.1 \cdot 10^{-4}$	$8.3 \cdot 10^{-4}$
1nm	Dense	600K	$1.1 \cdot 10^{-6}$	$4.0 \cdot 10^{-7}$
1nm	Dense	1000K	$3.4 \cdot 10^{-5}$	$2.8 \cdot 10^{-5}$
1nm	Dense	2000K	$1.3 \cdot 10^{-4}$	$1.3 \cdot 10^{-4}$
1nm	Dense, $Al_2O_{2.7}$	600K	$2.6 \cdot 10^{-7}$	$2.1 \cdot 10^{-7}$
1nm	Dense, $Al_2O_{2.7}$	1000K	$3.8 \cdot 10^{-5}$	$1.9 \cdot 10^{-5}$
1nm	Dense, $Al_2O_{2.7}$	2000K	$6.0 \cdot 10^{-4}$	$6.7 \cdot 10^{-4}$
1nm	Crystalline	600K	$3.1 \cdot 10^{-6}$	$6.7 \cdot 10^{-7}$
1nm	Crystalline	1000K	$3.3 \cdot 10^{-5}$	$2.4 \cdot 10^{-5}$
1nm	Crystalline	2000K	$1.0 \cdot 10^{-4}$	$1.3 \cdot 10^{-4}$
2nm	Amorphous	600K	$2.3 \cdot 10^{-6}$	$4.6 \cdot 10^{-7}$
2nm	Amorphous	1000K	$4.0 \cdot 10^{-5}$	$3.2 \cdot 10^{-5}$
2nm	Amorphous	2000K	$7.7 \cdot 10^{-5}$	$6.6 \cdot 10^{-5}$
2nm	Dense	600K	$8.1 \cdot 10^{-7}$	$6.9 \cdot 10^{-7}$
2nm	Dense	1000K	$3.6 \cdot 10^{-5}$	$2.5 \cdot 10^{-5}$
2nm	Dense	2000K	$4.9 \cdot 10^{-5}$	$5.2 \cdot 10^{-5}$
2nm	Dense, $Al_2O_{2.7}$	600K	$4.2 \cdot 10^{-7}$	$3.3 \cdot 10^{-7}$
2nm	Dense, $Al_2O_{2.7}$	1000K	$3.7 \cdot 10^{-5}$	$1.8 \cdot 10^{-5}$
2nm	Dense, $Al_2O_{2.7}$	2000K	$2.7 \cdot 10^{-5}$	$1.0 \cdot 10^{-5}$
2nm	Crystalline	600K	$8.3 \cdot 10^{-7}$	$7.8 \cdot 10^{-7}$
2nm	Crystalline	1000K	$3.3 \cdot 10^{-5}$	$1.9 \cdot 10^{-5}$
2nm	Crystalline	2000K	$4.9 \cdot 10^{-5}$	$5.2 \cdot 10^{-5}$
2nm, 8nm Core	Crystalline	600K	$6.9 \cdot 10^{-7}$	$9.9 \cdot 10^{-7}$
2nm, 8nm Core	Crystalline	1000K	$1.9 \cdot 10^{-5}$	$1.6 \cdot 10^{-5}$
2nm, 8nm Core	Crystalline	2000K	$1.3 \cdot 10^{-4}$	$9.2 \cdot 10^{-5}$

The diffusion coefficients in Table 1 are computed using equation 3.

$$\frac{\partial\left\langle r^2(t)\right\rangle}{\partial t} = 2dD \tag{3}$$

In equation 3, the number of dimensions, d, available for atomic diffusion is 3 for overall diffusion and 1 for radial diffusion [27]. The use of the bulk diffusion equation is reasonable, since during the time scales considered the movement of only the atoms initially on the surface are restricted by the particle boundary [31]. For radial diffusion we are concerned only with the MSD directed radially from the center of the nanoparticle. In equation 3, t is the elapsed time and ⟨r2(t)⟩ is the MSD of the atoms being tracked. The diffusion coefficients reported are for all of the core atoms, including those near the center of the nanoparticle. This is important since we would expect the mechanical and electrostatic effects to be larger near the core/shell interface, but because of the small sample sizes available, computing a radial distribution of diffusivity is unreliable.

By comparing the radial and overall diffusivities in Table 2.1, an interesting trend is observed. As the temperature increases, the radial diffusivity becomes a generally more important portion of the overall diffusivity of aluminum cations. This result indicates that once the aluminum core has melted the diffusion of aluminum cations is preferentially in the radial direction, as compared to the results prior to melting. This is possibly due to a high pressure gradient near the core/shell interface pushing atoms out into the shell. The magnitude of this pressure effect will be discussed in a later section. Another possibility is that once the core has melted the atoms are more mobile, so in addition to pressure, any other effects such as an electric field will increase diffusion. The radial diffusion data that do not correlate with this observation at 600K are for the 2nm thick crystalline oxide shells for both the 5.6nm and 8.2nm aluminum cores. These configurations show diffusion rates that are on par with the overall diffusivity, possibly indicating that one of the drivers of radial diffusion is proportionally stronger for these shell configurations at 600K. We will show in the following sections that the electric field is indeed strongest in the 2nm thick crystalline shells.

In Figure 2.4, the slope of the plot is the activation energy required for diffusion of aluminum cations, and it shows an expected decrease above the melting point of the core, at approximately 0.001/K. An Arrhenius plot of the diffusivity versus temperature is given for all eight of the oxide shell configurations used with the 5.6nm aluminum core in

this work. From Figure 2.4 we observe that a change in slope occurs near the melting point of the aluminum core, namely 1000K. This indicates that for temperatures above 1000K the activation energy required for cation diffusion is lower than for temperatures below 1000K. The increase in activation energy for the 1nm amorphous and dense oxygen poor shell is likely due to a lower melting point for these oxide shells. This is not the case for thicker or more crystalline shells where the oxide remains in the solid phase and does not undergo any phase transformation. In the remaining model systems the activation energy drops once the melting temperature is reached, indicating a change in diffusion mechanism. The primary changes that occur at around 1000K are the melting of the aluminum core, the associated volumetric expansion, and increased mobility of the aluminum atoms. This expansion is expected to greatly increase the pressure inside of the core and enhance the diffusion of aluminum cations radially outward through the oxide shell.

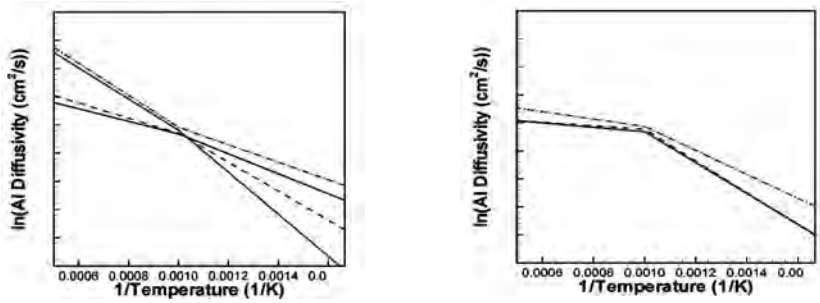

Figure 2.4: Arrhenius plot of ln(D) versus 1/T, where D is the diffusivity of the core aluminum atoms.

2.6 Induced Electric Field in Oxide Shell

One possible explanation for the computed rapid diffusion of aluminum atoms through the oxide layer is that they are driven by an induced electric field near the core/shell interface. The theory that oxidation growth proceeds via migration of charged particles is not a new one. In fact Carl Wagner proposed this theory in 1933 [15]. In a 1948 paper by Cabrera and Mott [10], the authors developed a theory focused on the growth of a thin oxide film on metal surfaces that is driven by an induced electric field. This electric field causes metal ions to migrate to the surface, increasing the oxide thickness until the induced

field is prevented by the thickening surface from causing further diffusion of metal cations. The maximum thickness of the oxide layer that is formed with this process increases with temperature, up to a critical temperature above which growth of the oxide layer will continue indefinitely.

Recent theoretical and experimental evidence points to the importance of the induced electric field described by Cabrera and Mott in the oxidation of oxide coated metal nanoparticles. Zhdanov and Kasemo [28] recently performed an analysis of the induced electric field in oxide coated nanoparticles. They found that by considering the size and geometry effect of nanoparticles coated with oxide shells, the induced electric field will be much stronger than that observed in a flat surface, thus increasing the associated oxidation rate exponentially in oxide coated nanoparticles. We have also observed the formation of hollow particles [9, Figure 2] during the oxidation of oxide coated aluminum, which we attributed to the faster diffusion of Al cations. Subsequently, Nakamura et al. [29] also observed formation of hollow metal oxide nanoparticles from oxidation of metals and attributed the rapid diffusion of metal cations through the oxide shell to the induced electric field. In the following sections we investigate the magnitude and effect of the induced electric field on the oxide coated aluminum nanoparticle system.

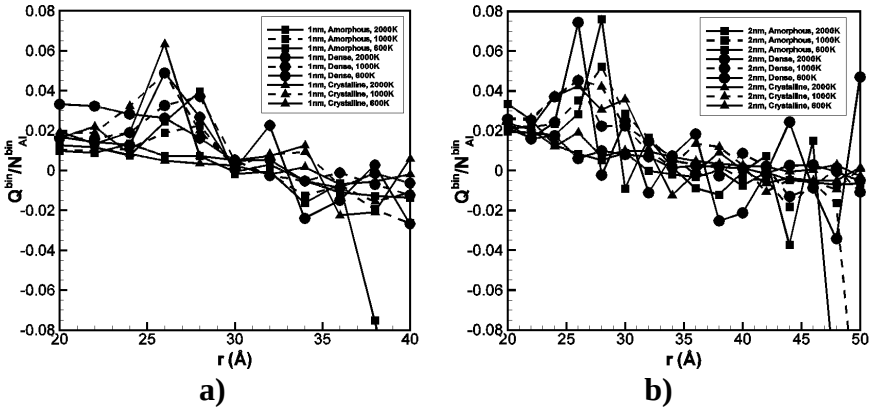

Figure 2.5: Radial charge distribution through the oxide shell (a) 1nm shell and (b) 2nm shell.

In the current simulation effort, rapid diffusion of aluminum cations through the oxide layer is observed. An indicator of the strength of the electric field is the radial charge density, which is computed through the nanoparticle at 2Å radial intervals. The computed charge density is averaged over 100ps of simulation time. Although noisy, which is

partially caused by atomic diffusion, it is apparent that there is a negative charge gradient throughout the oxide shell. This charge gradient contributes to the out flow of positive charges and the mass flux of aluminum cations at the core/shell interface.

The difference in charge density between the inner and outer surfaces of the oxide shell indicates that an electric field is induced, which will drive aluminum cations near the core/shell interface to the outer surface where they will be exposed to oxygen and oxidize. An approximate interaction between an aluminum cation and the core and shell can be computed using Gauss's Law. By assuming the atomic charges to be distributed approximately homogeneously in the shell and the core, the electric field on the surface of the core can be estimated as the field from a single point charge at the center of the core, through equation 2. If we assume the charge to be evenly distributed in the oxide shell, then the electric field inside of the shell from the atoms in the oxide shell is zero.

$$E = \frac{Q_{core}}{4\pi\varepsilon_0 r^2} \tag{4}$$

In equation 4, Qcore is the total charge of the core, r is the radial position of the interfacial aluminum atom of interest, and ε_0 is the permittivity of a vacuum. Using equation 4 the electric fields from the various oxide coated models are computed in Table 2.2. Note on electric field units, N/C = 0.01 V/m.

Table 2.2: Total charge of aluminum core and associated electric field given for all of the core/shell configurations considered.

Shell Thickness	Type	Temperature	Q_{core} ($C*10^{-18}$)	E ($N/C*10^{10}$)
1nm	Amorphous	600K	8.28	1.10
1nm	Amorphous	1000K	5.67	0.75
1nm	Amorphous	2000K	1.47	0.20
1nm	Dense	600K	11.4	1.52
1nm	Dense	1000K	8.86	1.18
1nm	Dense	2000K	4.01	0.53

1nm	Dense, $Al_2O_{2.7}$	600K	7.91	1.05
1nm	Dense, $Al_2O_{2.7}$	1000K	6.38	0.85
1nm	Dense, $Al_2O_{2.7}$	2000K	1.09	0.14
1nm	Crystalline	600K	12.7	1.69
1nm	Crystalline	1000K	10.8	1.44
1nm	Crystalline	2000K	3.04	0.40
2nm	Amorphous	600K	13.3	1.77
2nm	Amorphous	1000K	11.9	1.58
2nm	Amorphous	2000K	4.61	0.61
2nm	Dense	600K	13.8	1.83
2nm	Dense	1000K	12.7	1.69
2nm	Dense	2000K	4.21	0.56
2nm	Dense, $Al_2O_{2.7}$	600K	11.6	1.54
2nm	Dense, $Al_2O_{2.7}$	1000K	11.1	1.47
2nm	Dense, $Al_2O_{2.7}$	2000K	7.80	1.04
2nm	Crystalline	600K	15.6	2.08
2nm	Crystalline	1000K	13.9	1.85
2nm	Crystalline	2000K	4.39	0.58
2nm, 8nm Core	Crystalline	600K	43.9	2.47
2nm, 8nm Core	Crystalline	1000K	42.6	2.40
2nm, 8nm Core	Crystalline	2000K	30.4	1.71

In Figure 2.6, the volume between the core surface and outer surface of the oxide shell is assumed to be a vacuum. For the purpose of computing the electric field, this assumption is valid so long as the charges in the oxide shell are distributed radially only. With a radially distributed charge, the electric field due to the oxide shell is zero

everywhere for atoms at the core/shell interface or inside the aluminum core.

The most obvious trend observed in Table 2.2 is the decreasing core charge and electric field strength with increasing temperature. This is likely due to the fact that as shown in Table 1, diffusivity increases as temperature increases, and smears the boundary between the core and shell. Another observed trend, albeit weaker, is an increase in electric field as the shell becomes thicker and more organized. So in going from an amorphous 1nm thick shell to a 2nm thick crystalline shell, we observe a 100% increase in the electric field strength. This observation is supported by the analysis of Zhdanov and Kasemo [28].

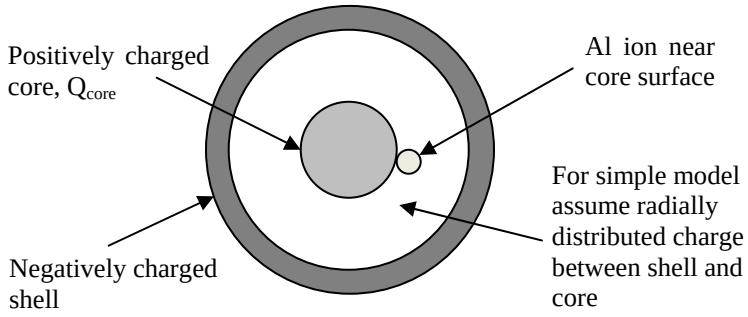

Figure 2.6: Schematic of assumed charge distributions affecting electric field around core surface aluminum atoms.

A more accurate method for computing the electric field at each ion is to use Coulomb's Law and to sum the discrete contribution from all the neighboring charges. Using this method is straight forward since there are a finite number of discrete charge carrying atoms. In Figure 2.7, the computed electric field, using equation 5, is plotted at each of the core aluminum atoms.

$$E = \frac{q}{4\pi\varepsilon_0 r^2}\hat{e}_r \tag{5}$$

In equation 5, $\hat{e}_r$ is the radial unit vector coming from the neighboring atom and q is the charge associated with the neighboring atom. Summing each of these vectors for all of the core atoms gives the results as shown in Figure 2.7 for 600K, 1000K, and 2000K.

In 2.7, the results are for the 5.6nm core with a 2nm thick crystalline shell. Note the generally radial direction of the field. The electric field plotted is within one order of magnitude of the simple model results, tabulated in Table 2.2, that assume a homogeneous charge distribution in the core and oxide shell.

The direction of the computed electric field indicates that the mass flux due to the electric field is directed out through the oxide shell. It does not act to randomly rearrange the atoms. The positively charged aluminum atoms will therefore be preferentially directed towards the outer surface of the oxide shell, where they will come into contact with oxygen ions and oxidize.

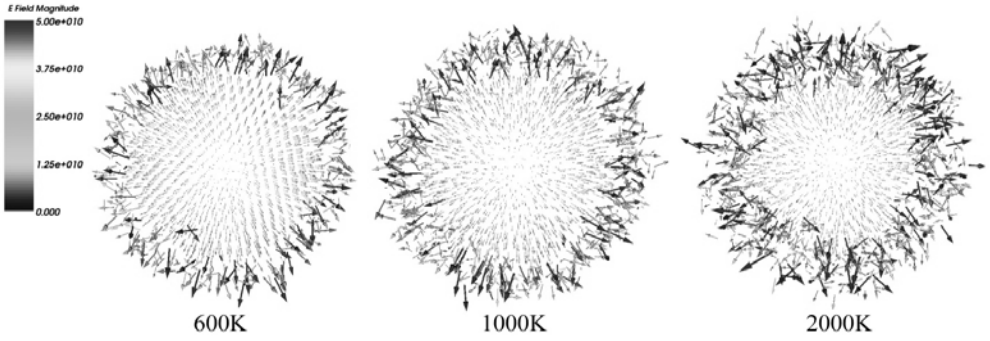

Figure 2.7: Electric field (N/C) at each of the core Al atoms in the nanoparticle core computed using Coulomb's Law.

With the diffusion coefficients previously computed and the electric field results computed here, it is possible to compute the mass flux due to concentration gradients (Jd), the electric field (Je), and the internal pressure (Jc). The relative magnitude of the effect of the electric field on Al ion diffusion can be computed using the Nernst-Planck equation, given in equation 6 [30].

$$J = -D\frac{dC}{dx} - \frac{zFDC}{RT}\frac{d\phi}{dx} + Cv \tag{6a}$$

$$J = J_d + J_e + J_c \tag{6b}$$

If we assume a zero molar concentration of Al cations in the shell and the bulk concentration at the interface, then the parameters for equation 4a are given as the following:

$$C = 0.1\,{}^{mol}\!/_{cm^3}$$
$$\frac{dC_{1nm}}{dx} = 1.0 \cdot 10^6\,{}^{mol}\!/_{cm^4}$$
$$R = 8.314\,{}^{C \cdot V}\!/_{mol \cdot K}$$
$$F = 96485\,{}^{C}\!/_{mol} \qquad (7)$$

The electric field computed in Table2.2 is the negative of the charge gradient dφ/dx.

The convective flux Jc in equation 4 is the drift velocity of metal ions through the core/shell interface due to constant force acting on the ions. The force on these ions comes from the pressure gradient and is due to the expanding aluminum melt. Only the radial drift velocity, and therefore the radial pressure gradient, in equation 6a is considered so that Jc can be rewritten as C (Dfr/kBT), where fr is defined as

$$f_r = -\frac{\partial V}{\partial r} = -\nabla p v_{Al} \qquad (8)$$

In equation 8, ∇p is the pressure gradient in the radial direction and vAl is the solubility of Al in the Al2O3 network [13]. The maximum pressure gradients observed in the simulations range from less than 1GPa/nm at 600K to 2GPa/nm at 1000K and above. For the solubility of Al in Al2O3 we have assumed a value that comes from previous analysis of oxygen and Al diffusion through Al2O3 and should therefore be a reasonable value. Assuming a value of about 0.02nm3 for the solubility of Al, vAl, it is possible to estimate the mass flux due to each term in equation 4. The diffusivity due to the drift velocity is directly proportional to vAl, but variations here of less than one order of magnitude would have little effect on the results in Table 2.3. The last column, labeled Ratio J_e to J, is the fraction of the total mass flux due to the induced electric field, with the balance due to the concentration gradient and drift velocities.

From the final column in Table 2.3, listing the ratio of Je to J, it is apparent that in all cases except for two, over 90% of the mass flux through the oxide shell is due to the induced electric field present at the core/shell. The exceptions to this 90% observation are the 1nm amorphous and 1nm dense Al2O2.7 shells at 2000K, which from

previous analysis appear to have undergone a phase change at this temperature. This illustrates the importance of considering the electric field in the oxide shell for any oxidation analysis of the oxide coated aluminum nanoparticle system. Another interesting trend is that the importance of the electric field in diffusion increases as the shell thickens and the temperature decreases. This trend, associated with the temperature, is expected since diffusion without an electric field is strongly temperature and pressure dependent, and at low temperatures diffusion would be very slow without an electric field. The trend associated with shell thickness requires some more thoughtful analysis. By considering the computed electric fields in Table 2.2, we observe that the magnitude does indeed increase with shell thickness, while the overall mass flux decreases, Table 2.2 and Figure 2.8.

Table 2.3: Diffusivity and mass flux computed at 600K, 1000K, and 2000K for all shell configurations with the 5.6nm core unless noted.

Shell Thickness	Configuration	Temp.	J ($mol/cm^2 \cdot s$)	D ($cm^2/s*10^{-8}$)	Ratio J_e to J
1nm	Amorphous	600K	4.20	1.97	0.98
1nm	Amorphous	1000K	11.97	13.6	0.96
1nm	Amorphous	2000K	53.45	424.0	0.83
1nm	Dense	600K	3.03	1.03	0.99
1nm	Dense	1000K	11.49	8.33	0.97
1nm	Dense	2000K	35.18	110.8	0.93
1nm	Dense, $Al_2O_{2.7}$	600K	2.13	1.03	0.98
1nm	Dense, $Al_2O_{2.7}$	1000K	8.06	7.88	0.96
1nm	Dense, $Al_2O_{2.7}$	2000K	46.27	426.0	0.78
1nm	Crystalline	600K	5.08	1.55	0.99
1nm	Crystalline	1000K	14.72	8.75	0.98
1nm	Crystalline	2000K	35.58	147.0	0.91

2nm	Amorphous	600K	3.31	0.97	0.99
2nm	Amorphous	1000K	18.49	10.0	0.98
2nm	Amorphous	2000K	23.73	65.2	0.94
2nm	Dense	600K	1.26	0.35	0.99
2nm	Dense	1000K	6.13	3.11	0.98
2nm	Dense	2000K	11.34	33.8	0.93
2nm	Dense, $Al_2O_{2.7}$	600K	3.69	1.23	0.99
2nm	Dense, $Al_2O_{2.7}$	1000K	7.99	4.58	0.98
2nm	Dense, $Al_2O_{2.7}$	2000K	5.27	8.38	0.96
2nm	Crystalline	600K	7.83	1.94	0.99
2nm	Crystalline	1000K	15.06	6.98	0.98
2nm	Crystalline	2000K	6.81	19.6	0.93
2nm, 8nm Core	Crystalline	600K	17.27	3.59	0.99
2nm, 8nm Core	Crystalline	1000K	24.31	8.61	0.99
2nm, 8nm Core	Crystalline	2000K	31.27	30.8	0.98

In Figure 2.8 we observe some interesting trends not necessarily apparent in Table 2.3. For nanoparticle systems at 600K and 1000K, the degree of crystallinity in the oxide shell does not appear to have a noticeable effect on the mass flux of the aluminum cations through the oxide shell. This result is interesting because we can conclude that the reaction rate for oxide coated aluminum nanoparticles in this size range will not be dependent on how the coating was formed or upon its thickness, up to 2nm.

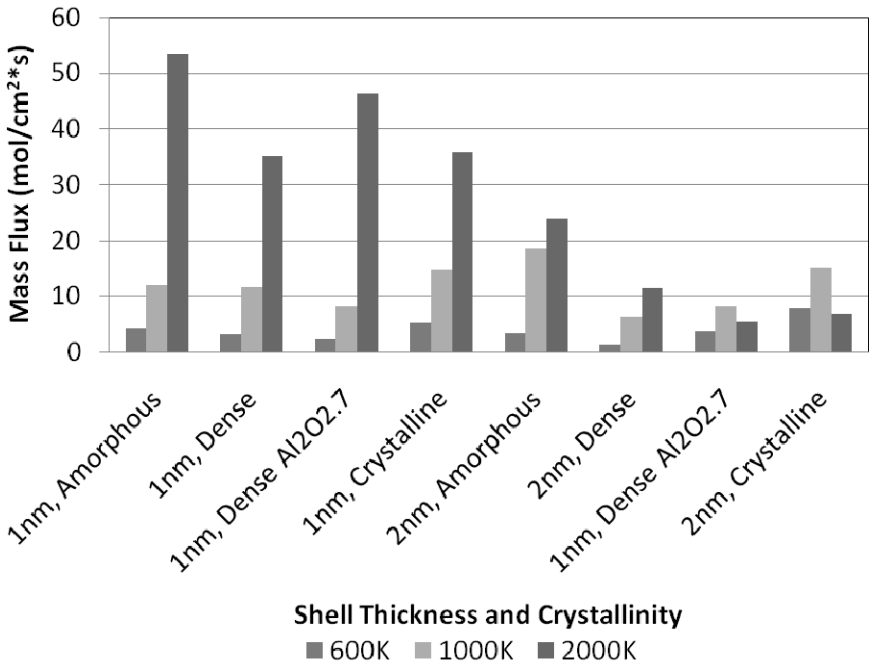

Figure 2.8: Plot of mass flux versus temperature and shell configuration.

The most apparent trend in Figure 2.8 is that the mass flux of aluminum atoms through the shell at 2000K decreases with increasing shell crystallinity and thickness. This result is likely due to the increased dependence of total mass flux on the concentration gradient and drift velocity terms in equation 6, as opposed to being solely due to the electric field. This is observed as lower values in the last column in Table 2.3 for 2000K versus 600K and 1000K. Since the heating rate required to reach 2000K before an appreciable amount of the core has diffused into the shell is so high (greater than 1012K/s), we would not expect this to be an experimentally observable result without some sort of very rapid heating method.

2.7 Computed Stress in Oxide Shell

When aluminum undergoes the phase change from solid to liquid it experiences a volumetric expansion of about 12%, i.e. the density decreases from 2.7g/cm3 to 2.4g/cm3. Due to this volumetric expansion of the aluminum in the nanoparticle core, it is expected that large tensile

stresses in the oxide shell will be generated. Other factors that will affect the stress in the shell include compression of the core due to surface tension, the bulk modulus of the liquid aluminum, differences in thermal expansion coefficients between the core and shell, and any plastic deformation of the shell that may occur prior to rupture.

A parametric analysis of the pressure and fraction of melt in the aluminum core was performed previously by Levitas et al. [3]. From Levitas's analysis, fracture of the shell is not expected to occur for ratios of core radius to shell thickness below 5, even for shell strengths approaching 50% of ideal. Using the thinnest shell considered by Levitas et al. [3], i.e. 2nm, would require a core of radius 10nm and result in a model with on the order of 10^6 atoms. When considering charge equilibration, such as in the ReaxFF empirical potential, this becomes a very expensive computation. For a direct comparison with this analysis we have simulated homogeneous heating of a 21nm diameter aluminum core coated by a crystalline 2nm thick oxide shell. With a shell thickness of 2nm this results in a core/shell ratio of about 5.3.

In order to compute the pressure in the nanoparticle core and shell, the virial stress [33,34] formulation is required because of the numerous multibody terms in the ReaxFF empirical potential. Results from the virial stress formulation include a stress tensor and pressure value at each of the atoms in the nanoparticle core and shell. The result of the virial stress formulation is a complete stress tensor at each atom multiplied by the atomic volume. By computing the trace of each of these tensors it is possible to obtain a pressure value at each atom. This pressure is then averaged over a period of 1ps-10ps. In Figure 2.9 the pressure is computed for the 5.6nm nanoparticle model with a 2nm thick, dense oxide shell. The pressure values are averaged within 0.4nm shells and over 10ps time periods.

In Figure 2.9 a positive pressure value is computed inside of the nanoparticle core, up to a radius of about 2nm (20Å). At the nanoparticle core/shell interface there is a rapid fluctuation in the pressure profile with a negative pressure in the remainder of the shell, indicating a tensile stress. Reasons for some of the noise observed in the pressure data include diffusion of atoms, particularly near the core/shell interface, lattice mismatch between core and shell, and a relatively small sampling size due to the number of simulated atoms. At the core/shell interface there is also the possibility of residual stresses due to mismatches in coefficients of thermal expansion. However, the overall trend is obvious, namely, that there is a compressive stress in the aluminum core and a tensile stress in the shell. Additionally, the pressure in the core increases appreciably when the system temperature is above the melting point of aluminum.

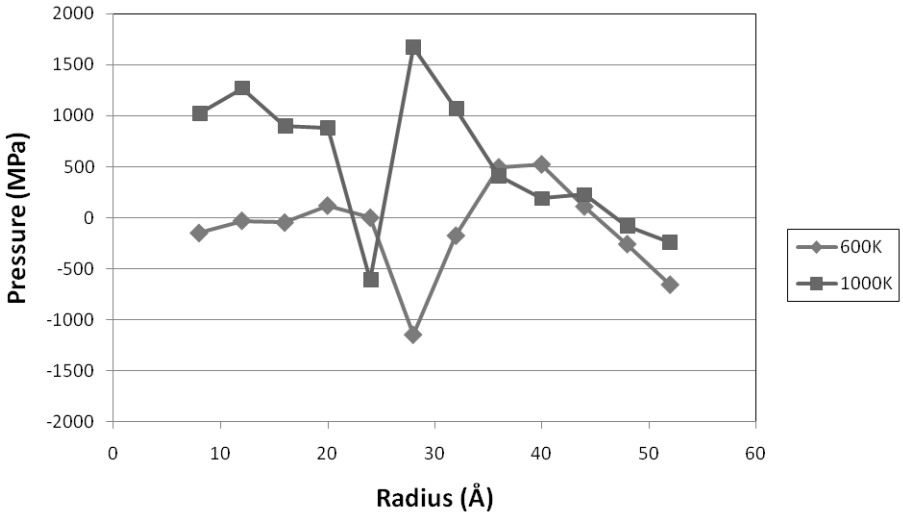

Figure 2.9: Radial pressure distribution for 5.6nm diameter aluminum core at 600K and at 1000K with 2nm thick dense oxide shell and a non-stoichiometric ratio of aluminum to oxygen.

The question then becomes: is the tensile stress in the shell high enough to cause failure, including cracking as some researchers have suggested may occur? [3,4] From these simulations and the mechanical analysis performed by Levitas et al. [4], the shell is not expected to rupture at these nanoparticle sizes. Furthermore we observe that the oxide shell does not crack, but rather aluminum ions diffuse through the shell to the oxide surface prior to forming aluminum oxide. For small nanoparticles Puri and Yang [5] suggest that complete oxidation occurs after the shell has melted, but from this effort and experimental observations [9,29] it appears clear that the induced electric field generates a diffusion rate sufficient to cause initiation of the oxidation process before melting of the shell. This diffusion process is expected to initiate the oxidation process with a high pressure gradient and electric field driving forces. After a sufficient number of the core atoms have diffused out through the shell to lower the pressure gradient across the oxide shell, only the electric field will drive diffusion. With the electric field driven diffusion and higher anticipated elasticity of the oxide shell at these small sizes, it is probable that the nanoparticle size at which mechanical failure of the oxide shell occurs is larger than suggested by previous efforts [3,4].

Simulations of the homogeneous heating of the 8.2nm core model result in the pressure profile shown in Figure 2.10. In this figure the pressure in the core and shell at ignition do not rise above approximately 1GPa, indicating that a homogeneously heated nanoparticle will not experience the high pressures necessary for rupture of the oxide shell. The low pressures observed in both model sizes, Figures 2.6 and 2.7, indicate that homogeneous heating is unlikely to produce the high pressure melt dispersion mechanism discussed elsewhere [3,4].

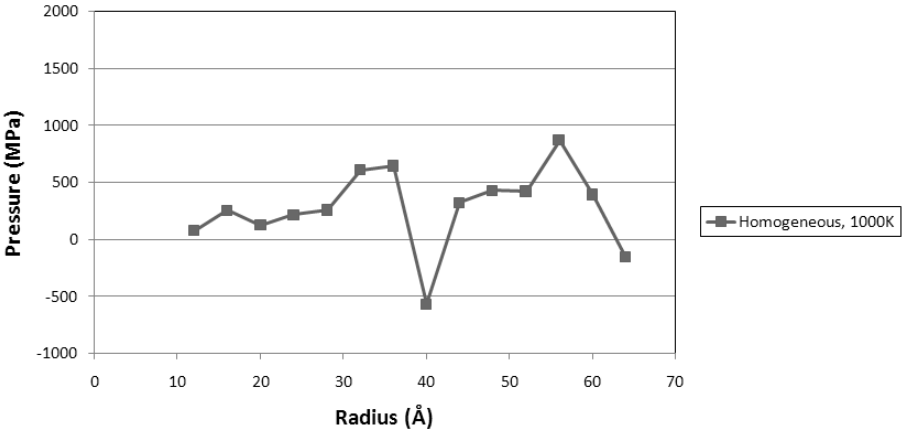

Figure 2.10: Radial pressure distribution for 8.2nm diameter aluminum core at 1000K with a 2nm crystalline oxide shell.

In the next section the same nanoparticle systems have been heated by laser heating in order to provide a heterogeneous radial temperature profile. It is expected that since the oxide shell will be at a lower temperature than in the homogeneous flame heating simulations, the mobility of the Al ions through the shell will be restricted, resulting in a higher pressure gradient at the core/shell interface.

2.8 Laser Heating Simulations

Laser heating is used in mass spectrometry analysis to rapidly heat a material sample until the atoms are ionized [35,36]. This heating method is considered here for oxide coated aluminum nanoparticles. We are interested in determining if the laser heating mechanism will cause a different failure process than the diffusion driven oxidation observed by

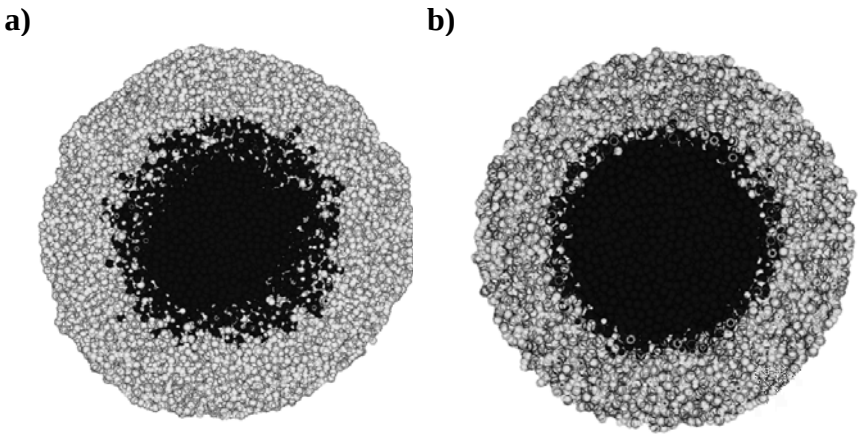

Figure 2.11: Plot of a 5.6nm aluminum core with a oxide shell at 1000K after 100ps (a), and the same nanoparticle heated using a laser resulting in a 1000K core and a 440K oxide shell after 100ps (b).

homogeneous flame heating of the nanoparticle core and shell. The laser heating method causes marginal heating in the oxide shell because the oxide shell absorbs energy inefficiently from the laser, resulting in a slow heating process, whereas the Al core is more efficient at absorbing the laser energy and is conversely heated very rapidly. The expected result of this heating method is a more brittle shell compared to what is observed during homogeneous heating of the oxide coated aluminum nanoparticle. It is anticipated that this heterogeneous heating process is more likely to result is mechanical failure of the oxide shell, or at least a higher internal pressure.

In Figure 2.11 we have plotted cross sections for a homogeneously and heterogeneously heated nanoparticle with a 5.6nm core and a 2nm thick crystalline shell after 100ps at 1000K. The cross section shown in Figure 2.11a is for the homogeneous heating process, whereas Figure 2.11b is for the heterogeneous laser heating process with the oxide shell held at 440K as assumed in the complete laser heating simulation.

In Figure 2.11, it is apparent that for the heterogeneously heated nanoparticle the amount of aluminum that has begun to diffuse through the oxide shell at 100ps is visibly lower than for the homogeneously heated nanoparticle. This supports the previous assumption that diffusion is restricted in the lower temperature oxide shell during laser heating when compared to the homogeneous heating process and is therefore more dependent upon the pressure gradient for diffusion, equation 6. The lower observed diffusivity is also expected to increase the pressures

computed in the core and oxide shell. Higher pressure values are more likely to result in mechanical failure of the oxide shell. In Figure 2.12 the pressure profiles for the laser heating and homogeneous heating process are compared.

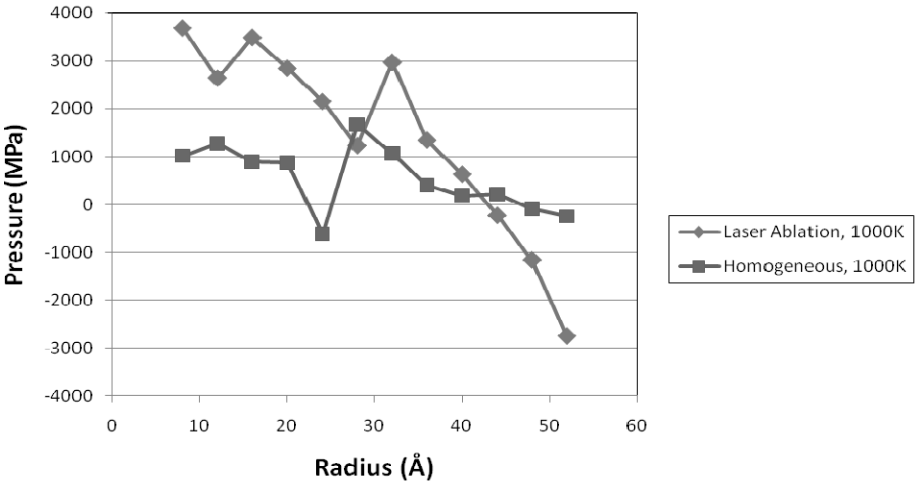

Figure 2.12: Pressure profile averaged over 8ps at 1000K for ambient heating and laser heating of 5.6nm core with 2nm crystalline oxide shell.

In Figure 2.12, a comparison of the radial pressure profiles for a homogeneously and heterogeneously heated oxide coated nanoparticle reveals a dramatic increase in the pressure magnitudes in the nanoparticle when laser heating is used. A compressive pressure in the nanoparticle core of about 3GPa is three times higher than that observed in the homogeneously heated core, likely due to the limited diffusion of core atoms and lower elasticity of the low temperature shell. The higher tensile stress, or negative pressure, in the oxide shell, combined with the lower aluminum ion diffusivity discussed previously, provides a clear indication that mechanical failure during the heterogeneous heating process is more likely than with the homogeneous heating process.

In order to investigate how the core and shell pressure results scale with core size we have computed the radial pressure distribution in the 8.2nm core model heated homogeneously and by laser heating, shown in Figure 2.10, and as was previously done with the 5.6nm core.

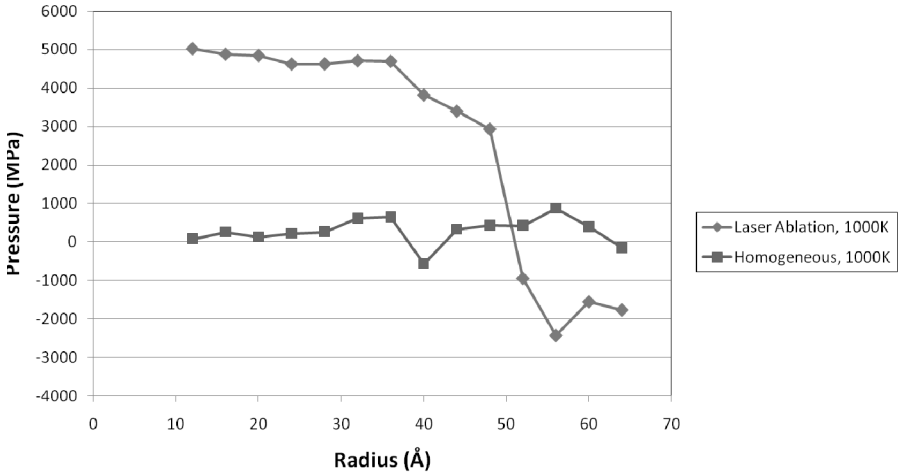

Figure 2.13: Pressure profile averaged over 8ps at 1000K for ambient heating and laser heating of 8.2nm core with 2nm crystalline oxide shell.

Most notable in comparing these pressure results, Figures 2.12 and 2.13, is the difference in pressure between the two systems. As the core size increases for the laser heating simulation, the pressure also increases noticeably. However, for the homogeneously heated nanoparticle case we do not observe the same trend; in fact little difference in pressure is seen with changes in core size. In Figure 2.14, the radial pressure profile is plotted for homogeneous heating of 5.6nm, 8.2nm, and 21nm aluminum cores coated with 2nm thick crystalline oxide shells.

Although some noise is present near the interface of the core and shell, a few conclusions may be drawn from these simulation results. First, the pressure through the core is homogeneous as would be expected and does not increase with core size. This supports our earlier observation that ignition of the oxidation process does not occur from a jump in pressure in the core from melting, but rather from enhanced mobility and the self-induced electric field in the nanoparticle. Second, the maximum compressive pressures in the core and tensile pressures in the shell are only around 1GPa, too low to cause failure of the oxide shell. This suggests that another ignition mechanism must be active at temperatures around 1000K, or slightly above the melting point of the aluminum core.

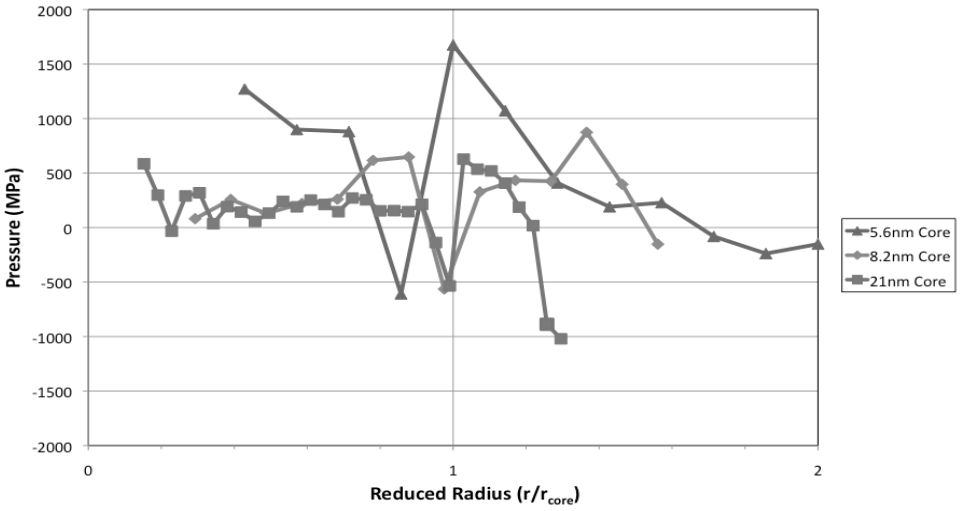

Figure 2.14: Reduced radius radial pressure profile (1.0 corresponds to core/shell interface) comparison for 5.6nm, 8.2nm, and 21nm aluminum cores coated with 2nm thick crystalline oxide shells.

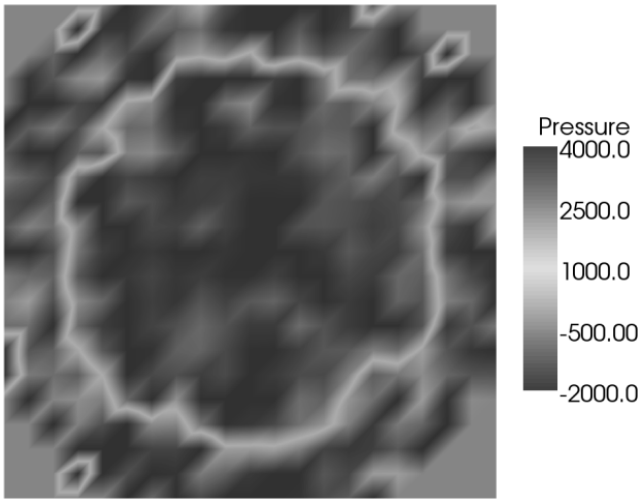

Figure 2.15: Cross section of 8.2nm core and oxide shell heated to 1000K by laser heating. Pressure units are MPa.

In order to visualize the steep pressure gradient at the core/shell interface we have computed the virial stress within 0.6nm voxels over 2ps intervals for the 8.2nm core model. In Figure 2.15 a cross section of the 8.2nm core heated to 1000K by laser heating with a 2nm crystalline shell is shown. The abrupt change in pressure at the core/shell interface reflects the large pressure gradient observed in Figure 2.13. The core is experiencing high pressures because of volumetric expansion upon melting while the oxide shell is under high negative pressure (tensile stress).

2.9 Formation of Hollow Aluminum Oxide Shells

Recent experimental efforts by Rai et al. [9] and Nakamura et al. [29] have both observed the formation of hollow aluminum oxide nanoparticles as a result of the oxidation of oxide coated aluminum nanoparticles. In the work by Rai et al. [9] we observed the formation of hollow spheres of aluminum oxide subsequent to the oxidation of aluminum nanoparticles at about 727K. The authors suggest that these hollow oxide shells are produced by the outward diffusion of aluminum through the oxide shell, as opposed to inward diffusion of oxygen. This observation is supported here by the high measured diffusion coefficients for aluminum cations and mass flux due to the electric field in the nanoparticle.

In order to better compare the inward diffusion of oxygen versus the outward diffusion of aluminum we have simulated a 5.6nm aluminum core with a 2nm crystalline oxide shell in a high density oxygen gas as shown in Figure 2.16. The diffusion of oxygen ions through the shell has the potential to limit the mass flux of aluminum cations emanating from the core, producing reactions inside of the oxide shell at the core/shell interface as opposed to on the nanoparticle surface. Oxidation in the core would potentially increase the internal pressure of the nanoparticle from volumetric expansion, resulting in mechanical failure of the oxide shell, but it would be unlikely to result in the hollow shells observed by Rai et al. [9].

In Figure 2.16, it is apparent that the diffusivity of aluminum cations through the oxide shell is observably higher than the diffusion rate of oxygen anions towards the core. This result indicates that oxidation will occur on or near the outer surface of the oxide shell rather than at or near the core/shell interface. By the oxidation reaction occurring on the outer shell surface, an outward growth of the oxide shell is observed, which ultimately results in a hollow aluminum oxide shell as observed experimentally [9,29]. One effect that may limit the mass flux of oxygen atoms into the oxide shell is that at higher temperatures the sticking

probability of the gas molecules is lower than for temperatures <623K [26].

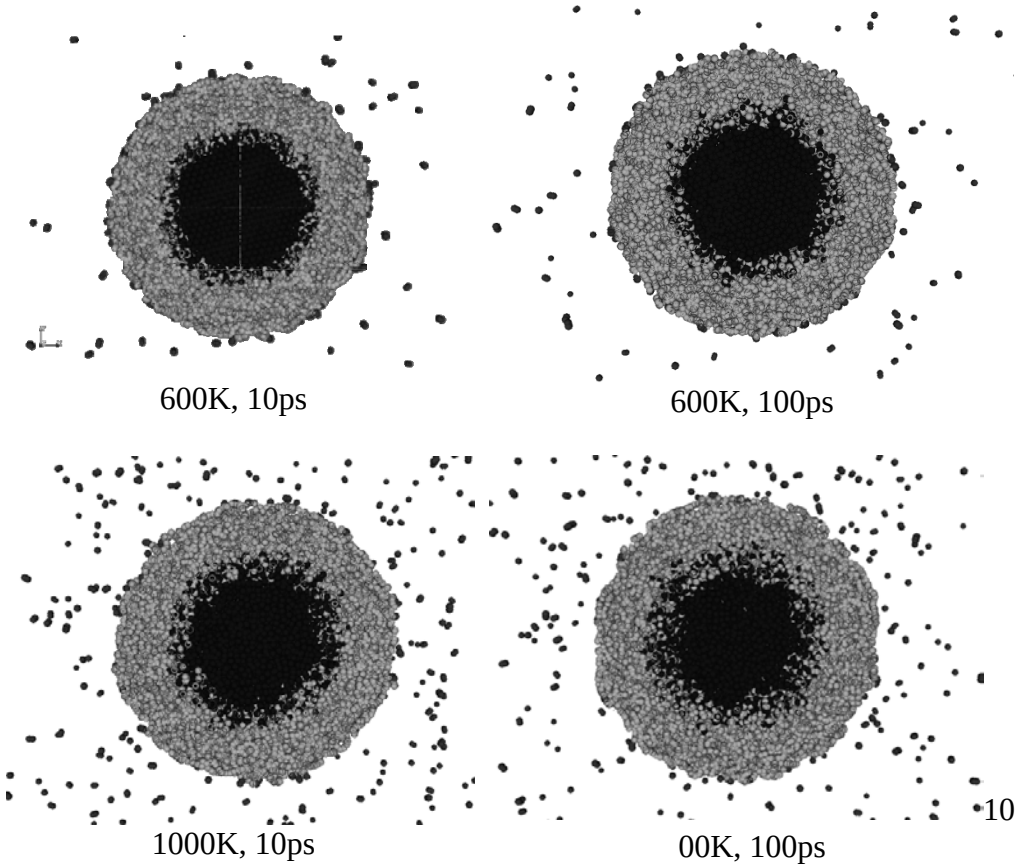

Figure 2.16: Cross section of oxide (gray) coated aluminum core (dark) showing surrounding oxygen atoms.

In Figure 2.16, higher rates of diffusion for aluminum cations are observed by aluminum atoms moving radially outward into the oxide shell atoms, while adsorbed oxygen atoms remain on the outer surface or desorb from the shell. Figures 2.16a and 2.16b are at 600K and represent 10ps and 100ps of simulation time, respectively. Figures 2.16c and 2.16d are at 1000K, after 10ps and 100ps, respectively.

2.10 Conclusions

For oxide coated aluminum nanoparticles we have found that the oxidation process is likely to occur by rapid diffusion of aluminum cations through the oxide shell as opposed to mechanical failure or melting of the shell, for heating rates as high as 1012K/s. The high level of measured aluminum cation diffusivity is driven not only by the volumetric expansion of the aluminum core, but primarily by the induced electric field in the oxide shell. This enhanced diffusivity due to the induced electric field is supported by theoretical analysis of the Cabrera-Mott effect for oxide coated nanoparticles. For homogeneously heated nanoparticles an extrapolation of the core size results would suggest that mechanical failure of the oxide is mitigated by fast diffusion of aluminum ions for core sizes larger than predicted by Levitas et al.[3,4].

Oxidation by rapid diffusion of aluminum ions to the nanoparticle surface is in agreement with published experimental efforts that have observed the formation of hollow aluminum oxide nanoparticles [9,29]. Diffusion of oxygen ions into the shell has also been considered but does not contribute appreciably when compared to the mass flux of aluminum to the nanoparticle surface.

2.11 Acknowledgments

The authors would like to acknowledge the support received by the U.S. Army Major Shared Resource Center (MSRC) at the Aberdeen Proving Ground, MD. Additional support was provided by the U.S. Army Research Office (ARO) and the University of Maryland Center for Energetic Concepts Development.

2.12 References

1. X. Phung, J. Groza, E. A. Stach, L. N. Williams, and S. B. Ritchey. “Surface characterization of metal nanoparticles,” *Materials Science and Engineering A*, 359, 261–268, 2003.
2. A. Rai, D. Lee, K. Park, and M. R. Zachariah. “Importance of Phase Change of Aluminum in Oxidation of Aluminum Nanoparticles,” *Journal of Physical Chemistry B*, 108, 14793–14795, 2004.
3. V.I. Levitas, B.W. Asay, S.F. Son, and M. Pantoya. “Melt dispersion mechanism for fast reaction of nanothermites,” *Journal of Applied Physics*, 89, 071909, 2006.
4. V.I. Levitas, B.W. Asay, S.F. Son, and M. Pantoya. “Mechanochemical mechanism for fast reaction of metastable intermolecular composites based on dispersion of liquid aluminum,” *Journal of Applied Physics*, 101, 083524, 2007.

5. P. Puri and V. Yang. “Thermo-Mechanical Behavior of Nano Aluminum Particles with Oxide Layers”, 46th AIAA Aerospace Sciences Meeting and Exhibit, Reno, NV, 7-10 January 2008.
6. A.C.T. van Duin, S. Dasgupta, F. Lorant, and W.A. Goddard III. “ReaxFF: A Reactive Force Field for Hydrocarbons,” *Journal of Physical Chemistry A*, 105, 9396–9409, 2001.
7. Q. Zhang, T. Çağın, A. van Duin, W.A. Goddard III, Y. Qi, and L.G. Hector, Jr. “Adhesion and Nonwetting-Wetting Transition in the Al/α-Al_2O_3 Interface,”*Physical Review B*, 69, 045423, 2004.
8. F.H. Streitz and J.W. Mintmire. “Electrostatic potentials for Metal-Oxide Surface and Interfaces,” *Physical Review B*, 50(16), 11996–12003, 1994.
9. A. Rai, K. Park, L. Zhou, and M.R. Zachariah. “Understanding the mechanism of aluminum nanoparticle oxidation,” *Combustion Theory and Modelling*, 10(5), 843–859, 2006.
10. N. Cabrera and N.F. Mott. “Theory of the Oxidation of Metals,” *Rep. Prog. Phys.*, 12, 163–184, 1948.
11. L. Zhou, A. Rai, and M.R. Zachariah. “Component and Morphology Biases on Qualifying Size and Composition of Nanoparticles using Single Particle Mass Spectometry,” *International Journal of Mass Spectometry*, 258, 104–112, 2006.
12. L. Zhou, K. Park, H. Milchberg, and M.R. Zachariah. “Understanding the Interaction of an Intense Laser Pulse with Nanoparticles: Application to Quantification of Single Particle Mass Spectometry,” *Aerosol Science and Technology*, 41, 818–827, 2007.
13. J. Dalla Torre, J.–L. Bocquet, Y. Limoge, J.–P. Crocombette, E. Adam, G. Martin, T. Baron, P. Rivallin, and P. Mur. “Study of self-limiting oxidation of silicon nanoclusters by atomistic simulations,” *Journal of Applied Physics*, 92(2), 1084–1094, 2002.
14. N. Pradeep, D.I. Kim, J. Grobelny, T. Hawa, B.J. Henz, and M.R. Zachariah, “Ductility at the nano scale: Deformation and fracture of adhesive contacts using atomic force microscopy,” *Applied Physics Letters*, 91, 203114, 2007.
15. C. Wagner. “Beitrag zur Theorie des Anlaufvorgangs,” *Z. Phys. Chem.*, B21, 25, 1933.
16. K.S. Martirosyan, I.A. Filimonov, and D. Luss. “Self-Heating by Joule Dissipation during Gas-Solid Combustion Reactions,” *Int. J. of Self-Propagation High-Temperature Synthesis*, 12(2), 91–98, 2003.
17. K.S. Martirosyan, D. Nawarathna, J.R. Claycomb, J.H. Miller Jr, and D. Luss. “Complex dielectric behavior during formation of $BaTiO_3$ by combustion synthesis,” *J. Phys. D: Appl. Phys.*, 39, 3689–3694, 2006.

18. I. Filimonov and D. Luss. “High-Temperature Oxidation of a Metal Particle: Nonisothermal Model,” *AIChE Journal*, 51(5), 1521–1531, 2005.
19. K.S. Martirosyan, J.R. Claycomb, J.H. Miller Jr, and D. Luss. “Complex dielectric behavior during formation of $BaTiO_3$ by combustion synthesis,” *J. Appl. Phys.*, 96, 4632, 2004.
20. A.T. Fromhold, jr, and E.L. Cook. “Kinetics of Oxide Film Growth on Metal Crystals: Thermal Electron Emission and Ionic Diffusion,” *Physical Review*, 163(3), 650–664, 1967.
21. C. Wagner. “Beitrag zur Theorie des Anlaufvorgangs,” *Z. Phys. Chem.*, B21, 25, 1933.
22. L.P.H. Jeurgens, W.G. Sloof, F.D. Tichelaar, and E.J. Mittemeijer. “Growth kinetics and mechanisms of aluminum-oxide films formed by thermal oxidation of aluminum,” *Journal of Applied Physics*, 92(3), 1649–1656, 2002.
23. J.H. Sinfelt. *Bimetallic Catalysis: Discoveries, Concepts and Applications*. Wiley, New York, 1983.
24. J. Uppenbrink and David J. Wales. “Structure and energetic of model metal clusters,” *Journal of Chemical Physics*, 96(11), 8520–8534, 1992.
25. B. Eapen, V. Hoffman, M. Schoenitz, and E. Dreizin. “Combustion of Aerosolized Spherical Aluminum Powders and Flakes in Air,” *Combustion Science and Technology*, 176(7), 1055–1069, 2004.
26. V. Zhukov, I. Popova, and J.T. Yates. *Surface Science*, 441, 251, 1999.
27. S. Ogata, H. Iyetomi, K. Tsuruta, F. Shimojo, A. Nakano, R.K. Kalia, and P. Vashishta. “Role of atomic charge transfer on sintering of TiO_2 nanoparticles: Variable-charge molecular dynamics,” *Journal of Applied Physics*, 88(10), 6011–6015, 2000.
28. V.P. Zhdanov and B. Kasemo. “Cabrera–Mott kinetics of oxidation of nm-sized metal particles,” *Chemical Physics Letters*, 452, 285–288, 2008.
29. R. Nakamura, D. Tokozakura, H. Nakajima, J.-G. Lee, and H. Mori. “Hollow oxide formation by oxidation of Al and Cu nanoparticles,” *Journal of Applied Physics*, 101, 074303, 2007.
30. C.G. Zoski. *Handbook of Electrochemistry*. Elsevier, 2007.
31. P.P. Mitra, P.N. Sen, L.M. Schwartz, P. Le Doussal. “Diffusion Propagator as a Probe of the Structure of Porous Media,” *Physical Review Letters*, 68(24), 3555–3558, 1992.
32. M.A. Trunov, M. Shoenitz, and E.L. Dreizin. “Effect of polymorphic phase transformations in alumina layer on ignition of aluminum particles,” *Combustion Theory and Modeling*, 10(4), 603–623, 2006

33. Cormier, J., Rickman, J. M. & Delph, T. J. “Stress calculation in atomistic simulations of perfect and imperfect solids,” *J. Appl. Phys*. 89, 99-104, 2001.
34. Clausius, R. “On a mechanical theory applicable to heat,” *Philosophical Magazine* 40, 122-127, 1870.
35. L. Zhou, A. Rai, and M.R. Zachariah. “Component and Morphology Biases on Qualifying Size and Composition of Nanoparticles using Single Particle Mass Spectometry,” *International Journal of Mass Spectometry*, 258, 104–112, 2006.
36. L. Zhou, K. Park, H. Milchberg, and M.R. Zachariah. “Understanding the Interaction of an Intense Laser Pulse with Nanoparticles: Application to Quantification of Single Particle Mass Spectrometry,” *Aerosol Science and Technology*, 41, 818–827, 2007.
37. S. Chowdhury, K. Sullivan, N. Piekiel, L. Zhou and M. R. Zachariah “Diffusive vs. Explosive Reaction at the Nanoscale,” *J. Phys. Chem. C* in press.
38. L. Zhou, N. Piekiel, S. Chowdhury, D. Lee and M. R. Zachariah "Transient ion ejection during nanocomposite thermite reactions," Journal *of Applied Physics* 106, 083306 (2009).

Chapter 3

Triaminoguanidinium 1-Methyl-Nitriminotetrazolate – From Simulation to Existence

Thomas M. Klapötke and Jörg Stierstorfer

The design and implementation of the new energetic material triaminoguanidinium 1-methyl-5-nitriminotetrazolate (TAG-1MeAt NO_2), which is a promising alternative to the secondary explosive RDX (hexogen), is described. Prior to any attempt to synthesize the target compound, the corresponding molecular and thermodynamic properties were predicted using *ab initio* methods, which employ high level, quantum chemical computations. This was done using the atomization method in combination with CBS-4M enthalpies and is explained in Section 3.2. The expected detonation parameters such as detonation velocity, detonation pressure and heat of explosion were simulated on the basis of the calculated thermochemical parameters using the EXPLO5 code. Eventually, TAG-MeAtNO_2 was synthesized in lab scale and fully characterized spectroscopically and structurally (Section 3.3). Also the relevant sensitivities (impact, friction and electrostatic) were assessed experimentally and are discussed in Section 3.4. The long-term thermal stability of the compound was simulated and assessed on the basis of FLEXY-scan long-term TSC (thermal safety calorimetry) and DSC (differential scanning calorimetry) measurements. In these experiments the compatibility of TAG-1MeAtNO_2 towards various potential other ingredients (nitroguanidine and methylammonium nitrate) in energetic formulations was simulated. The short term thermal sensitivity under confinement was simulated in a Koenen (steel shell) test. The Koenen test, described in Section 3.4, can also be related to the detonation

performance of energetic materials.

3.1 Introduction

Due to red tape, chemical research is becoming more and more time consuming. However, new quantum mechanical methods and faster personal computers have come to form the basis of modern approaches in designing new molecules. The prediction of performance, density, stability and sensitivity of high energy dense materials (HEDM) is an ongoing topic in many research groups worldwide. Important criterion for meaningful secondary explosives are the detonation velocity V_D, the detonation pressure p_{CJ} as well as the energy released upon explosion. Thereby the focus lies on the synthesis of compounds which feature values as high as possible for all of these parameters in order to obtain maximum performance.

Another critical factor is the density ρ of the explosive, since the detonation pressure is directly proportional to the density squared ρ^2. In contrast, detonation velocity depends more on the molar quantity of gaseous products formed as well as the solid state density. Also, endothermic heats of formations ($\Delta_f H°$) are required for effective energetic materials. Moreover, the new explosive should be cheap to synthesize, stable towards temperature, compatible to binders and plasticizers, storable for long periods and of course safe to handle. For safety reasons it should only detonate under specific conditions.

Increasing environmental concerns over the last few years have also raised the requirements of HEDMs, making new replacements for the commonly used toxic RDX highly desired. Therefore, explosives with high nitrogen contents have become the focus, because the environmentally benign dinitrogen N_2 molecule is the main reaction product, whereas the amount of the more reactive, undesirable byproducts – nitrogen oxides (N_xO_y), NH_3 or HCN – is greatly reduced. The high, negative enthalpy of formation for the decomposition products and the diminution of carbon residues are further advantages of nitrogen rich compounds.

Promising energetic materials have been synthesized based on 5-amino-1*H*-tetrazole (5-AT, Figure 3.1a).[1] Due to its considerable nitrogen content and its stability towards impact, friction and heat, together with the overall low cost and easy availability, it is an appropriate precursor for the formation of new explosives.

The stability of 5-AT is based on the aromatic ring system within the molecular structure of this compound. The presence of various substituents changes the characteristics of the compound significantly. Alkyl groups substituted at the atoms N1, N2 or C5 raise the stability of

the compounds while electron withdrawing substituents destabilize the synthesized compound.

To prepare new energetic materials, tetrazolates and tetrazolium salts are often used since they are mainly endothermic compounds that also exhibit a high nitrogen content. In addition, these compounds are considered less toxic, easier to handle due to their high kinetic and thermal stability and easier to prepare. Disadvantages of tetrazolates and tetrazolium compounds include possible contamination of ground water owing to their high water solubility. On the other hand, they show higher densities and stabilities based on their lattice energy. The formation of ionic structures is a popular approach for the synthesis of new energetic materials.

With all of the stipulations placed on modern *HEDMs*, it is hard to find a single molecule which meets all of the requirements. One exception is the title compound based on 1-methyl-5-nitriminotetrazole (Figure 3.1c).

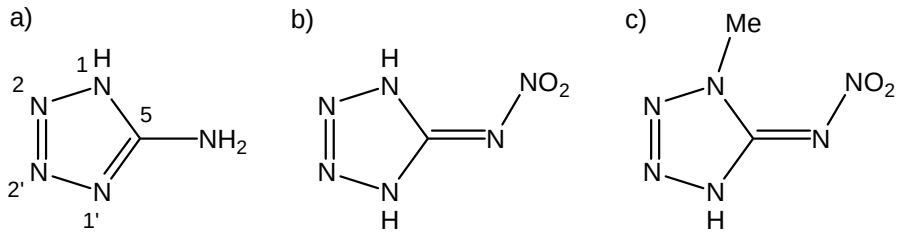

Figure 3.1: Structural formulas of 5-amino-1*H*-tetrazole (a), 5-nitrimino-1,4*H*-tetrazole (b), 1-methyl-5-nitrimino-4*H*-tetrazole (c).

5-Nitriminotetrazoles are valuable compounds because of the combination of the nitrogen-rich backbone as a fuel and the nitro group as an oxidizer. Neutral 5-nitrimino-1,4*H*-tetrazole (Figure 3.1b) offers great detonation values (e.g. $V_D \approx 9500$ m s^{-1}) on the one hand but high sensitivities and a low decomposition temperature (122 °C) on the other.[2] Therefore, an important step is manipulation of the tetrazole ring through attaching different functional groups to control the energetic properties and sensitivities. Through the advent of modern computers, this optimization process, which used to require extensive

experimentation, can now be done theoretically. Also, combinations of the original energetic tetrazolate anion with different endothermic cations can be easily evaluated using the *ab initio* method explained in the following section. Because of the different properties that each of the pairs exhibit, selection of anions and cations has to be carefully considered. Potential candidates are introduced in Figures 3.2 and 3.4.

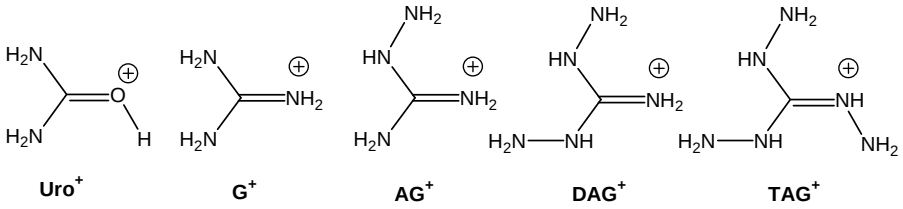

Figure 3.2: Structural formulas of the cations uronium (Uro^+), guanidinium (G^+), 1-aminoguanidinium (AG^+), 1,3-diaminoguanidinium (DAG^+), 1,3,5-triaminoguanidinium (TAG^+).

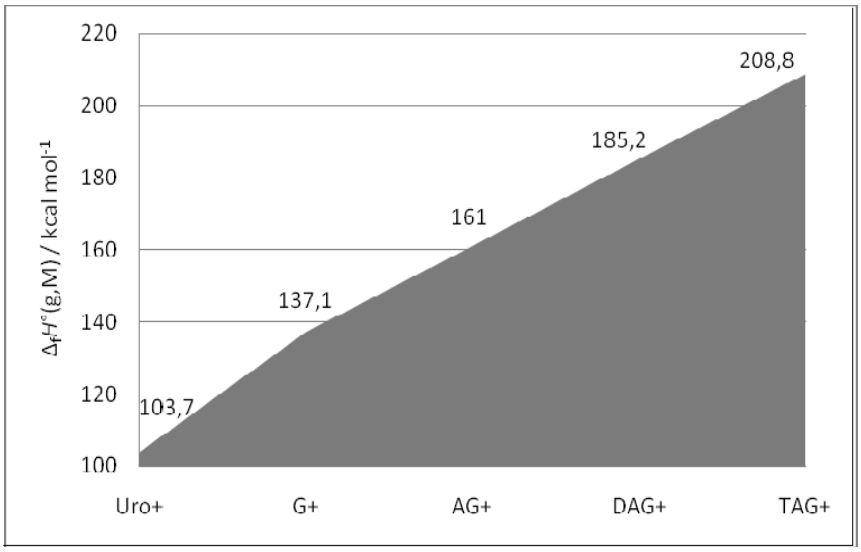

Figure 3.3: Gas phase enthalpies of formation (kcal mol^{-1}) of the cations uronium (Uro^+), guanidinium (G^+), 1-aminoguanidinium (AG^+), 1,3-diamino-guanidinium (DAG^+), 1,3,5-triaminoguanidinium (TAG^+).

Most of tetrazolate anions show different energetic properties but comparable heats of formation (Figure 3.5). In contrast, nitrogen rich cations significantly differ in their heat of formation (Figure 3.3). Unfortunately, there exist only a few energetic cations that are stable in air at room temperature. Therefore, usually hydrazinium as well as guanidinium derivatives are used, which exhibit a high nitrogen and low carbon content Up to now, it has been ascertained in many publications that the triaminoguanidinium cation shows the most promise as an energetic cation.

The selection of the anion determines stability and performance characteristics of the complex, and thus the anion must have high density, good thermal stability, low sensitivity and a good oxygen balance. As mentioned, the 1-methyl-5-nitriminotetrazolate anion shows an appropriate combination of the desired criteria.

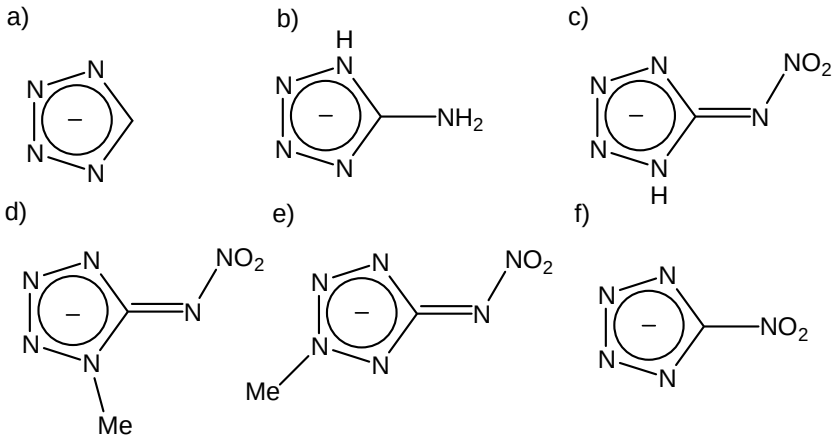

Figure 3.4: Structural formulas of different tetrazolate anions: tetrazolate (a), 5-aminotetrazolate (b), 5-nitrimino-1*H*-tetrazolate (c), 1-methyl-5-nitrimino-4*H*-tetrazo-late (d), 2-methyl-5-nitrimino-4*H*-tetrazolate (e), 5-nitrotetrazolate (f).

3.2 Prediction of Heat of Formation

As described in Section 3.1, performance of *HEDM*s can be related to their density, composition and heat of formation. The latter can be calculated adequately by using the atomization method. The enthalpies (*H*) and free energies (*G*) were calculated using the complete basis set (CBS) method of Petersson and coworkers in order to obtain very accurate energies. The CBS models use the known asymptotic

convergence of pair natural orbital expressions to extrapolate from calculations using a finite basis set to the estimated complete basis set limit. CBS-4 begins with a HF/3-21G(d) structure optimization; the zero point energy is computed at the same level. It then uses a large basis set SCF calculation as a base energy, and a MP2/6-31+G calculation with a CBS extrapolation to correct the energy through second order. A MP4(SDQ)/6-31+(d,p) calculation is used to approximate higher order contributions. In this study we applied the modified CBS-4M method (M referring to the use of minimal population localization), which is a re-parametrized version of the original CBS-4 method and also includes some additional empirical corrections. [3,4] The enthalpies of the gas-phase species M were computed according to the atomization energy equation 1.[5,6]

$$\Delta_f H°_{(g,\,M,\,298)} = H_{(Molecule,\,298)} - \sum H°_{(Atoms,\,298)} + \sum \Delta_f H°_{(Atoms,\,298)} \qquad \textbf{(1)}$$

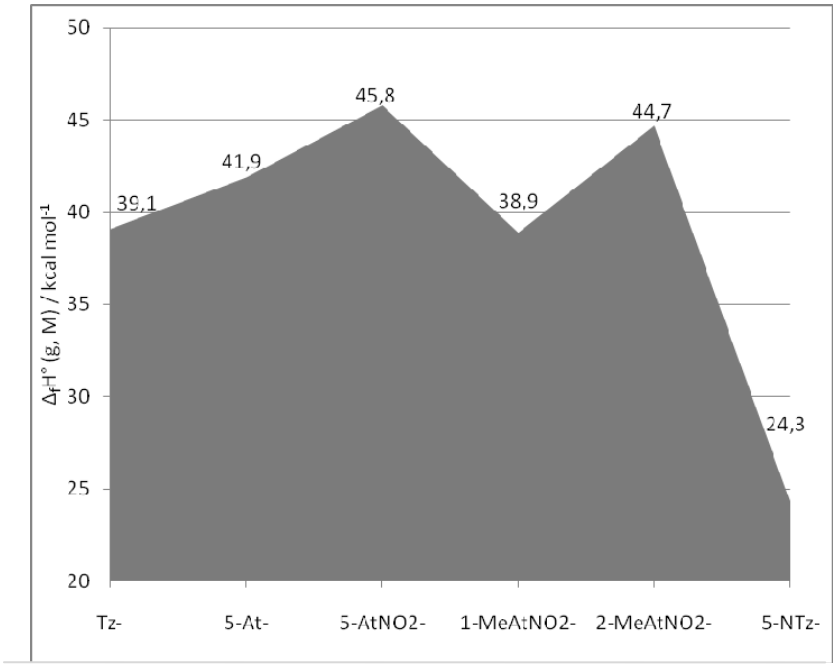

Figure 3.5: Gas phase enthalpies of formation (kcal mol^{-1}) of the anions tetrazolate (Tz^-), 5-aminotetrazolate ($5\text{-}At^-$), 5-nitrimino-1*H*-tetrazolate ($5\text{-}AtNO_2^-$), 1-methyl-5-nitrimino-4*H*-tetrazolate ($1\text{-}MeAtNO_2^-$), 2-methyl-5-nitromino-4*H*-tetrazolate ($1\text{-}MeAtNO_2^-$), 5-nitrotetrazolate (NTz^-).

Tables 3.1–3.7 show exemplarily the calculation steps towards the heat of formation of triaminoguanidinium 1-methyl-5-nitrimino-tetrazolate, abbreviated with TAG-1MeAtNO$_2$ (**1**).[7] All calculations were carried out using the Gaussian G03W (revision B.03) program package.[8]

Table 3.1: CBS-4M results.

	p.g.	$-H^{298}$ / a.u.	$-G^{298}$ / a.u.	*NIMAG*
TAG^+	C_3	^1A	371.197775	371.236698
1-Me-$AtNO_2^-$	C_1	^1A	556.194636	556.239163
H		0.500991	0.514005	0
C		37.786156	37.803062	0
N		54.522462	54.539858	0
O		74.991202	75.008515	0

Table 3.2: Literature values for atomic $\Delta_f H°^{298}$ / kcal mol^{-1}

	NIST
H	52.1
C	171.3
N	113.0
O	59.6

Table 3.3: Enthalpies of the gas-phase species M.

M	M	$\Delta_f H°$(g,M) / kcal mol^{-1}
TAG^+	$C(NH–NH_2)_3^+$	+208.8
1-Me-$AtNO_2^-$	$C_2H_3N_6O_2^-$	+40.6

The lattice energies (U_L) and lattice enthalpies (ΔH_L) were calculated from the corresponding molecular volumes (Table 3.4) according to the

equations provided by Jenkins *et al.*[9] and are summarized in (Table 3. 5).

Table 3.4: Molecular volumes.

	V_M / Å^3	V_M / pm^3
$[TAG]^+$	108 [a]	0.108
$[1\text{-Me-AtNO}_2]^-$	154 [b]	0.154
$[TAG][1\text{-Me-AtNO}_2]$ (**1**)	262 [b]	0.262

[a] back-calculated and averaged from V([TAG][NO_3]) and V([TAG][Cl]) using the molecular volumes for Cl^- and NO_3^- from the literature [9]; [b] from literature [9].

Table 3.5: Lattice energies and lattice enthalpies.

	V_M / nm^3	U_L / kJ mol^{-1}	ΔH_L / kJ mol^{-1}	ΔH_L / kcal mol^{-1}
1	0.262	470.4	475.4	113.6

With the calculated lattice enthalpies (Table 3.5) the gas-phase enthalpies of formation (Table 3.3) were converted into the solid state (standard conditions) enthalpies of formation (Table 3.6). These molar standard enthalpies of formation (ΔH_m) were used to calculate the molar solid state energies of formation (ΔU_m) according to equation (2).

$\Delta U_m = \Delta H_m - \Delta nRT$ (Δn being the change in moles of gaseous components) (**2**)

The enthalpy of formation of the solid species TAG-1MeAtNO$_2$ (**1**) ($\Delta_f H°$(s,M)) was calculated to be +135.8 kcal mol^{-1}.

Table 3.6: Solid state energy of formation ($\Delta_f U°$).

	$\Delta_f H°$(s) / kcal mol^{-1}	Δn	$\Delta_f U°$(s) / kcal mol^{-1}	M / G mol^{-1}	$\Delta_f U°$(s) / kJ kg^{-1}
1	+135.8	–13	+143.5	248.2	+2419.0

The prediction of energetic properties of new compounds can be performed by computing their detonation parameters using different computer codes (EXPLO5, Cheetah). The most important parameters are: energy of explosion ($U_{Exp.}$), detonation pressure p_{CJ}, detonation velocity ($V_{Det.}$), temperature of explosion ($T_{Ex.}$), and volume of decomposition gases (V_0). By using the energy of formation and the density obtained either by X-ray crystallography or by pycnometer measurements, several detonation parameters of energetic compounds including the atoms C, H, N, O, Al and F can be calculated by using the EXPLO5 computer program.[10,11] This program is based on the steady-state model of equilibrium detonation and uses BKW E.O.S for gaseous detonation products and Cowan-Fickett E.O.S. for solid carbon.[12] The calculation of the equilibrium composition of the detonation products is done by applying modified White, Johnson and Dantzig's free energy minimization technique. The program is designed to enable the calculation of detonation parameters at the Chapman Jouguet (CJ) point. The BKW equation in the following form was used with the BKWN set of parameters (α, β, κ, θ) as stated below the equations, and X_i being the mol fraction of *i*-th gaseous product, k_i is the molar covolume of the *i*-th gaseous product: $pV / RT = 1 + xe^{\beta x}$

$$x = (\kappa \Sigma X_i k_i) / [V (T + \theta)]^{\alpha}$$
$$\alpha = 0.5,\ \beta = 0.176,\ \kappa = 14.71,\ \theta = 6620.$$

The calculations were performed using the maximum density of **1** according to its crystal structure (1.57 g cm^{-1}). Compound **1** is a promising explosive since the detonation pressure (p_{CJ} = 273 kbar) and velocity (V_D = 8770 m s^{-1}) clearly exceed the calculated values for TNT (p_{CJ} = 202 kbar, V_D = 7150 m s^{-1}), which is the reference still applied in military and civil sectors. The performance of **1** is even similar to RDX (royal demolition explosive; p_{CJ} = 346 kbar, V_D = 8936 m s^{-1}), which is mostly used in military explosives.[13]

Table 3.7: Comparison of the physico-chemical properties of compound 1 and RDX.

	TAG 1MeAtNO$_2$	**RDX**
Formula	$C_3H_{12}N_{12}O_2$	$C_4H_8N_8O_8$
Molecular Mass (g/mol)	248.21	222.1

Impact sensitivity (J)[a]	10	7.5
Friction sensitivity (N)[b]	240	120
Electrostatic sensitivity (J)[c]	0.8	0.2
N (%)[d]	67.72	37.84
Ω (%)[e]	–64.46	–21.61
$T_{dec.}$ (°C)[f]	210	210
ρ (g cm^{-3})[g]	1.57	1.82
$\Delta_f H_m°$ (kJ mol^{-1})[h]	569	67
$\Delta_f U°$ (kJ kg^{-1})[i]	2423	402
calculated values using EXPLO5		
$-\Delta_E U_m°$ (kJ kg^{-1})[j]	4888	6043
T_E (K)[k]	3210	4368
P_{CJ} (kbar)[l]	273	346
V_D (m s^{-1})[m]	8770	8936
V_0 [L kg^{-1}][n]	886	794

[a,b] BAM methods, see Ref. [14–19]; [c] OZM electrostatic discharge device; [d] Nitrogen content; [e] Oxygen balance; [f] Decomposition temperature from DSC (β = 5 °C min^{-1}); [g] estimated from X-ray diffraction; [h] Molar enthalpy of formation; [i] Energy of formation; [j] Energy of Explosion; [k] Explosion temperature; [l] Detonation pressure; [m] Detonation velocity; [n] Assuming only gaseous products.

3.3 Synthesis

As calculated and explained in the previous section, compound **1** is a new secondary explosive whose performance can compared to hexogen (RDX, 1,3,5-trinitro-1,3,5-triazacyclohexane). However, in microtox tests the toxicity of **1** has been found to be approximately 500 times lower than that of RDX. Therefore, **1** has been investigated intensively in our research group in strong collaborations with ARL (US Army Research Laboratory). Triaminoguanidinium 1-methyl-5-nitriminotetrazolate can be prepared easily by different metatheses reactions shown in Schemes 3.1-3.3.

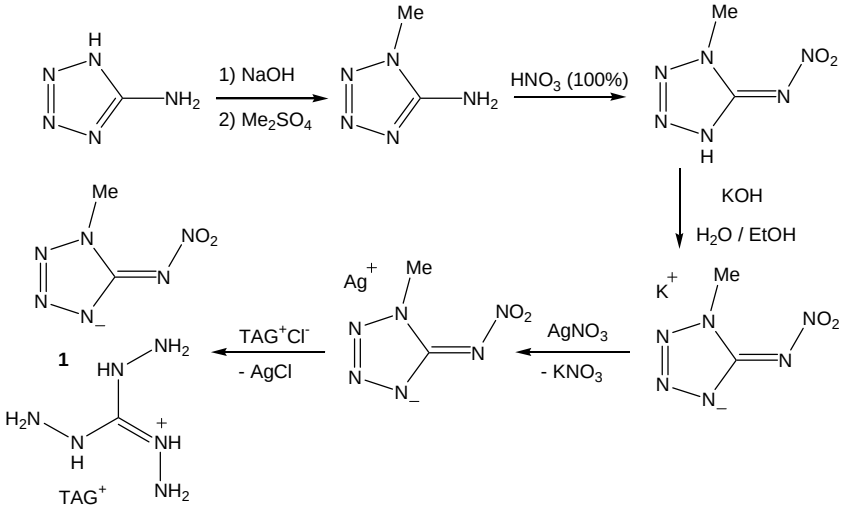

Scheme 3.1: Synthesis of TAG-1MeAtNO$_2$ using the low solubility of silver chloride as the driving force.

The disadvantage of the shown synthetic protocol Scheme 3.1 is the use of expensive as well as light sensitive silver derivatives, which are hard to handle in larger scales. A further facile metathesis reaction using low soluble potassium perchlorate is shown in Scheme 3.2.

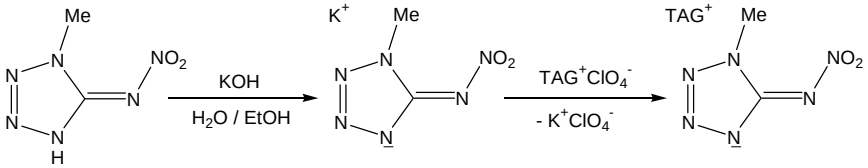

Scheme 3.2: Synthesis of TAG-1MeAtNO$_2$ via the formation of KClO$_4$.

Unfortunately, this reaction pathway evinces a large downside. Triaminoguanidinium perchlorate used in the synthesis is an extremely energetic compound with sensitivity values higher than those of lead azide.

The best synthesis of triaminoguanidinium 1-methyl-5-nitriminotetrazolate follows the protocol presented in scheme 3.3. The deprotonation reaction using cheap aminoguanidine bicarbonate was

performed in water, obtaining a yield of 97%. The second reaction was performed in a dioxane/water mixture using an excess of hydrazine hydrate.

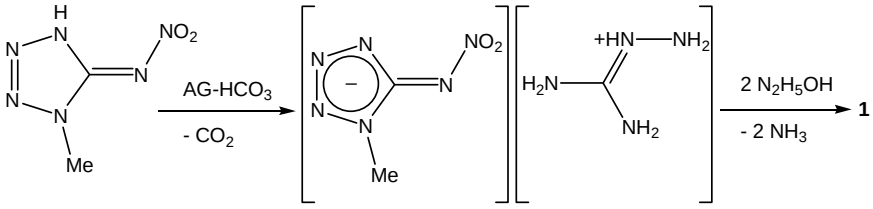

Scheme 3.3: Improved Synthesis of TAG-1MeAtNO$_2$.

The presented synthesis reduces the five step protocol (Scheme 3.1) to only two steps.

3.4 Testing

3.4.1 Sensitivities

The impact sensitivity tests were carried out according to STANAG 4489 [14] modified according to instruction [15] using a BAM (Bundesanstalt für Materialforschung) drophammer.[16] The friction sensitivity tests were carried out according to STANAG 4487 [17] modified according to instruction [18] using the BAM friction tester. The classification of the tested compound results from the "UN Recommendations on the Transport of Dangerous Goods".[19] The exact values in comparison to those of RDX have been given in Table 3.7. Concerning the impact sensitivity (10 J), compound **1** has to be classified as "sensitive" and therefore handled with special safety precautions. Regarding the friction sensitivity (240 N), **1** is also classified as "sensitive." The electrostatic discharge sensitivity (ESD) test was carried out using an electric spark tester ESD 2010EN (OZM Research) operating with the "Winspark 1.15 software package."[20] The value of compound **1** (0.8 J) is 4 times less sensitive than that of RDX (0.2 J) by using the same grain sizes (0.25-0.5 mm).

3.4.2 Koenen Steel Shell Test

The shipping classification and also relative explosion performance under confinement of energetic materials can be investigated by the *Koenen* steel shell test.[21,22] The explosive is placed in a non-reusable, open-ended, flanged, steel tube (thimble), which is capped off by a

closing plate with variable orifice (0–10 mm), through which formed gaseous decomposition products are vented. A defined volume of 25 mL of the compound is loaded into the flanged steel tube, and a threaded collar is slipped onto the tube from below. The closing plate is fitted over the flanged tube and secured with a nut. The explosion is initiated via thermal ignition using four *Bunsen* burners, which are started simultaneously. The test is completed when either rupture of the tube or no reaction is observed, after heating the tube for a minimal time period of at least 5 minutes. In case of the tube's rupture the fragments are collected and weighed. The appearance of the fragmentation degree (Table 3.8) determines whether an explosion occurred. The reaction is evaluated as an explosion if the tube is destroyed into three or more pieces. TNT destroys the steel sleeve up to an orifice width of 6 mm, RDX and HMX even up to 8 mm.[23]

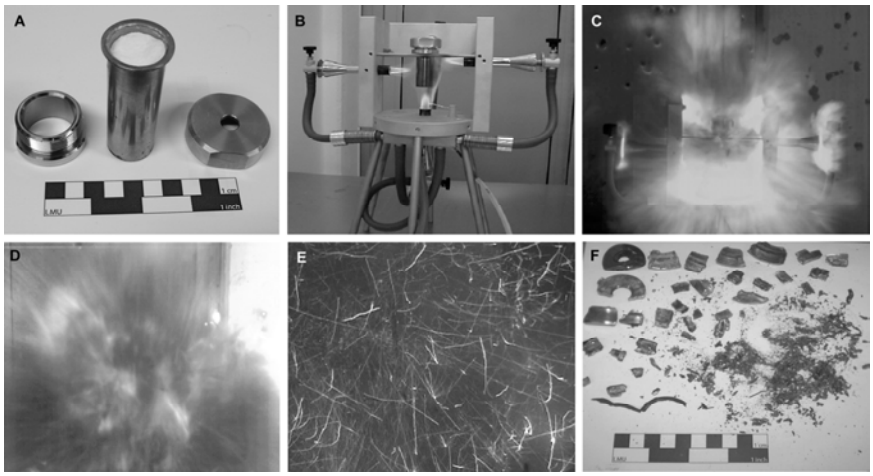

Figure 3.5: A) Steel sleeve with screw cap (hole width 10 mm), B) Koenen test setup, C) Start of detonation, D) 0.5 ms after start of detonation, E) Blistering metal shivers, F) Collected fragments.

The *Koenen* test of triaminoguanidinium 1-methyl-5-nitrimino tetrazolate was performed with 27 g using a closing plate with an orifice of 10 mm. The first trial was a success as indicated by the rupture of the steel tube into many small fragments. Compared to TNT and RDX the performance of compound **1** is obviously better, although the calculated detonation parameters of RDX are slightly higher.

The valuation of a substance in order to its thermal sensitivity under confinement is combined in Table 3.9.

Table 3.8: Fragmentation degree

Types of Fragments	Description	Result
0	Thimble is unchanged	–
A	T. plate is dented in	–
B	T. plate and sides are dented in	–
C	T. plat is broken	–
D	T. is teared up	–
E	T. is put in two parts	–
F	T. is destroyed in three or more big pieces, which can be connected	Explosion
G	T. is destroyed into little pieces, top is undamaged	Explosion
H	T. is damaged in a lot of little pieces, the top is damaged too	Explosion

Table 3.9: Validation guidelines

Valuation	Diameter [mm]
Non sensitive	$Ø < 2$
Few sensitive	$2 \leq Ø < 10$
Sensitive	$10 \leq Ø < 16$
Very sensitive	$16 \leq Ø < 20$
Extreme sensitive	$Ø \geq 20$

3.4.3 Differential Scanning Calorimetry (DSC)

The thermal behavior of salt **1** was determined using a DSC measurement. The DSC experiment was performed under constant nitrogen flow (20 mL min^{-1}) in a covered Al-container with a hole (0.1 mm) for gas release on a Linseis PT 10 DSC,[24] calibrated by pure indium and zinc standards at a heating rate of 5 °C min^{-1}. The thermal

behavior of ≈ 2 mg of **1** in the temperature range from 50 ° to 300 °C is illustrated as DSC plot in Figure 3.6. Compound **1** melts above 158 °C and decomposes above 210 °C.

To simulate the compatibility with other energetic compounds, the same DSC experiment was run with an equivalent mixture of **1**, methylammonium nitrate and nitroguanidine. Neither compound influences the thermal behavior of **1**. It can be concluded that **1** is compatible, at least with these ingredients.

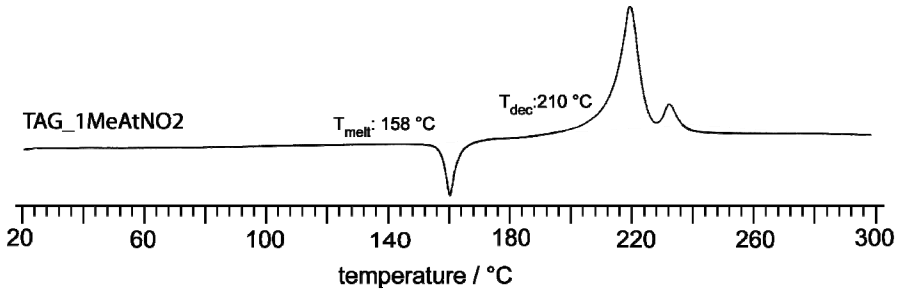

Figure 3.6: DSC plot (endo down) of compound 1 (5 °C min^{-1}); melting point, T_{onset}: 158 °C; temperature of decomposition, T_{onset}: 210 °C

3.4.4 Thermal Safety Calorimetry (TSC)

The assessment of process safety and the classification of materials into the appropriate risk categories is based on an evaluation of the material by reaction calorimetry and is also strongly influenced by thermal safety analysis. The measured values and results supplied by the FlexyTSC are prerequisites for a dependable characterization of a substance or substance blends. In addition, long term stabilities can be simulated by "Thermal Safety Calorimetry," for example using a Systag FlexyTSC [25] in combination with a RADEX V5 oven. The test can be undertaken as long-term isoperibolic or isoperibolic step evaluations in glass test vessels at atmospheric pressure with about 200 mg of the compounds. The long-term stability test is one of the interim hazard classification criteria (UN 3c), in which the testing material has to be stable at 75°C for 48 hours. It has been shown that tempering the substance for a defined time at higher temperature correlates to an estimated storage period at room temperature. Compound **1** was proved to be stable at 75 °C for at least 50 hours.

3.5 Conclusions

Triaminoguanidinium 1-methyl-5-nitrominotetrazolate (**1**) was predicted to be a promising secondary explosive. For this, we used a calculated (CBS-4M in combination with the atomization method) heat of formation, an estimated density, and the EXPLO5 computer code. Afterwards, the compound was synthesized by different routes, keeping potential problems of scale up in mind. The explosive performance under confinement was simulated successfully using the "Koenen Steel Sleeve Test." The thermal stability as well as the compatibility with other energetic ingredients was simulated in DSC experiments. In addition, the long-term stability has been proved by a TSC measurement and the sensitivities have been evaluated. Finally, it can be concluded that compound **1** could be an alternative to RDX, and regarding its energetic properties it is even better than predicted before.

3.6 Acknowledgments

Financial support of this work by the Ludwig-Maximilian University of Munich (LMU), the European Research Office (ERO) of the U.S. Army Research Laboratory (ARL), the Armament Research, Development and Engineering Center (ARDEC) and the Strategic Environmental Research and Development Program (SERDP) under contract nos. W911NF-09-2-0018 (ARL), W911NF-09-1-0120 (ARDEC), W011NF-09-1-0056 (ARDEC) and 10 WPSEED01-002 / WP-1765 (SERDP) is gratefully acknowledged. The authors acknowledge collaborations with Dr. Mila Krupka (OZM Research, Czech Republic) in the development of new testing and evaluation methods for energetic materials and with Dr. Muhamed Sucesca (Brodarski Institute, Croatia) in the development of new computational codes to predict the detonation and propulsion parameters of novel explosives. We are indebted to and thank Drs. Betsy M. Rice and Brad Forch (ARL, Aberdeen, Proving Ground, MD) and Mr. Gary Chen (ARDEC, Picatinny Arsenal, NJ) for many helpful, inspiring discussions and support of our work. Both authors acknowledge financial support by CECD and ETC.

3.7 References

1. J. Stierstorfer, Ph.D. thesis, Energetic materials based on 5-aminotetrazole, Ludwig-Maximilians-Universität München, 2009.
2. T. M. Klapötke, J. Stierstorfer, *Helv. Chim. Acta* 2007, *70*, 2137-2160.
3. J. W. Ochterski, G. A. Petersson, J. A. Montgomery Jr., *J. Chem. Phys.* 1996, *104*, 2598.

4. J. A. Montgomery Jr., M. J. Frisch, J. W. Ochterski, G. A. Petersson, *J. Chem. Phys.* 2000, *112*, 6532.
5. L. A. Curtiss, K. Raghavachari, P. C. Redfern, J. A. Pople, *J. Chem. Phys.* 1997, *106(3)*, 1063.
6. (a) E. F. Byrd, B. M. Rice, *J. Phys. Chem.* 2006, *110(3)*, 1005–1013; (b) B. M. Rice, S. V. Pai, J. Hare, *Combust. Flame* 1999, *118(3)*, 445–458.
7. T. M. Klapötke, J. Stierstorfer, A. U. Wallek, *Chem. Mater.* 2008, *20*, 4519-4530.
8. (a) M. J. Frisch et al., Gaussian 03, Revision B04, Gaussian Inc., Wallingford, CT, 2004.
9. (a) H. D. B. Jenkins, H. K. Roobottom, J. Passmore, L. Glasser, *Inorg. Chem.* 1999, *38(16)*, 3609-3620. (b) H. D. B. Jenkins, D. Tudela, L. Glasser, *Inorg. Chem.* 2002, *41(9)*, 2364-2367. (c) H. D. B. Jenkins, L. Glasser, *Inorg. Chem*. 2002, *41(17)*, 4378-88.
10. (a) M. Sućeska, *Propellants, Explos., Pyrotech.* 1991, *16*, 197–202 ; (b) M. Sućeska, *Propellants, Explos. Pyrotech.* 1999, *24*, 280–285.
11. (a) EXPLO5.V2, M. Sućeska, *Proc. of 32nd Int. Annual Conference of ICT*, July 3-6, Karlsruhe, Germany, 2001, pp. 110/1 a software for determining detonation parameter; (b) M. Suceska, *Proc. of 30th Int. Annual Conference of ICT*, June 29–July 2, Karlsruhe, Germany, 1999, 50/1.
12. M. L. Hobbs, M. R. Baer. Calibration of the BKW-EOS with a Large Product Species Data Base and Measured C-J Properties, *Proc. of the 10th Symp. on Detonation*, ONR 33395–12, Boston, MA, July 12–16, 1993, p. 409.
13. J. Köhler, R. Meyer, Explosivstoffe, 9th edn., Wiley-VCH, Weinheim, 1998, pp. 166-168.
14. NATO standardization agreement (STANAG) on explosives, *impact sensitivity tests*, no. 4489, 1st ed., Sept. 17, 1999.
15. WIWEB-Standardarbeitsanweisung 4-5.1.02, Ermittlung der Explosionsgefährlichkeit, hier der Schlagempfindlichkeit mit dem Fallhammer, Nov. 8, 2002.
16. http://www.bam.de
17. NATO standardization agreement (STANAG) on explosive, *friction sensitivity tests*, no. 4487, 1st ed., Aug. 22, 2002.
18. WIWEB-Standardarbeitsanweisung 4-5.1.03, Ermittlung der Explosionsgefährlichkeit oder der Reibeempfindlichkeit mit dem Reibeapparat, Nov. 8, 2002.
19. Impact: Insensitive > 40 J, less sensitive ≥ 35 J, sensitive ≥ 4 J, very sensitive ≤ 3 J; friction: Insensitive > 360 N, less sensitive = 360 N, sensitive < 360 N a. > 80 N, very sensitive ≤ 80 N, extreme sensitive

≤10 N; According to the UN Recommendations on the Transport of Dangerous Goods (+) indicates: not safe for transport.
20. (a) http://www.ozm.cz/testing-instruments/small-scale-electrostatic-discharge-tester.html. b) S. Zeman, V. Pelikan, J. Majzlik, *Central Eur. J. Energ. Mat.* 2006, *3*, 45. c) D. Skinner, D. Olson, A. Block-Bolten, *Propellants, Explos., Pyrotech.* 1997, *23*, 3.
21. (a) J. Köhler, R. Meyer, A. Homburg, in "Explosives", 6th edn., Wiley-VCH, Weinheim, 2007, p. 162 (b) Prüfung der thermischen Empfindlichkeit (Stahlhülsenverfahren), WIWEB Standardarbeits-anweisung 410/001, Neufassung, 1st edn., 01.06.1997 (c) http://www.sms-ink.com/ products_koenen.html
22. V. A. Ostrovskii, M. S. Pevzner, T. P. Kofman, I. V. Tselinskii, *Targets Heterocycl. Syst.* 1999, *3*, 467.
23. J. Köhler, R. Meyer, Explosivstoffe, 9th edn., Wiley-VCH, Weinheim, 1998, pp 166-168.
24. http://www.linseis.com
25. http://www.systag.ch

Chapter 4

Functionally Graded Energetic Materials: Simulation-based Design of Materials

Hugh Bruck

This chapter presents a new *Simulation-based Design of Materials* approach to creating energetic materials using Functionally Graded Materials. The concept has recently been developed in a joint collaboration between the University of Maryland (UMD) and Indian Head-Naval Surface Warfare Center (IH-NSWC) through the Center for Energetic Concepts Development (CECD). This approach has been facilitated by previous efforts at IH-NSWC to apply a new process, known as Twin Screw Extrusion (TSE), for continuously manufacturing energetic polymer composites. It takes advantage of the continuous nature and superior mixing characteristics of the TSE process to manufacture a new concept for propellants and explosives: *Functionally Graded Energetic Materials (FGEMs*).

Section 4.1 is a discussion of the benefits of FGEMs. In Section 4.2, the principles for simulation-based design of FGEMs are reviewed. Section 4.3 summarizes the inverse design procedure for FGEMs. Sections 4.4, 4.5, and 4.6 discuss process, burning rate properties, and ballistic performance simulations of FGEMs. Section 4.7 discusses the optimization of composition gradients for FGEMs. Finally, Section 4.8 presents an example of using FGEMs as a new combinatorial materials science approach to better formulate energetic materials.

4.1 Benefits of FGEMs

The development of advanced energetic materials is of significant interest for a variety of military applications. A new approach to

developing these materials is the engineering of composition gradients within an energetic device. Such a concept, known as *Functionally Graded Energetic Materials (FGEMs)*, can result in energetic devices with fewer combustion products that are more environmentally insensitive, more reliable, and multifunctional.

FGEMs are based on the fundamental concept that solid composite energetic materials can be designed to gradually vary in composition from one location to another in order to optimize the distribution of properties for energetics applications [1]. For example, solid propellants are currently limited by chemistry to their own set of burning rate characteristics, which when combined with a certain grain geometry and nozzle configuration limits the possible thrust profiles achievable for a given rocket motor. Pintle nozzles have been used to achieve some throttling capability, but this adds complexity and weight to what is ordinarily a relatively simple design[2,3].

FGEMs have the potential to change the entire landscape of solid rocket motor design by replacing the conventional geometrically-complex homogeneous grains for solid rocket motors with an axial gradient in the energetic material formulation where the volume fraction of ingredients, such as 30 and 200 micron AP particles (V_{AP}), are gradually varied (Figure 4.1). The simpler geometry does not have the undesirable stress concentrations present in a conventional grain that end up reducing the reliability of the grain due to the formation of cracks. Also, the gradient in the energetic polymer composite formulation offers new possibilities to the designers of advanced energetics concepts that are not possible with the geometrically-complex homogeneous grains. Furthermore, it is also possible to improve rocket motor performance by replacing atar-perforated grains with a circular or no perforated grain that has the same performance but burns more efficiently, because it possesses a functionally graded architecture where the variation in V_{AP} along the length of the grain produces a corresponding difference in burn rate. It can be noted that the burn rate is related not only the volume fraction of AP particles, but the particle size distribution as well.

4.2 Principles for Simulation-based Design of FGEMs

The simulation-based design of FGEMs is substantially different from conventional energetic materials, so the design principles for solid composite energetic materials that are primarily based on composition and geometry are not adequate when it comes to simulating the manufacturing and performance attributed to compositional gradients. To deal with the inadequacies, FGEMS can be treated as discontinuously-reinforced polymer composites with energetic ingredients whose

composition gradients are directly controlled by the processes used to fabricate them, such as Twin Screw Extrusion (TSE). Of primary concern for TSE is characterizing and simulating the relationship among the extruder screw geometry, transient processing conditions, and the gradient architecture that evolves in the extruder. Recent interpretations of the Residence Time Distributions (RTDs) and Residence Volume Distributions (RVDs) for polymer composites in the TSE are used to develop new convolution process models for simulating the compositional gradients in the direction of extrusion.

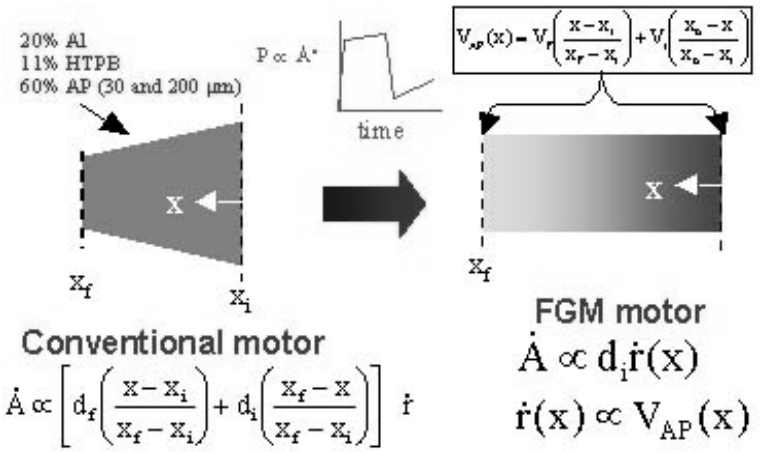

Figure 4.1: Comparison of traditional solid rocket motor concept with FGM concept [1]

Once the composition gradient FGEM is designed using RVDs, it is necessary to employ new approaches for characterizing the sections of the extrudate using optical and combustion analysis to determine gradient architectures and associated burning rates. Reduced-run mixtures-experiment design can be employed for characterizing the burning rate variation as a function of processing conditions and propellant formulations. This data can then be used in modified Petite Ensemble Models for predicting burning rates.

To predict performance, such as in a rocket motor, the new process and burning rate models must be employed in new computational ballistics models. These models then form the basis for a simulation-based Inverse Design Procedure (IDP) capable of determining gradient architectures for grains in solid rocket motors that possess tailored

burning rate distributions that conform to user-defined performance specifications. An additional benefit of the simulation-based design is that it serves as a basis for a new combinatorial materials science approach to formulating energetic materials.

4.3 Inverse Design Procedure

The simulation-based design of FGEMs can be performed via an IDP [1]. The IDP can be summarized as follows (Figure 4.2):

1. Define the required target performance or the system objectives
2. Select the material components for the graded architecture
3. Evaluate the material structure and its properties from various relationships
4. Evaluate the optimal gradient of the materials using Genetic Algorithm
5. Fabricate the optimal FGM through processes such as twin-screw extrusion
6. Test the fabricated FGM for the required properties
7. If the required properties are not achieved, either choose different components for the FGM architecture or redefine the optimization parameter

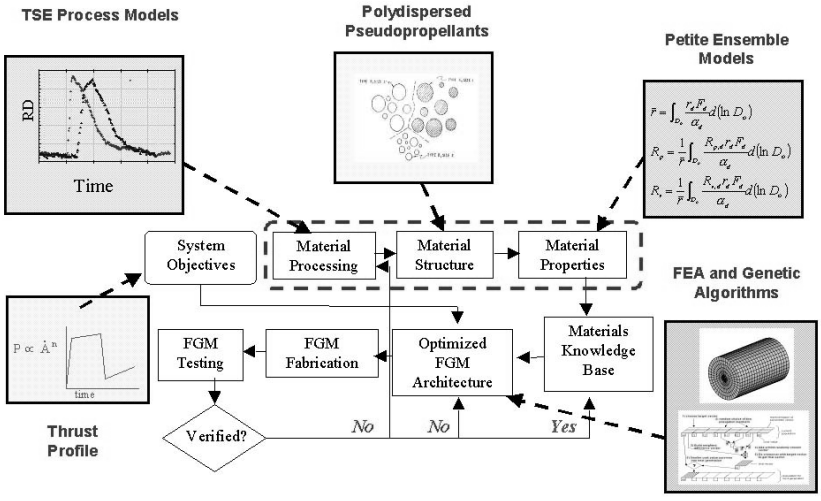

Figure 4.2: Flowchart illustrating the Inverse Design Procedure for FGEMs [1].

In the present discussion, we are interested in the description of the design and fabrication of FGEMs. It is assumed that the ingredients for the energetic composite material are given, so the material knowledge base is limited to this ingredient formulation. Therefore, the focus of the inverse design procedure is on integrating process, property, and performance models with optimization methods, like Genetic Algorithms.

4.4 Process Simulation

To create FGEMs, continuous polymer composite processing techniques like Twin Screw Extrusion (TSE) are used. In general, the TSE is a linear, continuous, time-invariant system described by $\Phi(t)$ with input signal, $u(t)$, whose response, y(t), can be predicted using the *convolution integral* [2]:

$$y(t) = \int_0^t \Phi(t-\tau)u(\tau)d\tau \tag{1}$$

In the extrusion context, equation (1) can be transformed into the volume domain as:

$$C(v) = \int_0^\infty \hat{\bar{g}}(v-v')\,H(v')\,dv' \tag{2}$$

where $\hat{\bar{g}}(v)$ is a characteristic of the process that is independent of processing conditions, $H(v)$ is the Heaviside step function representing the step input of the filler (i.e., 0 for negative arguments and 1 for positive) and $C(v)$ is the response to the step input of the filler, i.e., the composition gradient, assuming that the melt absorbance is linearly proportional to composition of the filler [3]. This assumption is valid at low compositions of the filler where Rayleigh static light scattering principles predict that the scattered intensity of light scales linearly with number of particles [4,5], i.e., composition of the filler.

In order to establish the processing-structure relationship and predict the composition gradient, the characteristic of the process that is independent of the processing conditions has to be identified. A master curve ($\hat{\bar{g}}(v)$) can be obtained by modeling the normalized residence volume distributions (RVDs) as a characteristic of the process in equation (2) to obtain the composition gradient [6]. The normalized RVDs, which can be obtained experimentally using *in situ* optical probes,

can be modeled in various ways [7-11] to obtain the master curve ($\hat{\bar{g}}(v)$). Without loss of generality, the applicability of the approach can be demonstrated by modeling the normalized RVDs using simple empirical equations based on transfer functions that represent a series of perfect batch mixers [12,13]. An order transfer function that corresponds to the mixing occurring in the screw and the die zones of the extruder was used. In the Laplace domain, it can be represented as:

$$G(s) = \frac{a^n e^{-v_d s}}{(s+a)^n} \tag{3}$$

where, v_d is the delay volume and a is the shape factor. The inverse transform gives the model in the volume domain as:

$$g(v) = \frac{a^n}{n!}(v - v_d)^{n-1} e^{-a(v-v_d)} \tag{4}$$

Figure 4.3 shows a representative normalized RVD that was obtained experimentally and the curve obtained by modeling it with the normalized form of equation (4) [14]. Figure 4.4 shows the composition gradient predicted by the convolution integral compared with *in situ* optical measurements from the extrudate, which validates the simulation.

4.5 Simulation of Burning Rate Properties

For determining the material gradient and distribution in a propellant, a model is required to describe the combustion process. Based on the prediction of this model, the performance of the FGEM can be optimized. For this investigation a steady-state combustion model called the Petite Ensemble Model (PEM) is used [15]. The PEM is based on a statistical treatment of the propellant surface with multiple flame structure centered about characteristic oxidizer particles so that each oxidizer type can be treated as a mono-dispersed propellant (i.e., pseudopropellant). This model can be summarized by the following equations:

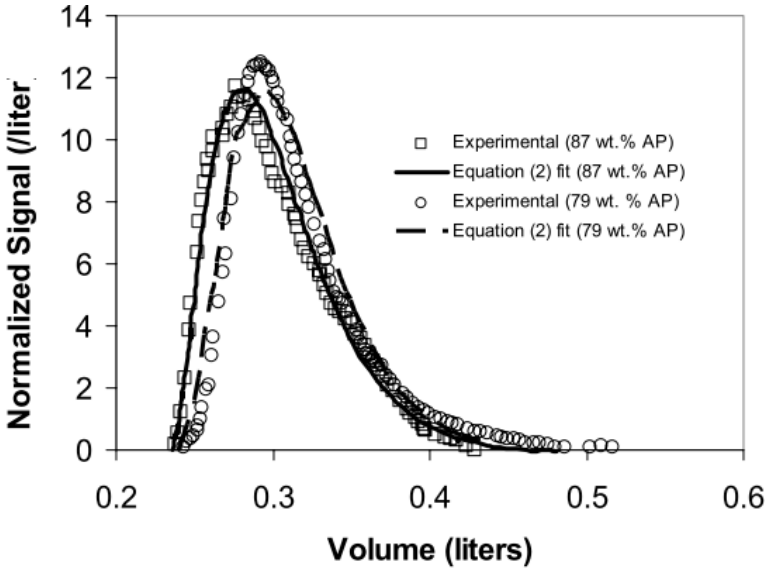

Figure 4.3: Modeling the normalized RVD for a TSE used to process solid composite propellant formulations with 79 and 87 wt. % AP [14].

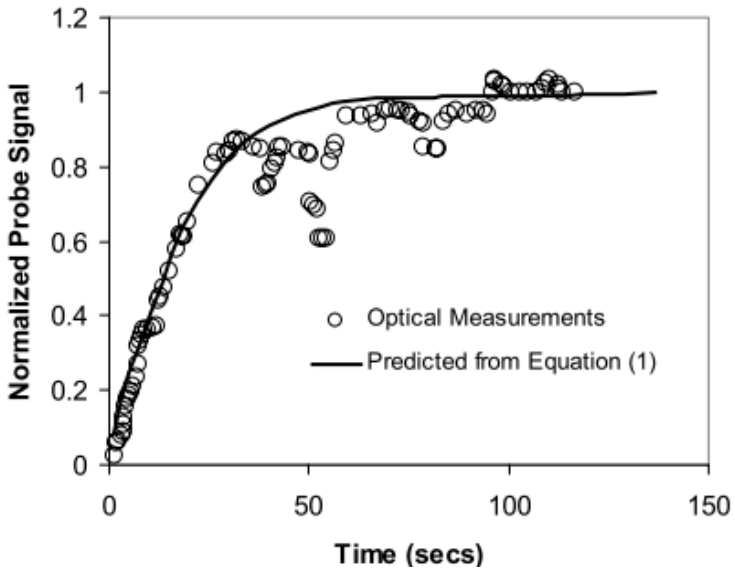

Figure 4.4: The compositional gradient predicted via the convolution integral for a step input change compared with *in situ* optical measurements of the extrudate [14].

$$F_{\mathrm{d}} = \frac{1}{(2\pi \ln\sigma)^{1/2}} \exp\left[-\frac{1}{2}\left(\frac{\ln D_o - \ln \overline{D}_o}{\ln\sigma} \right)^2 \right] \tag{5}$$

$$\bar{r} = \int_{D_o} \frac{r_d F_d}{\alpha_d} d(\ln D_o) \tag{6}$$

$$R_p = \frac{1}{\bar{r}} \int_{D_o} \frac{R_{p,d} r_d F_d}{\alpha_d} d(\ln D_o) \tag{7}$$

$$R_v = \frac{1}{\bar{r}} \int_{D_o} \frac{R_{v,d} r_d F_d}{\alpha_d} d(\ln D_o) \tag{8}$$

where F_d is the overall oxidizer distribution function, D_o is the oxidizer particle diameter, $\overline{D}_o$ is the mean oxidizer particle diameter, σ is the oxidizer distribution function mode width parameter, r is the composite propellant mean burning rate, r_d is the burn rate for a pseudopropellant, α_d is the pseudopropellant oxidizer mass fraction, R_p is the composite propellant pressure coupled response function, $R_{p,d}$ is the pseudo-propellant pressure coupled response function, R_v is the composite propellant velocity coupled response function, and $R_{v,d}$ is the pseudopropellant velocity coupled response function. PEM predictions of the variation in burning rate with composition for TSE processed energetic materials can be seen in Figure 4.5.

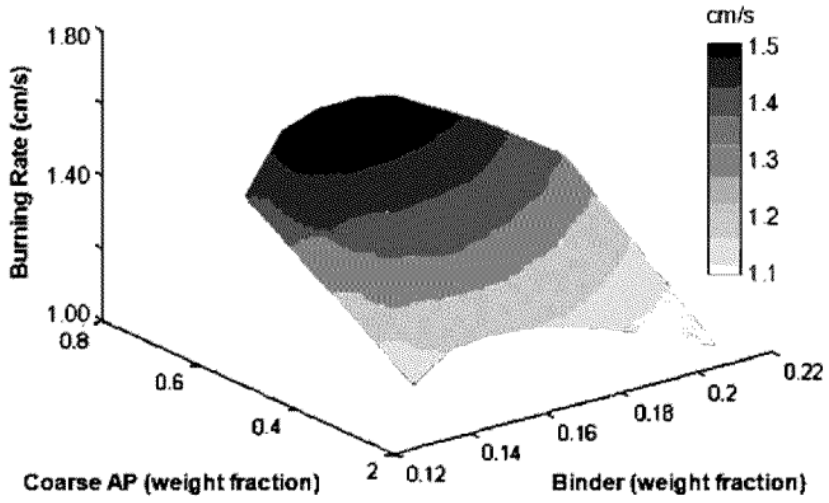

Figure 4.5: PEM prediction of variation in burning rate with composition for TSE processed energetic materials [16].

The PEM has also been modified to predict the effects of processing conditions in addition to composition on burning rate [16]. Given the power-law dependence of burning rate on pressure and quadratic dependence on the screw speed, it was determined that the experimental measurements can be predicted by modifying the PEM predictions using the following rule-of-mixtures composition-dependent power-law relationship with pressure based on St. Robert's Burning Rate Law:

$$r_{mod} = r_{PEM}[\alpha(\beta V_{APF}+(1-\beta)V_{APC})P^{\wedge}(\gamma(\beta V_{APF}+(1-\beta)V_{APC}))]*(c_1+c_2z) \quad (9)$$

where r_{mod} is the modified PEM predictions, r_{PEM} is the original PEM prediction, V_{APF} is the volume fraction of fine AP particles, V_{APC} is the volume fraction of coarse AP particles, P is the pressure, α, β, and γ are variables that define the specific details of the compositional dependence of the coefficient and exponent in the power-law relationship, and c_1, c_2, and c_3 are the coefficients associated with a quadratic relationship to screw speed, z, obtained from response surface analysis. Burning rates determined along the composition gradient using acoustic strand burning rate tests can be seen in *Figure 6a*, while comparisons with the predictions from the modified PEM in Equation (9) can be seen in *Figure 6b*.

4.6 Simulation of Ballistic Performance

There are several challenges when one considers the ballistics of rocket motors using functionally graded propellants. First, the burning rate parameters are continuously changing. Preliminary results from the previous section indicate that burning rates may be intentionally altered by as much as 50%. Second, the thermochemistry of the propellant is also varying constantly as the composition changes. Finally, the solid propellant density changes as the gradient architecture changes throughout the web of the propellant. Codes currently available to industry cannot take into account all of these challenges.

As a first attempt to predict the performance of solid rocket motors using functionally graded propellants, a numerical ballistic simulation has been developed that takes into account all of the problems that other codes used to predict performance of conventional solid propellants do not [17]. Since this ballistic simulation is to be used as part of larger IDP, care must be taken to balance the accuracy of the results with the overall run-time of the code. Since the IDP may require many iterations, the run time of the ballistics code must be kept to a minimum while maintaining reasonable accuracy.

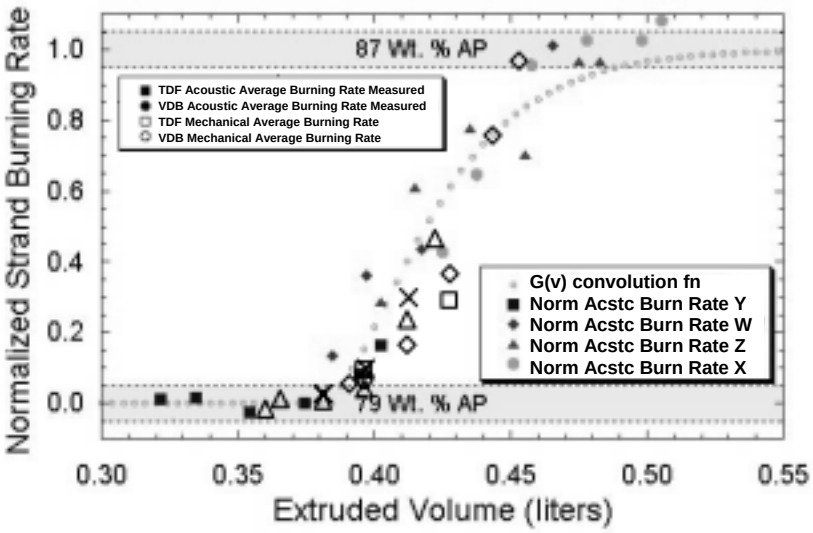

(a)

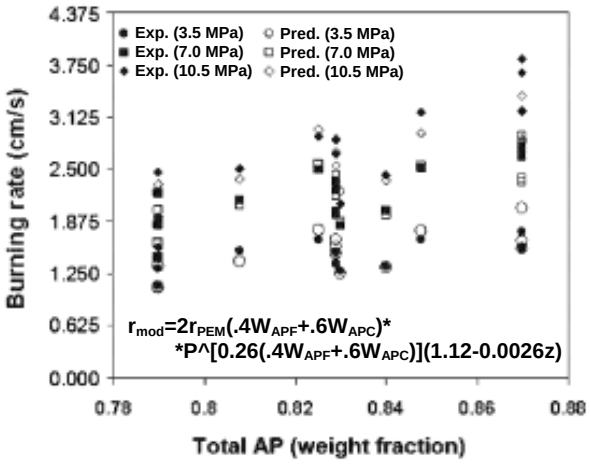

(b)

Figure 4.6: (a) Normalized burning rates along composition gradients measured using acoustic strand burning rate tests, and (b) comparison with predictions using the modified PEM in Equation (9) [14].

Once the propellant gradients have been specified, the simulation predicts the performance of the rocket motor. The model in the simulation assumes that each web gradient has unique burning rate properties, thermochemistry, and density. The code calculates the density of the propellant as a function of web thickness, runs the NASA CEA '00 computer code to determine the thermochemistry at every single web gradient that was specified, and extracts all of the data that is of interest for ballistic calculations, such as the flame temperature, c*, molecular weight of the gases, specific heat ratio, and gas constant [18]. The code creates tables of these parameters versus burning web thickness.

Once the solid propellant density and thermochemical calculations have been made, the simulation can address the internal ballistics and performance calculations. During the ballistic calculations, the code references the tables created earlier as it monitors the propellant web burned. It marches in time, calculates web burned, and compares the web burned to the specified gradients. If the web burned is somewhere in between the gradients, the code will linearly interpolate for the thermochemical properties of the propellant and burning rate parameters.

The ballistics routine predicting the performance of the rocket motors is calculated from first principles. The control volume considered is depicted in Figure 4.7. The following assumptions were made when constructing the model:

1. Heat transfer was negligible.
2. The mass added by the burning propellant is at the adiabatic flame temperature of the propellant at the specified gradient.
3. The combustion gases behave as a perfect gas.
4. Frictional forces between the propellant surface and combustion gas were negligible.
5. Erosive burning was not considered.

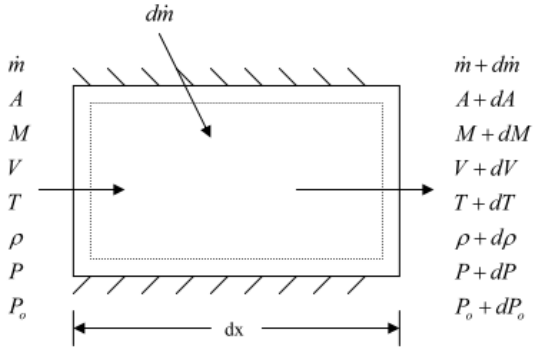

Figure 4.7: Differential Control Volume [17].

When considering these assumptions and logarithmically differentiating the principle equations [19, 20], the resulting equations are obtained:

State : $$\frac{dP}{P} = \frac{d\rho}{\rho} + \frac{dT}{T} \tag{10}$$

Continuity : $$\frac{d\dot{m}}{\dot{m}} = \frac{d\rho}{\rho} + \frac{dA}{A} + \frac{dV}{V} \tag{11}$$

Energy : $$C_p dT + \frac{dV^2}{2} + \frac{V^2}{2}\frac{d\dot{m}}{\dot{m}} = 0 \tag{12}$$

Momentum : $$\frac{dP}{P} + \frac{\gamma M^2}{2}\frac{dV^2}{V^2} + \gamma M^2 \frac{d\dot{m}}{\dot{m}} = 0 \tag{13}$$

Mach Number : $$\frac{d\left(M^2\right)}{M^2} = \frac{dV^2}{V^2} - \frac{dT}{T} \tag{14}$$

In addition, the static and stagnation pressures are related through isentropic flow relations, which when logarithmically differentiated yields:

$$\frac{dP_o}{P_o} = \frac{dP}{P} + \frac{\frac{\gamma M^2}{2}}{\left[1 + \frac{\gamma - 1}{2} M^2\right]} \frac{d\left(M^2\right)}{M^2} \tag{15}$$

The rocket motor geometry is broken into axial elements of equal size. Equations (10) - (15) are applied to each element for determining the incremental property contribution from each element. The incremental contribution is then combined with the incoming properties, as depicted in Figure 7. This combination then becomes the incoming set of properties for the next element. The incremental mass generation rate of combustion products, m_g, is related to the density of the products, ρ_p, the burn area, A_b, and the burning rate, r_b, as follows:

$$\dot{m}_g = \rho_p A_b r_b \tag{16}$$

The burning rate is determined from the composition, processing conditions, and pressure using the modified petite ensemble model presented in equation (9).

Once the calculation has been performed for each element, the final ballistic calculations can be made, starting with equation (18). The conservation of mass can be used to determine the change of mass, m, in the combustion chamber from the exiting mass flow rate, $\dot{m}_e$, and the total mass generation rate of combustion products, $\dot{m}_{gt}$, as follows:

$$\frac{dm}{dt} = \dot{m}_{gt} - \dot{m}_e \tag{17}$$

The exiting mass flow rate is determined from the exit throat area, A_t, using the choked flow assumption:

$$\dot{m}_c = \frac{P_c A_t}{c^*} \tag{18}$$

The equation of state for an ideal gas can then be used to relate the mass to the state variables, chamber pressure, chamber volume, V_c, and chamber temperature, T_c, as follows:

$$m = \frac{P_c V_c}{R_g T_c} \tag{19}$$

Differentiating (20) and combining it with (18) yields:

$$\frac{dm}{dt} = \frac{d}{dt}\left(\frac{P_c V_c}{R_g T_c}\right) = \frac{P_c}{R_g T_c}\frac{dV_c}{dt} + \frac{V_c}{R_g T_c}\frac{dP_c}{dt} - \frac{P_c V_c}{R_g T_c^2}\frac{dT_c}{dt} - \frac{P_c V_c}{R_g^2 T_c}\frac{dR_g}{dt}$$
$$= \dot{m}_{gt} - \dot{m}_e \tag{20}$$

The rate of change of the instantaneous chamber volume, $V_c(t)$ is given by:

$$\frac{dV_c}{dt} = \frac{\dot{m}_{gt}}{\rho_p} \tag{21}$$

Substituting (22) into (21) and rearranging yields:

$$\frac{dP_c}{dt} = \frac{R_g T_c}{V_c}\left(\dot{m}_g - \dot{m}_e\right) - \frac{P_c \dot{m}_g}{V_c \rho_p} + \frac{P_c}{T_c}\frac{dT_c}{dt} + \frac{P_c}{R_g}\frac{dR_g}{dt} \tag{22}$$

Where chamber pressure is solved incrementally by:

$$P_{c_{i+1}} = P_{c_i} + \frac{dP_c}{dt}\Delta t \tag{23}$$

The time step, Δt, is represented by:

$$\Delta t = \frac{P_c V_c}{5(1-n)(R_g T_c \dot{m}_c)} \tag{24}$$

which is approximately $1/5^{th}$ of the propellant gas residence time in the combustion chamber. Both the time derivative of T_c and R_g are calculated via a one-sided difference technique from the thermochemical data. The thrust of the rocket motor, F, is then calculated in the following manner:

$$F = C_f P_c A_t \tag{25}$$

where:

$$C_f = \sqrt{\frac{2\gamma^2}{\gamma-1}\left(\frac{2}{\gamma+1}\right)^{\frac{\gamma+1}{\gamma-1}}\left[1-\left(\frac{P_c}{P_e}\right)^{\frac{\gamma-1}{\gamma}}\right]} + \frac{P_e - P_a}{P_c}\varepsilon \tag{26}$$

and:

$$\varepsilon = \frac{A_e}{A_t} = \frac{\left(\frac{P_c}{P_e}\right)^{\frac{1}{\gamma}}\left(\frac{2}{\gamma+1}\right)^{\frac{1}{\gamma-1}}}{\sqrt{\left[1-\left(\frac{P_c}{P_e}\right)^{\frac{\gamma-1}{\gamma}}\right]\left(\frac{\gamma+1}{\gamma-1}\right)}} \tag{27}$$

Since ε is a known variable, (31) can be used to solve iteratively for the nozzle exit plane pressure, P_e. Once P_e is known, it is fed into (30) to solve for the thrust coefficient, C_f, from the isentropic expansion factor for the combustion products, γ.

An example of the difference in the simulated pressure and thrust profiles for an end-burning non-graded and continuously graded rocket motor can be seen in Figure 4.8 for the same mass fraction of oxidizer. It shows the pressure and thrust history predictions for two separate end burning propellant grains, one with a conventional composite propellant, and another with a graded propellant. This example shows how using just one propellant configuration could create a boost-sustain system while utilizing a very simple grain geometry by optimizing the distribution of the oxidizer.

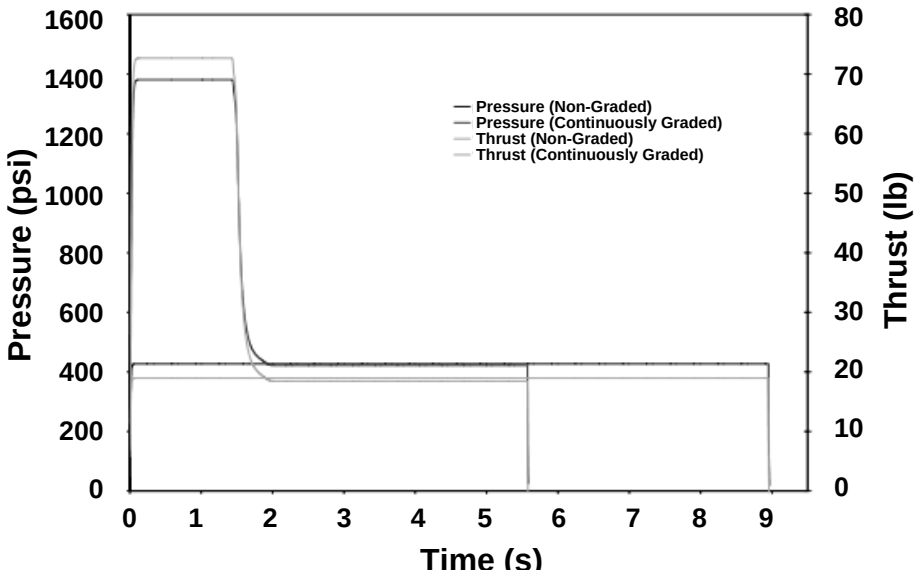

Figure 4.8: Comparison of simulated pressure and thrust profiles for a non-graded and continuously graded end-burning rocket motor with the same mass fraction of oxidizer [17].

Figure 4.9 shows the output from the ballistics code for both continuously graded propellants and conventional composite propellants when a center-perforated grain configuration is used. In both Figures 8 and 9, the propellant web starts out with a high burning rate and ends with a low burning rate. These high and low burning rates were considered the limits for this study, and as

such, calculations were performed for the high and low burning rate propellants if they were considered conventional homogeneous propellants. The transition from high to low burning rates is done in a continuous manner. Curiously, in Figure 4.9 it is noted that the graded propellant experiences a "hiccup" in which the pressure actually becomes higher than in the case of the high burning rate propellant. This phenomenon is a result of the gradient selected for this example and the changing burning surface area of the center-perforated grain. The results predicted by the ballistics code demonstrate that with sufficient computational resources, it may be possible to generate nearly any thrust profile desired by utilizing functionally graded solid propellants. This ballistics code, when coupled with the IDP discussed earlier, will allow a designer, after making some basic sizing calculations, to select a mission thrust profile and input the profile into the IDP and have it return the processing conditions necessary to generate the corresponding gradient architecture.

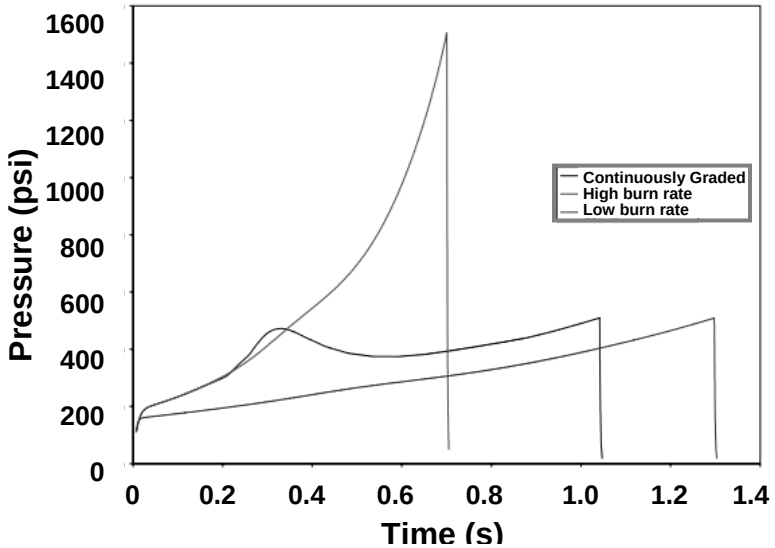

Figure 4.9: A simulated pressure profile for a continuously graded rocket motor in a center-perforated configuration compared to the high and low burning rate performance [17].

4.7 Optimization of Composition Gradients

To complete the IDP of FGEMs, it is necessary to utilize the previously described simulation tools to optimize the composition gradient [1]. One of the most robust optimization tools is the Genetic Algorithm (GA), which is particularly suitable for searching complex multi-variable solution spaces. The genetic algorithm consists of these steps:

1. Define an objective function
2. Generate an initial random population of solutions
3. Evaluate the performance of the population using the objective function, and apply reproduction, crossover and mutation to the old population to generate the children from the parents
4. Repeat step 3 until the stopping criteria is reached

The GA used to optimize the graded material distribution employs a Differential Evolution strategy, which is an advanced form of GA. It is comprised of three sub-programs:

1. *Definition of the objective function:* The objective function, whose minimum is to be found out, is defined in this section. This could incorporate the finite element analysis of the system to obtain the parameters required to evaluate the objective function.
2. *Declaration of initial values:* Various parameters – the number of population members, targeted value of the objective function, initial guesses of the values of the variables, range of values for the population members, optimization strategy to be used, minimum and maximum number of iterations, etc. – are specified in this routine. This routine calls the main part of the program, described below.
3. *Differential Evolution routine:* This routine uses different strategies to generate a set of children from the parent population and evaluates their "fitness" or the value of the defined objective function. Since in this case our goal is to minimize the value of the objective function, the fitness of a member is based on how low the evaluated objective function value is. This procedure is repeated until a population member is obtained that gives the minimum objective function value.

To utilize this GA, the minimum value of the objective function should be known beforehand to detect convergence. Although the GA will converge to the vicinity of the optimum faster, it may take many more iterations to reach the absolute minimum. One drawback of this GA is the inability to constrain the search space. However, it is possible to

penalize the objective function to confine the search. Recently, it has been demonstrated that the efficiency of the GA can be enhanced using the graded architecture [21]. This makes it feasible to integrate the process and performance models with the optimization method in the inverse procedure for developing the novel continuous processing technology to fabricate functionally graded energetic materials.

4.8 Combinatorial Development of New Energetic Formulations

Another important conclusion that can be drawn from the simulation-based materials by design approach for FGEMs is obtained by comparing the burning rates obtained at various compositions in the FGEMs with burning rates obtained from homogeneous compositions manufactured using a Design of Experiments (DOE) reduced mixtures approach (*Figure 11*)[22, 23].

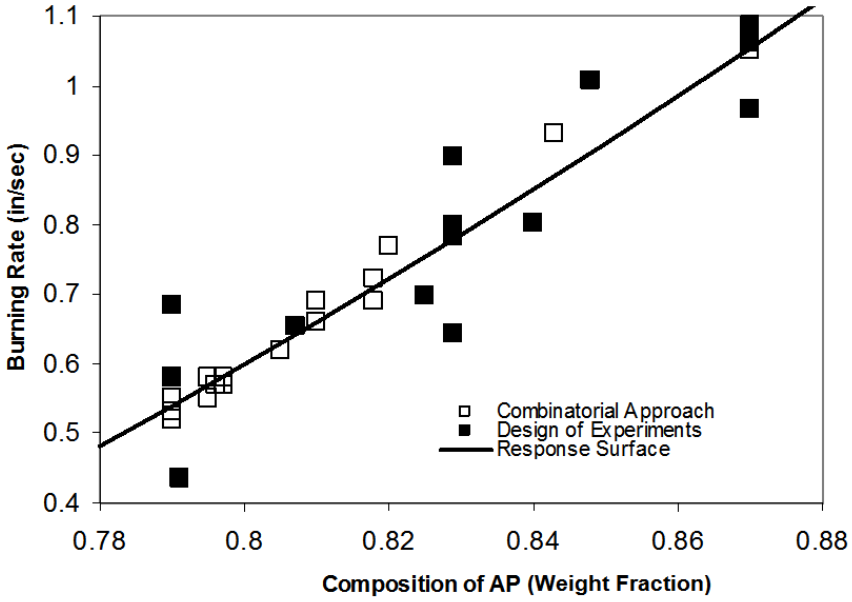

Figure 4.10: Comparison of burning rate properties obtained from a combinatorial approach using simulation-based materials by design and a conventional design of experiments using a reduced mixtures approach [23].

From this comparison, FGEMs can also be viewed as a new combinatorial materials science approach for the development of advanced energetic materials formulations using microscale or nanoscale ingredients (e.g., nanoaluminum, nanoRDX, composite particles). This is an exciting new capability for the formulations community and is a simpler, faster, and more cost effective approach to developing advanced energetic materials than that using more conventional batch processes with a DOE approach. Also, FGEMs also do not suffer from batch-to-batch variations that cause significant variability in the burning rate properties in Figure 10. Thus, FGEMs are a better way to formulate new energetic materials using the simulation tools described in this chapter.

4.9 References

1. H.A. Bruck, F.M. Gallant, and S. Gowrisankaran. Development of a Novel Continuous Processing Technology for Functionally Graded Composite Energetic Materials using an Inverse Design Procedure, Proceedings of the 2002 SEM Annual Conference & Exposition, 296-302, 2002.
2. H.S. Fogler, *Elements of Chemical Reaction Engineering*, Upper Saddle River, NJ, Prentice Hall, 1999.
3. F.M. Gallant, H.A. Bruck and A. Kota. Fabrication of Particle-reinforced Polymers with Continuous Gradient Architectures Using Twin Screw Extrusion Processing, Journal of Composite Materials, 38, 1873-1893, 2004.
4. G.H. Meeten (Ed.), Optical Properties of Polymers, Elsevier Applied Science Publishers, New York, NY, 1986.
5. R.A.L. Jones, Soft Condensed Matter, Oxford University Press, Oxford, UK, 2002.
6. P. Elkouss, D.I. Bigio, M.D. Wetzel, S.R., Raghavan, AIChE Journal 52, 1451, 2006.
7. P. Naor and R. Shinnar, Industrial and Engineering Chemistry Fundamentals 2, 278, 1963.
8. G. Pinto and Z. Tadmor, Polymer Engineering and Science 10, 279, 1970.
9. D. Wolf and D.H. White, AIChE Journal 22, 122, 1976.
10. L.P. B. M. Janssen, L. R.W. Hollander, M.W. Spoor, and J.M. Smith, AIChE Journal 25, 345, 1979.
11. M. Thompson, J.P. Puaux, A.N. Hrymak, and A.E., Hamielec, A. International Polymer Processing 10, 111,1995.

12. J. Gao, G.C. Walsh, D. Bigio, R.M.Briber, and M.D. Wetzel, AIChE Journal 45, 2541, 1999.
13. L. Chen, L., G.H. Hu, and J.T. Lindt, Polymer Engineering and Science 35, 598, 1995.
14. F.M. Gallant, and H.A. Bruck. Fabrication of Graded Energetic Materials using Twin Screw Extrusion Processing, NSWC Technical Digest, 2006.
15. R.L. Glick and J.A. Condon.. Statistical Analysis of Polydisperse, Heterogeneous Propellant Combustion: Steady State, Thirteenth JANNAF Combustion Meeting, CPIA Publication Number 281, 11, 313-345, 1976.
16. F.M. Gallant, S.E. Prickett, and H.A. Bruck. Effects of Twin Screw Extrusion Processing on the Burning Rate of Composite Propellants, Propellants, Explosives, and Pyrotechnics, 31, 456-465, 2006.
17. G. Young, H.A. Bruck, and S. Gowrisankaran. Modeling of Rocket Motor Ballistics for Functionally Graded Propellants, JSC CD-24: Proceedings of the 39th JANNAF Combustion Subcommittee Meeting, Colorado Springs, CO, 1-12, 2003.
18. B.J. Mcbride and S. Gordon. Computer Program for Calculation of Complex Chemical Equilibrium Compositions and Applications, NASA Reference Publication 1311, June 1996.
19. A.H. Shapiro. The Dynamics and Thermodynamics of Compressible Fluid Flow, Vol. 1, Ronald Press Company, New York, 1953.
20. G.L. Armstrong. An Analysis of the Instantaneous Performance Characteristics of Nozzleless Solid Rocket Motors, M.S. Thesis, Purdue University, May 1990.
21. H. Surendranath, H.A. Bruck, and S. Gowrisankaran. Enhancing the Optimizations of Material Distributions in Composite Structures Using Genetic Algorithms, International Journal of Solids and Structures, 40, 2999-3020, 2003.
22. F. M. Gallant, S. E. Prickett, M. Cesarec, and H.A. Bruck. Ingredient and Processing Effects on the Burning Rates of Composite Rocket Propellants Utilizing a Reduced-Run Mixture-Process Experiment Design, Chemometric and Intelligent Laboratory Systems , 90, 49-63, 2007.
23. F.M. Gallant, H.A. Bruck, S.E. Prickett, and M. Cesarec. Graded Polymer Composites using Twin Screw Extrusion: A Combinatorial Approach to Developing New Energetic Materials", Composites Part A: Applied Science and Manufacturing, 37, 957-969, 2006.

Chapter 5

Small Scale Model Testing in Investigations of Energetic Materials – Dynamic Effects Laboratory

William L. Fourney, Uli Leiste, and Leslie C. Taylor

The effects of energetic materials on structures and materials is a complex subject that must have experimental results to aid in understanding expected outcomes and in developing computer codes that can be utilized to predict these outcomes. Unfortunately, full scale explosive testing is very expensive, and the associated violence makes visualization and instrumentation quite difficult. Very small scale testing has been shown to be able to predict quite accurately, in some situations, the results of full scale testing. Small scale testing is cost efficient, more easily observed, and more easily instrumented. Over the past 10 years small scale testing in the Dynamic Effects Laboratory at the University of Maryland has been used to successfully study the response of structures and soils to explosive detonation. We have used small scale testing to predict full scale results in underwater cratering and channeling, the loading (both pressures and impulse) on military vehicles due to the detonation of buried mines, the positive effects of bottom shaping for military vehicles to reduce this loading, and the movement of obstacles underwater by explosive charges. In all cases, the small scale testing results have been supplied to code developers within the DOD to hone their computer simulations, and in all cases they have been used to develop scaling laws that would be applicable to full scale situations.

5.1 Underwater Cratering

Small scale model testing is relatively inexpensive compared to full size testing and permits much more visualization of the process being investigated. The figure below gives a demonstration of how high speed

photography coupled with small scale testing can be used to fully understand dynamic events.

In Figure 5.1, photographs are given that were taken during the event (in this case a charge buried at a given depth in water covered soil). The test bed in this case is a cross section of a charge buried beneath sand, which had a cover of water that was approximately equal to the depth of burial of the charge. In the first frame the charge is just being detonated. By the time the second frame is taken (4 ms after detonation), all of the water has been blown away from the detonation site and the sand is also being ejected from the site. This process continues and a crater is formed in the wet sand. In the fifth frame, shown at 334 ms after detonation, the water that was thrown away from the site is rushing back in, bringing some sand with it. In the last frame shown the water filled crater has been formed and everything is in equilibrium. This technique was used to investigate the mechanisms involved in underwater cratering and channeling for various water depths above the soil and various depths of burial of the explosive charge. For channeling tests, the explosive spacing and the timing of the detonations were investigated. The results obtained identified different mechanisms that came into play for various water depths (i.e. deep, intermediate, and shallow), and it was found that optimum crater and channel sizes were obtained in the case of shallow water situations and the limits of this shallow water regime were determined. Any depth of water can be made to be shallow by increasing the size of charge used for the excavation. These small scale results were then successfully scaled up to full scale situations. The figure shown below is an example of how well the small scale tests can be used to predict full scale results.

Results were compared from a test conducted at Weston Super-Mare in the UK (Test AA) resulting in a channel approximately 50 feet in length, and small scale testing (Test 412) resulting in a channel of approximately 1 foot. Test 412 used four RP-80 detonators (203 mg of PETN/RDX each) and had a depth of water of 0.47 inches and a depth of burial of the charges of 0.91 inches. Test AA used four 8 pound charges of PE 4 and was conducted with a water height of 12 inches and depth of burial of the charges of 24 inches. In order to successfully scale the results from small scale testing to full scaled, the scaled tests have to be conducted very carefully. In all of the tests conducted within the Dynamic Effects Laboratory, typical charge sizes range from a few milligrams to a few grams of explosive, and results have been successfully used to predict charge sizes ranging from 10 to 300 pounds of TNT or military explosives.

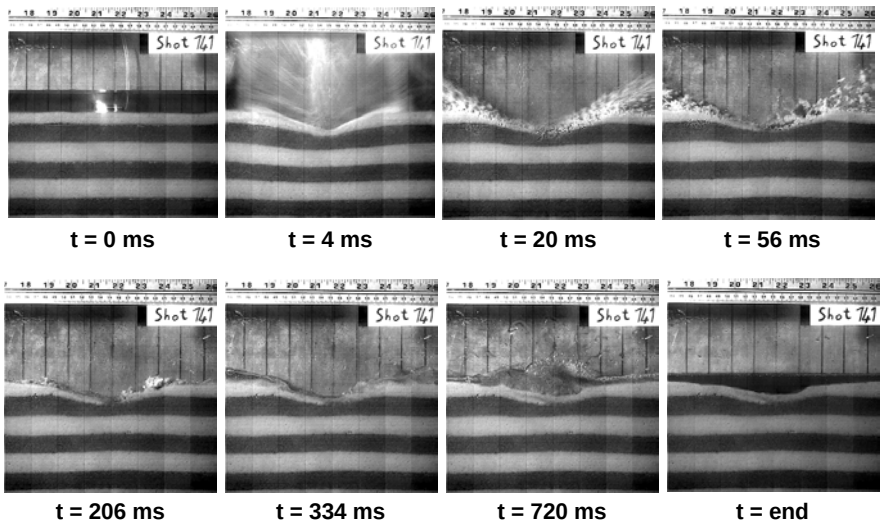

Figure 5.1: Small scale cratering tests.

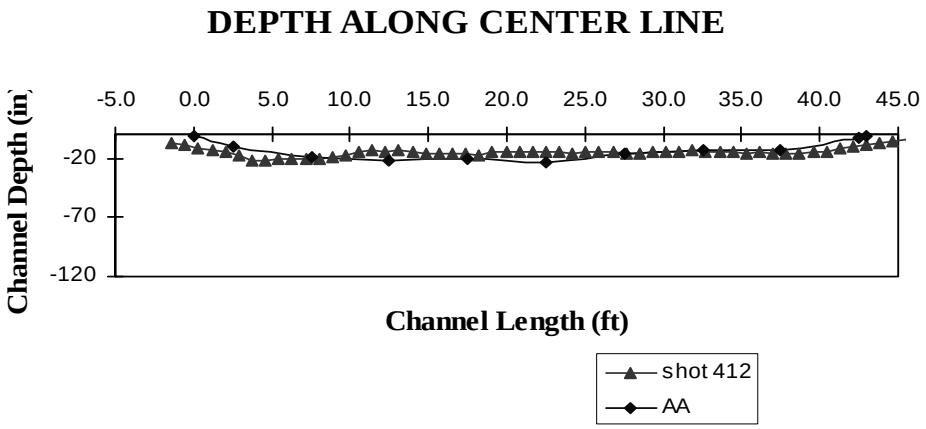

Figure 5.2: Comparison of scaled up small scale channel results with full scale results.

5.2 Loading on Vehicles Due to Mines Detonating

Recently, the DOD has become very interested in knowing more about the loading on vehicles that are subjected to the detonation of buried mines. In the Dynamic Effects Laboratory we have been looking

at several aspects of this problem. We have conducted small scale testing to investigate the impulse delivered to vehicles and have looked at the benefits to be obtained from the shaping of vehicle bottoms (V shaped bottoms). We have also conducted tests measuring pressures being applied to vehicles due to the detonation of mines – those both in the open and buried in soils.

5.3 Impulse Measurements

The figure below shows a comparison of small scale results scaled up to 10 pounds of TNT with various stand off distances and depths of burial. The data shown is the impulse applied to target plates weighing approximately 30,000 pounds as measured in testing conducted at ARL in Aberdeen, Md. (in the VIMF) in the summer of 2004. In these tests the full charge size was either 5 or 10 pounds of TNT (based upon standoff distance), and the largest charge size used in the small scale test was 3.3 gm. The stand off distances for the target plates ranged from 0 (plate on the ground) to 16 inches (for 10 lb. TNT), and the depth of burial of the full size charges ranged from 4 to 12 inches.

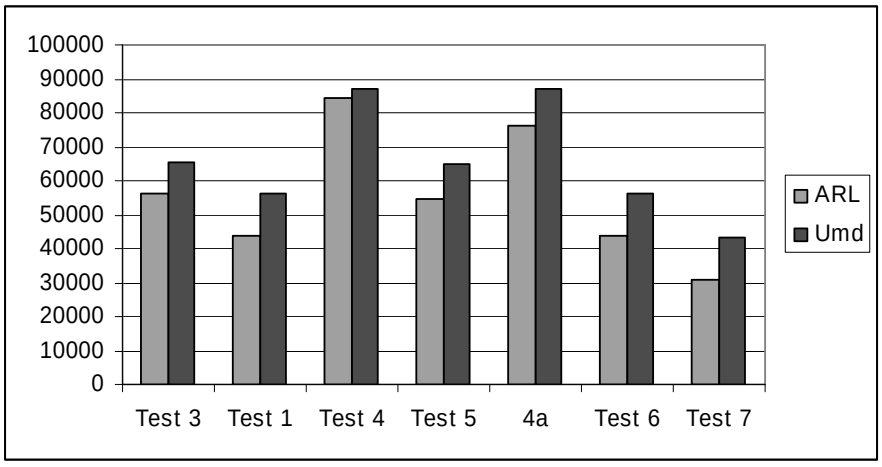

Figure 5.3: Comparison of small scale predictions with full scale results – Plate Impulse

This impulse comes from pressures being applied to the bottom of the vehicle (or target plate). If the pressure time profiles are known for each point on the plate, then these integrated over both time and position would yield the impulse being applied to the plate. Since we had been so

successful in the measurement of impulse, we also wanted to find the pressure time profiles as a function of location on the target plate. The results of that series of tests are described in the following section.

We have also conducted a number of tests to determine how impulse varies with the media in which the charge is buried and also how the impulse is distributed along the plate. We conducted tests in dry sand, saturated sand, and water. That is, the media being ejected upwards by the detonation of the explosive are either dry sand, saturated sand, or water. We conducted tests with two inch diameter plates, four inch diameter plates, 6 inch diameter plates, etc., all the way up to 19 inch diameter plates. All plates weighed the same amount so that weight was not a factor. Figure 5.3a shows the results from this series of tests.

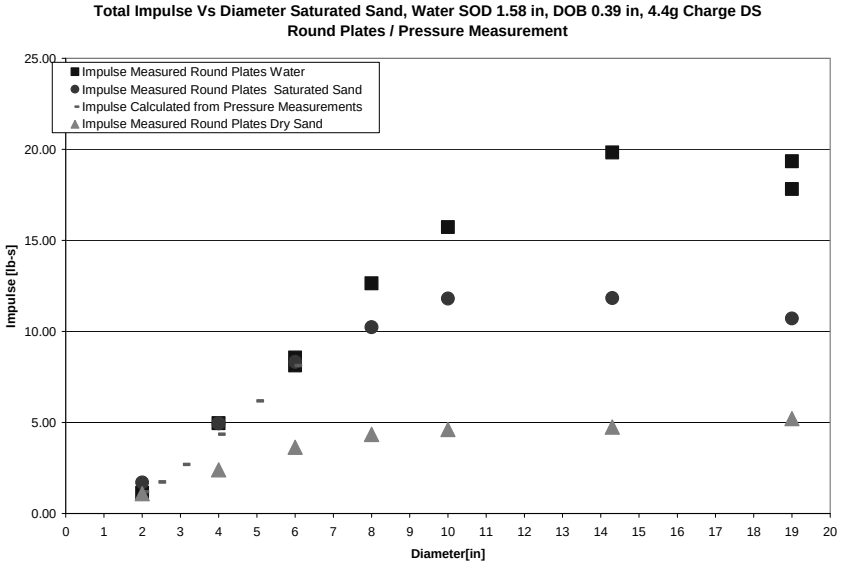

Figure 5.3a: Impulse distributions for dry sand, saturated sand, and water.

For smaller plates some of the sand ejected by the detonation bypasses and does not load the plate. As the plates get larger and larger, more of the sand being ejected loads the plate until finally a diameter is reached where all of the sand strikes and loads the plates. The squares are for water, the circles are for saturated sand, and the triangles are for dry sand. Water provides almost four times larger impulse than does dry sand, and saturated sand provides about 2.5 times more impulse than

does dry sand (for the same size charge, same stand off distance, and the same depth of burial). The loading from the water seems to be more spread out. That is, it takes a bigger plate to capture all the water than it does to capture all the saturated or dry sand.

With the recent development of MRAP vehicles for military use there was an interest in how bottom shaping could affect the loading due to the detonation of buried mines. Figure 5.3b shows a vehicle that was of interest.

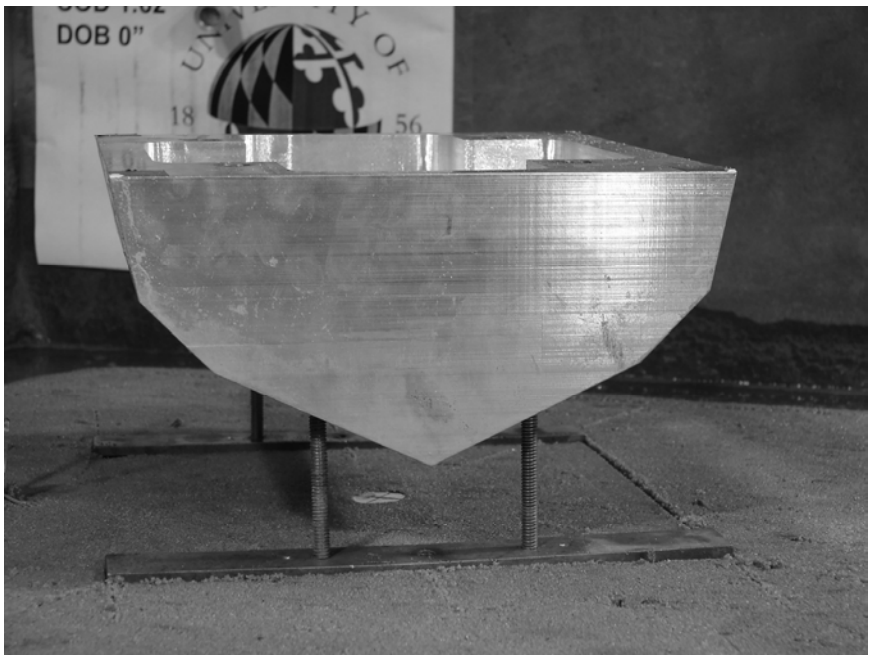

Figure 5.3b: Hull shape of interest to the military.

The shape shown has three different bottom angles with the steepness of the angle increasing as one leaves the vehicle bottom. We conducted a very large number of scaled model tests. In all, the test series consisted of approximately 50 separate tests. We investigated three different depths of burial and three different stand off distances. For each of these conditions we looked at a flat plate configuration and two different angled bottom configurations. In addition, in some tests we varied the weight of the "vehicle" to determine the effect of vehicle mass on the impulse delivered to the vehicle. We also conducted a small

number of tests to determine how detonations away from the center of the vehicle would affect the loading on the vehicle. Figure 5.3c shows how the impulse varied at a given standoff distance as a function of depth of burial for the various "vehicles" tested. The top curve (defined by the triangles) is the results obtained for a flat bottom. The middle set of curves (defined by the diamonds) is the results obtained for the angled bottom vehicles. The lowest curve (defined by the circles) is for an angled bottom vehicle that is also angled in the direction of travel. That is, the nose of the vehicle is lower than the rear of the vehicles, giving an angle in both directions. As can be seen from the figure the angled vehicle drops the impulse from a little over 6 to about 2.5. This is quite a decrease in loading and well worth the effort of shaping the bottom.

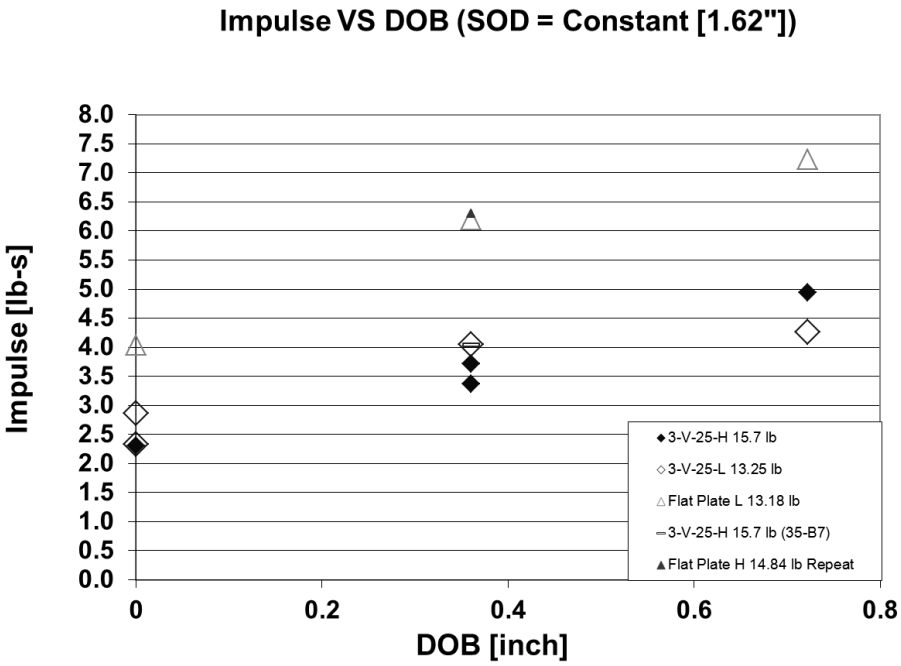

Figure 5.3c: Impulse versus depth of burial for a fixed standoff distance - V Hull.

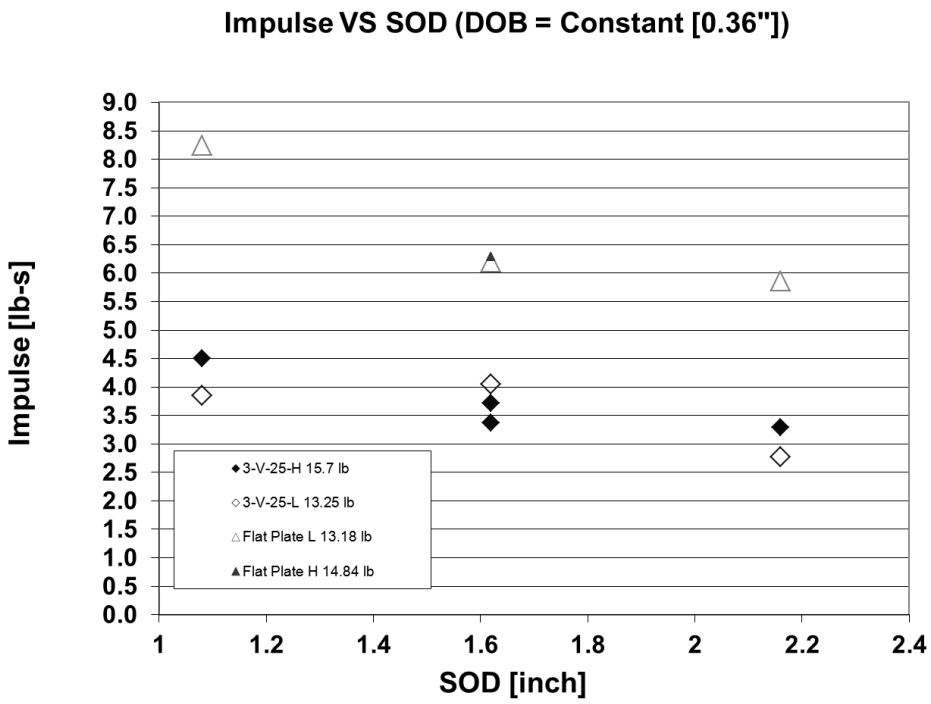

Figure 5.3d: Impulse versus standoff distance for a fixed depth of burial – V Hull.

Figure 5.3d gives similar results but shows the effect of standoff distance at a given depth of burial. Again there is a significant drop in load for the angled vehicle.

Figure 5.3e shows how impulse varies if the charge is not detonated directly under the center of the vehicle. For these cases we found that the angular momentum applied to the vehicle was very small compared to the linear momentum. For that reason we show only linear impulse in the figure. The width of the vehicle in this case was a little larger than 8 inches so that the points shown in the graph represent results when the charge is under center (0), halfway out along the side (2+), at the edge of the vehicle (4+), and beside the vehicle (6+). The midway point appears to give the worst result but it is not much larger (4.9 versus 3.8) than the impulse that occurs when detonation is under the center of the vehicle.

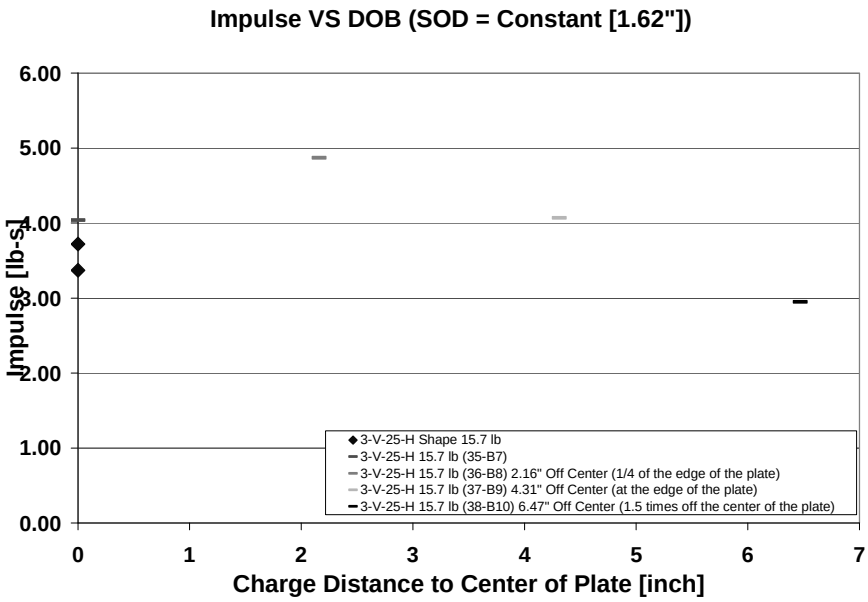

Figure 5.3e: Impulse as a function of Off Center Position – V Hull.

5.4 Pressures on Target Plates

We had an interest in both pressures resulting from the ejecta from detonating mines that are soil covered and also from air blast pressures resulting from detonation of explosives in free air.

5.4.1 Due to Buried Mines

For the case of a buried mine the mechanism of the pressure build up on the bottom of a target plate is felt to be due to the very fast moving soil coming to rest when it strikes the plate. In fact there could be three different mechanisms of pressure loading on a plate. If the charge is not covered with soil and is detonated a very high pressure, the shock wave will move through the air and will load anything in its path. If the target plate is in contact with the soil in which the explosive is buried, then upon charge detonation, stress waves from the soil will pass into the target plate and these stress waves will create pressures in the plate. In most cases of interest to the U S. Military, the vehicle is not in contact with the ground and the charge is buried. As a result, for the normal

buried mine incident, air blast loading and stress wave loading are not important. Instead, the soil that surrounds the undetonated charge is thrown away from the detonation site at very high rates of speed. We have observed in our model testing sand/soil velocities on the order of twice the speed of sound. This soil is then brought to rest against the bottom of the vehicle, creating very high stagnation pressures. In some cases these very high pressures rupture the bottom, killing all inside. In cases where rupture does not occur the vehicle and its passengers are thrown into the air and the occupants are subjected to very high accelerations and loading. We were interested in the latter case and wanted to measure the pressures applied to the bottom of the vehicle. Figure 5.4 shows a single frame from a test where the explosive was buried at a relatively deep depth. Notice that the sand/soil is rising in a relatively smooth dome.

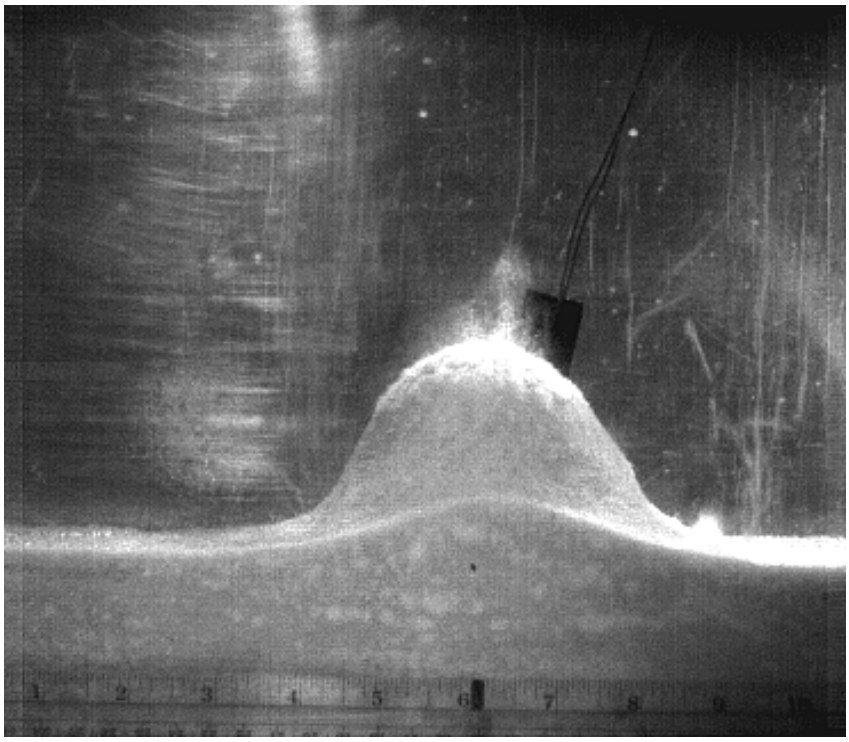

Figure 5.4: Dome of sand being thrown up from a deeply buried charge.

Figure 5.5 shows our test set up for measuring pressures. We placed a plate at a given standoff distance from the soil air interface and placed Kolsky bars flush with the face of the plate. When the charge is detonated the upward traveling sand strikes the end of the Kolsky bars and a stress wave travels up the bar and is recorded at a strain gage located about 1 foot along the bar. This stress pulse is recorded before the reflection of the stress wave again reaches the strain gage location.

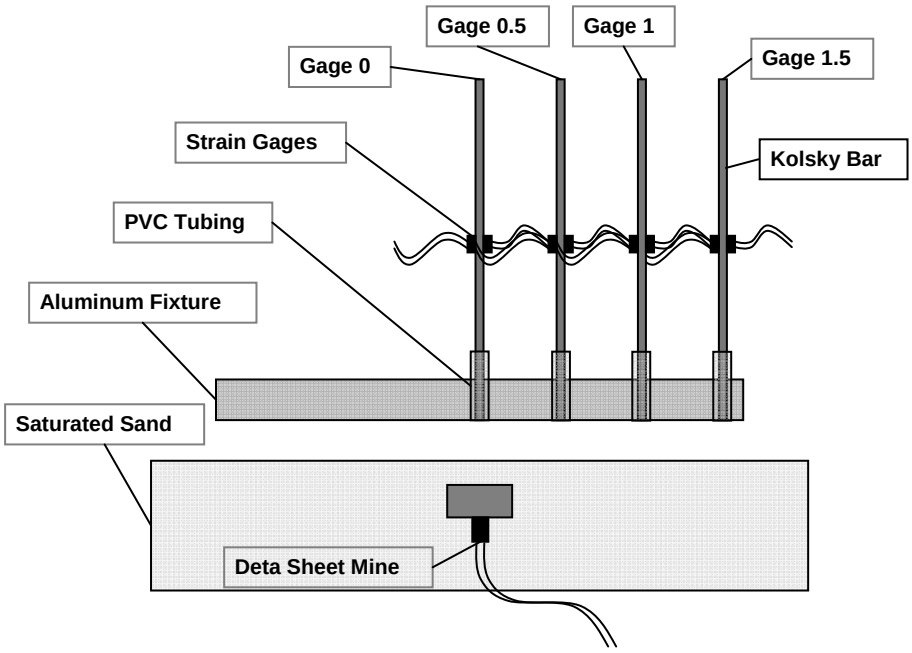

Figure 5.5: Test setup for measurement of pressures.

Figure 5.6 gives the results of our initial attempts to measure pressures on the bottom of vehicles. In that figure the results of 6 different tests are presented – some with different size charges – but the distances have been scaled so that in a perfect world all results should define a single curve. Note also that these results were for a case where the depth of burial was quite shallow. For a charge size of 10 pounds of TNT the depth of burial of the charge would be only 4 inches with a standoff height to the bottom of the vehicle of 16 inches. As can be seen from the figure, the results at distances farther from the plate center are

not too bad, but the results, especially near the center of the plate, are not at all what might be expected. Notice in particular that right at the center of the plate measured pressures range from 130,000 psi to about 255,000 psi. These results were very confusing and we began to investigate why they were so different. Figure 5.7 shows one frame from a high speed test in which the depth of burial of the charge was shallow. Compare this figure to the picture in Figure 4, and it is clear that for a shallow buried charge the dome is not smooth but rather has sharp jets moving much faster than the overall dome velocity. Perhaps an even better picture of how non uniform the upward moving dome in the case of a shallow buried explosive can be is given in Figure 5.8. In that picture the dome is shown interacting with a clear rubber sheet and demonstrates clearly that some parts of the dome are moving much faster than other parts.

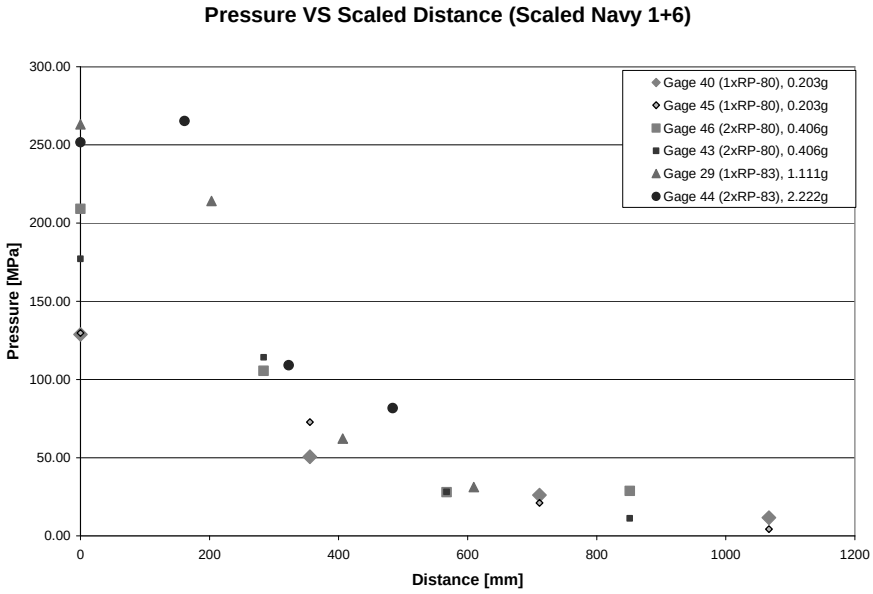

Figure 5.6: Measurements of pressure as a function of distance from plate center.

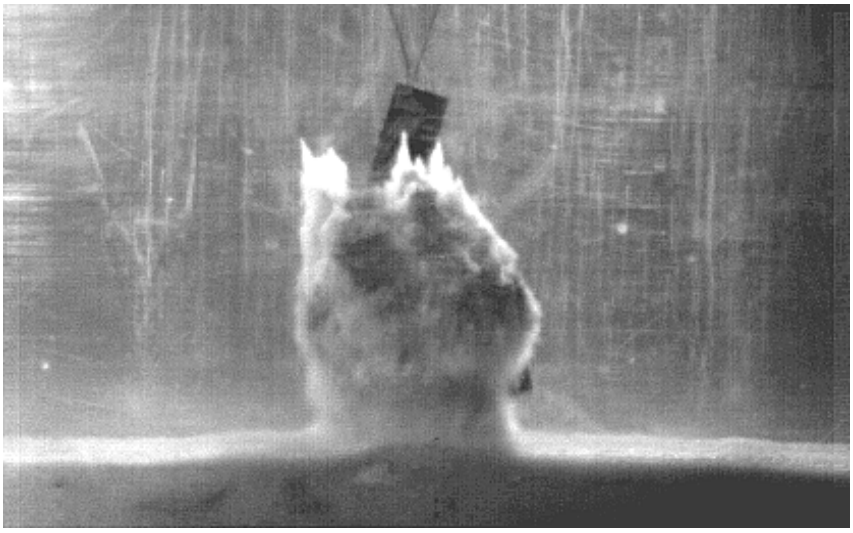

Figure 5.7: Upward moving dome from shallow buried charge detonation.

Figure 5.8: Interaction of upward moving soil from a shallow buried explosive with a clear rubber sheet.

This non uniform (unsmooth) dome would mean that whichever part of the plate is hit by the faster moving jets would have much higher pressures applied than those parts of the plate hit by the slower moving sand in the rest of the dome. We therefore decided to measure the pressures at multiple locations at any given distance from the center of the plate. Figure 5.9 shows the test setup used to record pressures at multiple locations but at a constant distance from the plate center.

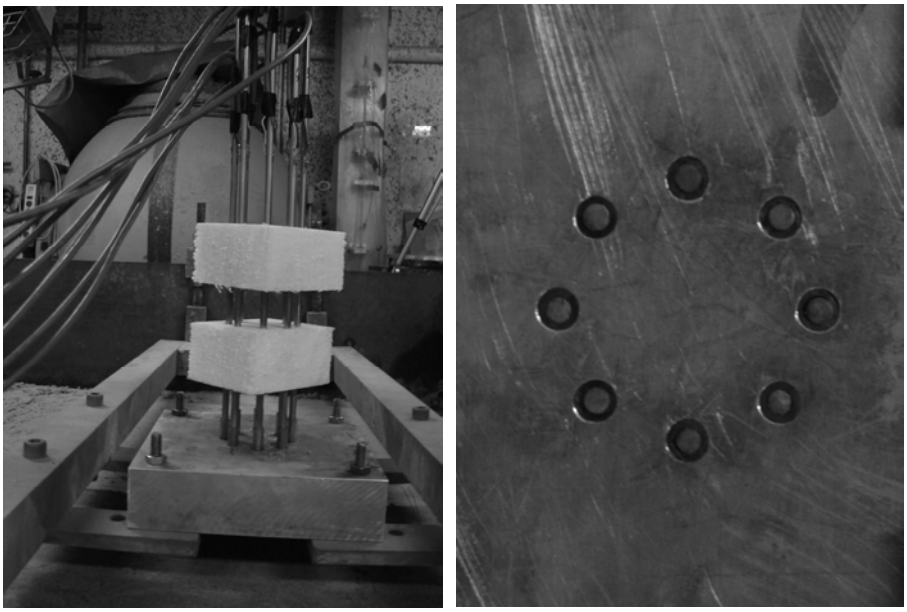

Figure 5.9: Use of multiple Kolsky Bars at any given distance from the center of the plate to obtain maximum, minimum, and average pressure values at that point.

Figure 5.10 shows the maximum pressure measured at any given location (open circles), the average of 7 pressures measured at any given location from the plate center for three different tests (the – marks), and finally, the average pressures at any given location from averaging all pressure measurements at that location (filled diamonds). Notice that the average of all the pressure measurements (the filled diamonds) define a nice nearly continuous curve. From this data it appears that the maximum pressure may not occur at the center of the plate, and we have other evidence to verify that this could indeed be the case. More importantly,

notice that if one averages the pressures measured by eight Kolsky Bars at a common distance from the plate center and then repeats it for two more independent identical tests, the three averages agree nicely. It is apparent from these measurements that due to the nature of the dome being thrown from the detonation site, at any given point one may or may not encounter a jet, and therefore at any given point the pressure measurement might vary greatly from test to test with the same conditions. However, if one averages the pressures measured around a circle with any given diameter for any given test, this average is predictable. From looking at Figure 5.10 it appears that the curve defining the maximum pressures measured is very similar in shape to the curve defining the average pressures but is merely shifted upward. We are in the process of investigating what causes this chaotic behavior and how it might be predicted.

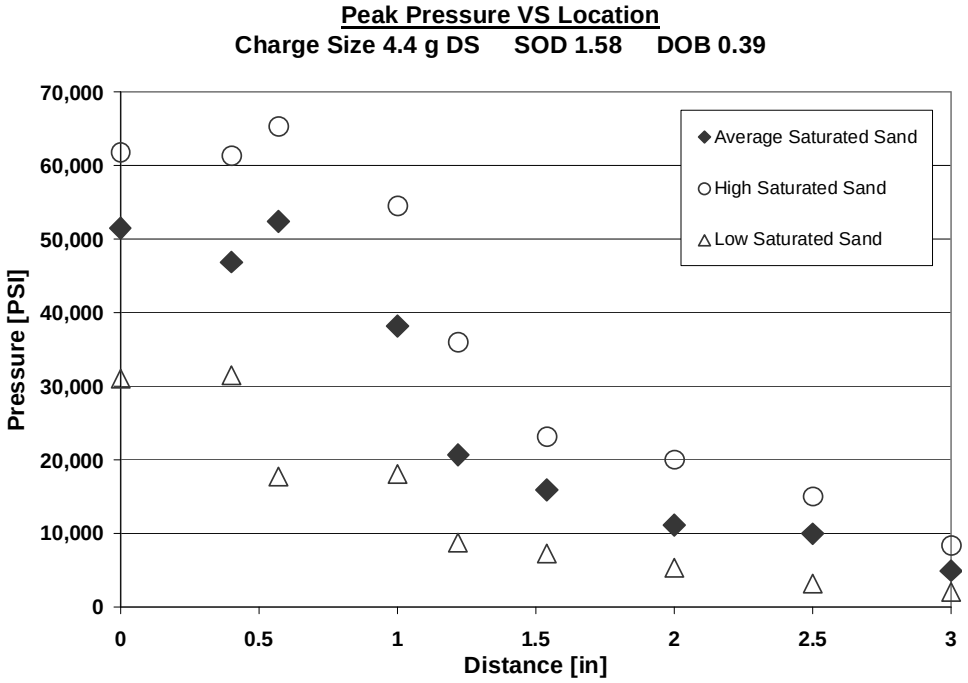

Figure 5.10: Pressures as a function of distance from plate center.

5.5 Air Blast Pressure

Pressures caused in air due to the detonation of an unburied (or buried) charge are also of interest to the military. This overpressure travels from a detonation site and can cause physical harm to anyone within that high pressure zone. We have also done some small scale testing for this situation. Figure 5.11 shows the test set up.

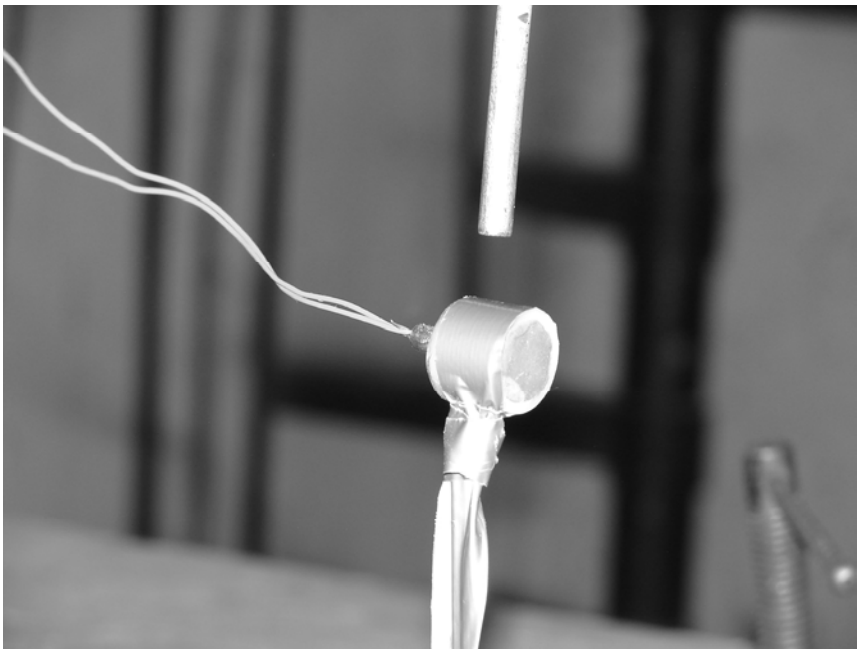

Figure 5.11: Test set up to measure air over pressure due to charge detonation.

For these tests different charge sizes were used and the standoff distance from the charge was varied as well. Charge sizes of 1.5, 3, and 6 gm were utilized and the standoff distance was increased from 0.5 inches to 3.0 inches. Figure 5.12 presents the pressure time profiles from two different tests with the same charge size and standoff distance.

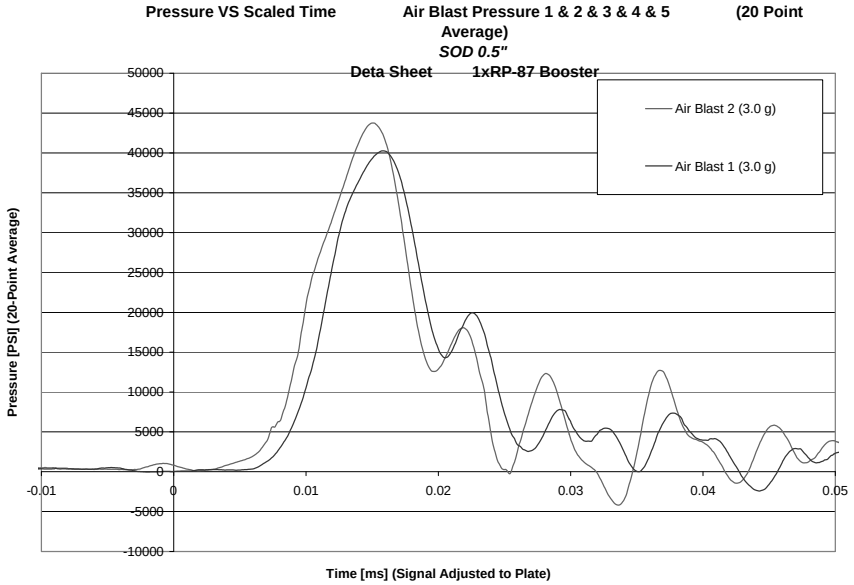

Figure 5.12: Pressure time profiles from two identical tests using 3 gm of PETN.

Notice from the figure the good reproduction in the pressure time profiles. The sinusoidal oscillations that occur after the peak pressure is reached (around 0.02 ms) are likely from the pressure wave reaching the strain gage location and "squeezing" on the gage as the very high pressure pulse passes the strain gage location. That is, the pressure increase on the end of the bar causes a stress wave to run up the bar faster than the pressure disturbance in the air travels up the bar. When the air pressure wave reaches the strain gage it causes a disturbance that is superposed on the stress wave signal. In all the tests that we conducted the pressure profiles were extremely good and very reproducible from test to test. Figure 5.13 shows a comparison of pressures applied to a target plate from air blast obtained from full scale testing and small scale testing, and the agreement is remarkably good. Keep in mind that the small scale testing used no more than 6 gm of explosive and the results shown in Figure 5.13 are for any size explosive charge.

We also measured impulse on target plates as a result of air blast in this series of tests. Figure 5.14 shows the test set up and Figure 5.15 gives some typical results. In this series of tests we used the high speed video to track the position of the plate as a function of time and used that

data to determine the kickoff velocity of the plate after the charge was detonated. From this information we found the impulse by equating that to change in linear momentum.

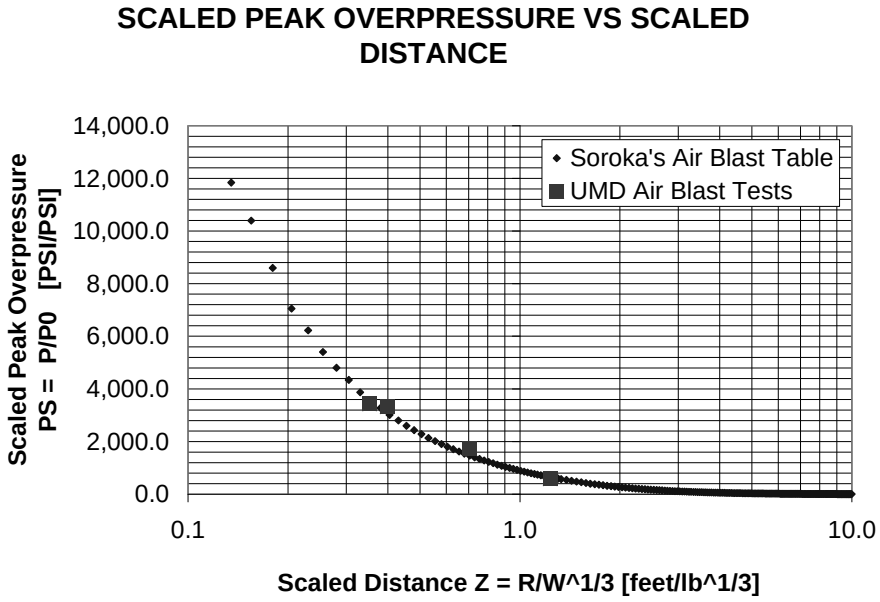

Figure 5.13: Comparison of pressure predictions from the UMD air blast tests and established tables from the military.

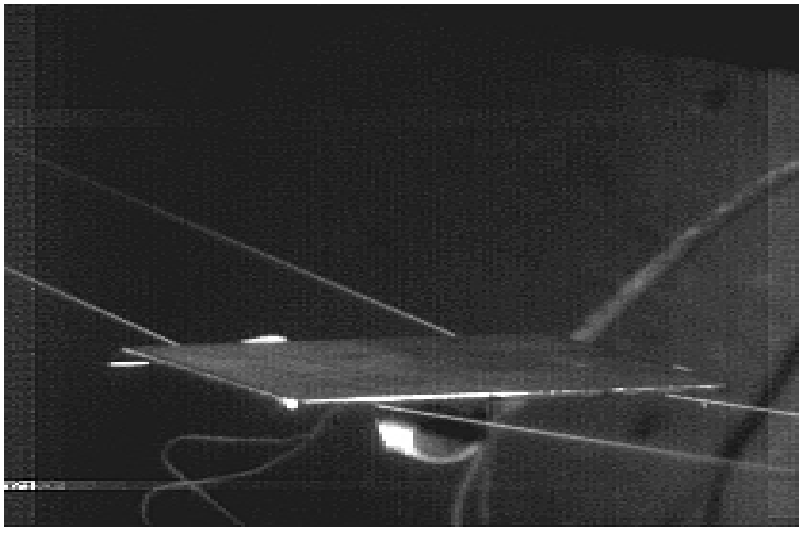

Figure 5.14: Test setup for plate impulse due to air blast.

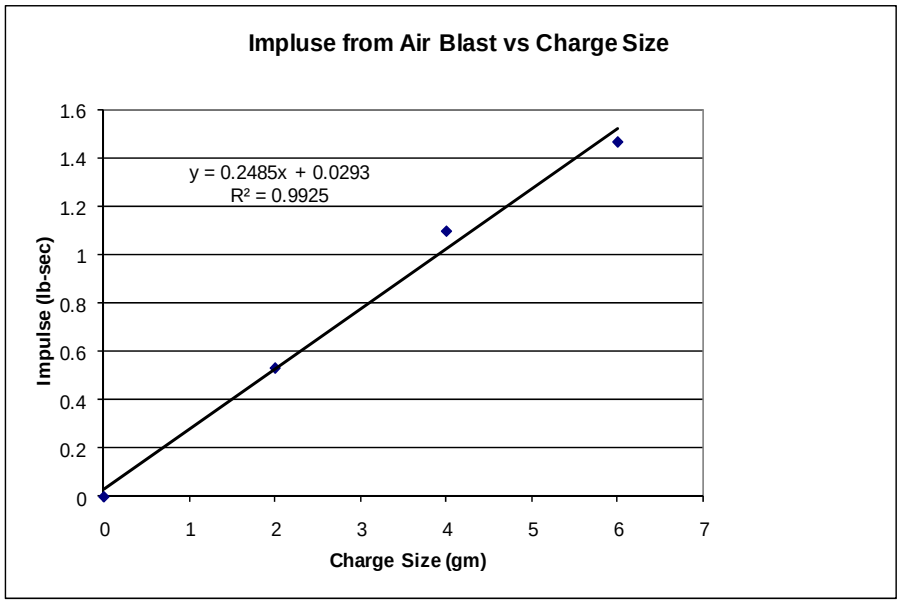

(a)

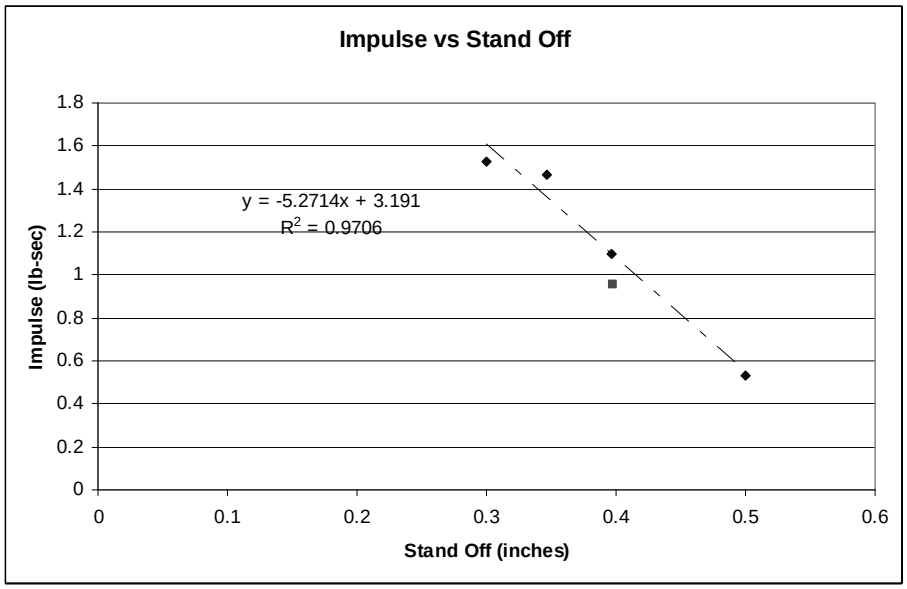

(b)

Figure 5.15: Impulse from air blast as a) a function of charge size and b) as a function of standoff distance.

It appears that impulse builds up quickly as the charge size is increased and falls off even more quickly as the standoff distance increases.

5.6 Obstacle Movement Underwater

The Navy has an interest in knowing the amount of displacement that would be given underwater obstacles (such as hedgehogs, tetrahedrons, and cement blocks) due to the detonation of explosives underwater. If they are trying to assault a beachhead and the shallow waters have been filled with these obstacles, the obstacles must be removed or displaced before a successful assault can be accomplished. Within the Dynamic Effects Laboratory, we conducted small scale testing to determine if the motion of such obstacles subjected to underwater detonations could be predicted at small scale. Figure 5.16 shows some of the models of different size tetrahedrons that were used in that testing. Also shown in that figure is an RP-80 that was used as the explosive source. We were trying to predict what would happen in the full scale if a Mark 82 or Mark 84 bomb were used as the explosive source.

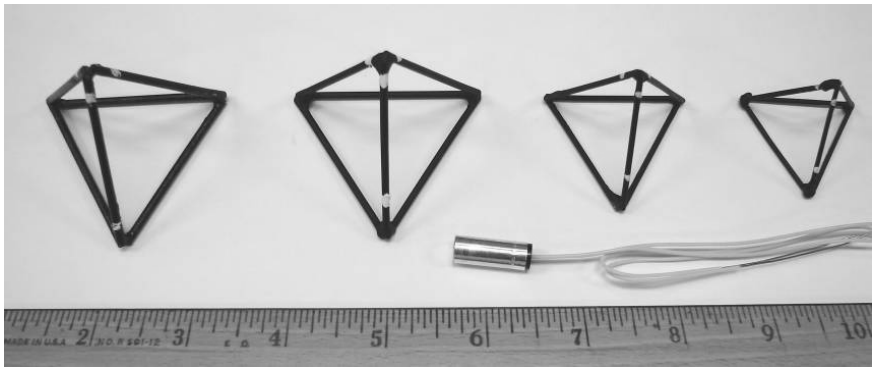

Figure 5.16: Models of tetrahedrons used in small scale testing.

Figure 5.17 shows the experimental setup used. The tank shown had four sides and a bottom – all made from polycarbonate so that the motion of the obstacles could be determined in three dimensions. Two cameras were used – one from the side and one from the bottom – by using the mirror shown in Figure 5.17. Of course corrections were needed to account for the different index of refraction for the water versus air. Figure 5.18 shows the trajectories determined in one of the small scale

tests for two different tetrahedrons that were different distances from the explosive charge.

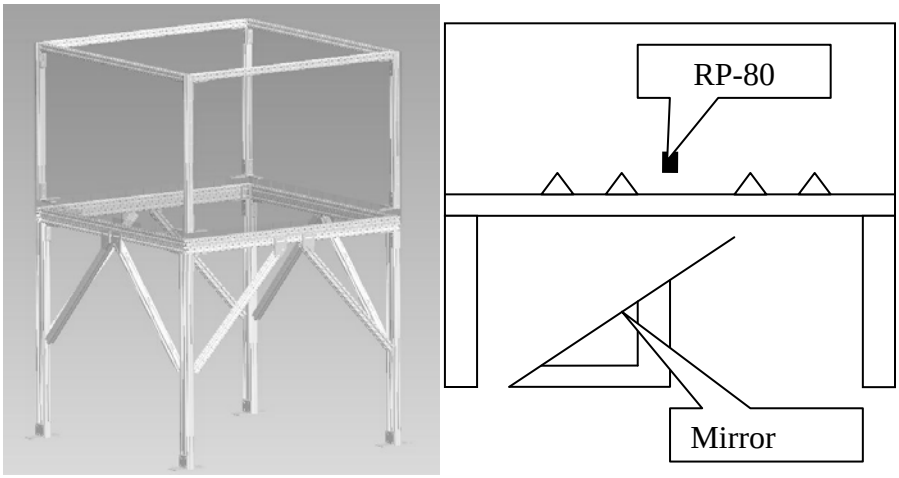

Figure 5.17: Tank used to investigate motion of obstacles.

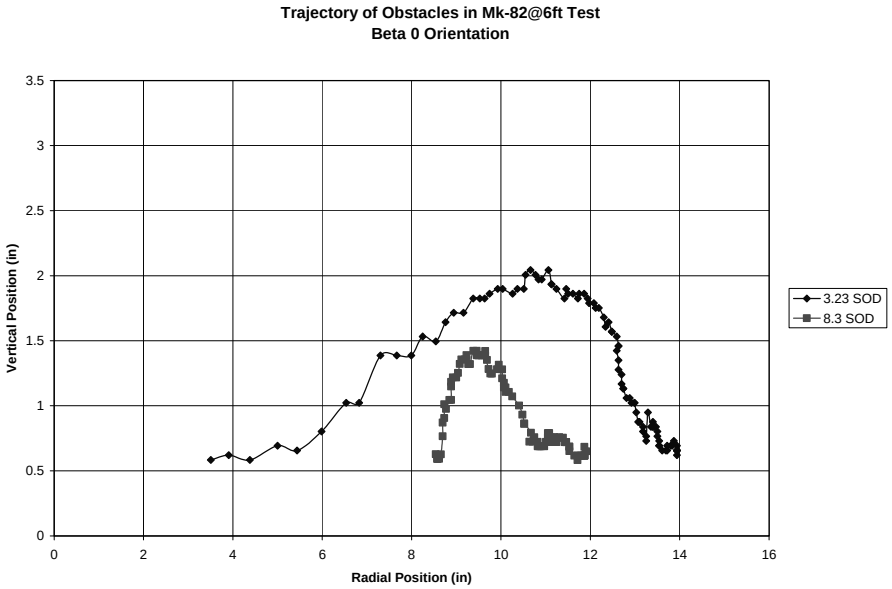

Figure 5.18: Trajectories measured with high speed cameras for two obstacles at different distances from the charge.

Figure 5.19 compares the movement of underwater obstacles (tetrahedrons) from tests at very small scale to that in a series of tests conducted at SRI to predict results for using bombs to move obstacles out of the way to allow an unimpeded amphibious assault of a beach.

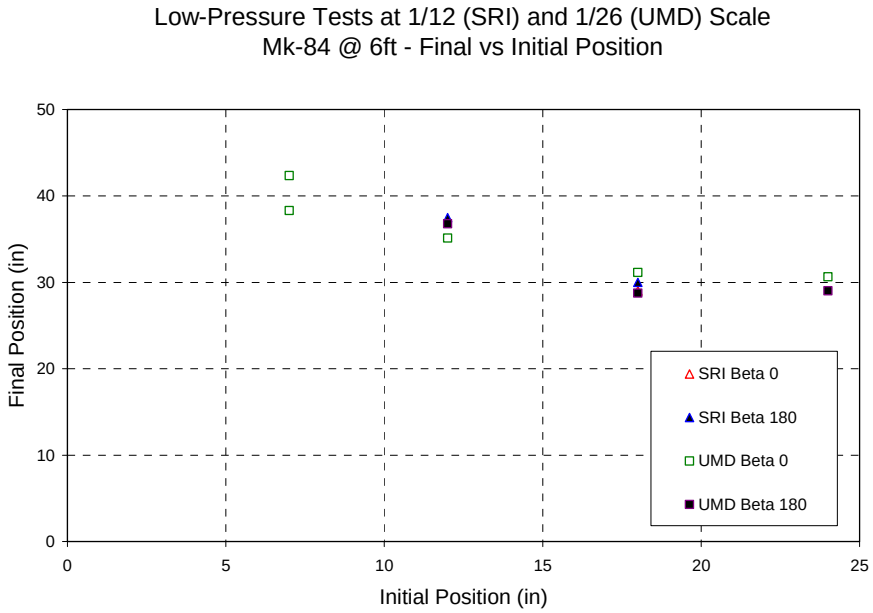

Figure 5.19: Comparison of underwater obstacle movement for two different size test series.

The squares (both open and filled) are from tests at 1/26 full scale conducted at Maryland. The triangles are from 1/12 scale testing conducted at Stanford Research Institute. The Beta 0 and Beta 180 notations refer to which side of the tetrahedron faced the charge – either the point (Beta 0) or the flat (Beta 180). We found that we could predict quite accurately the motion as long as the obstacles did not fly out of the water. Once they left the water our small scale tests could no longer predict the final position.

5.7 Summary

We hope that we have demonstrated with the examples in this chapter that small scale testing can be used quite effectively not only to provide valuable data to assist in the development of computer codes but

also, if the tests are carefully conducted, to predict the results for full sized explosive events. Small scale testing is very inexpensive, and visualization and instrumentation are much easier to accomplish than in full scale testing. We are currently looking at possible ways of mitigating the loading on military vehicles from the detonation of buried mines. The list of references given below is a more detailed explanation of the test series described in this chapter.

5.8 References

1. "Underwater cratering and channeling with explosives," with L. Taylor and D. Robeson, The International Journal for Blasting and Fragmentation, Vol. 3, No. 2, pp. 165-183, 1999.
2. "Visualization of Cratering in an Underwater Environment," by W. L. Fourney, D.J. Goodings, R.J. Bonenberger, and H. U. Leiste, The International Journal of Blasting and Fragmentation, 2002, Volume 6, Number 1.
3. "Explosive Impulse on Plates," W.L. Fourney, Uli Leiste, R. Bonenberger, & D. Goodings, FRAGBLAST International Journal on Fragmentation and Blasting, 2005, Vol. 9, number 1, pp 1-18.
4. "Mechanism of Loading on Plates Due to Explosive Detonation," by W.L. Fourney, Uli Leiste, R. Bonenberger, & D. Goodings, FRAGBLAST International Journal on Fragmentation and Blasting, 2005, Vol. 9, number 4, pp 205-217.
5. "The Effect of Angled Bottoms on the Impulse Delivered to Armored Vehicles," by Kevin Genson, W. L. Fourney, & Leslie Taylor, International Journal on Blasting and Fragmentation, 2008, Vol. 2, Num 1, pp 54-69.
6. "Pressures Acting on Targets Subjected to Explosive Loading," by W. L. Fourney, Uli Leiste, and Leslie Taylor, Blasting and Fragmentation, 2008, Vol. 2, Num 2, pp 167-188.
7. "Target Loading From A Submerged Explosion," Wardlaw, Andrew, Fourney, W. L., Leiste, U., Blasting and Fragmentation, 2008, Vol. 2., Num. 3, pp 211-226.
8. " Yield Surfaces for Granular Flows Applied Explosively," W. G. Szymezak, U. Leiste, & W. L. Fourney, Blasting and Fragmentation, 2009, Vol. 3., Num. 1, pp 43-72.
9. "Application of 3D Image Correlation for full field transient plate deformation measurements during blast loading," Vikrant Tiwari, Michael Sutton, S. R. McNiell, Shaowen Xu, Xiaomin Deng, William L. Fourney, & Damien Bretall, International Journal of Impact Engineering, Vol. 36, 2009, pp. 862-874.

10. Inverse Hybrid Method for Determining Pressure Loading on Plates due to Buried Mines," Damien Bretall & W. L. Fourney, Blasting and Fragmentation, 2009, Vol. 3, Num. 2, pp 89-114.
11. "Target Loading from a Submerged Explosion," Andrew Wardlaw**,** W.L. Fourney and Ulrich Leiste, accepted for publication, Shock & Vibration.

Chapter 6

Development and Application of a Computational Model for Multiphase Explosions

Thomas P. McGrath II and Gregory S. Jackson

This chapter discusses the development of new modeling capabilities for multiphase explosions containing a dispersed particle phase. The development of new algorithms and modeling tools for compressible multiphase flows provides a basis of assessing the dispersion of particles (inert or reacting) by high energy shock waves generated from energetic devices, as well as of determining the effect of particle dispersion and reaction on energetic performance. The model treats all phases as fully-compressible and accurately treats the mathematical characteristics of the dispersed phase. The governing equations are solved using a Godunov-based numerical method driven by a multiphase Riemann solver. These approaches have been implemented into a multi-dimensional flow solver to simulate multiphase explosions. The power of the simulation tool is demonstrated in three examples: 1) a nitromethane explosive with interspersed steel particles, 2) a PETN explosive with interspersed glass particles, and 3) aluminum combustion in post-explosion detonation wave propagation. The results illustrate critical relationships that may assist future design of multiphase explosives.

6.1 Motivations for Multiphase Explosion Models

A large fraction of explosive events involve multiple phases. Often, these events include particles that are dispersed by the rapid expansion associated with the release of chemical bond energy from energetic materials. Understanding the behavior of such multiphase explosions is critical for many applications, including hazard/risk assessment, energetic material development, and propulsion. For hazard/risk

assessment, events related to improvised explosive devices (IEDs), coal dust explosions, and gas-phase explosions with particulate debris are of concern. Multiphase effects can be driving forces in these events, and the hazard assessment community can benefit from validated and verified computational models. In energetic materials development, many modern day explosives rely on metalized materials with slower-reacting particles dispersed within an energetic matrix. Assessing the dispersion of particles in secondary reaction events after the initial energetic material ignition is another example of where multiphase explosion models can be utilized. Finally, many advanced propulsion technologies for underwater or other applications may depend on multiphase energetic materials. Design optimization of such technology requires detailed models that can predict the behavior of such events within the context of the propulsion system.

Despite the numerous applications and widespread interest, the dynamics of multiphase explosions remain poorly understood. The very short time scales and high temperatures and pressures of explosion events, coupled with the complexity of flows, make experimental investigations difficult. Few studies have utilized adequate diagnostics to provide valuable insight and results for basic model validation (Zhang et al. 2001, Carney and Lightstone 2009, Liu et al. 2010). During the explosion, high-speed dispersed particles can complicate traditional pressure measurements, destroy instrumentation, and inhibit effectiveness of optical diagnostic techniques.

The difficulty and scarcity of experimental studies have led to several researchers developing numerical modeling tools to study multiphase explosions. However, there are still unresolved issues related not only to the model algorithms but also to the governing equations themselves. Complexities of phase interactions combined with compressibility of the dispersed phase (as well as the fluid phase) present considerable conceptual challenges related to the governing equations, particularly the so-called nozzling terms and the equation of state for the dispersed phase.

One of the most influential numerical studies on multiphase explosions is that published by Baer and Nunziato (1986), which has been the basis for numerous subsequent studies. In their study, Baer and Nunziato proposed a system of governing equations for a reactive two-phase flow in granular explosives, which treats both phases as fully compressible and allows for complete non-equilibrium between the phases. To close the system of equations, a dynamic compaction equation governing the evolution of dispersed-phase volume fraction was introduced. Use of an evolutionary equation for volume fraction overcomes difficulties encountered when rigid pressure equilibrium

constraints are applied, which can lead to an ill-posed mathematical model.

Gonthier and Powers (2000) adopted the model of Baer and Nunziato (1986) but deleted the nozzling terms in the governing equations. They used a higher-order Godunov numerical scheme with an approximate Riemann solver for the two-phase flow equations. Saurel and Lemetayer (2001) generalized Baer and Nunziato's model and proposed a numerical technique aimed at computing both multi-fluid and multiphase problems. Multi-fluid problems differ from multiphase problems in terms of discretization. In multi-fluid problems the various phases are discretized on the grid, while in multiphase problems they are not. Unlike Baer and Nunziato (1986), Saurel and Lemetayer introduced infinite relaxation parameters for pressure and velocity to enforce pressure and velocity equilibrium among phases. The assumption of pressure equilibrium is often justified in multiphase explosion modeling, but velocity equilibrium is not. Velocity non-equilibrium is, in fact, a critical feature in many multiphase explosion scenarios, necessitating a numerical method accounting for these effects.

The above numerical models have assumed that the pressure of a dispersed phase is equal to that of the constituent material of the individual particles or grains. This assumption may be justified in the case of densely-packed granular flows, but is not valid in general. Rather, as particle loadings dilute, both the pressure and the sound speed of a dispersed phase go to zero, which modifies the characteristics of the governing equations and impacts the numerical solution. Properly representing the mathematical characteristics of the governing equations, and developing an accurate solution technique, was a motivation for developing the new model used in the current work.

Zhang, et al. (2001) presented a numerical model and experimental validation for the explosive dispersal of solid particles. Their model extended the Baer and Nunziato model to dilute particle flow and used a heuristic equation of state for the dispersed particle phase. A Godunov-based method was applied to the gaseous phase but a flux-corrected-transport McCormack scheme was used for the particle phase. The mixing of such numerical schemes is problematic from a general modeling structure point of view, but nonetheless their results provide valuable insight into multiphase explosion phenomenology.

More recent numerical studies on multiphase detonations include papers by Papalexandris (2004, 2005). Papalexandris studied the effects of inert and reactive particles on detonation waves in gases, but in those studies the particles were assumed to always be dilute and incompressible, which limits the applicability of this model in many realistic explosion scenarios.

This chapter presents a unique compressible multiphase flow model for the study of multiphase explosions. Specifically, the model focuses on explosions containing a dispersed particle phase and is motivated by the lack of a fully satisfactory model in the literature. The model applies a Godunov-based numerical technique driven by an approximate multiphase Riemann solver. All phases are treated as compressible, and full non-equilibrium among phases is allowed. Numerical calculations using this model are compared to experimental data, demonstrating the accuracy of the model and highlighting multiphase explosion phenomenology.

6.2 Model Description

Computational modeling is achieved through numerical solution of the compressible multiphase flow equations. The mathematical model allows each phase *k* to retain separate physical properties, including volume (or volume fraction α), density (ρ), velocity (u), energy (E), temperature (T), and pressure (P). The retention of separate physical properties is necessary for modeling the mechanical and thermal non-equilibrium among phases that is inherent in multiphase explosions. The governing equations for each phase *k* are provided here as transient partial differential equations:

$$\frac{\partial \alpha_k \rho_k}{\partial t} + \nabla \cdot \left(\alpha_k \rho_k u_k \right) = \dot{m}_k \tag{6.1}$$

$$\frac{\partial \alpha_k \rho_k u_k}{\partial t} + \nabla \cdot \left(\alpha_k \rho_k u_k \otimes u_k \right) + \nabla \left(\alpha_k P_k \right) = P_i \nabla \alpha_k + \dot{m}_k u_R + F_k \tag{6.2}$$

$$\frac{\partial \alpha_k \rho_k E_k}{\partial t} + \nabla \cdot \left(\alpha_k \rho_k u_k E_k \right) + \nabla \cdot \left(\alpha_k u_k P_k \right) = P_i \left(\frac{\partial \alpha_k}{\partial t} - \frac{\dot{m}_k}{\rho_R} \right) + \dot{m}_k E_R + F_k \cdot u_i + Q_k \tag{6.3}$$

$$\frac{\partial \alpha_k \rho_k \upsilon_k}{\partial t} + \nabla \cdot \left(\alpha_k \rho_k u_k \upsilon_{k,j} \right) = \omega_{k,j} \tag{6.4}$$

$$\frac{\partial \alpha_k}{\partial t} + u_i \cdot \nabla \alpha_k + \phi_k \nabla \cdot u_i = \mu \left(P_k - P_k' \right) + \frac{\dot{m}_k}{\rho_R} \tag{6.5}$$

Equations 6.1-6.3 govern the evolutions of mass, momentum, and energy. Terms on the left-hand side of these equations are conservative

within each phase. Terms on the right-hand side are non-conservative and represent inter-phase exchange including mass production ($\dot{m}$), drag force (F), and heat transfer (Q). Equation 6.4 represents convection of a scalar quantity (υ), such as species mass fraction. Equation 6.5 governs the evolution of phase volume. It is an extension of the dynamic compaction equation presented by Baer and Nunziato (1986) and is discussed in detail by McGrath (2008). In the above equations, the subscripts i and R represent interfacial and reacting quantities, respectively. Global conservation of mass, momentum, and energy dictate the following constraints to equations 6.1-6.5:

$$\sum_k \dot{m}_k = 0 \tag{6.6}$$

$$\sum_k P_i \nabla \alpha_k + \dot{m}_k u_R + F_k = 0 \tag{6.7}$$

$$\sum_k P_i \left(\frac{\partial \alpha_k}{\partial t} - \frac{\dot{m}_k}{\rho_R} \right) + \dot{m}_k E_R + F_k \cdot u_i + Q_k = 0 \tag{6.8}$$

The governing equations (6.1-6.5) form a set of coupled, non-linear, partial differential equations that must be solved numerically. An explicit finite-volume method is employed in which all phases are solved on an Eulerian grid. The solver is specifically focused on modeling flows containing both continuous and dispersed (particulate) phases. Particles are expected to be much smaller than the length-scale of the computational mesh, making the Eulerian approach to modeling the dispersed phase both efficient and attractive.

The model employs time-splitting to divide the governing equations into convective and source terms that are solved independently within a single time-step. The convective portion of the governing equations consists of those terms on the left-hand side of equations 6.1-6.5, plus the first term on the right-hand side of equations 6.2 and 6.3. These are solved with a Godunov-type method using a multiphase Riemann solver. The strategy is closely related to that applied by previous studies (Collela 1985, Wardlaw et al. 2003) as discussed fully elsewhere (McGrath 2008). The remaining terms in the governing equations are considered to be source terms. These represent the inter-phase exchange of volume, mass, momentum, and energy due to pressure relaxation, chemical reaction, drag, and heat transfer. Closure requires the assignment of relations for the mass production rate, drag force, heat transfer rate, and compaction viscosity μ. Relations used to model these terms are described below. The mathematical expressions do not contain derivatives and are easily solved with standard methods for ordinary differential equations in the context of the time-split solution.

Expressions for mass production rate are necessary in simulations containing reactive particles. All such simulations presented in this work are performed in the context of a single-step reaction mechanism governed by a global rate law. Two options for modeling the mass conversion are used. The first assumes an infinite rate of reaction resulting in a 'mixed is burned' model. This model is valid in mixing-limited scenarios and provides an upper bound for the reaction rate. The second option applies a finite rate law fit to an empirical correlation of particle burn time. The mass conversion rate is derived by combining burn time correlations with the assumption of a uniformly regressing spherical particle. A previous correlation (Beckstead 2005) provides the following expression for the change in mass of a burning particle:

$$\dot{m}_p = -\frac{\pi}{2ab}\rho_p D_p^{3-b} P^c T^d X_{O2} \tag{6.9}$$

Correlations for drag and heat transfer are taken directly from the literature. Both assume spherical particles. The drag force applied is presented below. Here, the base drag force is calculated from a standard drag law, with the drag coefficient dependent on the relative Reynolds number (Crowe et al. 1998). The base force is then modified to account for the volume fraction of the phases (Wen and Yu 1966). This results in an increased drag in regions of dense particle flow.

$$F = \alpha_C^{-3.7} F_0 = \alpha_C^{-3.7}\left(3\pi D_p \mu_C C_d \left(u_C - u_D\right) N\right) \tag{6.10}$$

$$\text{where} \quad \begin{array}{ll} C_d = 1 + 0.15\,\mathrm{Re}^{0.687}; & if\ \mathrm{Re} < 1000 \\ C_d = 0.01833\,\mathrm{Re}; & if\ \mathrm{Re} \geq 1000 \end{array} \tag{6.11}$$

Heat transfer is calculated as a function of the temperature difference among the phases and the local Nusselt number using common correlations for spherical particles in laminar and turbulent flow (Crowe et al. 1998, Ranz and Marshall 1952a and 1952b).

$$Q = \pi D \lambda_C Nu \left(T_C - T_D\right) N \tag{6.12}$$

To model the pressure relaxation process, an expression for the compaction viscosity μ is required. For all simulations shown here, μ is

taken as infinite. Phases within a computational cell fully relax to pressure equilibrium at the end of each time-step. This assumption is reasonable when particles are both smaller than the Eulerian cell size ($D_p << \min(\Delta x, \Delta y, \Delta z)$) and stiffer than the surrounding media, as will be the case in simulations presented here.

The modeling strategy described is implemented into a computational solver focused on simulating the dynamics of multiphase explosions containing a dispersed particle phase. The solver allows for simulations in 1-D to 3-D with options for spherical, cylindrical, or Cartesian coordinates. For gas-phase materials, multiple equation of state (EOS) formats are available, including the Mie-Gruneisen for condensed phase materials, and Jones—Wilkins—Lee (JWL) (Hertel and Kerley 1998, Lee et al. 1973) for gas phase materials. Detonation modeling is accomplished with a history variable reactive burn (HVRB) technique (Hertel and Kerley 1998). The model implementation has been observed to be robust and accurate, comparing well with multiple experimental datasets.

6.3 Simulation Results

This section describes the application of the computational model to three multiphase explosion problems and presents the results. The first two scenarios involve the detonation of explosive charges containing inert particles. These scenarios showcase the explosion dynamics and particle dispersion process without the complication of reacting particles, and allow for validation of the computational model with existing experimental data. The final scenario presented is taken from a recent investigation of aerobic aluminum particle combustion in the post-detonation environment. The effects of both aluminum particle size and reaction rate model on computational predictions of aerobic particle combustion are discussed.

6.3.1 Nitromethane-Steel Particle Explosion

The first multiphase explosion investigated is based on past experiments (Zhang et al. 2001) that investigated the explosive dispersal of solid particles. In the experiments, a multiphase explosive charge was detonated in air, and data on the time evolution of the leading shock and particle fronts was collected along with pressure data. The explosive charge was spherical and consisted of a packed bed of 463 μm spherical steel particles saturated with sensitized nitromethane. Particles occupied 62% of the initial explosive composition by volume. The charge was mounted above the ground and centrally detonated, resulting in an approximately spherical explosion in the time-frame of interest. Further

details on the experimental setup can be found in the original publication (Zhang et al. 2001).

Numerical simulations of this experiment were performed in 1-D spherical coordinates. Condensed phase materials, including condensed explosives and steel particles, were modeled using the Mie-Gruneisen EOS (Hertel and Kerley 1998). Gas-phase materials, including detonation products and air, were modeled using the JWL EOS (Lee et al. 1973). High explosive detonation was modeled with the history variable reactive burn (HVRB) method (Hertel and Kerley 1998).

The packed nature of the initial particle configuration makes accounting for particle-particle interactions critical to accurately simulating the explosion dynamics. Initially, the particles are in direct contact with one another, leading to strong interaction. However, as the explosion products expand, the spacing between particles quickly increases and the volume fraction drops, making direct particle interactions negligible. To account for the particle interactions, a heuristic equation of state for dispersed phase pressure was applied. The technique accounts for the functional dependence of pressure on volume fraction, as discussed in detail elsewhere (McGrath 2008).

Results from the numerical simulation are presented at selected times in Figure 6.1. The continuous phase (nitromethane and air) velocity is shown, along with the dispersed phase (particle) velocity and volume fraction. The particles are initially accelerated by a combination of the dispersed phase pressure gradient and the drag force resulting from velocity non-equilibrium with the surrounding fluid. As particles expand outwards, the volume fraction quickly drops, removing the influence of the dispersed phase pressure. A consequence of this is that the particle velocity is no longer reduced by the effects of volumetric expansion. The continuous phase velocity, however, is affected by the volumetric expansion and drops as the shock front propagates radially outward. These factors allow the particle front, which initially trails the shock front in the continuous phase, to catch and surpass the leading shock at approximately 0.5 ms. Once past the shock front, the particle front continues to separate from the shock within the time-frame shown. The ability of the particles to run away from the shock is a function of the particle momentum, which in this case is relatively large because of the particle size, density, and velocity.

Figure 6.2(a) compares the numerical and experimental trajectories of the leading shock and particle fronts with respect to time. The experimental values have been digitized from the original work (Zhang et al. 2001). The numerical results summarize the phenomena illustrated in Figure 6.1. The shock front leads the particle front until approximately 0.5 ms, at which point the particle front overtakes the shock. The particle

front then continues to separate from the shock over the time-frame shown. The experimental data agrees well with the numerical results. The data shows that the particle front escapes the shock between 0.4 and 0.6 ms, which closely bounds the numerically predicted escape time of 0.5 ms. The experimental trajectories for both the shock and particle fronts also agree well with the numerical results before and after the time of escape.

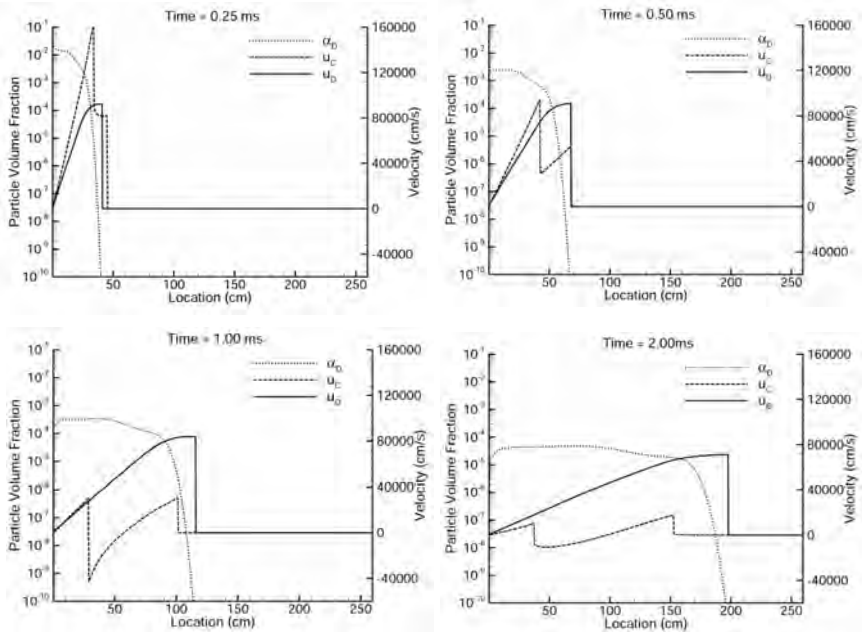

Figure 6.1: Velocity and volume fraction profiles from nitromethane/steel particle detonation at select times.

Figure 6.2(b) compares the numerical and experimental peak pressures with respect to distance from the charge. Results are shown both for the nitromethane charge containing steel particles described above, and for a pure nitromethane charge of the same diameter. Peak pressures for the pure nitromethane charge are also digitized from the original work (Zhang et al. 2001). In both cases, the numerical results closely match the experimental data. The model correctly predicts the reduction in peak pressure that occurs with the addition of particles. This reduction in pressure is a function of both the reduced mass of energetic material in the charge, and the transfer of momentum and energy from the high explosive to the particles.

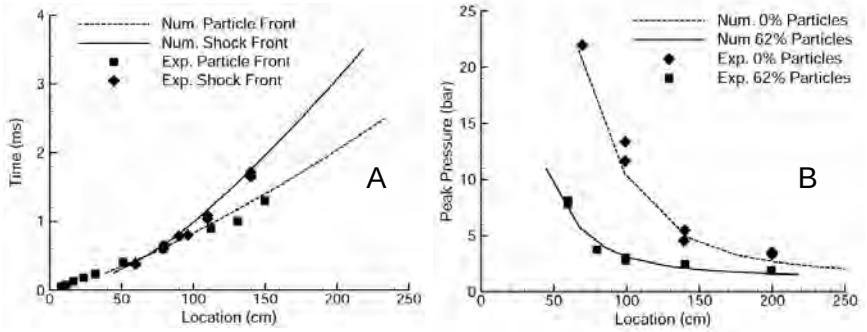

Figure 6.2: Comparison of experimental and numerical results for: (a) shock and particle front locations, and (b) peak pressure vs. distance.

6.3.2 PETN-Glass Particle Explosion

The second multiphase explosion example is based on experiments performed recently (Carney and Lightstone 2008). The initial explosive mixture consists of PETN mixed with spherical soda-lime glass particles. PETN is a relatively sensitive solid explosive that detonates fully at the charge sizes of interest. Its detonation products are clear, allowing for the use of optical diagnostic techniques. The glass particles are 3 μm in diameter and are loaded at an initial volume fraction of 0.10. The explosive charges are 1 inch right cylinders with a length to diameter ratio of one. They were suspended in air and detonated in the center of the top face of the cylinder. Fast-framing camera images taken in a shadowgraph configuration provide the particle and shock front locations at multiple times.

Numerical modeling was performed in 2-D cylindrical coordinates. As in the previous example, condensed phase materials are modeled using the Mie-Gruneisen EOS, while gas phase materials are represented with the JWL EOS. The detonation event was again modeled with the HVRB technique. Key differences between this example and the previous one include the initial particle loading and particle size. The initial particle loading in this example is 10% by volume, negating the effects of dispersed phase pressure gradient (McGrath 2008). The particles are also two orders of magnitude smaller than those in the previous example. These factors contribute to a significant difference in the explosion dynamics.

Results from the numerical simulation are compared with images from the experiment in Figures 6.3 and 6.4. Results are taken at 10 and 20 μs after detonation, respectively. Plots include contours of volume

fraction, a solid line indicating shock front location, and a dashed line indicating detonation product front location. The numerical results show that nearly the entire volume behind the shock front contains particles, but that virtually no particles exist outside the shocked region. While the particles are sufficiently accelerated to escape the detonation products, they do not efficiently escape the leading shock. This is in contrast to the results shown in the previous example, where the particles surpass and separate from the shock. The particles in the current simulation are two orders of magnitude smaller than those in the previous simulation, in addition to being less dense. Because of this, the particles have significantly less momentum than the larger particles investigated previously, even if accelerated to equivalent velocities. The reduced particle mass and momentum are responsible for the inability of the particles to escape the leading shock. When particles attempt to pass the leading shock, they immediately experience an increased drag force as they enter the ambient atmosphere. The increased drag quickly reduces the momentum of the particles, which are then recaptured by the shock.

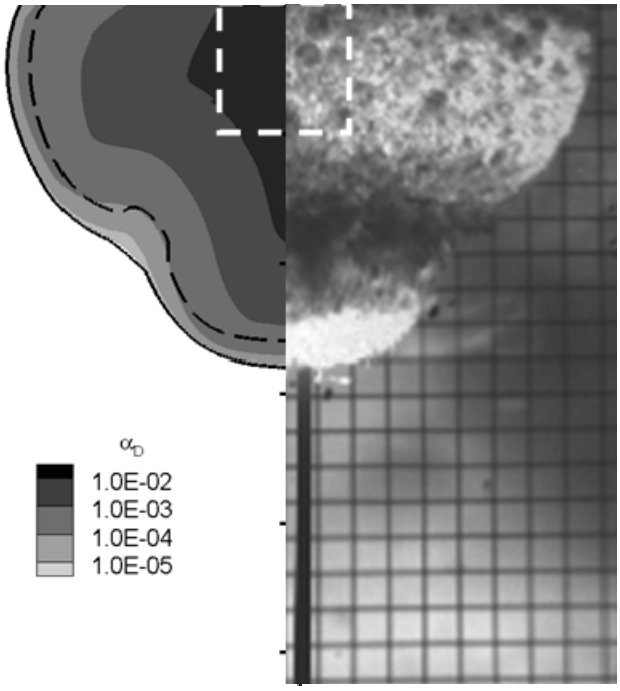

Figure 6.3: Comparison of numerical results with experimental imaging at 10 μs after detonation.

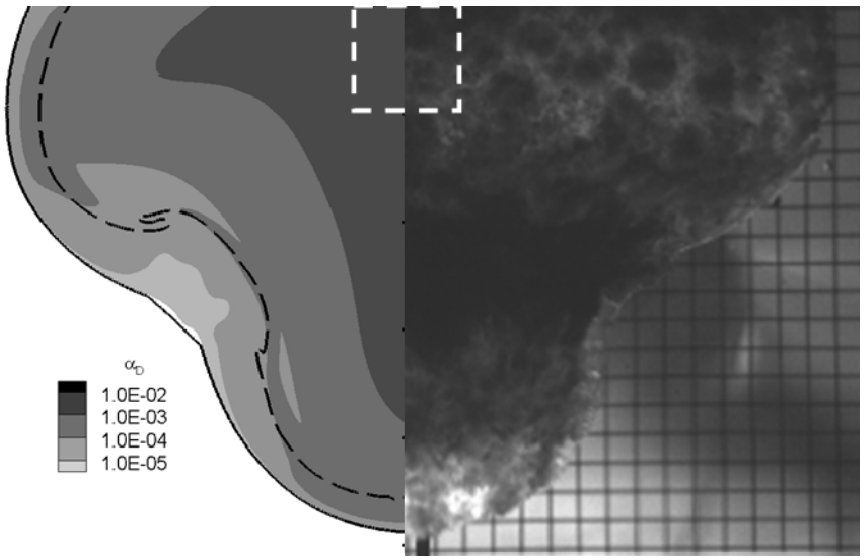

Figure 6.4: Comparison of numerical results with experimental imaging at 20 μs after detonation.

The numerical results are strongly supported by the images from the experiment. While the detonation products of pure PETN are optically clear, this clarity is removed in locations where particles are present. As predicted by the model, nearly the entire volume behind the leading shock front is observed to contain particles in the experiment. The particle front is aligned with the shock front except in isolated areas of the 20 μs image. In this image, the shock leads the particles by a small distance near the elbow of the blast where the radial and axial plumes meet. These areas are similar to those predicted to have the smallest volume fraction of particles as shown by the contours.

To better quantify the numerical and experimental results, the location of the leading particle front was tracked with respect to time along a line broadside of the charge. The results of this comparison are shown in Figure 5. Excellent agreement between the experimentally measured and numerically predicted particle front trajectories is found. The numerical results lie well within the error of the experiment. Hence the model produces not only good qualitative agreement with experiment, but also good quantitative agreement. These results further validate the numerical modeling techniques proposed in this work.

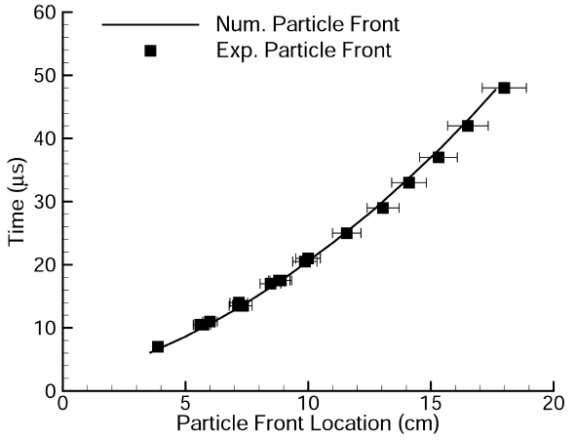

Figure 6.5: Experimental and numerical particle front trajectories broadside of PETN/glass particle explosion.

6.3.3 Modeling Post-Detonation Aerobic Aluminum Combustion

Understanding the post-detonation combustion of metal particles in fuel-rich explosive formulations is a goal of the energetic community. While particle burning models are well established in the combustion community, models calibrated to detonation environments are still in need of development. In this final example, computational predictions of aerobic (with outside air) aluminum particle combustion are presented. Results obtained with two bounding rate models are presented for three different particle sizes. These results are explained in further detail in the recent work of McGrath (McGrath et al. 2009b).

Numerical simulations mimic experiments performed by Carney and Lightstone (2009). A 2.5 cm right cylinder of HMX-based explosive loaded with 35% (by mass) aluminum particles was suspended in air and top-detonated. Particles were nominally spherical with median diameters ranging from 1-31 μm. Simulations are performed in two-dimensional cylindrical coordinates. The booster charge is assumed to undergo a constant volume explosion at time zero. Detonation of the main charge is calculated using the HVRB model. Condensed materials are modeled with the Mie-Gruneisen EOS, while gases used the JWL EOS.

Three phases are present in the computation. The first is a continuous phase consisting of high explosive, detonation products, oxygen (O_2), and nitrogen (N_2). The second and third phases are dispersed and consist of aluminum and Al_2O_3 particles, respectively. Computations were performed with aluminum particle diameters of 1, 10, and 31 μm. The diameters of all aluminum particles in a given

simulation are assumed to be identical and uniformly distributed throughout the charge at time zero. Particle diameter then evolves through space and time as a function of the local mass and number densities of the particulate phase. The particle combustion process is modeled as a single-step reaction: $2Al(s) + 1.5O_2(g) \rightarrow Al_2O_3(s)$.

Mass conversion rate is modeled either with the empirical rate law given in equation 6.9, or with an infinite rate model representing a mixing-limited scenario. Parameters used in the empirical rate law are fit to a summary of aluminum particle burn times (Beckstead 2005), which were obtained in combustion environments. The parameters are: a = 464, b =1.8, c = 0.1, d = 0.2 (cgs units).

Contour plots from simulations conducted with 1, 10, and 31 μm particles are presented in Figures 6.6 and 6.7. Results are plotted at 10 and 25 μs after detonation. Contours on the left of each sub-figure show a mass production rate of Al_2O_3, while those on the right show the volume fraction of Al_2O_3. Dotted lines show the location of the detonation product front (drawn at a mass fraction of 50%). Solid lines represent the leading shock front. A dashed outline of the initial charge geometry is also included to provide a sense of scale.

Results in Figure 6.6 were obtained using the empirical rate law based on Beckstead's correlation of particle burn times (hereafter referred to as the finite rate law). The effect of particle diameter on the computed results is considerable. At 10 μs, reaction of aluminum particles with the surrounding atmosphere is apparent in both the 1 and 10 μm results; however, the magnitude of the mass production rate and the volume of Al_2O_3 created are much greater for the smaller particle size. In the case of 31 μm particles, no reaction is present at 10 μs. At 25 μs, reaction is present for all three particle sizes, but at vastly different magnitudes. The mass production rate of Al_2O_3, as well as the volume of Al_2O_3 created, is greatest in the simulation containing the smallest particles, and least in the simulation containing the largest particles. For the 31 μm particles, reaction is only present in a very limited area at the tip of the downward expanding plume, and the volume of Al_2O_3 created is not visible at the contour levels plotted.

Results shown in Figure 6.7 were obtained in simulations applying the infinite rate law for aluminum combustion with the outside air. Because the reaction rate is infinite, the contours of mass production exist as a thin line of high intensity where reaction occurs. The location of this line denotes the front at which sufficiently hot aluminum particles meet oxygen from the outside air; here reaction occurs instantaneously. In the 1 and 10 μm simulations, reaction is observed at both 10 and 25 μs and the volume fraction contours of Al_2O_3 appear similar on the scale

plotted. Results obtained with the 31 μm particles are quite different. No reaction is visible at 10 μs, and only limited reaction occurring around the tip of the downward plume is visible at 25 μs.

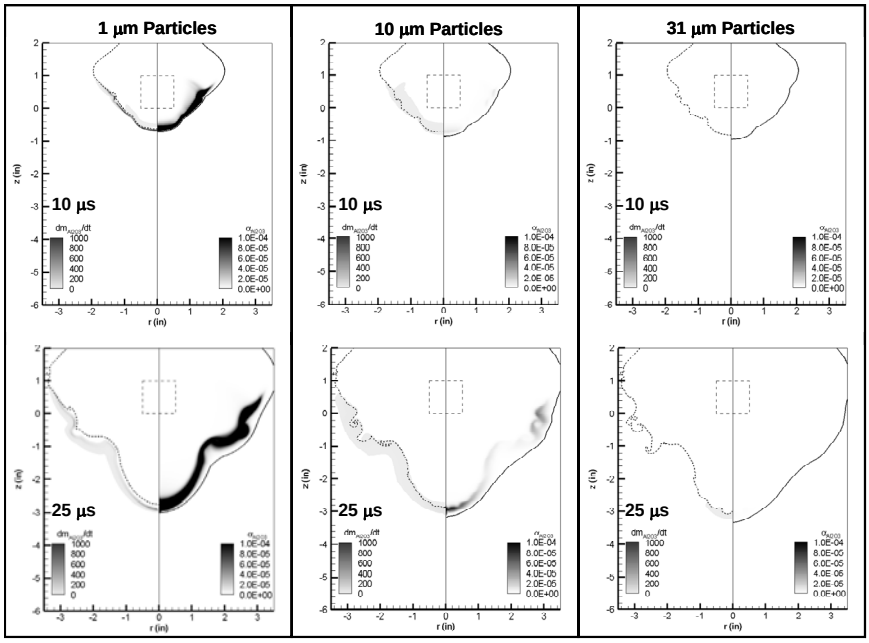

Figure 6.6: Finite reaction rate predictions of aerobic Al_2O_3 production vs. particle size.

Comparing results obtained with the finite and infinite reaction rate models yields a number of interesting observations. First, results obtained with the 1 μm particles are similar under both rate laws. The width of the reaction zone is visibly thicker when the finite rate law is applied, but the volume fraction contours indicate that similar amounts of Al_2O_3 are being produced. In the case of 10 μm particles, the effect of the rate law is more apparent. Intensity of the Al_2O_3 production rate is damped under the finite rate law, resulting in a substantial reduction in the total amount of Al_2O_3 produced. This trend also applies in the case of 31 μm particles.

These results demonstrate the sensitivity of the aerobic combustion process to initial particle size as well as the rate law applied. The results were extended in the original work (McGrath et al. 2009b) for

comparison with time-resolved emission spectroscopy measurements. The comparison indicated important characteristics of the respective rate models, including the inability of the empirical rate law to capture particle size dependencies in the post-detonation environment. This example highlights the utility of the computational model for analyzing complex multiphase explosion dynamics and extracting critical observations needed by the energetics community.

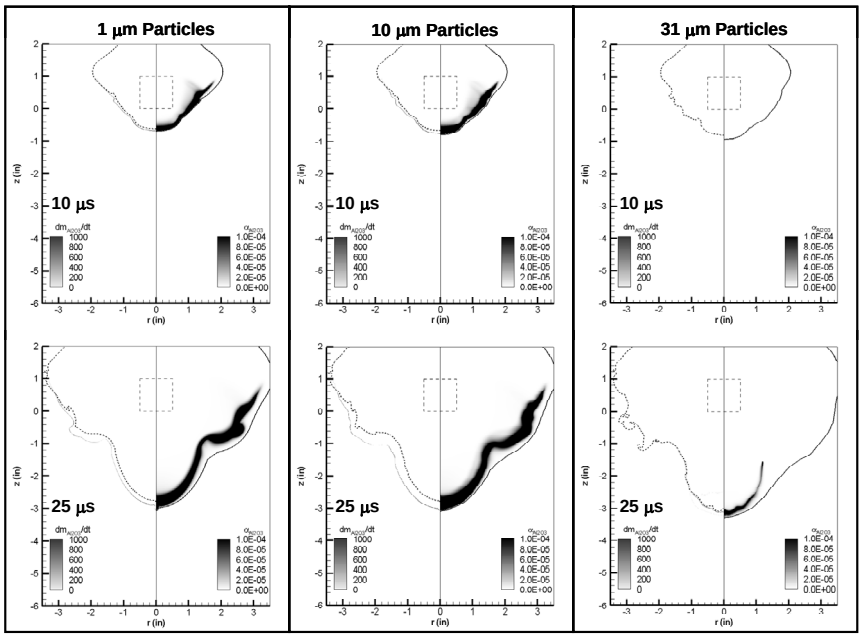

Figure 6.7: Infinite reaction rate predictions of aerobic Al_2O_3 production vs. particle size.

6.4 Conclusion

This chapter presents the development and application of a computational model for multiphase explosions. The governing equations for compressible multiphase flows were discussed, along with their numerical solution. Three application examples were presented. Simulation results obtained with inert particles were used to validate the model and understand the complex dynamics of particulate dispersion driven by explosive events. Results obtained with reacting particles were used to investigate the effect of reaction rate models on predicted results,

and are extended in the original work (McGrath et al. 2009b) to interpret the accuracy of existing rate laws in post-detonation environments. These examples highlight the accuracy of the computational model and showcase the application of the model for understanding multiphase dynamics and interpreting experimental results. Further development and refinement of such modeling and simulation techniques and capabilities will be necessary to understand increasingly complex energetic systems, enable energetic technology development, and mitigate risks from explosive materials and environments.

6.5 Acknowledgments

The authors wish to acknowledge the technical contributions of Dr. Andrew Wardlaw, Dr. Matthew Tanner, Dr. Joel Carney, and Dr. James Lightstone (all from Indian Head). Dr. Wardlaw provided invaluable technical guidance on the development of numerical techniques and their application in computational environments. Dr. Tanner provided expertise in particle combustion as well as programming assistance. Dr. Carney and Dr. Lightstone provided experimental results as well as insight into the phenomena observed. The authors also wish to thank the sponsors of this work. Funding was provided by Mr. Robert Kaczmarek and the Indian Head Core Research program, as well as Mr. William Wilson from the Defense Threat Reduction Agency.

6.6 References

1. Baer, M. R., and Nunziato, J. W., *Int. J. Multiphase Flow*, vol. 12(6), 861 (1986).
2. Beckstead, M. W., *Comb. Expl. Shock Waves*, 41(5), 533 (2005).
3. Carney, J. R. and Lightstone, J. M., "Post-Detonation Combustion of Aluminum Particles: Aluminum Particle Size Dependence," Proc. of the Sixth U.S. National Combustion Mtg., Ann Arbor, MI (May 17-20, 2009).
4. Carney, J. R. and Lightstone, J. M., (Personal Communication 2008).
5. Colella, P., *SIAM J. Sci. Stat. Comp.*, 6(1), 104 (1985).
6. Crowe, C., Sommerfeld, M., and Tsuji, Y., *Multiphase Flows with Droplets and Particles*, CRC Press, New York, NY, 1998.
7. Gonthier, K. A. and Power, J. M., *J. Comput. Phys*., 163, 376-443 (2000).
8. Hertel, E. S., and Kerley, G. I., *CTH Reference Manual: The Equation of State Package*, Technical Report SAND98-0947, Sandia National Laboratory, Albuquerque, NM (1998).
9. Lee, E., Finger, M., and Collins, W., *JWL Equation of State Coefficients for High Explosives*, Technical Report UCID-16189,

Lawrence Radiation Laboratory, Berkley, CA (1973).
10. Liu. Q. M., Bai, C. H., Li, X. D., Jiang, L., and Dai, W.X., *Fuel*, 89, 329 (2010).
11. McGrath II, T. P., "Numerical Modeling of Multiphase Explosions," Ph.D. Dissertation, University of Maryland, College Park (2008).
12. McGrath II, T. P., "Effect of Volume Fraction Evolution on the Mathematical Model for Compressible Multiphase Flows," Proc. American Physical Society SCCM Meeting (2009).
13. McGrath II, T. P., Tanner, M. W., Carney, J. R., and Lightstone, J. M., "Numerical Modeling of Post-Detonation Aerobic Aluminum Combustion," 43rd JANNAF Combustion Symposium, La Jolla, CA (December 7-11, 2009).
14. Papalexandris, M. V., *J. Fluid Mech.*, 507, 95 (2004).
15. Papalexandris, M. V., *Combust. Flame*, 141, 216 (2005).
16. Ranz, W. E. and Marshall, W. R., *Chem. Eng. Prog.*, 48, 141 (1952a).
17. Ranz, W. E. and Marshall, W. R., *Chem. Eng. Prog.*, 48, 173 (1952b).
18. Saurel, R. and Lemetayer, O., *J. Fluid Mech.*, 431, 239 (2001).
19. Toro, E. F., *Riemann Solvers and Numerical Methods for Fluid Dynamics*, 2nd Ed., Springer-Verlag, Berlin/New York, 1999.
20. Wardlaw, A. B., Luton, J, A., Renzi, J. R., Kiddy, K. C., and McKeown, R. M., "The Gemini Euler Solver for the Coupled Simulation of Underwater Explosions", NSWCIHD Technical Report 2500, Indian Head, MD (2003).
21. Wen, C. Y., and Yu, Y. H., *Chem. Engr. Prog. Symp. Series*, 62, 100 (1966).
22. Zhang, F., Frost, D. L., Thibault, P. A., and Murray, S. B., *Shock Waves*, 10, 431 (2001).

Chapter 7

Wave Transmission Through Soft-Tissue Matter

Marcelo F. Valdez and Balakumar Balachandran

In this chapter, a review of different models and approaches that have been undertaken to study blast wave interactions with soft tissue matter is provided. It is the intention of the authors to describe the highly complex phenomena under study, point out the main challenges and gaps, and outline future directions in this particular research area.

A nonlinear visco-elastic model is presented in the main body of this chapter, and this model is incorporated into a system for studying the interaction between blast waves and rigid structures supported by a visco-elastic material. This visco-elastic model is used to characterize brain tissue behavior based on experimental data. Subsequently, a reduced-order model of a brain fiber is constructed to study wave propagation along brain fibers. This chapter is organized as follows. Section 7.1 contains a discussion of the different factors associated with the phenomena under study. In Section 7.2, brain injury mechanism concepts are introduced. In Section 7.3, a partial review of the studies carried out on trauma brain injury are presented, both for direct impact and blast related insults. Section 7.4 includes a simplified nonlinear visco-elastic model to simulate soft tissue behavior. In Section 7.5, the authors present a model that accounts for fluid-structure interaction between air waves and a rigid structure supported by a visco-elastic material. In Section 7.6, the use of the nonlinear visco-elastic model to characterize brain tissue behavior is described. A reduced-order model for studying wave propagation along brain fibers is presented in the next section. Concluding remarks are collected and presented in Section 7.8.

7.1 Introduction and Problem Description

The Mild Traumatic Brain Injury (MTBI) Committee of the Head Injury Interdisciplinary Special Interest Group of the American Congress of Rehabilitation Medicine has defined MTBI as traumatically induced physiological disruption of brain function manifested by at least one of the following: *i*) any period of loss of consciousness; *ii*) any loss of memory for events immediately before or after the accident; and *iii*) any alteration in mental state at the time of the accident. Recently, blast induced traumatic brain injury (BTBI) has become an important issue, particularly in combat related environments, as there is confirmed evidence that traumatic brain injury can be developed after exposure to blast originated from an explosion.

Experimental studies with animals suggest that the incoming primary blast wave is transmitted through the skull to the central nervous system [Clemedson, 1956; Chavko et al., 2007]. In addition, it has been proposed [Bhattacharjee, 2008] that blast waves, upon striking the human body, produce a transfer of kinetic energy and induce fast oscillating pressure waves in the main blood vessels that travel up through the neck into the central nervous system, causing damage of axonal fibers and neurons.

Although brain injury mechanisms during direct (collision) and indirect (sudden acceleration/deceleration) impact have been widely studied [Schmitt et al., 2007, Voo et al., 1996], little is known about the inherent injury mechanisms associated with blast related traumatic brain injury.

Blast loading transients involves time scales of the order of 10^{-3} to 1 msec depending on the intensity of the explosion [Kambouchev, 2007]. Common head impacts are characterized by time scales of about 10 to 16 msec [Zhang et al., 2004]. The threshold for mild TBI, based on sports injury data, is roughly 50 g. On the other hand, the differential pressure acting on the human body and due to a blast wave traveling at sonic speed can produce accelerations up to 300 g. Strain levels ranging from 15 sec^{-1} to 21sec^{-1} have been associated with the occurrence of axonal injury. Due to the much shorter duration of blast loadings compared to head impacts, it is expected that higher strain rates develop under blast loadings.

Models of blast induced traumatic brain injury need to consider the following: *i*) highly complex geometry of the human head and its components; *ii*) strong shock waves traveling in air as a consequence of an explosion; *iii*) fluid-structure interaction between blast waves and deformable structures such as the human body, and between cerebro-spinal fluid (CSF) and the brain and skull; *iv*) nonlinear material

behavior of brain tissue; and *v*) link between the biomechanics of the human head under blast insults and indicators of occurrence of TBI (e.g., Svetlov et al., 2009). Although a complete study of blast induced traumatic brain injury must take all of the above mentioned aspects into account, it is important to develop a fundamental understanding by isolating the relevant physics.

The overall goal of the ongoing research pursued by the authors in the Center for Energetic Concepts Development (CECD) at the University of Maryland is to develop a fundamental understanding of wave transmission and wave interactions associated with blast induced traumatic brain injury. To this end, in this article, the authors have developed reduced-order models to aid the following: *i*) development of fundamental insights into wave propagation phenomena in the skull-brain system; *ii*) enhancement of understanding of the influence of nonlinear visco-elastic properties on the dynamic behavior of rod-like structures; and *iii*) experimental characterization of soft tissue.

7.1.1 Basic Head Anatomy

A schematic representation of the main components of the human head is provided in Figure 7.1. The cranium can be divided in four main components in order from the outside to the inside: the scalp, the skull, meninges, and the central nervous system [Schmitt et al., 2007].

The scalp is about 5 mm to 7 mm thick and it consists of the skin that provides support to hair and covers the skull. The adult skull consists of several bones fused together, with the mandibulae articulated to it. The inner surface of the cranial vault is concave with an irregular plate of bone forming the base. This base plate contains a large hole (foramen magnum) through which the brainstem passes into the spinal cord.

Below the skull, and preventing the brain from making direct contact with internal bones, there are three membranes called the *meninges*. The outermost meninge is called the *dura mater*, a tough and fibrous membrane. Resembling a spider web, the *arachnoidea mater* follows. Both membranes are separated by the subdural space. Finally, the last meninge is the *pia mater*, which is separated from the arachnoidea mater by the subarachnoidal space. The subarachnoidal space is filled with circulating cerebro-spinal fluid (CSF), which surrounds completely the brain, serving not only as a protective media but also as a support for the brain's weight. The pia mater is in direct contact with the brain.

The brain stem is at the center of the head, and it connects the cerebellum and cerebrum to the spinal cord. There are also interior membranes that separate different regions of the brain; for example, the *falx cereberi*, which is a part of the dura mater, partially separates the left

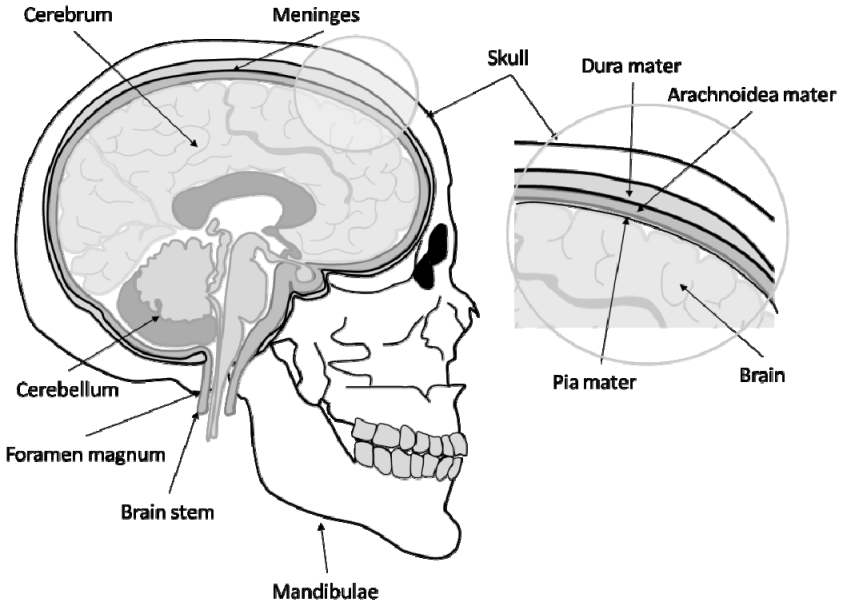

Figure 7.1: Human head and its components.

hemisphere from the right hemisphere, and the *tentorium cerebelli* separates the cerebellum from the cerebrum.

7.1.2 Blast Waves

An explosion in a fluid media constitutes the release of a large amount of energy in a very short period of time. The source of energy can be chemical, electrical, stored energy as compressed gas, and so on. As a product of the explosion, and as consequence of the compressibility of the air, a shock front develops.

A shock travels at supersonic speeds, whereas the air behind it remains in the subsonic regime. Through the shock wave, pressure, temperature and density changes are practically discontinuous [Engineering design handbook, 1974].

The shock front ideally separates the unperturbed atmosphere ahead of it from the perturbed atmosphere behind it. The air in the latter region is characterized by high pressures and constitutes what is called the *blast wave*. If a blast wave is produced in still, homogenous air, and the source that produces it is spherically symmetric, then the blast wave is called an *ideal* or a *classical blast wave*. Clearly, under the previous assumptions, the variables that describe the phenomenon are only a function of the distance to the source of the explosion.

If the pressure were to be measured at a given distance from the explosion source, then the time history of the pressure would resemble that depicted in Figure 7.2. Two phases can be recognized: a positive phase, with pressures above the ambient pressure level; and a negative phase, with pressures below the ambient pressure level. When the shock wave reaches the desired location, after a time t_a, it produces an almost discontinuous increase in pressure. After this event, the pressure decays down to a value below the ambient pressure level, from where it starts to recover to finally reach the ambient pressure level again.

The modified Friedlander equation, which provides a description of the pressure time history at a fixed location, is commonly used for modeling explosions. It reads as follows

$$p(t) = p_0 + p_s^+ \left(1 - \frac{1}{T^+}\right) e^{-bt/T^+}$$

where the parameters, p_s^+, T^+, and b are determined by fitting experimental data.

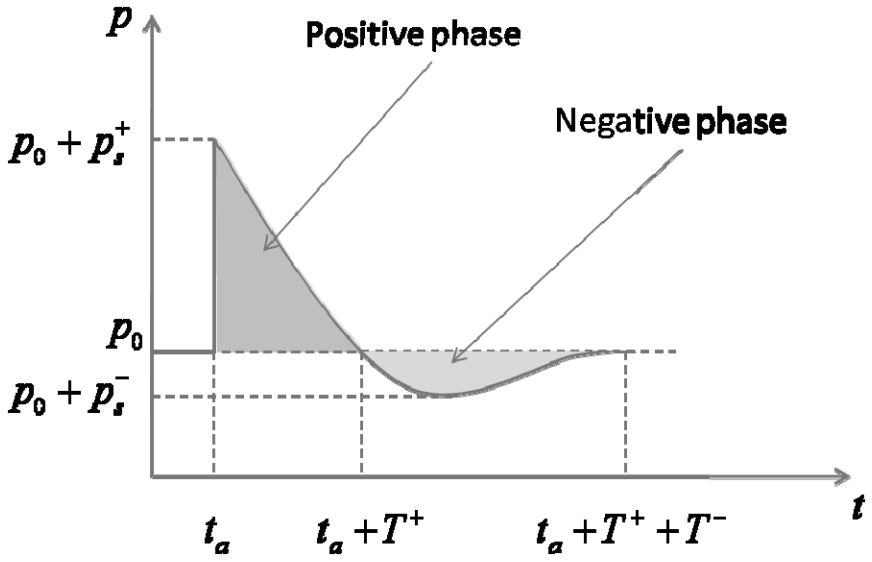

Figure 7.2: Ideal blast wave time history of the pressure.

7.1.3 Fluid-Structure Interaction Phenomena

The interaction of blast waves with the human head results in wave propagation through various different media; that is, air, skull, CSF, and finally, into the brain where stress and strain waves develop. In addition, extremely short time scales of the order of 10^{-3} to 1 msec characterize this particular fluid-structure interaction phenomenon. Therefore, significant energy deposition at high strain rates over very short time durations is expected to take place in the brain matter.

In the context of blast related traumatic brain injury, two different kinds of fluid-interaction phenomena can be considered. One of them is an external interaction between the incoming blast wave and the human head, and the other is an internal interaction between the CSF and the brain and the walls of the cranial vault. As a consequence of the first type of interaction, deformation in the skull can be produced, as well as wave reflection. The role of the second interaction is still not well understood and remains to be explored. However, it has been argued that the CSF protects the brain against external loadings and from impacts with the inner walls of the skull.

7.1.4 Brain Tissue Material Properties

Experiments with swine and rat brain tissue in tension, compression and shear deformation reveal that brain tissue behaves as a nonlinear visco-elastic material [Mendis et al., 1995, Miller and Chinezi, 2002, Brands et al., 2004, Darvish and Crandall, 2001, Shen et al., 2006, Hrapko et al., 2006]. However, strain rates at which experiments have been conducted are usually much lower than those expected under blast insults. Brain tissue characterization at high strain rates is a significant gap that remains to be filled.

It has been argued that stress relaxation due to visco-elastic effects may play a secondary role under blast loadings, as a consequence of the short time scales when compared with experimentally obtained relaxation times [Nyein et al., 2008].

Most of the developed models of brain tissue behavior do not consider brain damage. To the best of the authors' knowledge, the study of El Sayed et al. (2008) represents one of the few studies that incorporate brain damage modeling. Brain tissue nonlinear behavior and heterogeneity are properties that can potentially lead to energy localization in the brain matter, and consequently, mechanical injuries.

7.1.5 Pathophysiology of Blast Injuries

In general, the effects of blast waves over obstacles are considered fourfold: *primary effects*, arising from the direct influence of the blast overpressure on the object; *secondary effects*, constituting the damage

produced to the object by the impact of other objects accelerated by the blast; *tertiary effects*, produced when the body itself is accelerated by the blast, producing a posterior collision against walls, ground, and so on; and finally, *quaternary effects*, which include burning, blindness and inhalation of toxic gases produced due to the explosion. All of these mechanisms act simultaneously in the event of an explosion, but only primary effects can be regarded as a unique and distinctive characteristic of blast interactions. The brain injury mechanisms activated by primary effects are not completely understood in the scientific community. Secondary and tertiary effects can clearly induce damage to the human brain as they constitute direct impacts.

Several studies on blast related trauma brain injury [Bochicchio et al., 2008] have shown that brain injury dynamically evolves well after the time of the injury. Therefore, patients who do not show evidence of brain injury in a first assessment may show evidence of significant injury at a posterior time. This observation shows the difficulty in identifying blast induced traumatic brain injury during a first diagnosis.

7.2 Brain Injury Mechanisms

There exist two commonly accepted theories to explain brain concussions. According to the "shear strain theory" proposed by Holbourn in the 1940s [Holbourn and Phill, 1943], brain damage is mainly caused by high shear strains developed in the brain tissue as a consequence of rotational acceleration and relative motion between the brain and the skull.

The "cavitation theory" proposed by Gross in 1958 is based on the argument that translational brain-skull relative motion during an impact leads to the development of a pressure gradient, with negative values on the opposite side of the impact (contrecoup). The negative pressure is low enough to produce small bubbles of vapor in the CSF. Posterior restitution of the pressure produces the sudden collapse of the bubbles, originating highly localized forces on the brain surface. This mechanism, in combination with deformation and posterior restitution of the skull, generates cavitations that extend to the whole brain mass.

Experimental confirmation of the proposed mechanisms has been reported, but there is still no conclusive answer as to which mechanism is really the cause of a brain injury.

As can be appreciated, theories for brain concussion under direct or indirect impact (sudden acceleration or deceleration) involve rigid body motion of the brain. Zou et al. (2007) have studied the mechanism of brain contusion by separating the problem into rigid body and brain deformation dynamics. The authors concluded that for low speed impacts, the mechanisms of brain injury are governed by rigid body

displacements within the skull. Conversely, at high impact speeds, it was concluded that the deformation of the brain plays a primary role.

On the basis of the above mentioned studies as well as those mentioned in the next section, it is supposed that there may be fundamental differences between brain injury mechanisms associated with direct and indirect impacts and those associated with a blast wave loading. The extremely short duration of blast wave interactions suggests that the blast brain injury is primarily dominated by the propagation of strain waves through the skull and into the brain, in the absence of relative skull-brain motion. Consequently, neither cavitation theory nor shear strain theory may be appropriate for explaining brain injury mechanisms activated by blast wave interactions.

7.3 Different Efforts: Features and Findings

Though research on blast induced traumatic brain injury is relatively recent, the study of traumatic brain injury caused by direct and indirect impacts started over 60 years ago. Therefore, a substantial body of research on the latter is available. This section reviews different efforts and discusses their features and the findings.

Models ranging from simplified to anatomically detailed ones have been proposed in order to study the dynamics of the head-brain system subjected to either direct impact or indirect impacts. These models can also be categorized as analytical or computational models that also include finite element models.

Analytical models are important for isolating and understanding the physics of the phenomena. Usually these models make use of a few variables and parameters so that closed-form solutions or numerical solutions can be obtained. On the basis of experimental characterization of brain tissue properties, which shows that the dynamic bulk modulus of the human brain is approximately that of water, several of the analytical models found in the literature deal with the dynamics of spherical or ellipsoidal shells filled with a water-like fluid.

Young (2003) developed an analytical model consisting of a fluid filled spherical shell to study impacts with elastic bodies. It was concluded that impacts with heavy objects were unlikely to produce large dynamic pressure gradients inside the head, whereas lighter objects could cause high pressure transients. The difference between the two cases is given by the elapsed time of the impact, which is shorter for the latter case.

Baghaei et al. (2009) developed a mathematical model of the head-brain system to investigate the damping characteristics of the subarachnoid space and meninges and the relative motion between the skull and the brain during a blunt head impact. The model consisted of an elastic

spherical shell that surrounded a visco-elastic material layer, which was attached to the shell through a distribution of Kelvin visco-elastic elements. These elements model the CSF and interface between the brain and the skull. It was concluded that after the impact, the brain motion is rapidly damped by the visco-elastic interface. Halabieh and Wan (2008) developed a two-dimensional, geometrically simple model to study the coup-contrecoup phenomenon, with emphasis on the role played by the CSF.

If additional details are to be considered, such as geometrical details of the skull, internal membranes, nonlinear material properties, CSF fluid, and so on, then the development of analytical models becomes cumbersome and somehow unjustified. For this reason, the study of human head dynamics under impacts has moved towards computational or finite element models. This trend is likely to continue when fluid-structure interaction aspects, such as blast wave interactions, are considered. Different finite element models have been proposed for the study of the brain injury mechanisms associated with direct and indirect impacts. Simplified models consisting of fluid filled cylindrical or ellipsoidal shells have been developed by Ruan et al. (1991) and DiMasi et al. (1995). Ruan et al. studied the importance of the interior membranes at the resonance frequencies and pressure distribution in the intracranial contents after an impact. In the work of DiMasi et al., different impact conditions have been studied, including pure rotation, pure translation, and a combination of both.

Two-dimensional models, in which the focus is on a particular section of the head, have also been extensively developed. Chu and Bottlang (2002) assess the importance of CSF in reducing shear strain during an impact. Wittek and Omori (2003) investigated the effects of the brain-skull boundary conditions on the response of the system, and they discussed the importance of modeling the subarachnoid space and the CSF as a fluid.

Anatomically detailed models that include components such as the scalp, three layered skull, CSF, interior membranes, and brain matter have been developed by Hosey and Liu (1981), Ruan et al. (1994), Kumaresan and Radhakrishnan (1996), Willinger et al. (1999), Huang et al. (2000), Brands (2002), Wittek and Omori (2003), Zhang et al. (2005), Suh et al. (2005), Imielinska et al. (2006), Zong et al. (2006), Pinnoji and Mahajan (2007), and El Sayed et al. (2008), among others. For a review of the finite element models developed up to 1996, the reader is referred to the work of Voo et al. (1996). Next, a brief discussion is provided on the different aspects of these studies as well as the relevant findings.

Ruan et al. observed that higher pressure peaks are realized inside the brain for rear impacts rather than for front impacts. In the work of

Kumaresan and Radhakrishnan, the importance of the partitioning membranes and the neck in the head injury has been assessed. Responses to occipital, frontal, and parietal loading were analyzed, and only the coup-contrecoup mechanism was observed in all cases except during parietal loading. The inclusion of the neck was observed to reduce the pressure peaks. Finally, a helmet model was incorporated and was shown to reduce the pressure peaks as well. Huang et al. validated an anatomy based finite element model with experimental data. Indirect impact simulations were carried out, and high gradients of intracranial pressure and concentrations of shear stress were observed in the brain. The negative contrecoup pressure was not sufficient to produce cavitation. Zhang et al. developed a model by including the neck structure up to the seventh cervical bone. It was observed that the intervertebral discs represent a major weakness in the context of neck injuries. Suh et al. investigated the brain deformation caused by frontal head impact, and the intracranial pressure and the relative displacement between the skull and the brain.

Imilinska et al. presented a novel approach for solving coupled fluid dynamics (air, CSF) and structural dynamics (cranium, brain tissue) during ballistic and blast impacts. A model of a helmet is also included in their work. Zong et al. observed three paths for energy transmission during a head impact, two of them in the skull and one through the brain. The spinal cord was observed to have high values of power flow, raising questions about integral head-neck protection. Pinnoji and Mahajan developed a complete finite element model to compare the response of the human head under frontal impacts with and without the use of a helmet. The helmet was shown to reduce the coup pressure, but no influence on the contrecoup pressure was detected. It was observed that for low-speed impacts, low densities of the helmet padding resulted in low contact forces and coup pressures. El Sayed et al. developed a biomechanical model for traumatic brain injury and soft tissue damage. Frontal and oblique impacts with external objects were examined, and predictions of extension, intensity, and reversibility of tissue damage were made. The model was shown to be able to reproduce permanent brain tissue damage.

The material constitutive properties adopted for the different components vary from one study to another, but a general trend observed by the authors is the use of linear elastic material properties for the skull and interior membranes. On the other hand, the brain matter has been modeled in a variety of different ways. These include water-like fluid models, linear and nonlinear elastic material models, and linear and nonlinear visco-elastic material models. In order to simplify the modeling, the CSF is usually regarded as a thin layer with bulk

properties of water. Due to this, the fluid-structure interactions between the skull-brain system and the CSF are not addressed.

With regard to blast wave interactions, analytical models developed to study brain injuries have been limited. However, most of the finite element models developed for studying head impacts can be extended to simulate blast wave interactions with the human head, provided fluid models and fluid-structure interaction schemes are appropriately incorporated. In some related studies, not directly associated with brain injury, interactions between fluid filled shells and shock waves are assessed [Peralta and Raynor, 1964, Iakovlev, 2002, 2007]. Moss et al. (2009) carried out numerical simulations of explosion generated blast waves and a water-filled "human head." Skull deformation was proposed as a new mechanism for brain injury resulting from blast waves. Nyein et al. (2008) developed a numerical model to study the interactions between a detonation shock wave and the human head. They concluded that direct interaction and propagation of the shock wave is possible through the skull to the brain.

7.4 Nonlinear Visco-Elastic Model

A nonlinear visco-elastic material behaves as a hyper-elastic material at both slow and fast deformation rates, but with different properties in each case. For intermediate deformation rates, on the other hand, the material depicts rate dependent, hysteretic behavior [Belytschko et al., 2001].

In their ongoing work, the authors have been using a simple, one-dimensional nonlinear visco-elastic model to investigate blast wave interactions as well as wave propagation phenomena in a longitudinal brain fiber bundle. The visco-elastic model is based on the general Maxwell's model; that is, it consists of a nonlinear spring in parallel with a certain number of Maxwell's modes, each of which in turn is composed of a nonlinear spring in series with a dashpot, as shown in Figure 7.3. In this model, a hyper-elastic constitutive law is considered for describing a nonlinear spring. The dissipation captured through the dashpots is linear in the strain rate. The visco-elastic element has a cross-section area A and a length L. The quantities γ_1, γ_2, …, γ_N are internal variables that are related to the mechanism of energy dissipation. The quantities σ_1, σ_2, …, σ_N are stresses in the corresponding Maxwell's modes, and the quantity σ_∞ is the stress in the nonlinear spring in parallel. The total force applied to the visco-elastic element is given by

$$F = \left(\sigma_{\infty} + \sum_{n=1}^{N} \sigma_i \right) A$$

To describe the nonlinear elastic part of the model, an incompressible hyper-elastic Mooney-Rivlin constitutive law is considered. With certain variations, this constitutive law has been used in other studies to model brain tissue material [e.g. Mendis et al., 1995]. It can be shown that for a uniaxial stress state, the true stress σ, as a function of the stretch ratio λ, is given by

$$\sigma = 2\left(\lambda^2 - \frac{1}{\lambda} \right)\left(c_1 + \frac{1}{\lambda} c_2 \right)$$

where c_1 and c_2 are material constants, and the stretch ratio is defined as

$$\lambda = \frac{L}{L_0}$$

with L_0 being the original length of the element. As a consequence of the incompressibility of the material, the cross-sectional area of the element changes according to

$$A = \lambda^{-1} A_0$$

with A_0 being the original cross-sectional area.

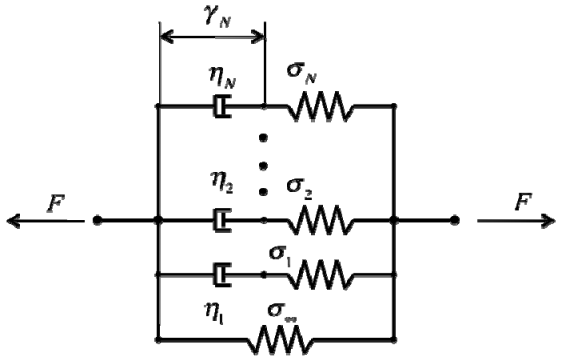

Figure 7.3: General nonlinear Maxwell's one-dimensional visco-elastic model.

7.5 Interaction of Acoustic Waves with Visco-Elastically Supported Mass

In order to gain insights into the interactions of blast waves with visco-elastic systems, here, the authors present a model for studying fluid-structure interactions between acoustic pressure waves and a point mass supported by a nonlinear visco-elastic element as shown in Figure 7.4. This approach is similar to that used by Kambouchev (2007) to study the interactions of blast waves with isotropic plates supported by a visco-elastic system. However, in the current work, the visco-elastic support is nonlinear in nature, as opposed to the linear Kelvin visco-elastic support used by Kambouchev.

Small perturbations in the fluid variables (velocity u, density ρ, and pressure p) are assumed, and the perturbed quantities are expressed as

$$u = u_0 + \tilde{u} \qquad p = p_0 + \tilde{p} \qquad \rho = \rho_0 + \tilde{\rho}$$

where u_0, p_0 and ρ_0 are the unperturbed velocity, pressure and density; and $\tilde{u}$, $\tilde{p}$ and $\tilde{\rho}$ are small perturbations. It can be shown that $\tilde{p}$ and $\tilde{\rho}$ are governed by the linear wave equation as follows

$$\frac{\partial^2 \tilde{p}}{\partial t^2} - a^2 \frac{\partial \tilde{p}}{\partial x^2} = 0$$
$$\frac{\partial^2 \tilde{\rho}}{\partial t^2} - a^2 \frac{\partial \tilde{\rho}}{\partial x^2} = 0$$

where a is the speed of sound in air given by

$$a^2 = \frac{\partial p}{\partial \rho}$$

The solution for the pressure is given by d'Alembert's formula; that is,

$$\tilde{p}(x,t) = f(x - at) + g(x + at)$$

where $f(x - at)$ and $g(x + at)$ are two arbitrary functions. In the present context, the first function describes a wave moving to the right (incoming wave) and the second function describes a wave moving to the left (reflected wave). The expressions for the density and velocity can be derived from the pressure solution.

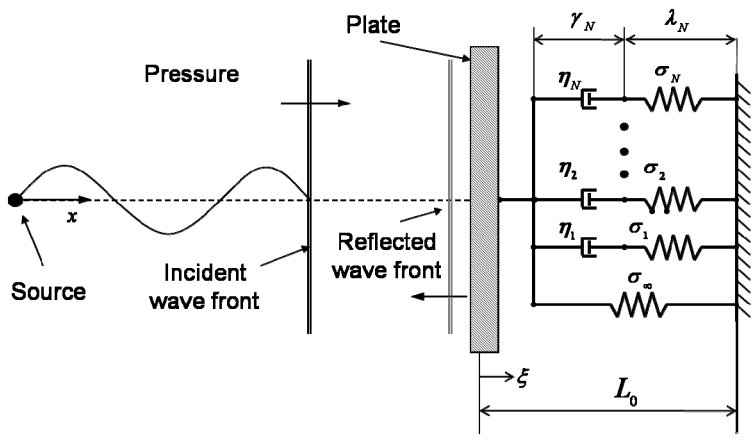

Figure 7.4: Model for interaction between acoustic wave and nonlinear visco-elastic support.

In this approach, the authors consider an exponential incident pressure wave of the form

$$f(x-at)=\begin{cases} p_s e^{\frac{x-at}{at_i}} & x-at\le 0 \\ 0 & x-at>0 \end{cases}$$

where t_i is a characteristic time and p_s is the peak overpressure.

Let the position of the mass be given by ξ. After applying the conservation of linear momentum to a fluid particle located on the surface of the mass, an expression for the evolution of the reflected wave is obtained. This expression reads as

$$\frac{\partial g}{\partial t}=-\left[\dot{\xi}+a\right]\left[\rho\ddot{\xi}+f'(x-at)\right]$$

where the overdot indicates a time derivative and the prime denotes a spatial derivative.

Next, the equations of motion of the visco-elastic system are derived. The total stretch of the visco-elastic element λ_∞ is given by

$$\lambda_\infty(\xi) = \frac{L_0 - \xi}{L_0}$$

The stretch λ_i of the nonlinear springs in the Maxwell's mode *i* is related to λ_∞ by

$$\left[\lambda_i \frac{L_0}{2} + \gamma_i \frac{L_0}{2}\right] = \lambda_\infty L_0 \Rightarrow \lambda_i + \gamma_i = 2\lambda_\infty$$

with γ_i being the stretch of the linear dashpot. Since the damping of the system is linear, γ_i is related to the stress in the Maxwell's mode *i* as follows:

$$\frac{L_0}{2}\dot{\gamma}_i \eta_i = \sigma_i$$

After manipulating the equations, it can be shown that the coupled, fluid-structure interaction equations governing the system can be put in the form

$$\ddot{\xi} = \frac{1}{m}\left[\sigma_\infty(\lambda_\infty) + \sum_{i=1}^{N}\sigma_i(\lambda_i) + f + g\right]\lambda_\infty A_0$$

$$\dot{\lambda}_i = -\frac{1}{L_0}\left[\frac{2}{\eta_i}\sigma_i(\lambda_i) + \dot{\xi}\right]$$

$$\vdots \quad = \quad \vdots$$

$$\dot{\lambda}_N = -\frac{1}{L_0}\left[\frac{2}{\eta_N}\sigma_N(\lambda_N) + \dot{\xi}\right]$$

$$\frac{\partial g}{\partial t} = -\left(\dot{\xi} + a\right)\left[\frac{\rho}{m}\left[\sigma_\infty + \sum_{i=1}^{N}\sigma_i + f + g\right]\lambda_\infty A_0 + f'(x - at)\right]$$

where *N* is the number of Maxwell's modes considered. Also the stress-stretch relationship for element *i* and element ∞ is given by

$$\sigma_\infty = 2\left(\lambda_\infty^2 - \frac{1}{\lambda_\infty}\right)\left(c_{1\infty} + \frac{1}{\lambda_\infty}c_{2\infty}\right)$$

$$\sigma_i = 2\left(\lambda_i^2 - \frac{1}{\lambda_i}\right)\left(c_{1i} + \frac{1}{\lambda_i}c_{2i}\right)$$

Similarly to Kambouchev (2007), the following non-dimensional parameter, which indicates the ratio of fluid mass and the plate mass is introduced:

$$\beta_0 = \frac{t_i \rho_0 a}{m}$$

In addition,

$$\frac{d}{d\lambda_\infty}\sigma_\infty\bigg|_{\lambda_\infty=1} = E_\infty = 6\left(c_{1\infty} + c_{2\infty}\right)$$

and,

$$\frac{d}{d\lambda_i}\sigma_i\bigg|_{\lambda_i=1} = E_i = 6\left(c_{1i} + c_{2i}\right)$$

Furthermore, the following non-dimensional variables are defined:

$$\zeta = \frac{\xi a \rho_0}{p_s t_i} \qquad \tau = \frac{t}{t_i} \qquad \varphi = \frac{g}{p_s} \qquad \nu = \frac{f}{p_s}$$

$$p_0 = \frac{p_s}{\rho_0 a^2} \qquad \beta_0 = \frac{t_i \rho_0 A_0 a}{m} \qquad \overline{\sigma}_\infty = \frac{\sigma_\infty}{p_s} \qquad \overline{\sigma}_1 = \frac{\sigma_1}{p_s}$$

$$\kappa_0 = \frac{E_\infty t_i}{L_0 \rho_0 a} \qquad \kappa_i = \frac{E_i t_i}{L_0 \rho_0 a} \qquad \alpha_{0i} = \frac{\eta_i}{\rho_0 a} \qquad \overline{L}_0 = \frac{L_0 a \rho_0}{p_s t_i}$$

It can be shown that the non-dimensional equations of motion are given by

$$\ddot{\zeta} = \beta_0\left[\overline{\sigma}_\infty\left(\lambda_\infty\right) + \sum_{i=1}^{N}\overline{\sigma}_i\left(\lambda_i\right) + \phi + \nu\right]\lambda_\infty$$

$$\dot{\lambda}_i = -\frac{1}{\bar{L}_0}\left[\frac{2}{\alpha_{0i}}\bar{\sigma}_i\left(\lambda_i\right)+\dot{\zeta}\right]$$
$$\vdots \quad = \qquad\qquad \vdots$$
$$\dot{\lambda}_N = -\frac{1}{\bar{L}_0}\left[\frac{2}{\alpha_{0N}}\bar{\sigma}_N\left(\lambda_N\right)+\dot{\zeta}\right]$$
$$\frac{\partial \nu}{\partial \tau} = -\left(p_0\dot{\zeta}+1\right)\left[\beta_0\left[\sigma_\infty + \sum_{i=1}^{N}\sigma_i + f + g\right]\lambda_\infty + \frac{\phi'}{p_0}\right]$$

7.5.1 Results

The model described above can be employed to assess the protective effectiveness of a visco-elastic system when it is subjected to a blast wave. Therefore, the focus is on the impulse transmitted to the mass by the incoming pressure wave. The total available impulse carried by the incoming wave is given by

$$I_i = p_s t_i$$

The ratio of the maximum impulse transmitted to the mass to the available impulse is given by

$$\frac{I_p}{I_i} = \frac{\max\left(m\dot{\xi}\right)}{p_s t_i}$$

For simplicity, only one Maxwell's mode (N=1) is employed in the nonlinear visco-elastic model. Initially, the mass is at rest and the nonlinear springs are unstretched; that is,

$$\zeta(0)=0 \qquad \lambda_\infty(0)=1$$
$$\dot{\zeta}(0)=0 \qquad \lambda_1(0)=1$$

The authors assume that when the incoming wave reaches the mass at $t=0$, the reflected and the incoming waves have the same value, as it would happen in the case of a wave reflecting from a rigid wall [e.g., Kambouchev, 2007]. This means

$$\nu(0)=1$$

For different values of α_0, the maximum impulse transmitted to the mass for $\kappa_1 = \kappa_0 = 1$ is shown in Figure 7.5. The maximum impulse

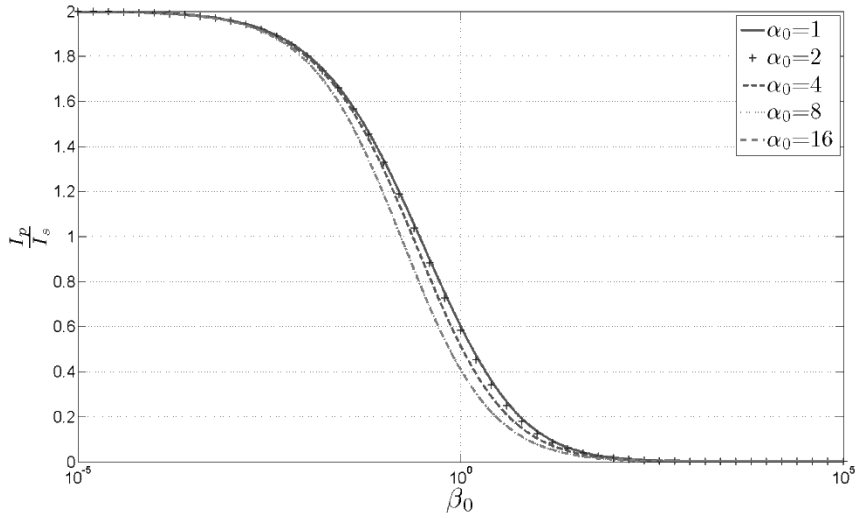

Figure 7.5: Impulse transmitted as a function of the mass ratio factor for $\kappa_1 = \kappa_0 = 1$.

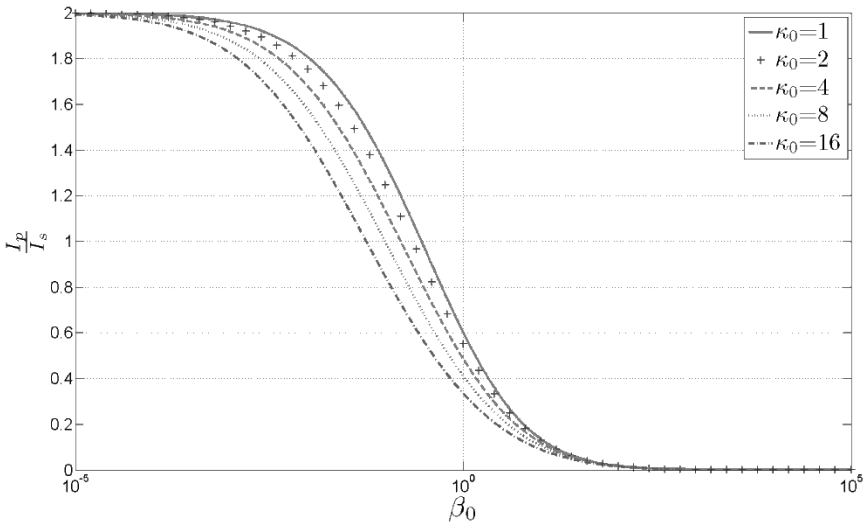

Figure 7.6: Impulse transmitted as a function of the mass ratio factor for $\alpha_0 = 1$ and $\kappa_1 = 1$.

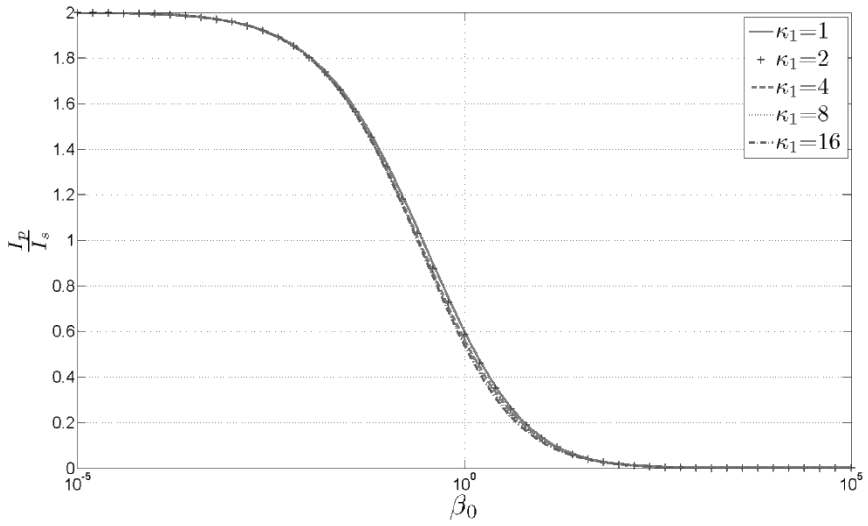

Figure 7.7: Impulse transmitted as a function of the mass ratio factor for $\alpha_0 = 1$ and $\kappa_0 = 1$.

transmitted to the mass for $\kappa_1 = \alpha_0 = 1$ and different values of the parameter κ_0 is shown in Figure 7.6. The same information is shown in Figure 7.7 for $\kappa_0 = \alpha_0 = 1$ and different values of κ_1. The results show that as the mass decreases, the impulse transmitted to it by the incoming pressure wave decreases. Furthermore, as the damping in the system increases, the transmitted impulse also decreases. In addition, it is noted that the influence of the parameter κ_0 over the impulse transmitted to the mass is more substantial than the influence of the remaining parameters. These results suggest that light hard shells are more effective in protecting against blasts than heavy shells.

7.6 Brain Tissue Experimental Characterization

In this section, the visco-elastic model discussed previously is used to characterize brain tissue behavior. In order to obtain the model parameters, the visco-elastic model presented in Section 7.4 is fitted to available experimental data. In this case, data from compression experiments on swine brain tissue [Miller, 2002] are used. It is noted that the strain rates considered in these experiments are low, and intended to be representative of surgical procedures, and even the highest strain rate

considered in this work is low compared to those expected to occur due to a blast loading. The experimental set up for a compression test on brain tissue matter is schematically shown in Figure 7.8.

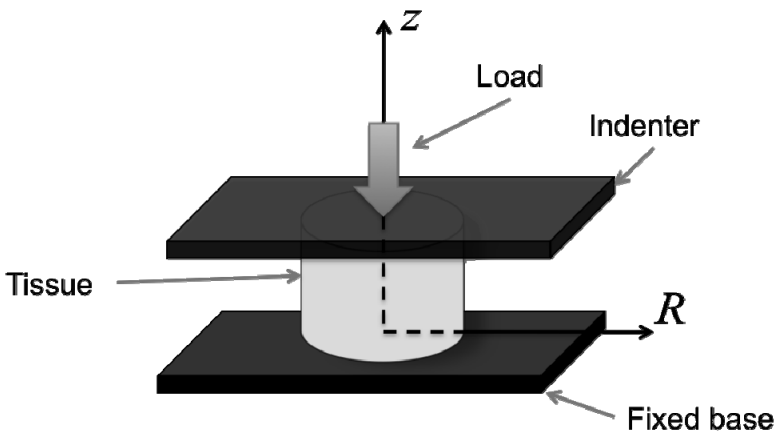

Figure 7.8: Experimental setup for a compression test on swine brain tissue.

Table 7.1: Estimated parameters

Strain Rate	0.64 sec^{-1}	0.64 □ 10^{-2} sec^{-1}
$C_{1\infty}$	324 Pa	156 Pa
$C_{2\infty}$	445 Pa	212 Pa
C_{11}	647 Pa	666 Pa
C_{21}	695 Pa	185 Pa
η_1	234 Pa.sec/m	161 Pa.sec/m

In order to perform the model identification, the authors have used the nonlinear ODE parameter estimation tool (Grey-box) from the Matlab System Identification Toolbox. For simplicity, only one Maxwell mode is used in the visco-elastic model. The experimental data used corresponds to strain rates of 0.64 sec^{-1} and 0.0064 sec^{-1}. Since the parameters in the visco-elastic model do not explicitly depend on the

strain rate, a different set of parameters is obtained for each value of the strain rate.

The obtained constants for the different two strain rates are shown in Table 7.1. Comparisons between the experimental data and the estimated model with curve-fitted parameters at the two considered strain rates are shown in Figure 7.9.

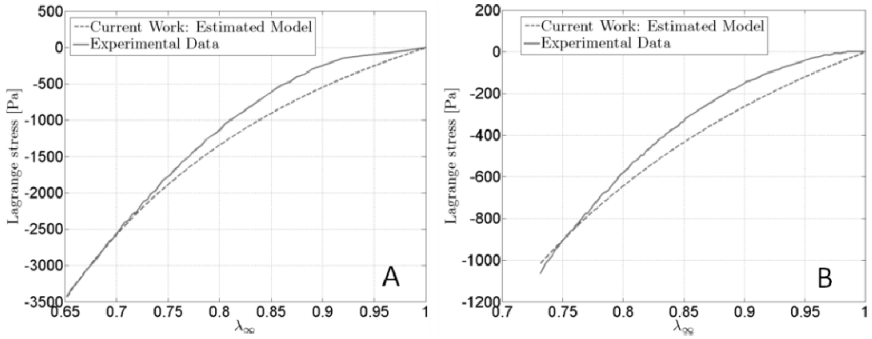

Figure 7.9: Comparison between experimental data and fitted viscoelastic model. A: Strain rate of 0.64 sec^{-1}. B: Strain rate of 0.0064 sec^{-1}.

7.7 Wave Propagation in a Brain Fiber

As stated previously, the dynamic behavior of the human brain under blast loadings is most likely to be dominated by tissue deformation and stress and strain wave propagation rather than rigid body translation and rotation. The brain matter is internally composed of a system of fibers as depicted in Figure 7.10. These fibers provide possible pathways for stress and strain wave propagation.

It is hypothesized by the authors that due to the nonlinear behavior of the brain tissue, stress localization along the longitudinal brain fibers may be present and constitute a potential injury mechanism under blast loadings. In order to study wave propagation in the brain, the modeling approach is as follows. A collection of aligned brain fibers is approximately considered as a longitudinal nonlinear rod. Next, a reduced-order model of the rod is obtained through a discretized system representation. In this model, the masses are linked together by nonlinear visco-elastic elements, whose governing equations were previously derived in Section 7.4. The fibers are considered fixed at one end and free at the other. The model under consideration is schematically shown in Figure 7.11.

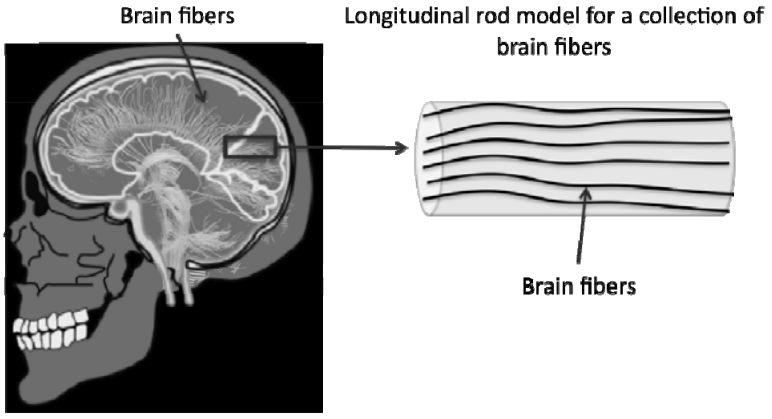

Figure 7.10: Modeling approach to study wave propagation in brain fibers.

As a first approximation, it is assumed that the shape of the pressure pulse that reaches the brain fibers is similar to that of the incoming blast wave that impacts the skull. This represents a very rough approximation since a part of the energy carried by the blast wave that reaches the human head is expected to be redistributed through wave reflections and skull deformations before reaching the fibers. With this, a blast-like force is applied to the left most mass of the system as shown in Figure 7.11. This force is given by

$$F(t) = F_0 e^{-t/T}$$

where T is a characteristic time, which is related to the duration of the "impact" or "blast loading." In this model, no fluid-structure interaction is considered, since the authors are only interested in wave propagation in a brain fiber bundle.

7.7.1 Results

The reduced order model described in the previous section is employed to study the wave propagation through a brain fiber group. Three elements are considered as shown in Figure 7.11. For identification purposes, the elements are numbered from left to right. The brain fiber is considered to be homogeneous; therefore all the visco-elastic elements have the same properties. The parameters of each of the nonlinear visco-elastic elements are the ones obtained in § 7.4.2 for the

highest value of strain rate value. In the following cases, the loading amplitude is given by,

$$F_0 = 1000$$

Two values of the loading characteristic time considered in the present study are $T_1 = \pi/25$ and $T_2 = \pi/100$. The stress generated in each of the visco-elastic elements is shown in Figure 7.12 as a function of the non-dimensional time. The time normalization is obtained by dividing the time through the characteristic time T as $\tau = t/T$.

The time variation of the strain rate in each of the visco-elastic segments is shown in Figure 7.13. From the figures, a propagation of a longitudinal stress wave can be observed through the elements of the system. Also, it is remarked that the stress in the fiber reaches a minimum value (negative, compressive stress) in the third visco-elastic element; that is, in the rightmost element. This is due to the amplification of the stress as a consequence of the constructive interference between the wave travelling to the right and the wave travelling to the left, which resulted from the reflection from the right boundary. The previous observation is independent of the characteristic time of the loading and may indicate that stress localization in a homogeneous brain fiber is achieved near the constrained end of it. Furthermore, since a significant portion of brain fibers end at the center of the brain (Figure 7.10), the previous results suggest that damage, if present, may occur near the center of the brain even when no visible damage is observed at the outer surface of it. Finally, it is observed that there is a decrease in the magnitude of the stress peak as the characteristic time of the loading decreases. By contrast, the strain rate presents a negative (compressive) peak at the first and third elements. As the characteristic time decreases, the magnitude of the strain rate peak in the first element becomes larger than that in the last element. However, the stress peak is reached at the third element.

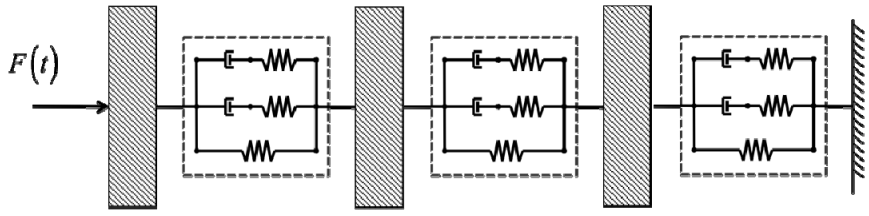

Figure 7.11: Discrete lumped-mass model of a brain fiber.

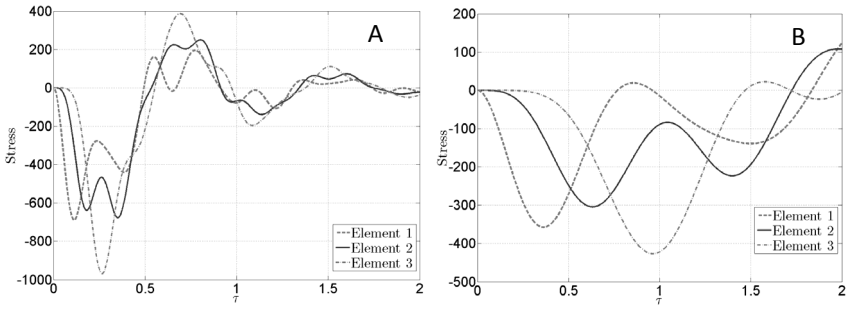

Figure 7.12: Stress time history in each viscoelastic element. A: $T = \pi/25$**. B:** $T = \pi/100$**.**

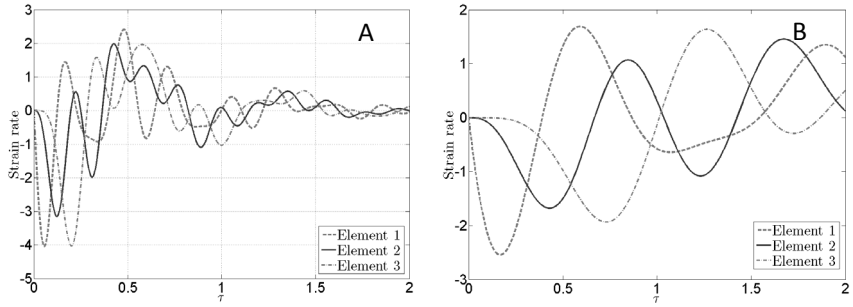

Figure 7.13: Strain rate time history in each viscoelastic element. A: $T = \pi/25$**. B:** $T = \pi/100$**.**

7.8 Concluding Remarks

In this chapter, a brief description of the different aspects that encompass the study of blast wave interactions with brain tissue has been provided. Although the study of brain concussion mechanisms has reached a certain level of maturity, the study of brain injury mechanisms activated by blast loadings is still in its early stages. Hence, reduced-order models, such as those discussed in this chapter, may be helpful to understand some of the associated physics. Although complete computational models, such as finite element models, may be necessary to get detailed as well as quantitative information, reduced-order models can play a role in identifying the directions to be pursued.

It is a hypothesis of the authors that blast waves reaching the human head and travelling directly through the skull to reach the brain matter

may activate energy localization mechanisms along certain preferred pathways. Brain fiber systems, such as those illustrated above, may serve as these pathways. As discussed in this chapter, nonlinear material properties can play an important role in determining how energy is channeled through these pathways. In addition, the work presented in this chapter should help us understand the formation of high stress zones within the fiber bundles. Effective protective equipment may also be tailored to provide alternative energy pathways, with the goal of attenuating energy transfer to the brain matter.

A preliminary two-dimensional finite element model that is being studied is shown in Figure 7.14. In this reduced-order model, air is considered as an acoustic media, and a skull-brain system model is represented as a section filled with water. Fluid-structure interactions between the air and the skull are taken into account. An impulsive perturbation is introduced at a certain spatial location in the air domain to simulate a transient loading. This loading generates pressure waves that reach the skull system, cause skull deformation, and lead to the development of stress waves in the brain as shown schematically in Figure 7.14. Although such two-dimensional models are helpful in understanding wave phenomena, the development of complete three-dimensional models with appropriate level of attention to brain structure details is important for getting a better understanding of wave propagation and energy localization in the brain.

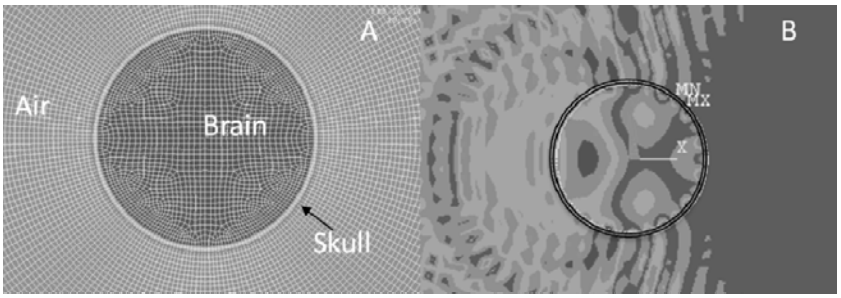

Figure 7.14: Two-dimensional finite element model for blast wave interaction study. A: Detail of the finite element mesh. B: Pressure contours developed after waves reach the skull-brain system.

7.9 Acknowledgements

The authors acknowledge interactions with Drs. Davinder K. Anand, Henry Haslach, and James Short of CECD.

7.10 References

1. American Congress of Rehabilitation Medicine: Definition of mild traumatic brain injury. *Journal of Head Trauma Rehabilitation* 8, 86-89, 1993.
2. S. M. Baghaei, A. M. Sadegh, and S. M. Rajaai. A Mathematical head/brain model for investigation of damping characteristics of SAS in low velocity head impact. *25th Southern Biomedical Engineering Conference IFMBE Proceedings* 24, 283-286, 2009.
3. T. Belytschko, W. K. Liu, and B. Moran. *Nonlinear finite element for continua and structures*, John Wiley and Sons, 2000.
4. Y. Bhattacharjee. Shell shock revisited: Solving the puzzle of blast trauma. *Science* 319, 406-408, 2008.
5. G. V. Bochicchio, K. Lumpkins, J. O'Connor, M. Simard, S. Schaub, A. Conway, K. Bochicchio, and T.M. Scalea. Blast injury in a civilian trauma setting is associated with a delay in diagnosed of traumatic brain injury. *The American surgeon* 74(3), 267-270, 2008.
6. D. Brands. Predicting brain mechanics during closed head impact: numerical and constitutive aspects. Ph.D. thesis, Eindhoven University of Technology, 2002.
7. D. W. A. Brands, G. W. M. Peters, and P. H. M. Bovendeerd. Design and numerical implementation of a 3-D non-linear viscoelastic constitutive model for brain tissue during impact. *Journal of Biomechanics* 37(1), 127-134, 2004.
8. M. Chavko, W. A. Koller, W. K. Prusaczyk, and R. M. McCarron. Measurement of blast wave by miniature fiber optic pressure transducer in the rat brain. *Journal of Neuroscience Methods* 159(2), 277-281, 2007.
9. Y. H. Chu and M. Bottlang. Finite element analysis of traumatic brain injury. 10th Annual Symposium on Computer Methods in Orthopaedic Biomechanics, Dallas, TX, 2002.
10. C. J. Clemedson. Shock wave transmission to the central nervous system. *Acta Physiologica Scandinava* 37, Issue 2-3, 204 – 214, 1956.
11. K. K. Darvish and J. R. Crandall. Nonlinear viscoelastic effects in oscillatory shear deformation of brain tissue. *Medical Engineering & Physics* 23(9), 633-645, 2001.
12. F. P. DiMasi, R. H. Eppinger, and F. A. Bandak. Computational analysis of head impact responses under car crash loadings. *Proc. 39th Stapp Car Crash Conf., Society of Automotive Engineers*, San Francisco, California, 425-438, 1995.
13. T. El Sayed, A. Mota, F. Fraternali, and M. Ortiz. Biomechanics of traumatic brain injury. *Comput. Methods Appl. Mech. Engrg*. 197**,**

4692–4701, 2008.
14. Engineering design handbook. *Explosion in Air, Part one*. AMC pamphlet 706-181. US Army Material Command, Alexandria VA, 1974.
15. A. G. Gross. A new theory on the dynamics of brain concussion and brain injury. *Journal of Neurosurgery* 15(5), 548-561, 1958.
16. O. Halabieh and J. W. L. Wan. Simulating mechanism of brain injury during closed head impact. *Biomedical Simulation*, 107-118, 2008.
17. A. H. S. Holbourn. The mechanics of brain injury, *British Medical Bulletin* 3(6) 147-149, 1945.
18. R. R. Hosey and Y. K. Liu. A homeomorphic finite element model of the human head and neck. *Finite elements in biomechanics*: Wiley & Sons pp. 379-401, 1982.
19. M. Hrapko, A. W. van Dommelen, G. W. M. Peters, and J. S. H.M. Wismans. The mechanical behaviour of brain tissue: large strain response and constitutive modelling. *Biorheology* 43(5), 623–636, 2006.
20. H. M. Huang, M. C. Lee, S. Y. Lee, W. T. Chiu, L. C. Pan, and C. T. Chen. Finite element analysis of brain contusion: an indirect impact study. *Med. Biol. Eng. Comput.* 38(3), 253-259, 2000.
21. S. Iakovlev. Interaction of a spherical shock wave and a submerged fluid-filled circular cylindrical shell. *Journal of Sound and Vibration* 255(4), 615-633, 2002.
22. S. Iakovlev. Submerged fluid-filled cylindrical shell subjected to a shock wave: fluid-structure interaction effects. *Journal of Fluid and Structures* 23(1), 117-142, 2007.
23. C. Imielinska, A. Przekwas, and X.G. Tan. Multi-scale modeling of trauma injury. *Computational Science – ICCS* 3226, 822-830, 2006.
24. N. Kambouchev. Analysis of blast mitigation strategies exploiting fluid-structure interaction. Ph.D. thesis. Massachusetts Institute of Technology, 2007.
25. S. Kumaresan and S. Radhakrishnan. Importance of partitioning membranes of the brain and the influence of the neck in head injury modelling. *Med.Biol. Eng. Comput.* 34(1), pp. 27-32, 1996.
26. K. K. Mendis, R. L. Stalnaker, and S.H. Adyani. A constitutive relationship for large deformation finite element modeling of brain tissue. *Journal of Biomechanical Engineering* 117, 279-285, 1995.
27. Matlab. System identification toolbox. User's guide. http://www.mathworks.com/accesss/helpdesk/help/toolbox/ident/.
28. K. Miller and K. Chinzei. Mechanical properties of brain tissue in tension. *Journal of Biomechanics* 35(4), 483-490, 2002.

29. W. C. Moss, M. J. King, and E. G. Blackman. Skull flexure from blast waves: a mechanism for brain injury with implications for helmet design. *Physical Review Letters* 103(10), 108702, 2009.
30. M. Nyein, A. Jerusalem, R. Radovitzky, D. Moore, and L. Noels. Modeling blast-related brain injury. 26th *Army Science Conference*, December 2008.
31. L. A. Peralta and S. Raynor. Initial response of a fluid-filled, elastic circular, cylindrical shell to shock wave in acoustic medium. *The Journal of the Acoustical Society of America* 36 (3), 476-488, 1964.
32. P. K. Pinnoji and P. Mahajan. Finite element modelling of helmeted head impact under frontal loading. *Sadhana* 32(4), 445-458, 2007.
33. J. S. Ruan, T. Khalil, and A. I. King. Human head dynamic response to side impact by finite element modeling. *Journal of Biomechanical Engineering* 113, 276-283, 1991.
34. J. S. Ruan, T. Khalil, and A.I. King. Dynamic response of the human head to impact by three-dimensional finite element analysis. *Journal of Biomedical Engineering* 116, 44-50, 1994.
35. K. U. Schmitt, P. F. Niederer, M. H. Muser, and F. Walz. *Trauma biomechanics: accidental injury in traffic and sports*. Springer-Verlag, 2007.
36. F. Shen, T. E. Tay, J. Z. Li, S. Nigen, P. V. S. Lee, and H. K. Chan. Modified bilston nonlinear viscoelastic model for finite element head injury studies. *Journal of Biomechanical Engineering* 128, 797-801, 2006.
37. S. I. Svetlov, S. F. Larner, D. R. Kirk, J. Atkison, R. L. Hayes, and K. K. W. Wang. Biomarkers of blast-induced neurotrauma: profiling molecular and cellular mechanisms of blast brain injury. *Journal of Neurotrauma* 26(6), 913-921, 2009.
38. C.M. Suh, S. H. Kim, and S. Y. Oh. Analysis of traumatic brain injury using a finite element model. *Journal of Mechanical Science and Techonology* 19(7), 1424- 1431, 2005.
39. L. Voo, S. Kumaresan, F. A. Pintar, N. Yoganandan, and A. Sances., Jr. Finite-element models of the human head. *Medical & Biological Engineering & Computing* 34(5), 375-381, 1996.
40. R. Willinger, H.S. Kang, and B. Diaw. Three-dimensional human head finite-element model validation against two experimental impacts. *Annals of Biomedical Engineering* 27(3), 403–410, 1999.
41. A. Wittek and K. Omori. Parametric study of effects of brain-skull boundary conditions and brain material properties on responses of simplified finite element brain model under angular acceleration impulse in sagittal plane. *JSME International Journal, Series C* 46(4), 2003.

42. P. G. Young. An analytical model to predict the response of fluid-filled shells to impact- a model for blunt head impacts. *Journal of Sound and Vibration* 267(5), 1107-1126, 2003.
43. Q. H. Zhang, E. C. Teo, and H.W. Ng. Development and validation of a C0-C7 FE complex for biomechanical study. *Journal of Biomechanical Engineering* 127, 729-735, 2005.
44. L. Zhang, K. H. Yang, and A. I. King. A proposed injury threshold for mild traumatic brain injury. *Journal of Biomechanical Engineering* 126(2), 226-236, 2004.
45. Z. Zong, H. B. Lee, and C. Lu. A three-dimensional human head finite element model and power flow in a human head subject to impact loading. *Journal of Biomechanics* 39(2), 284–292, 2006.
46. H. Zou, J. P. Schmiedeler, and W.N. Hardy. Separating brain motion into rigid body displacement and deformation under low-severity impacts. *Journal of Biomechanics* 40(6), 1183–1191, 2007.

Chapter 8

Simulation-based Synthesis of Planning Logic for Autonomous Unmanned Sea Surface Vehicles

Maxim Schwartz, Petr Svec, Atul Thakur, and Satyandra K. Gupta

A major issue in the development of increased autonomy for Unmanned Surface Vehicles (USVs) is the time and expense of developing the software necessary to handle a large variety of missions and all the variations in the encountered environments. This chapter describes a new approach for automated development of planning logic using simulation-based synthesis. The planning logic is represented as a decision tree that consists of high-level controllers as building blocks, conditionals and other program constructs. We used strongly-typed Genetic Programming (GP) based evolutionary framework for automatic generation of planning logic for blocking the advancement of a computer-driven intruder boat toward a valuable target. Our results show that the automatically generated planning logic was able to find and exploit repetitive motion patterns in the intruder's behavior for effective blocking.

8.1 Introduction

Technological advances in unmanned surface vehicles (USVs) have enabled the unmanned boats to be considered in search, rescue, recovery, surveillance, and reconnaissance applications [1-3]. In many cases it may be impractical or too dangerous for humans to perform some of these tasks. Currently, most USVs are semiautonomous. This means that the way-points programmed into them are initially determined by human navigators. The built-in navigation planners employ deliberative and reactive obstacle avoidance (OA) modules to ensure safe movement

between the way points. Some also compute new way points or employ a few emergency actions, such as abort and stop, in response to fault conditions.

The most comprehensive USV system to the date is the Control Architecture for Robotic Agent Command and Sensing (CARACaS) [4] developed by the Jet Propulsion Laboratory (JPL). The system utilizes algorithms used on the Mars Exploration Rover (MER) and the Earth Observation 1 (EO1) Sciencecraft Orbiter to provide a control capability for USVs. The Space and Naval Warfare Systems Center, San Diego, is known for its autonomous navigation and OA architecture for USVs that supports both deliberative and reactive OA [5]. They extended the deliberative part of the navigation planner to generate paths consistent with the "rules of the road" – International Regulations for Preventing Collisions at Sea (COLREG) guidelines during all stages of the planning [6]. These rules are increasingly being implemented into the USV navigation systems. There are a few other USV navigation systems and platforms. These include the MIT kayak platform [7, 8], the navigation, guidance, control systems, and the mission control system of the DELFIM USV [3], Springer USV for environmental monitoring [2], the autopilot of the MESSIN system [9], the USV prototype Charlie [10], the navigation of USVs satisfying the rules of the road [11], vision-based docking [12], and cooperation of swarming unmanned ground and aerial vehicles [13]. For a detailed description of the current state of USV autonomy, see [14].

A major issue in the development of increased autonomy for robotic vehicles such as USVs is the time and expense of developing the software necessary to handle a large variety of missions and all the variations in the encountered environments. This is a truly challenging task and requires writing hundreds of thousands of lines of code by human programmers.

We have developed a new approach for developing planning software that operates autonomous USVs. This approach takes advantage of the significant progress in virtual environments and machine learning. The basic idea behind our approach is as follows. The USV explores the virtual environment by randomly trying different moves. USV moves are simulated in the virtual environment and evaluated based on their ability to make progress toward the mission goal. If a successful action is identified as a part of the random exploration, then this action will be integrated into the logic driving the USV. We anticipate that there may be portions of the mission, where trial and error alone will not be adequate to discover the right decision rule. In such cases, two additional approaches are utilized to make progress in acquiring the right logic. The first involves seeding the system with the logic employed by humans to

solve a challenging task. The second approach is to restrict the action space based on some type of feasibility criteria. Here we focus specifically on automated generation of a reactive planning logic used for blocking the advancement of an intruder boat towards a valuable target, under the assumption that the intruder's attacking logic is fully classified and thus can be modeled. The important requirement on the intruder's attacking logic is that it is human-competitive in the sense that its efficiency approaches the efficiency of strategies exhibited by human-driven intruders.

An overview of our approach is shown in Figure 8.1. Our first major task is development of a physics-based meta-model. High fidelity simulation of USV is time consuming and cannot be used for discovering decision rules or trees used in planning. We are currently developing a meta-model by conducting off-line simulations of the USV in the sea. This simulation accounts for wave and USV interactions. The meta-model provides information about turning radius, steady state velocity, and acceleration as a function of rudder angle and throttle position. Section 8.3 provides more details on this component.

We have developed a mission planning system with an evolutionary module for evolving planning decision trees as the main component. Particularly, we utilized the genetic programming (GP) [15, 16] as one of the robust evolutionary techniques to automatically generate decision trees expressing blocking logic for the USV. Instead of automatically generating a program composed of low-level controller actions (steer left/right, go straight), we generate a decision tree that consists of high-level controllers as building blocks (go in front of the intruder, etc.), together with conditionals and other program constructs. Section 8.4 provides more details on this.

The genetic programming has been used for automatically generating hierarchically-structured computer programs in various domains. These programs usually have a tree structure and are generated using an algorithm fundamentally similar to the traditional genetic algorithm (GA) [17]. There are many applications of GP in the control and planning domains. For example, in the field of UAVs, a goal homing and circling behavior was evolved for a fixed-wing UAV [18]. Further, the steady-state genetic algorithm was used for evolution of decision trees controlling the behavior of a group of UAVs involved in survey missions [19]. Another example includes evolution of controllers for behaviors like obstacle avoidance [20, 21], wall-following [22], line following [23], light seeking, robot seeking [21], box pushing [24], vision-driven navigation [25], or game playing [26-30].

To be able to discover a general planning logic in a competitive setting, the co-evolutionary process can be used. This process

automatically generates challenging test cases for the current individual being evolved. Competitive fitness and co-evolution were first explored in the context of the Iterated Prisoner's Dilemma in [31]. Koza further discussed GP based co-evolution for a simple discrete planning logic game in [16]. Reynolds discussed how to use competitive co-evolution for evolving strategies for players in the pursuit and evasion game positioned in a continuous geometric environment [32]. More recently, a game planning logic was evolved using competitive co-evolution for an ant taking part in the Ant Wars contest [26]. Similarly, RoboCode [27, 28] is another example of using simulated co-evolution for generating human-competitive game planning logic for competing tanks in a grid based environment. Multi-population competitive co-evolution is used for developing more general high-level controllers in the car racing domain [29]. The work described in [30] shows evolutionary architecture for evolving team tactics for a combative 2D gaming environment using GP. The evolved solutions are often marked as human-competitive, meaning that their performance is equal to or higher than the performance of human-designed solutions [33].

In order to combine all the elements of the project into a cohesive system, we have designed a USV simulation environment. This integrates various components of the project into a complete simulation system and acts as a simulation platform for the evolutionary module. One of the components of the USV simulation environment is the virtual environment (VE) based simulator (see Figure 8.2), which serves as an emulator of the real USV environment and contains gaming logic that allows human players to play against each other or against the computer. The game is used to evaluate computer generated planning logic and to set up benchmarks using human to human gaming. In the game, the player controlling the intruder boat must reach a protected target, while the player controlling the USV must block and delay the intruder as long as possible. The game logic is responsible for the rules of the game, game logging and replay, boat behaviors, and scoring. The game can be played on two computers over a network. In addition to offering basic gaming capabilities, the VE-based simulator provides collision detection and wave/boat physics to the objects in the scene. Section 8.5 provides more details about the USV simulation environment and the VE-based simulator it contains.

Measuring the quality of task outcomes from different robotic domains (mapping and localization, obstacle avoidance, search and rescue, etc.) is necessary in order to be able to compare different techniques or algorithms. This can be done first in a simulator to prevent any possible damage to robots, followed by rigorous testing in a real environment. It is important for the benchmark itself to be accurate. This

encourages other researchers to replicate it on the same problem so that they are able to accurately compare their own control or navigation strategies to existing ones.

Deployment of autonomous USVs in critical missions requires that the performance of the autonomous system matches with that of a remote controlled vehicle. Therefore, we have started an effort to assess the performance of automatically generated blocking logic compared to blocking maneuvers exhibited by human operators. We have used the USV simulation environment to compare the automatically discovered decision trees representing the blocking logic to the strategies used by human players. Our goal was to (1) automatically generate a USV's blocking logic against a deterministic hand-coded human-competitive intruder, and (2) compare its efficiency to the blocking logic exhibited by human operators when pitted against the same intruder. Section 8.6 provides more details on the evaluation methodology.

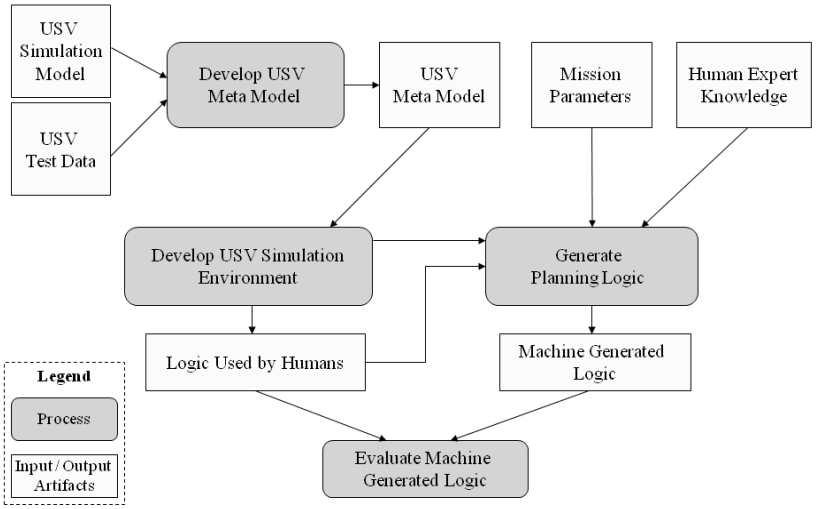

Figure 8.1: Overview of the overall approach.

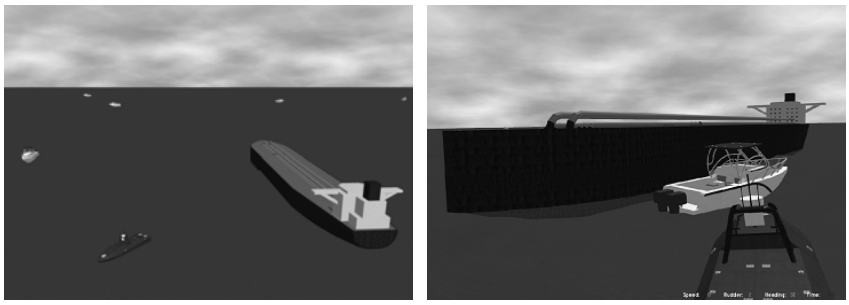

Figure 8.2: Virtual environment for simulation.

8.2 Reactive Planning Logic Executor Architecture

The complexity of interactions of a mobile robotic system suggests structured (non-monolithic) high-level controller architecture. The unmanned boats must behave based on the effect of several independent threads of reasoning. This is due to the highly parallel nature of events and processes in the real world. The high-level controller architecture can meet this requirement if it is modular, and when the modules can act simultaneously in a coordinated cooperation.

The navigation system resides inside the USV and consists of perceptual, reasoning /planning, localization, and behavioral components. The USV's planning logic executor itself (see Figure 8.3) is reactive, which means that it interprets and executes planning logic in a strict timely fashion. The final product of the execution is an action command taking over the controller for a certain period of time.

The reactive planning logic is a stored human-readable structure producing different motor actions (translation and steering velocities) in different situations. Its representation is a decision tree consisting of high-level controllers, conditional rules, standard boolean values and operators, conditional variables, program blocks, velocity commands, and commands for modification of virtual sensor parameters. See Figure 8.4 for an example of a simple planning logic for a USV.

The structure of a high-level controller is based on the behavior-based subsumption architecture [34]. This architecture decomposes a complicated high-level intelligent behavior (a high-level controller in our case) into a set of more solvable and simple behaviors (steer left /right, go straight, arrive) organized into layers. These primitive behaviors are finite state machines acting in response to sensor inputs and producing motor action outputs. Multiple behaviors of the high-level

controller can be activated simultaneously, producing different conflicting motor commands. This means that a certain amount of coordination is needed. Due to its robustness, we have chosen a priority-based arbitration mechanism, picking the motor action output of the behavior with the highest priority (e. g., obstacle avoidance) as the overall motor action output of the high-level controller. In this high-level controller structure, the behavior in the bottom layer has the highest priority (for example obstacle avoidance) while the behavior in the top layer represents the most abstract functionality.

The high-level controllers, which are the main building blocks of a planning logic, can be parameterized. The parameters of a high-level controller define its underlying property. For instance, for the *go-intruder-front* controller, one of the parameters defines the USV's relative goal position (in polar coordinates) in front of an intruder. This effectively allows the USV to cover all feasible positions, as defined by its planning logic around the intruder.

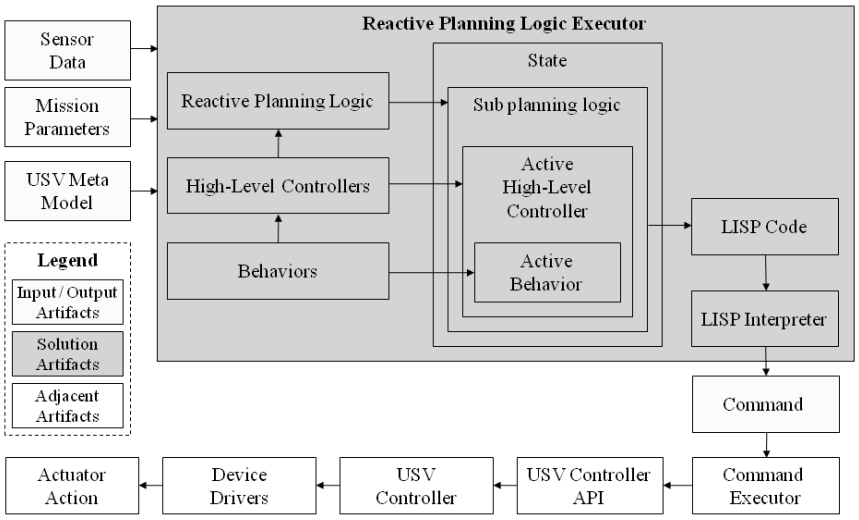

Figure 8.3: Reactive planning logic executor architecture.

The inputs into the reactive planning logic executor are sensor data, the description of mission parameters, and USV meta-model. The reactive obstacle avoidance behavior, which is a basic part of all high-level controllers, utilizes a virtual sensor field divided into four sensor cone areas (front left, front right, left, right). The sensor field has two parameters defining its reach and range (see Figure 8.5). In addition to

this virtual short-range sensor, the USV has a radar sensor on board, with which it can compute the state of the intruder boat (distance, direction, velocity, etc.). The state of the intruder boat is then directly used by conditionals inside the USV planning logic when the logic is executed. The ultimate outputs of the planning logic execution are waypoints for a low-level USV controller. At any particular moment, the logic executor can be in only one state. As Figure 8.3 shows, the planning logic interpreter takes the currently used planning logic as an input and produces an action command output. Based on the current sensor data readings and the fact that the executer finished performing the previously activated high-level controller, only one new high-level controller inside the planning logic can be activated. This high-level controller consists of multiple primitive behaviors and decides which one is used to produce the ultimate action output.

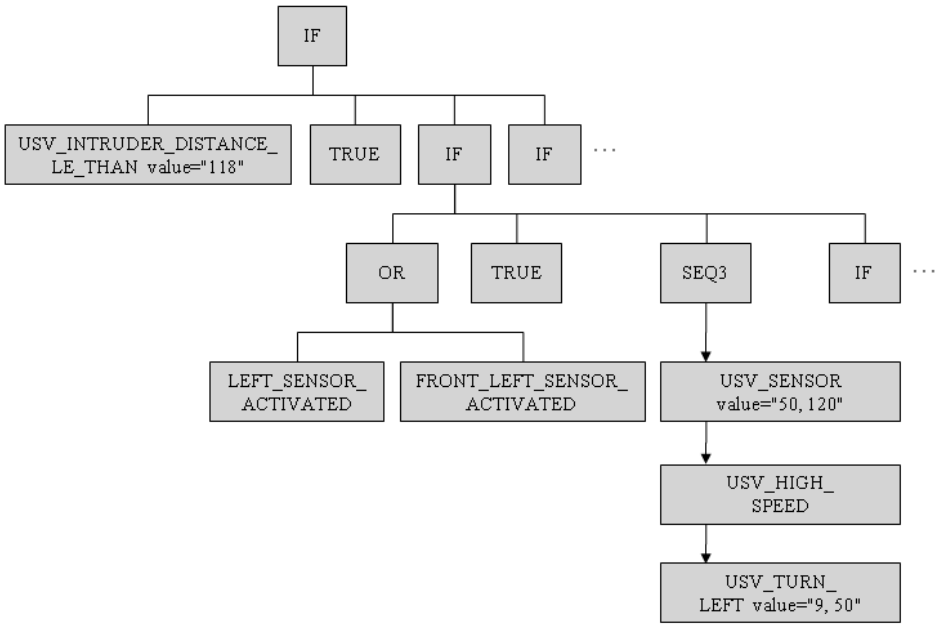

Figure 8.4: Example of a planning logic.

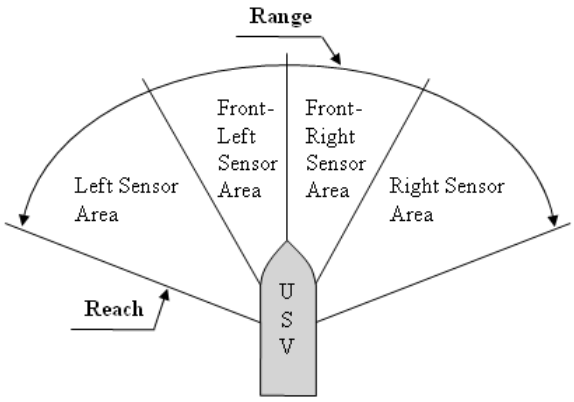

Figure 8.5: USV virtual visibility sensor model.

8.3 Development of Physics-based Meta Model

In this section, we will discuss the dynamics simulation model implemented in the system. The 6 degrees of freedom USV simulation model is used for computing the dynamics of the USV under any given sea-state. The governing equation of the USV is given in equation 1 [35].

$$\left.\begin{aligned} M_H \dot{v} + C_H(v)v + D_H(v)v + g(p) &= \overline{F_E} + \overline{F_P} \\ \dot{p} &= J_P(v) \end{aligned}\right\} \quad (1)$$

where,

$M_H = M_{RB} + M_A$: M_{RB} is the (6X6) inertia matrix and M_A is the (6X6) added mass matrix determined by Formula in Fossen [35],

$C_H = C_{RB} + C_A$: C_{RB} is the (6X6) Coriolis and Centripetal matrix and C_A is the (6X6) hydrodynamic Coriolis and Centripetal matrix,

D_H: (6X6) diagonal damping matrix (in practice is determined by system identification from experiments on the USVs),

$g(p)$: (6X1) restoring force vector,

F_E : (6X1) environment force vector,

F_P : (6X1) actuator force vector,

J_P : (6X6) Jacobian matrix,

v : (6X1) velocity vector relative to inertial frame and expressed in body-fixed frame, and

p : (6X1) vector representing position of USV relative to as well as expressed in the inertial frame of reference

In the past, Krishnamurthy et al. also implemented equation 1 for six degrees of freedom simulation of USV for the purpose of controller design [36]. Unlike the approach suggested by Krishnamurthy et al., which estimated the restoring force vector and wave force vector using an approximated simplified formula, we computed the instantaneous forces and moments by actually intersecting the USV geometry with the wave surface at the given location and time of the USV, resulting in a more accurate estimation of restoring force and moments. To compute the environment force we considered only the wave forces and ignored the effects of wind. We also ignored the wave breaking effect. To estimate the wave force we used the equation 2 [36, 37].

$$F_E = F_W = \begin{bmatrix} \left[-\rho \iint_{S_B} p_{dyn} \hat{n} dS \right]_{3\times 1} \\ \left[-\rho \iint_{S_B} p_{dyn} \vec{r} \times \hat{n} dS \right]_{3\times 1} \end{bmatrix} \quad (2)$$

where,

$p_{dyn} = \left(\frac{\partial \phi}{\partial t} + 0.5 \nabla \phi . \nabla \phi \right)$ is the dynamic pressure,

ϕ : Velocity potential ($\nabla \phi = V$), V is fluid velocity,

S_B : Instantaneous wet surface area of USV,

ρ : Density of water,

$\hat{n}$: Normal surface vector, and

$\vec{r}$: Position vector of points with respect to USV's body frame expressed in inertial frame.

By assuming the fluid as inviscid and irrotational, the velocity potential $\phi(x, y, z, t)$ and the wave elevation $\eta(x, y, t)$, where point (x, y, z) is expressed in inertial frame, is determined by solving the partial differential equation $\nabla^2\phi = 0$ subject to the following two boundary conditions [37]:

i. Kinematic boundary condition: Normal component of fluid velocity and boat velocity at the boundary between boat and fluid are equal, and

ii. Dynamic boundary condition: Pressure at the free surface is equal to the atmospheric pressure.

We computed the wave force by discretizing the equation 2 as shown in equation 3.

$$F_E = F_W = \begin{bmatrix} \left[-\rho \sum_{j=1}^{m} p_{dyn}(x_j, y_j, z_j; t)\vec{s}_j \right]_{3\times 1} \\ \left[-\rho \sum_{j=1}^{m} p_{dyn}(x_j, y_j, z_j; t)\left(\vec{r}_j \times \vec{s}_j\right) \right]_{3\times 1} \end{bmatrix} \quad (3)$$

where,

m: instantaneous number of triangular facets in the USV model exposed to water,

(x_j, y_j, z_j): position vector of j^{th} triangular facet expressed in inertial frame,

$\vec{r}_j$: position vector of j^{th} triangular facet with respect to USV center of gravity expressed in inertial frame,

$\vec{s}_j$: area vector of j^{th} triangular facet in the inertial frame.

The simulation technique described above is computationally expensive because at every time step it, (a) performs the geometric computation of the list of (m) wet facets representing instantaneous wet surface (S_B) of USV by intersecting USV geometry with wave surface $\eta(x, y, t)$, and (b) performs the surface integration to compute the force and torques using equation 3. In one of our tests on a Quad Core computer with a boat model with 950 facets, computing time for single

iteration of time step size 0.05 s was found to be 0.99 s. This is far from real time computation. We developed model simplification algorithms to reduce the computation time. Mainly, we used the following three simplification strategies to compute force due to ocean wave and USV interaction:

- **Clustering of contiguous facets:** The largest amount of computation time in evaluating equation 3 is spent in computing dynamic pressure p_{dyn}. In order to minimize such function calls we make use of the fact that the dynamic pressure values at the facets close to each other are similar. Such contiguous facets are clustered to reduce the number of dynamic pressure computation function calls, and hence the overall computation time is reduced.
- **Temporal coherence:** The force due to ocean wave-USV interaction does not vary significantly in a small period of time. The "smallness" of the time period, for which the forces can be assumed to be the same, is determined by the similarity of the ocean wave pattern in close proximity of the USV. If the ocean wave pattern does not change significantly in a short period of time, the force computed in previous time step can be reused, and hence net time spent on force computation can be reduced significantly.
- **Parallelization:** Pressure computed at various points on the USV wet surface are independent for a given simulation iteration. This makes the force computation highly amenable to parallelization. With the ease in availability of multi-core processors we can exploit the multithreading and reduce the computation time significantly.

Using all the approaches discussed in previous sections we were able to reduce the computation time by about 98% in our test cases. We repeated the same test as discussed before with simplification algorithms in place, and computing time was found to be 0.02 s for single iteration of time step size 0.05 s with an average error of 5.1% with respect to the computations performed without simplification. We thus obtained a real time rigid body simulation with a small error of 5.1% introduced due to simplification.

Although the simulator became computationally fast with the simplifications introduced in the previous subsections, the simulation speed needs to be much faster for the evolutionary process to be practicable. The computationally fast simulator can be run many times under different sea states for a given boat model and can be used to develop a meta-model. The meta-model will be a map between the initial state (position and velocity) and actuator action (rudder angle and

thruster rpm), and the final state (position and velocity) of the boat, under the given sea state for a given boat model. We are in the process of developing the meta-model.

8.4 Automated Generation of Blocking Decision Tree

Our solution to the problem of reactive planning was the use of a computer simulated evolution based on the Darwinian principles of survival and reproduction of the fittest. Using this phenotype evolutionary process, we evolved the actual decision tree representing a planning logic. The specific evolutionary method we used is the strongly-typed generational genetic programming (GP) [15, 16]. This is a robust stochastic optimization method that searches a large space of candidate hypotheses (programs) while looking for the one with the best performance (fitness value).

We were particularly interested in automatically discovering a blocking logic for slowing down the movement of an intruder toward the protected object. We assumed that the intruder boat utilizes a specific planning logic that can be classified. This deterministic logic is assumed to be human-competitive meaning that its performance is approaching the performance of human driven intruders.

The USV's blocking logic is defined in the context of a simple mission. During this mission, the USV must protect an oil tanker by patrolling around it while avoiding collisions with friendly boats and scanning the environment for a possible intruder. The environment around the oil tanker is divided into danger and buffer zones (see Figure 8.6). Once the intruder enters the buffer zone, the USV approaches the intruder boat and circles it for surveillance purposes. If the intruder enters the danger zone, the USV does its best to block the intruder, slowing the intruder's progress toward the protected object.

Instead of generating a decision tree composed of low-level controller actions (e.g., steer left/right, go straight), we utilized our evolutionary framework to automatically generate a decision tree consisting of high-level parameterized controllers as building blocks. Other components of this decision tree are conditional variables, standard boolean values and operators, program blocks, and other commands modifying the underlying properties of the simulated boat.

The GP used was generational imposing type constraints on the generated trees (strongly-typed GP trees). Standard tree transformation operators as crossover and mutation were used as defined by Koza [15]. This included shrink mutation for preventing bloat and a specific mutation operator for mutating parameters of high-level controllers and conditional variables. The initial values of all high-level controller

parameters and conditionals inside the initial set of randomly generated decision trees are either seeded or randomly generated. They are further mutated in the course of the evolution process, possibly improving the functionality of their parental high-level controllers.

During the evolutionary process, a newly created USV individual is evaluated against a particular human-competitive intruder in four different test scenarios. In each scenario, the intruder has a different initial orientation and distance from the target, and the USV always starts from an initial position closer to the target. The evaluation lasts for a maximum amount of time steps, which equals to five minutes in real time. The maximum speed of the USV is set to be 10% higher than the speed of the intruder. The fitness function is defined as the squared distance between the intruder and the target over all time steps. This distance is normalized due to the different initial distances of the intruder from the target in the test scenarios. The total fitness value of the USV planning logic is being maximized and is computed as an average of fitness values resulting from all four scenarios.

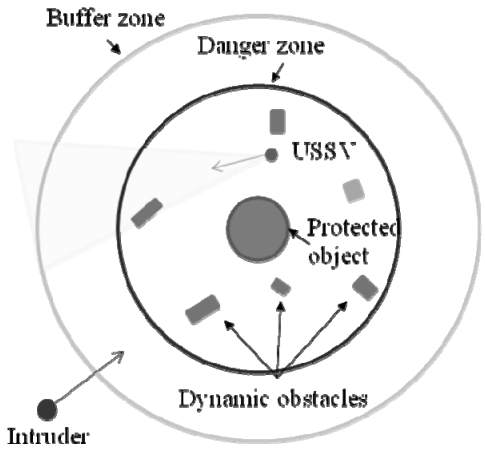

Figure 8.6: Simple mission:
USV protects area containing objects of interest.

8.5 USV Simulation Environment

In order to combine all the elements of the project into a cohesive system, we have designed a USV simulation environment. The simulation environment incorporates various aspects of the project, such

as the USV's planning logic executor and the dynamics simulation model described earlier, into a modular simulation framework where all the modules communicate with each other using a well defined, network-based communication protocol. As depicted in Figure 8.7, the four modules making up the simulation environment are: navigation planner, virtual environment-based simulator, sensor model and the controller model. The simulation begins in the virtual environment-based simulator, which sets the scene and provides the initial placement for all the objects in the virtual environment. Exact data about the positions of all the relevant objects are passed on, possibly over the network, to the sensor model. The sensor model acts as an emulator of the sensors, which the actual USV may use for gathering data about its environment. The purpose of the sensor model is to mimic the rate, accuracy, and completeness of the data that is outputted by an actual sensor like a camera. The sensor model is there to make sure that the navigation planner cannot “cheat” by employing perfect and complete data directly from the virtual environment-based simulator. This is due to the fact that the actual USV will not be operating in a very controlled environment where it receives exact coordinates for its position and the positions of other objects in the environment. The real USV must function using incomplete sensor data. The navigation planner is the USV's planning logic executor explained in Section 8.2. After it receives data from the sensor model, it executes its decision tree and produces a waypoint for the controller model. The controller model mimics the behavior of a boat’s on-board controller. It is tasked with receiving a waypoint and interacting with the virtual environment-based simulator to produce rudder and throttle outputs. Those outputs are then passed on to the virtual environment-based simulator, which in turn uses physics-based modeling of the boat and the waves to generate a new position and orientation for the controlled boat using the received throttle and rudder settings. The cycle then repeats, with the VE-based simulator passing on the positions and orientations to the sensor model. The whole modular infrastructure of the USV simulation environment is designed to support hardware in the loop simulations in the future, where different modules may be replaced with actual hardware – sensor model replaced by camera(s), VE-based simulator replaced by a small boat in a water tank, controller model replaced by an actual hardware controller, etc.

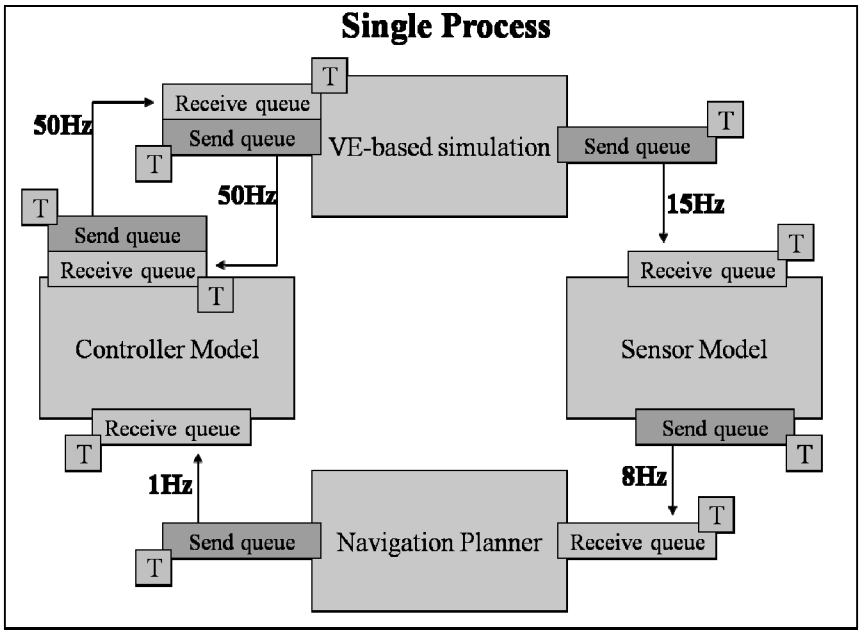

Figure 8.7: The four components of the USV Simulation Environment running in embedded mode. "T" blocks represent threads that manage the message queues.

The USV simulation environment is capable of running all the component modules in either embedded mode or separate process mode. In embedded mode, all four modules run within a single process as separate threads with one of the modules acting as the controller. In separate process mode, each module runs in a separate process, possibly on a separate machine. The separate process mode allows the USV simulation environment to harness the processing power of multiple machines, while the embedded mode simplifies testing and debugging of the system.

The communication pipeline, which is used by the system components to communicate with each other, is designed to insulate the communication infrastructure from the content and format of the messages by requiring that all messages submitted to the pipeline gain access to the transport mechanism only through an interface declared by the pipeline. Specifically, one of the modules may submit any class object to be transported to another module as long as the class of the object inherits and implements certain functions declared by the interface. The interface, in practice, is a C++ abstract class that declares a

set of pure virtual member functions. The primary functions which a class that wants to act as a message must implement are: serialize() and load data(). Each function takes an array of bytes as a parameter. When the function is called inside the class, the class must either store all of its data in the array or load data from the array into its member variables, depending on the function.

Within the pipeline messages are passed around using network sockets and the UDP/IP transfer protocol. Internally, the pipeline uses message queues for sending and receiving datagrams. Each queue is managed by a separate thread, which either waits for a datagram to arrive on a socket or waits for a message to be pushed onto the send queue. Threads are depicted in Figure 8.7 as "T" squares.

One of the four components in the USV simulation environment is the virtual environment-based simulator. The purpose of this simulator is twofold: to evaluate the automatically generated blocking planning logic and to serve as an emulator of the real environment in which the USV will operate.

A virtual environment can be a useful tool for prototyping USV planning logic and the navigation system. Use of a virtual environment, especially in the early stages of a project, can speed the development of the initial navigation system, because it allows one to avoid performing a lot of testing of the generated planning logic in the real world with real boats and numerous real world problems. In the early stages, a lot of progress can be made by simulating the real world with a virtual environment and using the virtual environment to simulate much of the data needed by the navigation system to generate effective mission logic. Later, real boats and real water can be substituted for the virtual environment to provide a more realistic scenario for the navigation system. As long as the interfaces are clearly defined, it will not matter to the navigation system whether the data is coming from the virtual environment or the real world. For these reasons, the virtual environment-based simulator is used in this project as an emulator of the real environment.

The other function of the VE-based simulator is to allow human versus computer testing. The simulator is capable of running a game in which human players are pitted against the computer driven virtual boats. This allows some rough verification of the generated mission planning logic. Human players can take control of an intruder boat and try to reach a protected target, while a USV, driven by computer generated logic, can carry out blocking strategies to try to prevent the human players from reaching their goal. Various measurements can then be made (e.g. time, distance) to assess the effectiveness of the generated blocking logic. A screen capture of a scene from the game is shown in Figure 8.8.

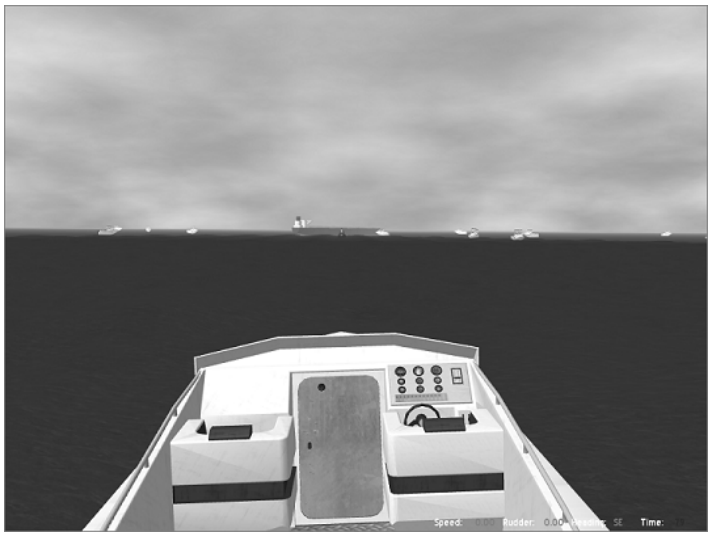

Figure 8.8: Intruder's perspective inside the virtual environment-based game. USV and oil tanker are up ahead.

The VE-based simulator offers a realistic 3D immersive world by implementing a physics based scene and incorporating rigid body dynamics, waves, and dynamic obstacles. The simulator also handles user input, which consists of keyboard strokes, mouse clicks and movements, or a Microsoft XBox controller interface. The XBox controller offers a very intuitive and familiar user interface, especially for experienced gamers. It is important to make the user interface as intuitive and as simple as possible so that the performance of the human operators, when compared to the performance of the computer reactive planning logic, is not biased by a poor user interface. The XBox interface allows the human player to control not only a boat, but also the translation and rotation of the view. It also allows switching among different vantage points.

All the boats in the environment are represented with realistic 3D models created using a CAD tool. The ocean is rendered using a dynamically generated triangulated mesh that is linked to a height map. The same height map is used to calculate bobbing motion for all the boats in the environment. Up to a certain distance from the view point, the triangles that make up the ocean surface are constantly updated and redrawn based on the height map queries. The dynamic ocean mesh was

broken up into a grid of tiles, where each tile represents an independent object. As the user's view moves and rotates, the simulator uses an efficient method to check which tiles are in view and which are no longer within the view angle. Tiles not within the view angle are made invisible to prevent the system from rendering unnecessary triangles. The dynamic ocean implementation also supports multiple levels of detail (LOD). Ocean tiles with a high LOD level have more triangles than those with a low LOD level. The detail level increases for the tiles that are closer to the view and decreases for those that are far from it. When the system signals an ocean tile to change its LOD level, the triangulated mesh for a specific tile is regenerated.

The game logic is responsible for the rules of the game, game logging and replay, boat behaviors, and scoring. Players must navigate the boats around various obstacles to perform their respective missions. Once models of all the boats are loaded into the scene, a physics-based dynamics model is used to govern the boat behavior. In human versus human mode the game is played on two computers over a network using User Datagram Protocol (UDP) and a client-server architecture. The game also supports the concept of a limited visual range. Each player is able to see only objects that are within a certain configurable radius of the boat they are driving.

The VE-based simulator supports collision detection for all objects in the environment so that objects are not allowed to pass through each other. Some basic boat physics has been implemented to deal with boat collisions. When two boats collide, they deflect each other depending on the collision point for each boat, and each boat's velocity, mass, and direction of travel. The deflection involves both translation and rotation. Upon collision, each boat receives a certain amount of damage. Too much damage results in the sinking of the boat. The computer driven boat is equipped with visibility sensors used for avoiding obstacles.

The simulator also supports logging so that games can be played back from different perspectives for visual analysis and inspection. The logging system records the movements of all objects during a game.

The boats serving as obstacles have randomly generated structured motion. During the initialization of the environment, a randomly generated sequence of actions, as well as their duration, is built for each boat.

8.6 Evaluation

8.6.1 Evaluation Protocol

The virtual environment based game that is part of the visualization system allows human players to play against each other or against the

computer. The player controlling the intruder boat must reach a protected object as quickly as possible, while the player controlling the USV must block and delay the intruder for as long as possible. The maximum time for the game is set to five minutes and the maximum speed of the USV is set to be 10% higher than the maximum speed of the intruder. The evaluation includes multiple rounds and in each round the USV is evaluated against a human or computer-driven intruder in four different test scenarios. In each scenario, the USV and intruder have different initial positions and orientations, and the USV always starts from an initial position closer to the target.

To get a fair assessment of the USV performance, the time values being compared must be normalized by 40 seconds baseline. This baseline represents the time needed to reach the target if the intruder is completely unobstructed. Any additional time above this baseline thus represents the effective delay time of the intruder when blocked by the USV. The efficiency of the USV's logic is thus measured in terms of the time delay applied on the intruder by the USV.

8.6.2 Evaluation Results

The whole evaluation process involved 7 trained volunteers playing either as USVs or intruders against other humans or a computer. First, we developed by hand two types of the intruder's deterministic planning logic and let human players as USVs play against the boats controlled by them. Then, we had the same human players play against each other, taking turns playing the role of the USV and the intruder. Comparing the applied time delays from both cases showed that the average efficiency of the two types of the hand-coded intruder (85 s) is 33% lower than the average attacking efficiency of human-driven intruders (64 s). This result proved that the hand-coded intruders are human-competitive and that they can be used for automated generation and subsequent evaluation of a blocking logic for the computer-driven USV.

Using human-competitive intruders, we let the mission planning system evolve planning logic for the USV. Then, we evaluated the evolved USV logic against the hand-coded intruders. The important result of this evaluation is that the mission planning system automatically generated planning logic that blocked these two specific intruders indefinitely, while human operators were able to block them for more than five minutes in only 5 from 56 evaluation scenarios.

8.7 Conclusions

We have developed a mission planning system for automatically generating reactive planning logic for USVs. The planning logic is represented as a decision tree, which consists of high-level controllers as

building blocks, conditionals and other program constructs. We used our strongly-typed GP-based evolutionary framework for automatic generation of planning logic for blocking the advancement of a computer-driven intruder boat toward a valuable target. We assumed that the intruder boat utilizes a specific deterministic human-competitive planning logic, which can be classified and thus modeled.

An important part of our work was to assess fairly the performance of the automatically generated USV's blocking logic. For this reason, we developed a virtual environment based game to compare the efficiency of the computer generated planning logic to the planning skills of human operators.

The results of our tests showed that the automatically generated USV's blocking logic was able to keep both tested intruders outside the target for more than 5 minutes, after which the evaluation was terminated. This is in sheer contrast to human players, who were able to delay the movement of intruders by only 85 seconds on average. It should be noted, however, that the computer generated USV's blocking logic is efficient only against a small group of specific intruders. We have started enhancing the mission planning system to be able to automatically develop a general blocking logic that can be used against a large variety of different intruders.

Another important result from our research is the finding that manual hand-coding of USV strategies, which are able to face even a very specific hand-coded human-competitive intruder, is a very challenging task. The use of evolutionary systems for generating the planning logic automatically by providing only a set of functional primitives and mission goals holds a great promise. Nevertheless, this must be supported by extensive involvement of human expert knowledge in the process to decide not only what functional logic primitives to use but also how to decompose the problem, especially when generating logic for more complex tasks.

Recently, we have built a physical infrastructure for testing radio controlled boats and started evaluating the generated planning logic in a real environment. Testing in a real environment adds some additional challenges due to the differences with the virtual environment (e.g. inaccurate sensors). We are continuously improving the virtual environment based boat simulations (high- and low-level controllers, environment dynamics, sensors, etc.) inside the mission planning system in order to generate a planning logic reflecting the real world dynamics.

8.8 Acknowledgments

This research has been supported in part by Office of Naval Research

Grant N00014-10-1-0585, NSF Grant CMMI-0727380, and Center for Energetic Concepts Development. Opinions expressed here are those of the authors and do not necessarily reflect opinions of the sponsors.

8.9 References

1. Cornfield, S. and J. Young, *Unmanned Surface Vehicles - Game Changing Technology for Naval Operations*, in *Advances in Unmanned Marine Vehicles*, G.N. Roberts and R. Sutton, Editors. 2006, The Institution of Electrical Engineers: Stevenage, United Kingdom.
2. Naeem, W., et al., *The Design of a Navigation, Guidance, and Control System for an Unmanned Surface Vehicle for Environmental Monitoring.* Proceedings of the Institution of Mechanical Engineers, Part M: Journal of Engineering for the Maritime Environment, 2008. 222(2): p. 67-79.
3. Alves, J., et al., *Vehicle and Mission Control of the DELFIM Autonomous Surface Craft*, in *14th Mediterranean Conference on Control and Automation, MED '06*. 2006. p. 1-6.
4. Huntsberger, T., et al., *Autonomous Operation of Unmanned Surface Vehicles (USV's)*. 2007.
5. Larson, J., M. Bruch, and J. Ebken. *Autonomous Navigation and Obstacle Avoidance for Unmanned Surface Vehicles*. In *Proceedings of SPIE Unmanned Ground Vehicle Technology VIII*. 2006.
6. Larson, J., et al., *Advances in Autonomous Obstacle Avoidance for Unmanned Surface Vehicles.* AUVSI Unmanned Systems North America, 2007.
7. Benjamin, M.R., J.A. Curcio, and P.M. Newman. *Navigation of Unmanned Marine Vehicles in Accordance with the Rules of the Road*. In *Proceedings 2006 IEEE International Conference on Robotics and Automation. ICRA 2006*.
8. Eickstedt, D.P., M.R. Benjamin, and J. Curcio. *Behavior Based Adaptive Control for Autonomous Oceanographic Sampling*. In *IEEE International Conference on Robotics and Automation*. 2007.
9. Majohr, J. and T. Buch, *Modelling, Simulation and Control of an Autonomous Surface Marine Vehicle for Surveying Applications Measuring Dolphin MESSIN*. In *Advances in Unmanned Marine Vehicles*, G.N. Roberts and R. Sutton, Editors. 2006, The Institution of Electrical Engineers: Stevenage, United Kingdom.
10. Caccia, M., et al., *Basic Navigation, Guidance and Control of an Unmanned Surface Vehicle.* Auton. Robots, 2008. 25(4): p. 349-365.
11. Lee, S., K. Kwon, and J. Joh, *A Fuzzy Logic for Autonomous Navigation of Marine Vehicles Satisfying COLREG Guidelines.*

International Journal Of Control Automation And Systems, 2004. 2: p. 171-181.
12. Dunbabin, M., B. Lang, and B. Wood, *Vision-Based Docking Using an Autonomous Surface Vehicle*, in *IEEE International Conference on Robotics and Automation, ICRA 2008*. 2008. p. 26-32.
13. Chalmers, R., et al., *Cooperating Unmanned Vehicles*. 2004.
14. Cornfield, S. and J. Young, *Unmanned Surface Vehicles - Game Changing Technology for Naval Operations*. In *Advances in Unmanned Marine Vehicles*, G.N. Roberts and R. Sutton, Editors. 2009, The Institution of Electrical Engineers: Stevenage, United Kingdom.
15. Koza, J.R., et al., *Genetic Programming IV: Routine Human-Competitive Machine Intelligence*. 2003: Kluwer Academic Publishers.
16. Koza, J., *Genetic Programming: On the Programming of Computers by Means of Natural Selection*. 1992: MIT press.
17. Goldberg, D., *Genetic Algorithms in Search and Optimization*. 1989: Addison-Wesley.
18. Barlow, G. and C. Oh, *Evolved Navigation Control for Unmanned Aerial Vehicles*. In *Frontiers in Evolutionary Robotics*. 2008, I-Tech Education and Publishing: Vienna, Austria. p. 596.
19. Richards, M., et al., *Evolving cooperative strategies for UAV teams*. 2005: ACM.
20. Barate, R. and A. Manzanera, *Automatic Design of Vision-based Obstacle Avoidance Controllers using Genetic Programming.* Lecture Notes in Computer Science, 2008. 4926: p. 25.
21. Nehmzow, U. *Physically embedded genetic algorithm learning in multi-robot scenarios: The PEGA algorithm*. 2002: Citeseer.
22. Dain, R., *Developing mobile robot wall-following algorithms using genetic programming.* Applied Intelligence, 1998. 8(1): p. 33-41.
23. Dupuis, J. and M. Parizeau. *Evolving a vision-based line-following robot controller*. 2006: IEEE Computer Society.
24. Koza, J. and J. Rice. *Automatic programming of robots using genetic programming*. 1992: Citeseer.
25. Gajda, P. and K. Krawiec, *Evolving a vision-driven robot controller for real-world indoor navigation.* Lecture Notes in Computer Science, 2008. 4974: p. 184.
26. Jaskowski, W., K. Krawiec, and B. Wieloch, *Winning Ant Wars: Evolving a Human-Competitive Game Strategy Using Fitnessless Selection.* Lecture Notes in Computer Science, 2008. 4971: p. 13.
27. Shichel, Y., E. Ziserman, and M. Sipper. *GP-Robocode: Using Genetic Programming to Evolve Robocode Players*. 2005: Springer.

28. Sipper, M., et al., *Designing an Evolutionary Strategizing Machine for Game Playing and Beyond.* IEEE Transactions on Systems, Man, and Cybernetics, Part C: Applications and Reviews, 2007. 37(4): p. 583-593.
29. Togelius, J., P. Burrow, and S. Lucas. *Multi-Population Competitive Co-evolution of Car Racing Controllers*. 2007.
30. Doherty, D. and C. O'Riordan. *Evolving Agent-Based Team Tactics for Combative Computer Games*. 2006.
31. Axelrod, R., *The Evolution of Strategies in the Iterated Prisoner's Dilemma.* Genetic algorithms and simulated annealing, 1987: p. 32-41.
32. Reynolds, C. *Competition, Coevolution and the Game of Tag*. 1994.
33. Koza, J., M. Streeter, and M. Keane, *Routine high-return human-competitive automated problem-solving by means of genetic programming.* Information Sciences, 2008. 178(23): p. 4434-4452.
34. Brooks, R.A., *Intelligence Without Representation.* Artificial Intelligence, 1991. 47: p. 139-159.
35. Fossen, T., *Guidance and control of ocean vehicles.* Chichester New York, 1994.
36. Krishnamurthy, P., F. Khorrami, and S. Fujikawa. *A Modeling Framework for Six Degree-of-Freedom Control of Unmanned Sea Surface Vehicles*. 2005: IEEE; 1998.
37. Newman, J.N., *Marine Hydromechanics*. 1977, Cambridge, MA: MIT Press.

Chapter 9

Simulation-based Design of Drive Mechanism for Flapping Wing Miniature Air Vehicles

Arvind Ananthanarayanan, Wojciech Bejgerowski, John Gerdes, Dominik Mueller, Satyandra K. Gupta, and Stephen Wilkerson

Flapping wing miniature air vehicles (MAVs) have significant potential in surveillance, search, rescue and reconnaissance applications. These applications require the MAV to carry payloads in the form of batteries, on-board cameras, sensors etc. In order to ensure that the payload capacity of the MAV is maximized for a given wing area and flapping frequency, we need to carefully design the drive mechanism to reduce its mass and ensure that it meets the intended functional requirements. The overall design approach described in this chapter incorporates the advances in modeling and simulation methods in kinematic and dynamic analysis, finite element analysis, and manufacturability analysis. We demonstrate the applicability of this design approach using two case studies.

9.1 Introduction

Flapping wing miniature air vehicles (MAVs) are expected to present several advantages over conventional MAVs [1-6]. Birds and insects are well known for their high degree of maneuverability and quiet flights. Hence, flapping wing locomotion offers the potential for very stealthy MAVs capable of a wide range of flight maneuvers. Flapping wing MAVs can also fly at low forward speeds. These capabilities suggest great potential for use in indoor operations, surveillance, and urban environments where obstacle avoidance is important.

The following issues need to be addressed for successful realization of flapping wing MAVs in practical applications:

- **Reduction in Drive Mechanism Weight**: Most applications of flapping wing MAVs require relatively heavy payloads in the form of on-board sensors, batteries, camera, etc. Hence, the overall weight of the MAV needs to be minimized. This also enables longer flight time, which is another fundamental requirement for most flapping wing MAVs. While the payloads generally offer limited potential for weight savings, the drive mechanism that converts the motor's rotary motion into the flapping motion of the wings is a source of weight savings and can be easily controlled by the designer.
- **High Power Transmission Efficiency**: The rotary motion of the motor is converted into flapping wing motions by the drive mechanism. The strict weight constraint on the MAV makes it beneficial to increase the efficiency of the power transmission and reduce the overall part count of the mechanism.
- **Low Cost**: In order to make flapping wing MAVs attractive in search, rescue, and recovery efforts, they should be disposable from the cost point of view.

Designing a drive mechanism requires simultaneous consideration of multiple factors. Usually, the primary objective is to minimize the weight of the drive mechanism. The secondary objective is to select the structure shape to minimize the manufacturing cost. The structure shape and size need to ensure that the forces acting on the mechanism do not induce excessive stresses. Furthermore, structure shape and size need to respect manufacturing constraints. In this chapter, an approach for decomposing this challenging problem into more manageable steps will be described, and different types of modeling and simulation tools will be presented to perform these steps.

9.2 Simulation-based Design Framework

The drive mechanism is a critical component of any MAV. The mechanism must convert the input energy source to the flapping action of the wings using an actuator. Potential forms of input energy are solar energy, wind energy, or simply a DC battery. Typical examples of actuators are DC motors and servo motors. MAVs are usually constructed using the following concept. First, an energy input is supplied to an actuator. Next, the actuator motion is converted to the flapping action of the wing using a drive mechanism. This flapping

action produces lift and thrust forces that sustain MAV flight. The design of the drive mechanism depends on the source of input energy, the actuator used, and the amount of power that has to be transmitted from the actuator to the wings. This section will present a simulation based design framework for realizing the design goal of an MAV drive mechanism, which converts the input energy to flapping action of the wings. The overall approach for realizing this design goal is illustrated in Figure 9.1.

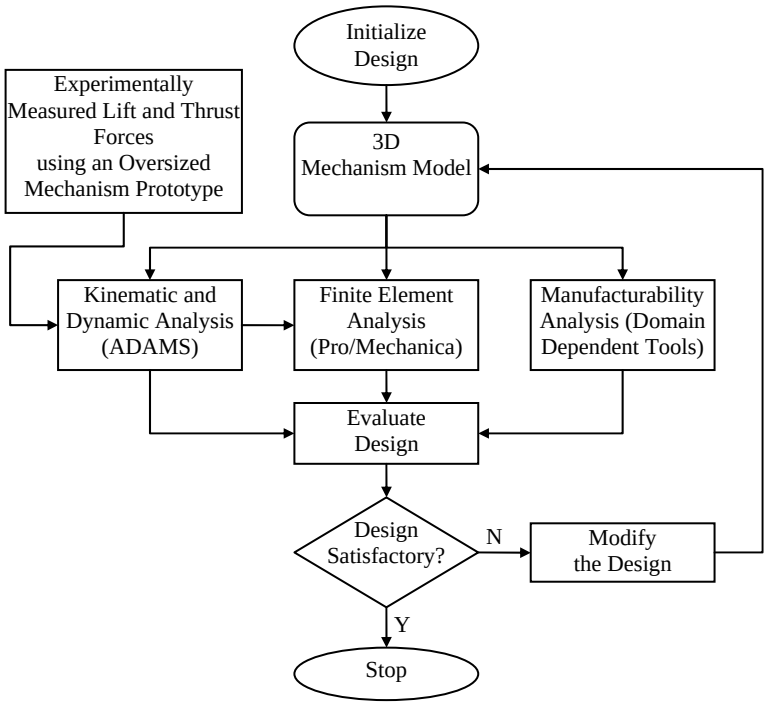

Figure 9.1: Overview of the approach.

In the first step, the designer identifies several design concepts for the drive mechanism. These concepts can be selected from a design repository after performing a feasibility check for the desired flapping action of the MAV, the input energy source and the actuator type to be used.

Subsequently, the design concept suitability has to be evaluated. The mechanism is evaluated based on the power transmission capability of

the input energy source, the actuators to be used, and geometric constraints. The mechanism model also depends on the properties of the materials used to realize the mechanism, such as density, structural rigidity, etc.

Good computational tools do not currently exist for estimating lift and thrust force generated by flapping wings. Therefore, an oversized and hence safe mechanism prototype needs to be used to experimentally measure the lift and thrust forces generated during the flapping motion. The experimentally measured lift and thrust forces are used in a detailed kinematic and dynamic analysis to develop an understanding of the forces acting on the structural members of the mechanism. Subsequently, the mechanism design is evaluated for performance using finite element analysis to evaluate the stresses on the structural members and manufacturability analysis to impose size constraints on the structural members. The manufacturability analysis on the MAV drive mechanism involves: 1) selection of an appropriate manufacturing process that can be used to fabricate the MAV drive mechanism, and 2) development of a detailed manufacturing framework based on the manufacturing constraints.

The final design of the MAV drive mechanism is obtained using an iterative process involving the steps outlined above. The following sections will present two case studies of drive mechanisms, which are used in different versions of MAVs.

9.3 Case Study 1: Design of the Small Bird

In this case study, steps towards creating an MAV platform that weighs less than 15 grams will be described. Figure 9.2 shows the schematic diagram of the drive mechanism concept. Based on the weight, size, and functionality constraints, a compliant mechanism was deemed suitable for realizing the drive mechanism [7-9]. Flexural members were incorporated into the mechanism to provide for distributed compliance in the structure, aiding the flapping motion.

Due to the weight constraint, a polymer was chosen as the material for the mechanism. Considering the choice of material, the small size scales involved, the shape complexity, and the desire for a scalable manufacturing process, injection molding using multi-piece molds was selected as the best choice for the manufacturing process [10-17]. Multi-piece molds have multiple mold opening directions. Designing multi-piece molds poses a significant design challenge due to increased mold cost, flash generation, and limited demoldability of the part.

Moreover, the complexity of the part shape and small size scale made it necessary to use multi-gate molds. Placement of gates is a

challenging problem, since multiple gates supplying the same cavity in the mold lead to weld-lines on the structure [12, 16]. The weld-line is a molding defect which weakens the part structure [18, 19]. Improper gate positioning may lead to a weld-line being positioned in a structurally demanding region of the part, thereby causing its failure.

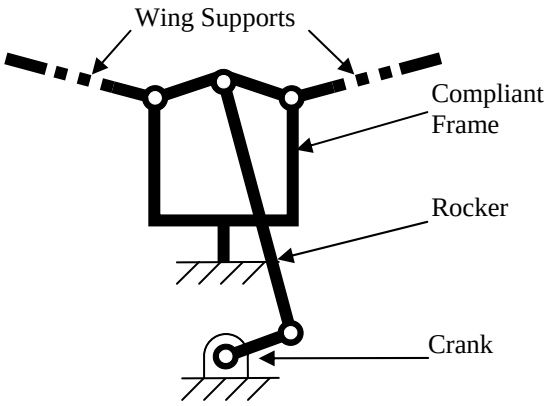

Figure 9.2: Small Bird drive mechanism concept.

The main decision variables for this problem were therefore part shape, size, parting line locations, gate locations, and sacrificial shape elements. The primary objective function for this problem was the mechanism weight minimization. The secondary objective function was the minimization of the number of mold pieces. The following three constraints needed to be satisfied. First, the stresses in the structure should not exceed the material limit. Second, the structure shape and size should meet molding process constraints. Finally, the gate placement should ensure the weld-line locations are outside the high stress areas of the structure.

9.3.1 Mechanism Shape Synthesis

The first step in the overall approach was to determine the detailed part shape and dimensions from the concept illustrated in Figure 9.2.

Mechanism shape synthesis can be carried out using the following three step approach. First, to generate the basic shape of the mechanism, the design concept was detailed by adding functionality and moldability constraints. Second, the constrained dimensions of the mechanism were determined by analyzing the mating components and motion

requirements. Third, parametric optimization and finite element analysis were utilized to determine the values of the remaining unconstrained critical dimensions.

To obtain the flapping wing action from the rotary input of the motor, a crank-rocker mechanism was designed based on the concept illustrated in Figure 9.2. The motor's rotational velocity is transferred to the crank through a gearbox to reduce the flapping frequency. The crank is connected to a rocker, which displaces the symmetrically placed wing arms. These arms are mounted (pivoted) on the compliant members, which allows for the displacement of the pivoting points and hence feasible mechanism action. Note that without the compliant members, this mechanism concept would be a stationary structure.

Disturbance forces caused by wind gusts during the MAV flight could potentially cause significant out of plane motion of the gears and wing supports on the mechanism. These issues were eliminated by use of a bi-planar design, as shown in Figure 9.3. This design allows for two-point support of several elements in the mechanism. This also constrains the motion of the wing supports to a single vertical plane between the supports. Restriction of out of plane motion is crucial to the mechanism efficiency and therefore the amount of thrust produced by the wings of the MAV. The bi-planar design also protects the mechanism from impact loads during landings. The area most exposed to impact loads is the lowest point on the frame. Hence the frame should be designed such that it provides an enclosure for the gears.

The issue of wobbling also affects the crank of the mechanism, which transmits the torque from the gear to the rocker. Due to significant forces during flapping motion, the two-point support of its rotation axis is essential.

In order to ensure moldability of the drive mechanism frame, fillets around the shafts were introduced to minimize the differences of the cavity cross-section and allow for better melt flow in the mold. This is shown in Figure 9.3.

After identifying the basic shape of the mechanism using the functionality and moldability constraints, the next step was to determine the dimensions of the mechanism based on functional requirements of the MAV. This was done using the following strategy. First, the fixed and free dimensions of the mechanism were identified. Next, the geometric and dimensional constraints posed by electronic actuators were accounted for. Finally, manufacturing considerations were accounted for before arriving at the final dimensions of the mechanism.

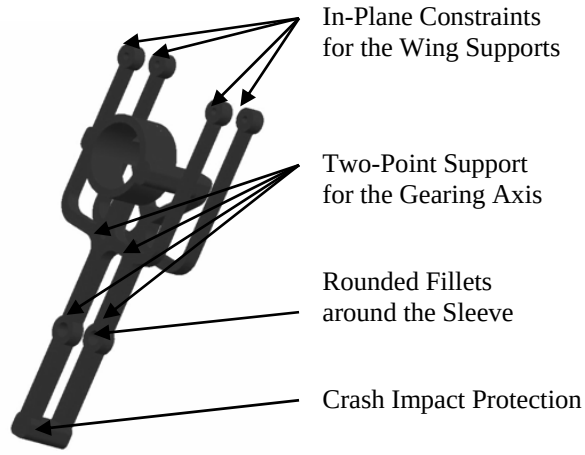

Figure 9.3: Bi-planar design of the drive mechanism frame.

Figure 9.4. shows representative dimensions for a mechanism of an MAV.

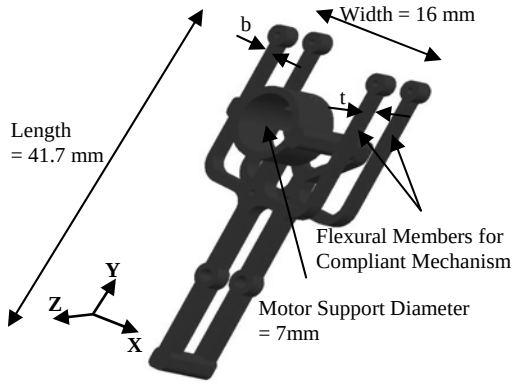

Figure 9.4: Fixed and free dimensions of the mechanism body.

9.3.2 Parametric Optimization

In order to perform structural analysis of the mechanism parts, the forces acting on them have to be estimated. Due to the bi-planar design of the mechanism frame, the out-of-plane forces resulting from the

motion were small. Therefore the kinematic modeling was simplified by treating the mechanism as planar.

Due to the distributed compliance of members as a functional characteristic, the drive was modeled as a pseudo-rigid body planar mechanism. The compliant members were modeled as rigid links with torsion springs at anchoring joints. The sensitivity analysis showed that the influence of the rotational stiffness change on the sought reaction forces is very minor.

Kinematic analysis of the model subsequently revealed the static and dynamic forces on the structural members during the mechanism operation. The inputs into this kinematic analysis were the external forces applied on the mechanism. For this case of the MAV, the two most significant forces are the reaction torque of the motor on the mechanism during its operation, and the external forces on the mechanism due to the wind speed. The reaction torque of the motor can be determined from the manufacturer specifications, while the force due to wind speed has to be obtained experimentally.

A linear test stand was used to measure the thrust and lift of the MAV [20]. When the MAV was attached horizontally to the testing platform, the measured average thrust was 0.077 N and the peak thrust was 0.098 N. The measured peak lift value was 0.150 N.

After constraining the dimensional parameters of the mechanism to accommodate the mechanical and electronic components required for the functionality of the MAV, the remaining critical unconstrained dimensions had to be determined, namely *b* and *t* as shown in Figure 9.4. These were assigned by design optimization based on finite element analysis.

The principle idea was to minimize the weight of the mechanism, yet the manufacturing and maximum allowable stresses constraints had to be satisfied. For example, the mold manufacturing constraint required the width *b* of the compliant members to be 0.89 mm.

Finite element analysis of six static maximum load cases was performed and the maximum von Mises stresses were plotted along the structure. The yield strength of the material was divided by the maximum value of stresses observed by the part to obtain the resulting factor of safety. The frame was designed to have a factor of safety of 1.75. This is an average value recommended for known materials, with certification under reasonably constant environmental conditions, subjected to loads and stresses that can be determined using qualified design procedures. Hence, the depth *t* of the compliant members was solved to be 1.52 mm.

The finite element analysis also identified the high stress and displacement regions. This is important for recognizing the areas that

cannot contain weld-lines, and therefore useful for the gate placement design stage for molding. This will be discussed in further detail in the next section.

9.3.3 Manufacturability Analysis

The first step towards the mold design solution involved determination of the appropriate parting lines, and thereby the total number of mold pieces required for molding the mechanism body. For the body frame considered in this case study, the design obtained – after incorporating the constraints of the functional requirements and performing the mechanics-based optimization – consisted of a non-critical shape element for the motor support. Regular polygonal (e.g., triangle, square, and hexagon) and circular shapes were considered for this element. The radius of the maximum circle contained in each shape was kept the same. Two different orientations were tried for each polygon. The first orientation involved a polygon edge aligned with the x-axis. The second orientation was derived by rotating the triangle by 60°, the square by 45°, and the hexagon by 30°. For each shape, the total number of mold pieces, required for molding the part using the steps outlined above, was determined. From this method, the shape of the motor support for the minimum number of mold pieces was established to be an inverted triangle.

After optimizing the non-critical shape elements, the mold design consisted of 5 mold pieces and 5 mold side cores. The mold pieces that constituted the mold assembly are shown in Figure 9.5. The demolding process for the part using this mold design is illustrated in Figure 9.6. After the mold piece design is obtained, it has to be checked for part demoldability and flash. After analysis of the part, sacrificial shape elements were added to the part, illustrated in Figure 9.7. Addition of the sacrificial shape element of an appropriate size in the top mold piece ensured that the overall part volume was sufficient to avoid flash and prevent under-filling of the part.

After mold piece design, the next step involved the placement of gates. Gate placement strategy is a very important mold design decision. The location of the gates on the part affects several important parameters, which are: 1) mold cavity filling, 2) warpage in the injection molded part, and 3) location of the weld-lines.

The first step to determine the position of the gates was to identify the feasible areas where the gate could be located on the part. Locating the gates on features subjected to high stress levels during operation is not recommended, as gates result in local stress concentrations. High stress areas were classified by:

- Functional stresses: Stresses appearing on the part during its regular operation;
- Demolding stresses: Stresses occurring during demolding of the part from the mold cavity.

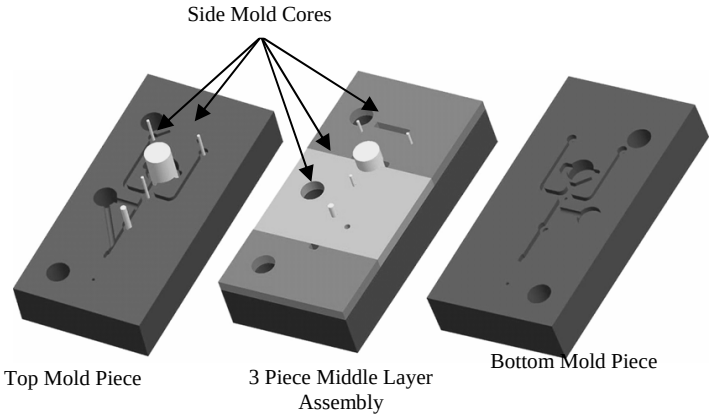

Figure 9.5: Mold design for body-frame fabrication.

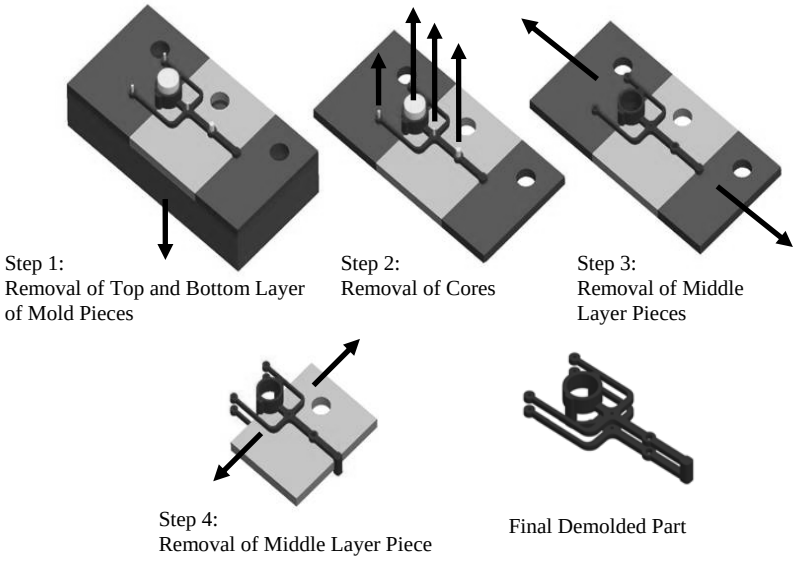

Figure 9.5: Parting surface design for in-mold fabrication of the body-frame.

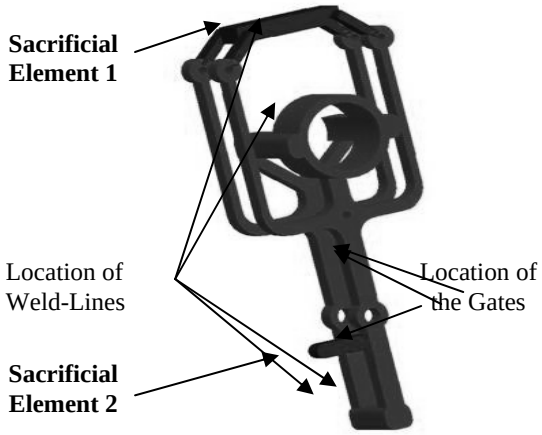

Figure 9.6: Sacrificial elements for absorbing weld-lines.

Hence, placement of gates in these high stress locations is undesirable, since it would result in even higher stress levels in these areas. Therefore, the feasible areas for the gate locations should be identified as regions that are not subjected to high stress levels. Once the feasible areas for the gate locations are identified, the next step involves determining the number of gates required to ensure appropriate part filling while managing warpage. In this step, the gates can be initially placed symmetrically within the part region containing the allowable gate locations. Filling simulations in Moldflow Plastics Insight reveals the effect of the gates on the part filling. However, the gate positions identified for appropriate mold filling may not ensure appropriate positions of weld-lines in the part. Hence, the next step involves positioning the gates such that the weld-line locations are acceptable. Weld-lines should not be located at areas that could potentially be exposed to high stresses.

Therefore, the gates needed to be moved to more appropriate regions to ensure proper weld-line locations. However, some situations may necessitate addition of a gate to alter the weld-line locations. While moving or adding the gates, it is important to ensure that the part filling is not adversely affected by the new gate positioning. Adding or repositioning the gates may not be sufficient to eliminate all the weld-lines that result from the part molding. Hence, a sacrificial shape element may have to be added to absorb the weld-lines occurring in the critical areas. The overall approach used for gate positioning and sacrificial shape element design to absorb weld-lines was outlined in [21].

Using this approach, the gate positioning problem was solved for the body-frame. Finally, using this approach, the sacrificial elements needed for appropriate molding of the mechanism frame were determined. The final gate placement and sacrificial structure design are illustrated in Figure 9.7.

9.3.4 Results

The drive mechanism parts were molded on a Milacron Babyplast injection molding machine using HIVAL ABS HG6.

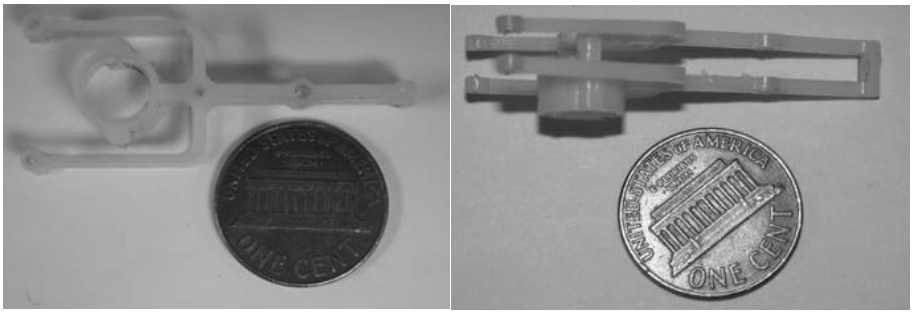

Top View Side View

Figure 9.7: In-mold fabricated body-frame.

Figure 9.8 shows the photograph of the part manufactured using the molding strategy discussed in the previous section. Careful visual inspection of the part revealed that the weld-line was present at the predicted location, illustrated in Figure 9.7. After successfully accomplishing the molding of the drive frame, the rocker and wing supports of the mechanism were also injection molded.

Finally, the MAV was assembled using the molded parts, the gears, and the electronics. The Small Bird MAV designed and developed in the Advanced Manufacturing Laboratory is illustrated in Figure 9.9. The MAV was hand-launched and was capable of holding a sustained flight with controlled ascent and descent. The authors successfully steered and landed the MAV indoors. The main performance specifications are listed in Table 9.1. Video of a successful flight can be found at http://terpconnect.umd.edu/~skgupta/UMdBird/.

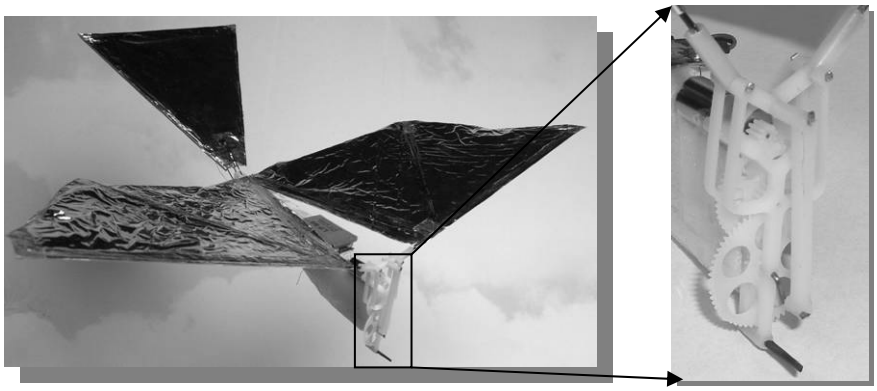

Figure 9.8: Small Bird MAV assembly.

Table 9.1: Performance attributes of the Small Bird MAV

Overall Max. Weight	15.4 g
Payload Capability	5.7 g
Max. Flapping Frequency	12.1 Hz
Flight Duration	5 min
Flight Velocity	4.4 m/s

9.4 Case Study 2: Design of the Jumbo Bird

In this case study the focus was on developing a platform that had a significantly higher payload capacity. The payload capacity translates directly into the weight of sensors and batteries that can be carried onboard the MAV, substantially increasing its practical application to various missions. This section will present the approach to design the Jumbo Bird MAV transmission mechanism.

In the previous case study, development of a small MAV, capable of successful and steerable flight, was presented. The transmission mechanism utilized geometrically distributed compliance; however, with increasing size of the MAVs, mechanisms with distributed compliance exhibit excessive deformations. Therefore, localized compliance in the mechanism becomes a more attractive option, due to both design scalability and compactness of the assembly.

Figure 9.10 shows the schematic diagram of the mechanism concept. Several flexural joints were incorporated into the mechanism to provide for a local (lumped) compliance in the structure to facilitate motion. To enforce the synchronization of the wing motions, a prismatic joint was introduced.

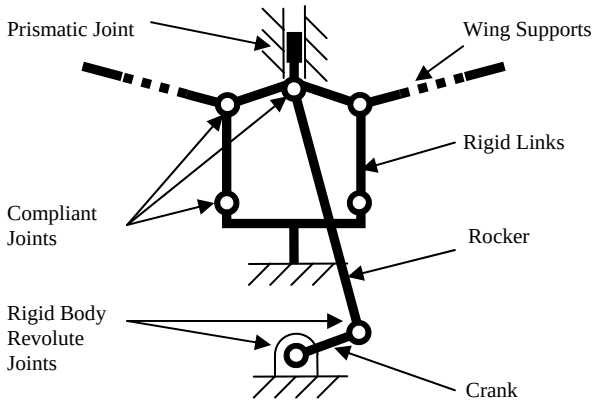

Figure 9.9: Jumbo Bird drive mechanism concept.

9.4.1 Mechanism Shape Synthesis

The first step in the design framework outlined in Figure 9.1 was to perform the shape synthesis of the MAV transmission mechanism. This included the development of the basic mechanism geometry from the concept illustrated in Figure 9.10, as well as identification of interlocking features on miniature compliant joints to achieve successful interconnection with the rigid links in a multi-material structure. Towards this end, the shape synthesis of the mechanism was carried out using the following three step approach. First, to generate a basic shape of the mechanism, the design concept was detailed by adding functionality and manufacturability constraints. Second, the constrained dimensions of the mechanism were determined by analyzing the mating components and motion requirements. Third, the miniature compliant joint geometry, necessary to achieve successful connection between incompatible polymers in a multi-material structure, was investigated.

The primary functional requirement for the MAV drive mechanism was to provide a synchronized flapping action of both wings. Importance of synchronization is emphasized, because it not only ensures the required flapping action for a successful flight of the MAV, but also

contributes to the overall stability and efficiency of the mechanism. The flapping range was determined to be 65° [21]. Preliminary tests indicated that the flapping frequency of 4 to 6 Hz was required to sustain the flight.

To achieve flapping wing motion from the rotary input of the motor, a crank-rocker mechanism, based on the concept illustrated in Figure 9.10, was designed. The motor's rotational velocity was transferred to the crank through a gearbox to obtain the required flapping frequency. The crank was connected to a rocker, which displaced the symmetrically placed wing arms. These arms were pivoted on supporting members, which allowed for the displacement of the pivoting point by utilization of a lumped compliance. To ensure symmetry in the flapping motion, a prismatic joint was introduced at the point where the rocker transferred the energy to the wing arms. This was crucial to the amount of thrust produced by the wings of the MAV. Figure 9.10 shows the developed mechanism design with characteristic features highlighted.

The experimental results showed that disturbance forces can cause significant out of plane motion of the rocker and the wing arms. To eliminate these issues, an additional frame was designed for physical constraint of the rocker motion to a single plane, and an undercut feature on the back of the prismatic joint was added to constrain its motion to only one degree of freedom. This is illustrated in Figure 9.10.

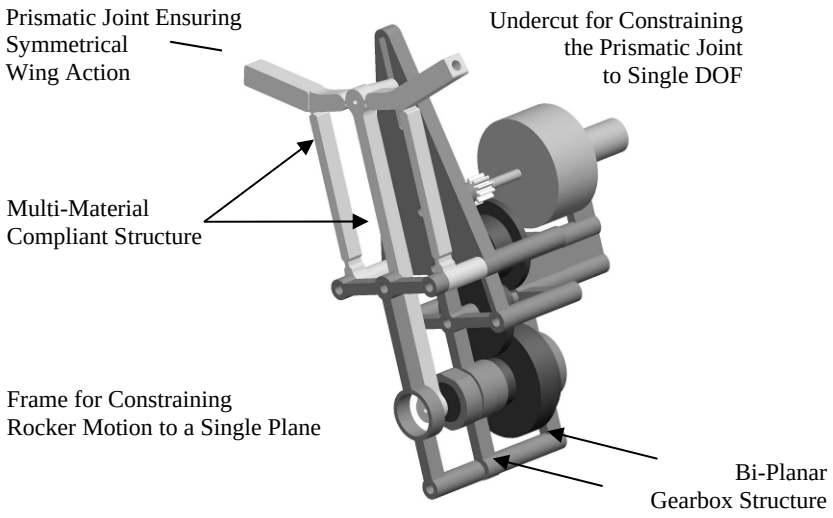

Figure 9.10: Jumbo Bird drive mechanism design.

In order to reduce the rotational velocity of the motor to match the flapping frequency requirement, a three-step gear reduction was designed. The gearbox utilized a bi-planar design. This allowed for two-point support of the gear axis and for prevention of the crank wobbling effect, induced by the torque transmission to the rocker. The bi-planar gearbox assembled with the frame constraining the rocker created a rigid tri-planar enclosure of the mechanism, preventing it from damage during MAV landing.

The drive mechanism utilized a multi-material compliant structure to transform the motor's rotational velocity to the flapping motion. This novel design combined seven rigid links connected with six compliant hinges to create a functional, single-piece mechanism. The molded structure consisted of the rocker, wing arms, and their supports. It also provided for the prismatic joint attachment point and a proper offset with respect to the crank.

In order to ensure the moldability of the multi-material compliant mechanism, fillets around the compliant joints were introduced to minimize the differences in the cavity cross-section and allow for robust hinge encapsulation in the rigid structure.

After identifying the basic shape of the mechanism using the functionality and moldability constraints, the next step is to determine the dimensions of the mechanism. Considering the functional requirements and constraints on the overall size of the MAV, it is important to first identify the constrained and free dimensions of the mechanism design. The constrained dimensions were identified from the functional requirements of the MAV.

The design of the mechanism required the rocker operational envelope to be placed between the wing arm supports. Therefore, the minimum separation between the supporting members was constrained to 19 mm. For the required flapping range of 65°, the relative angle on the wing arms was designed to be 15°, and the length of the crank and the rocker to be 4.1 mm and 45.7 mm, respectively. The range of flapping motion also determined the range for the prismatic joint to be at least 12 mm, to account for elastic deformations of the structure in operation due to loading. The gear axis separation and the range of motion for the prismatic joint determined the minimum length of the mechanism to be 66 mm.

Moldability constraints of the compliant mechanism frame required that the main parting direction of the mold had to be perpendicular to the frame plane. Therefore, the minimum thickness of the compliant joints was set to be 0.8 mm. The fixed dimensions of the mechanism based on the constraints described above are illustrated in Figure 9.12.

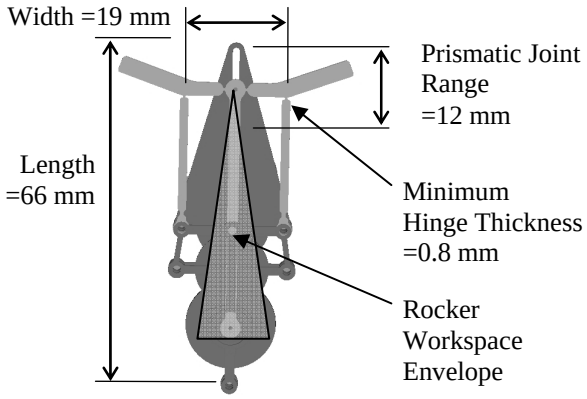

Figure 9.11: Constrained dimensions of the design.

9.4.2 Parametric Optimization

The next step in the approach outlined in Figure 9.1 was to develop models to allow for design optimization of the multi-material compliant drive mechanism of the MAV. To this end, the parametric models of the mechanism resulting from unconstrained dimensions developed in the previous section were employed, and the experimental data was used as the boundary conditions in design evaluation simulation. Since the overall functionality of the MAV depends on its payload capabilities, the weight of the drive mechanism should be minimized with constraints set on load transfer capabilities required by a specific application. The design variables used included sizing of the mechanism rigid links, critical for the drive functionality, as well as sizing dimensions of the miniature compliant joint cross-section. The experimental results of lift and thrust forces generated by MAV wings were inserted into a dynamic simulation model as input boundary conditions. The simulation was used to estimate propagation of the wing forces through the mechanism structure. The results were inputted into a finite element analysis software to calculate stresses and strains on the structure. To minimize the weight of the mechanism without risking its failure, parts were sized to achieve the required factor of safety.

Design optimization of the mechanism required knowledge of the forces acting on links and joints. Lift and thrust forces generated by the wings were measured experimentally [20]. The measured average thrust was 0.384 N, with peak amplitude of 1.724 N. Thrust values were recorded using a stationary platform without any external air stream. The measured average lift was 0.591 N, with the peak amplitude of

1.862 N. Lift values were recorded using a wind tunnel with a moving air stream to simulate the flight conditions.

Since the wings were mounted to the body of the MAV at both front and rear, only a fraction of the forces measured by the load cell were actually transmitted to the mechanism parts. To measure the force distribution over the wing mounting points, a small deflection frame was attached to the back of the wings. The frame deformations were optically measured and the forces were calculated from the deflections. Subtracting the forces observed as deflections on the frame from the total load cell measurements yielded the actual forces experienced by the mechanism.

The simulation of wing forces' propagation onto the mechanism parts was performed using a planar dynamics model. Due to the low operating frequency of the mechanism and a relatively low mass of the moving components, the weights of the mechanism's moving parts were observed as negligible. Therefore the inertial effects of the mechanism were ignored.

The mechanism was modeled using MSC Adams View R3 software. The model was used to analyze the distribution of reaction forces. Static equilibrium simulation for two full wing flap cycles was performed. Static cases were obtained, where the combined load on the structure induced the highest von Mises stresses. The most demanding and prone to failure mechanism components were identified as the rocker element and the wing arms. The most demanding hinges were present at the point where the rocker connects to the wing arms. The data points with the greatest magnitude of combined loading during the flapping cycle were chosen as inputs to the analysis, such that the factor of safety would correspond to the worst case scenario loading of the design.

After constraining the dimensional parameters of the mechanism to accommodate mechanical and electronic components required for the functionality of the MAV, the remaining mechanism dimensions had to be determined, namely the rocker thickness, wing arms' thickness, and the compliant hinge cross-section. These were assigned by a finite element analysis-based design optimization. The goal of the optimization was to minimize the weight of the mechanism while satisfying the manufacturability and maximum allowable stresses constraints.

The von Mises stresses in the mechanism were found from the worst case loading scenarios. The loading conditions found to induce the largest stresses in the mechanism were applied to the corresponding points on the 3D mechanism model.

The finite element analysis was performed using the Mechanica module of Pro/Engineer Wildfire 4.0 software. The analysis of the worst

case loading scenario was performed and the maximum von Mises stresses were plotted across the structure. The yield strength of the material was then divided by the peak stress to determine the resulting factor of safety. The value of the factor of safety was designed similarly to the first case study; however the value was increased to 2.0 due to the higher uncertainties associated with the use of composite material. Hence, the required cross-section dimensions of the rocker were found to be 2.1 x 2.5 mm, and of the wing arms to be 2.5 x5.1 mm. Similarly, the hinge cross-section dimensions were obtained. To allow for low-energy bending, the thickness of the hinge was determined to be 0.9 mm. Considering the forces transmitted by the miniature hinges from the rocker, the depth of the hinge was calculated to be 5.1 mm.

9.4.3 Manufacturability Analysis

This section will describe the development of a manufacturing process to create multi-material compliant mechanisms. This process was developed using the cavity transfer method. Additional considerations were given to the miniature scale involved.

The choice of a specific multi-material molding (MMM) method to realize compliant structures with miniature hinges is a trade-off between the mold complexity and cycle time. Several morphing cavity methods have been developed [17], offering a high level of automation. Due to the fact that morphing cavity methods need to allow for disassembly of the mold pieces, the complexity of the part shape drastically affects the complexity of the molds. Hence, the tooling cost and lead times are significantly increased. To reduce the mold complexity while maintaining the generality of the manufacturing approach, the cavity transfer method [22] was employed in this case study. Optimum mold design consists of minimum number of mold pieces. The chosen cavity transfer method resulted in a minimum number of two mold pieces for each of the molding stages.

The process sequence developed to manufacture a multi-material compliant MAV drive mechanism is presented in Figure 9.12. The first stage involved molding miniature hinges for realizing articulating joints in the mechanism. Demolded first stage components were then transferred to the second stage mold cavity. After the mold closing, the second stage fiber-enhanced polymer was injected into the multiple cavities to create the rigid links of the mechanism structure. Note that this step was an automated assembly operation, which took place directly inside the mold during the second stage molding. The compliant structure was then demolded and was ready to be assembled with the mechanism gearbox and the wings.

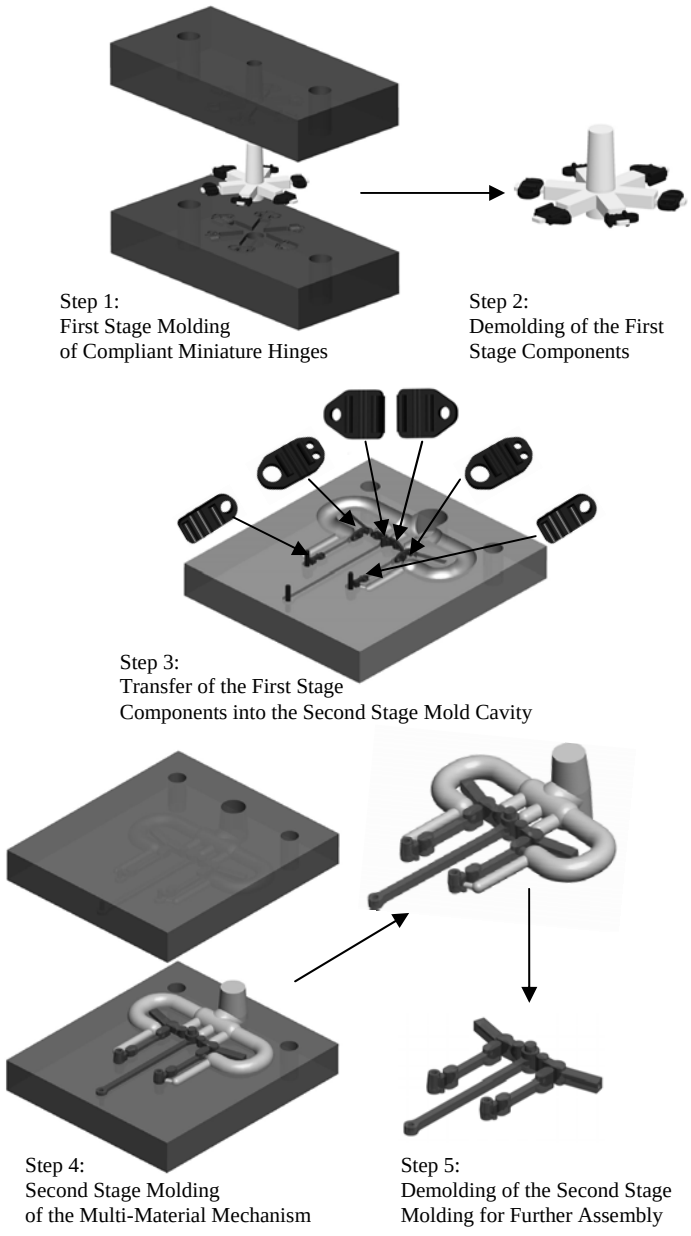

Figure 9.12: Overview of the developed MMM process.

Gate type and location are always important design variables in injection mold design, as they largely affect the cavity fill patterns. Improper choice of gate type and location induces unbalanced flow, which causes overpacking, high shear stress, and excessive warpage. The gate position also induces the fiber orientation for the filled polymers, influencing the properties of the molded part. Therefore, gate placement is of a great importance in achieving high quality products with required properties. Optimum gating will ensure the required structural properties of the product and will allow for easy demolding operation.

In the first stage of the process, compliant hinges were molded. To ensure long life of the hinge, the polymer chains should be oriented perpendicular to the hinge as they cross it. Therefore, film gates were used to provide for a flow front progression aligned with the flexural axis of the joint. Additionally, sacrificial features were added on the part. These served two separate functions: 1) As an extension of the gate, they allowed for a desired flow pattern along the whole length of the hinge, and 2) They allowed for an easy demolding operation, without the risk of damaging the miniature components. The gate and sacrificial feature of the first stage molding are shown in Figure 9.14(a).

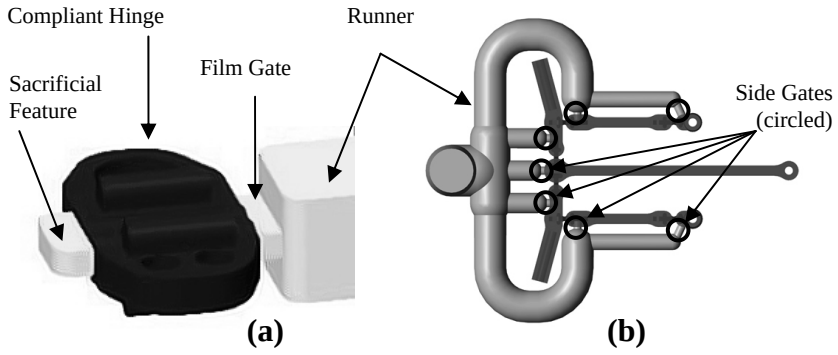

Figure 9.13: Gate designs used in the MMM process: (a) first-stage film gate, and (b) second-stage side gate layout.

In the second stage of the process, the multi-material mechanism frame was created by molding the rigid links over the first stage compliant hinges. Considering the functional requirements of the design, a glass fiber filled polymer composite was used to enhance the load transfer capabilities of the rigid links in the mechanism. However,

properties of filled polymer moldings are very dependent on the filler orientation across the part. Since the filling pattern inside the cavity is a strong function of the gate position, the gate positions had to be carefully designed to result in parts that fully utilize the enhanced material properties. Due to weight limitations in MAV applications, the volume of drive mechanism links needed to be minimized, which resulted in several elongated cavities in the second stage mold. Since the filler particles tend to get aligned with the polymer flow during the cavity filling phase, the side gate positions in these cavities were determined to lie on one of the ends, such that the resulting runner

layout would have the minimum number of relatively long channels. This gate layout was evaluated using mold filling simulation to ensure uniform orthotropic properties of the mechanism links molded from the glass fiber reinforced polymer. The gates were sized according to common injection molding guidelines [10]. The gate layout in the second stage molding is shown in Figure 9.14 (b).

The primary function of the runner system in injection molds is to supply the mold cavities with a molten polymer from the injection nozzle. Realizing multi-material compliant mechanisms with MMM process requires a specific runner layout design. Molding the second stage components over the first stage parts results in the cavity separation, and hence, multi-cavity molds. Each of these cavities needs a separate supplying runner. Since the cavity layout is determined by the mechanism functional design, and the gate positions for each cavity are often fixed, as described above, the main design objective for the runner system is to provide for a complete mold filling. Additionally, to provide for a strong encapsulation of the first stage moldings in the second stage parts, the second stage polymer flows should arrive at the pre-molded component from adjacent cavities in roughly the same amount of time. This is required for: 1) Minimization of highly directional forces that may be induced on the mold insert by an unbalanced flow pattern, resulting in the insert's displacement and failed molding, and 2) Strength improvement of the weld-line, formed when the second stage polymer flows around the first stage component. This is due to the fact that the weld-line strength increases with the temperature of the weld-line formation. Moreover, the polymer that solidifies inside the runner cavity is treated as production waste after demolding; therefore the volume of the runner system should be minimized.

9.4.4 Results

A multi-material compliant frame for the Jumbo Bird MAV drive mechanism was molded on a Milacron Babyplast injection molding machine. LDPE was used in molding the first stage components –

compliant joint inserts. Short glass fiber-filled (15% vol.) Nylon 6,6 was used in the second stage molding to create the rigid links of a multi-material compliant structure. Delrin® was used for manufacturing the crank, motor holder, and the gearbox frame for the mechanism.

Figure 9.15 shows the photograph of the multi-material molding of the compliant MAV drive frame manufactured using the cavity transfer method described in the previous sub-section. Careful visual inspection of the demolded part revealed no molding defects such as deep weld-lines, excessive warpage, or displaced compliant joints.

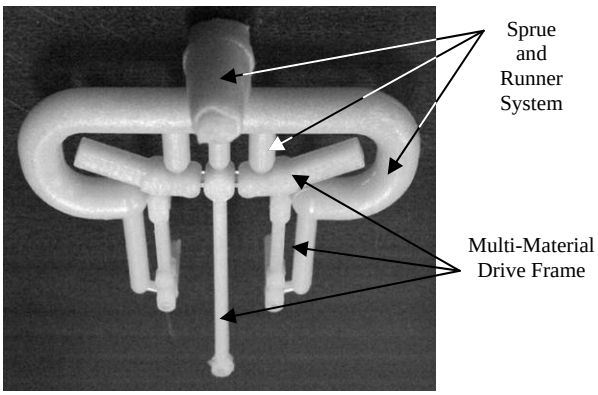

Figure 9.14: Multi-material molding of MAV drive frame.

After successfully molding the multi-material compliant drive frame, the mechanism was assembled using the molded and machined parts, along with off-shelf components, including gears, rods, and motor. The MAV body consisted of the drive mechanism, with wings attached on the front, and the tail servo-motor at the back, both connected with two carbon fiber rods and a foam body. The foam body served as housing for the motor speed controller and the remote control receiver, as well as the rear anchoring point for the wings.

A brushless motor was chosen to actuate the mechanism, because of its high efficiency and low weight. Then, the electronic components required for powering and controlling the MAV were matched from the lightest market-available options. These included the speed controller for the motor, the remote control receiver, the tail actuator and the battery cell. The assembly of the MAV is shown in Figure 9.16.

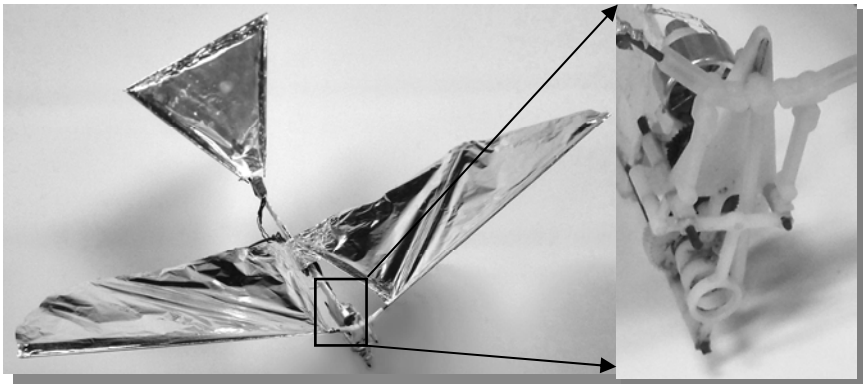

Figure 9. 15: Jumbo Bird MAV assembly.

The Jumbo Bird MAV designed and developed in the Advanced Manufacturing Laboratory was capable of: 1) A remote launch from a four-wheel RC vehicle, 2) Holding a sustained outdoor flight with controlled ascent, descent, and steering, and 3) Controlled landing in a safe area. The main performance specifications are listed in Table 9.2. Video of the successful indoor and outdoor flights can be found at: http://terpconnect.umd.edu/~skgupta/UMdBird/

Table 9. 2: Performance attributes of the Jumbo Bird MAV

Overall Max. Weight	71.0 g
Payload Capacity	33.0 g
Max. Flapping Frequency	6.1 Hz
Flight Duration	15 min
Flight Velocity	3.04 m/s

9.5 Conclusions

This chapter presented a modeling and simulation based approach required for the design and fabrication of MAV drive mechanisms. The overall framework of the design approach outlined incorporates the advances in modeling and simulations methods in kinematic and dynamic analysis, finite element analysis and manufacturability analysis.

Designers can use the methods presented in this chapter to design flapping wing MAV drive mechanisms of any size using different energy sources and actuation elements.

Case studies of two different MAV drive mechanisms have been presented, which utilize the general design framework described in this chapter. These drive mechanisms have been used in two different MAVs, differing significantly in weight and payload capabilities. The technical feasibility of both mechanism designs has been demonstrated through successful test flights of the MAVs. The drive mechanisms have been optimized for the performance of the MAV and their payload capacities. The Small Bird MAV was capable of a sustained flight with a maximum payload capacity of 5.7 grams (59% of total unloaded MAV weight). The Jumbo Bird MAV, on the other hand, was capable of carrying a 33 gram payload (87% of the total unloaded MAV weight). While airborne, the small bird performed very well in indoor conditions. The Jumbo Bird was found to be highly stable and controllable in both indoor and outdoor flights.

9.6 Acknowledgments

This research has been supported by the Army Research Office through MAV MURI Program (Grant Number ARMY W911NF0410176) and NSF grants DMI-0457058 and OCI-0636164. Opinions expressed in this paper are those of the authors and do not necessarily reflect opinions of the sponsors.

9.7 References

1. C. Galinski, and R. Zbikowski. Materials challenges in the design of an insect-like flapping wing mechanism based on a four-bar linkage. Materials & Design, Vol. 28 (3): pp. 783-796, 2007.
2. R. Madangopal, Z.A. Khan, and S.K. Agrawal. Biologically inspired design of small flapping wing air vehicles using four-bar mechanisms and quasi-steady aerodynamics. Journal of Mechanical Design, Vol. 127 (4): pp. 809-816, 2005.
3. T. Tantanawat, and S. Kota. Design of compliant mechanisms in minimizing input power in dynamic applications. Journal of Mechanical Design, Vol. 129 (10): pp. 1064-1075, 2007.
4. P. Zdunich, D. Bilyk, M. MacMaster, D. Loewen, J. DeLaurier, R. Kornbluh, T. Low, S. Stanford, and D. Holeman. Development and testing of the Mentor flapping-wing micro air vehicle. Journal of Aircraft, Vol. 44 (5): pp. 1701-1711, 2007.
5. A. Cox, D. Monopoli, D. Cveticanin, M. Goldfarb, and E. Garcia. The development of elastodynamic components for piezoelectrically

actuated flapping micro-air vehicles. Journal of Intelligent Material Systems and Structures, Vol. 13 (9): pp. 611-615, 2002.
6. S.K. Banala, and S.K. Agrawal. Design and optimization of a mechanism for out-of-plane insect wing-like motion with twist. Journal of Mechanical Design, Vol. 127 (4): pp. 841-844, 2005.
7. L.L. Howell. Compliant mechanisms. Wiley-Interscience, 2001.
8. N.D. Mankame, and G.K. Ananthasuresh. A novel compliant mechanism for converting reciprocating translation into enclosing curved paths. Journal of Mechanical Design, Vol. 126 (4): pp. 667-672, 2004.
9. H. Zhou, and K. Ting. Shape and size synthesis of compliant mechanisms using wide curve theory. Journal of Mechanical Design, Vol. 128 (3): pp. 551-558, 2006.
10. J.P. Beaumont. Runner and gating design handbook: Tools for successful injection molding. Hanser Gardner Publications, 2004.
11. J.P. Beaumont, R. Nagel, and R. Sherman. Successful injection molding: Process, design, and simulation. Hanser Gardner Publications, 2002.
12. J.Y.H. Fuh, Y.F. Zhang, A.Y.C. Nee, and M.W. Fu. Computer aided injection mold design. Marcel Dekker Inc., 2004.
13. D.O. Kazmer. Injection mold design engineering. Hanser Gardner Publications, 2007.
14. M.J. Madou. Fundamentals of microfabrication. CRC Press, 2002.
15. R.A. Malloy. Part design for injection molding. Hanser Gardner Publications, 1994.
16. G. Menges, W. Michaeli, and P. Mohren. How to make injection molds. Hanser Gardner Publications, 2001.
17. A.K. Priyadarshi, S.K. Gupta, R. Gouker, F. Krebs, M. Shroeder, and S. Warth. Manufacturing multi-material articulated plastic products using in-mold assembly. International Journal of Advanced Manufacturing Technology, Vol. 32 (3-4): pp. 350-365, 2007.
18. C. Fetecau, and F. Stan. Computational prediction of defects during injection molding in a complex part. Materiale Plastice, Vol. 44 (3): pp. 180-184, 2007.
19. C.H. Wu, and W.J. Liang. Effects of geometry and injection molding parameters on weld-line strength. Polymer Engineering and Science, Vol. 45 (7): pp. 1021-1030, 2005.
20. D. Mueller, H.A. Bruck, and S.K. Gupta. Measurement of thrust and lift forces associated with drag of compliant flapping wing for micro air vehicles using a new test stand design. Experimental Mechanics, 2010 (to Appear).
21. W. Bejgerowski, A. Ananthanarayanan, D. Mueller, and S.K. Gupta. Integrated product and process design for a flapping wing drive

mechanism. Journal of Mechanical Design, Vol. 131 (6): pp. 061006, 2009.
22. R.M. Gouker, S.K. Gupta, H.A. Bruck, and T. Holzschuh. Manufacturing of multi-material compliant mechanisms using multi-material molding. International Journal of Advanced Manufacturing Technology, Vol. 30 (11-12): pp. 1049-1075, 2006.

Chapter 10

Semi-Autonomous Task Space Manipulation of Robotic Manipulators

Yen-Chen Liu and Nikhil Chopra

Task space manipulation of multiple robotic manipulators by a single human operator is a challenging task. Synchronization has emerged as an important mechanism to achieve the desired cooperative behavior in the semi-autonomous robotic system. However, the focus of the current synchronization schemes has primarily been on joint-space control and in the absence of communication unreliabilities between the agents. In this chapter, we study the problem of task space synchronization and trajectory tracking for heterogeneous robots under dynamic uncertainties. Exploiting passivity based synchronization results developed previously, a new control algorithm is proposed to guarantee task space synchronization for a group of robotic manipulators. Both non-redundant and redundant robots are considered, and the proposed scheme is validated by a numerical example and experiments.

10.1 Introduction

It is well known that robotic manipulators can enhance the operational capability of human operators by operating in remote or possibly dangerous environments. However, a group of autonomous robotic manipulators in cluttered or possibly dynamic environments can be guaranteed to achieve only a small set of the desired tasks with possibly conservative performance. Hence, it is important to develop a framework where the human operator can intervene intermittently and ensure completion of the desired task. This semi-autonomous capability is important in several applications, such as urban search, battle space

rescue, unmanned aerial vehicle [1], health care [2] and exploration of remote planets [3]. However, most of the research on this topic has primarily focused on human-robot interaction with a single human operator and a single robot. Here we provide a semi-autonomous framework to solve the task space trajectory tracking problem for a group of robotic manipulators.

The semi-autonomous behavior is proposed based on the mechanism that utilizes synchronization with trajectory tracking, which was first proposed by Rodriguez and Nijmeijer in [4]. The problem of position synchronization of multiple cooperative robot system was solved in [4] with a linear semi-globally exponentially stable scheme. Contraction theory was used in [5] to guarantee synchronization and tracking on regular graphs with different time-scales for tracking and synchronization. Moreover, collective behavior with cooperation and synchronization based on passivity and dissipativity were proposed in [6–9]. It was shown in [9, 10] that it is possible to output synchronize nonlinear passive systems, provided the storage function is positive definite and the interagent communication graph is balanced. It was also demonstrated that the output synchronization property is robust to communication delays and switching interconnection topologies.

Output synchronization results have been successfully applied to the problem of teleoperation with communication delay in [11]. It was shown that position and velocity errors between the master and the slave robots can be driven to the origin independent of the delays and without using the wave variable. However, the master and slave robot in the scheme were required to have the same configuration and were not controlled in the task space. Building on this scheme, end-effector motion control in task space for teleoperators with different configurations was proposed in [12]. However, the scheme assumed kinematically similar master and slave robots, and without considering possible redundancy in the robotic systems. A recent paper [13] proposed a control scheme for teleoperation where both the master and slave systems are kinematically redundant. However, the master and slave robots were required to have the same degrees of freedom, and communication unreliabilities (for example time delay) between the agents were not considered.

Here, the authors develop semi-autonomous task space manipulation based on the synchronization results in [9] and [14]. These results are utilized to guarantee task space trajectory tracking and state synchronization for mechanical systems in the presence of dynamic uncertainties. The effect of time delays in communication on the trajectory tracking and synchronization of mechanical systems is also studied. Furthermore, both non-redundant and redundant manipulators

are considered, and the efficacy of the scheme is validated using simulations and experiments. The organization is as follows. The relevant background is discussed in Section 2, which is followed by our main results in Section 3. The proposed control algorithms are validated through a numerical example in Section 4 and experiments in Section 5. The results are finally summarized in Section 6.

10.2 Preliminaries

In order to set the background and notation for the following discussions, we consider a control affine nonlinear system of the form

$$\Sigma = \begin{cases} \dot{x} &= f(x) + g(x)u \\ y &= h(x) \end{cases} \tag{1}$$

where $x \in R^n$, $u \in R^m$, and $y \in R^m$. The functions $f(\cdot) \in R^n$, $g(\cdot) \in R^{n \times m}$, and $h(\cdot) \in R^m$ are assumed to be sufficiently smooth. The admissible inputs are assumed to be piecewise continuous and locally square integrable. For simplicity, we note that the dimensions of the input and output are the same, and $f(0) = 0$ and $h(0) = 0$.

Definition [9] The nonlinear system Σ is said to be passive if there exists a C^1 storage function $V(x) \geq 0$, $V(0) = 0$ and a function $S(x) \geq 0$ such that for all $t \geq 0$,

$$V(x(t)) - V(x(0)) = \int_0^t u^T(w) y(w) dw - \int_0^t S(x(w)) dw,$$

which can be written as

$$\dot{V}(x) = u^T y - S(x).$$

The system Σ is strictly passive if $S(x) > 0$ and lossless if $S(x) = 0$.

Communication topology and information exchange between agents can be represented as a graph. Some basic terminology and definitions from graph theory [15] are mentioned here in order to sufficiently follow the subsequent development.

Definition By a graph $\mathcal{G}$ we mean a finite set $\mathcal{V}(\mathcal{G}) = \{v_i, \ldots, v_N\}$, whose elements are called nodes or vertices, together with set $E(\mathcal{G}) \subset \mathcal{V} \times \mathcal{V}$, whose elements are called edges, which is an ordered pair of distinct vertices. An edge (v_i, v_j) is said to be incoming with

respect to v_j and outgoing with respect to v_i , and can be represented as an arrow with vertex v_i as its tail and vertex v_j as its head.

The in-degree of a vertex $v \in \mathcal{G}$ is the number of edges that have this vertex as a head. Similarly, the out-degree of a vertex $v \in \mathcal{G}$ is the number of edges that have this vertex as the tail. If the in-degree equals the out-degree for all vertices $v \in \mathcal{V}(\mathcal{G})$, then the graph is said to be balanced.

If, for all $(v_i, v_j) \in E(\mathcal{G})$, the edge $(v_j, v_i) \in E(\mathcal{G})$ then the graph is said to be undirected. Otherwise, it is called a directed graph. A directed graph is strongly connected if any two vertices can be joined by a path. Here, we assume that communication topology of the interconnected manipulator systems is balanced and strongly connected.

Following [16], in the absence of friction, the Euler-Lagrange equation for the robotic manipulator with n-degree of freedom is given as

$$M(q)\ddot{q} + C(q,\dot{q})\dot{q} + g(q) = u + J^T F, \tag{2}$$

where $q \in R^n$ is the vector of generalized configuration coordinates, $u \in R^n$ is the vector of generalized forces acting on the system, $M(q) \in R^{n\times n}$ is a symmetric, positive definite matrix, $C(q,\dot{q})\dot{q} \in R^n$ is the vector of Coriolis/Centrifugal forces, $g(q) = \dfrac{\partial G}{\partial q} \in R^n$ is the gradient of the potential function $G(q)$, and $J^T F$ is the reaction torque corresponding to the end-effector force, $F \in R^m$, exerted by the human operator, and J is the Jacobian matrix that is defined in the sequel. Under the assumption that we only consider manipulators with revolute joints in the current paper, the above equations exhibit certain fundamental properties due to their Lagrangian dynamic structure [16].

Property 1: The matrix $M(q)$ is symmetric positive definite and there exists positive constant λ_m and λ_M such that

$$\lambda_m I \le M(q) \le \lambda_M I.$$

Property 2: The Lagrangian dynamics are linearly parameterizable, which gives us that

$$M(q)\ddot{q} + C(q,\dot{q})\dot{q} + g(q) = Y(q,\dot{q},\ddot{q})\Theta,$$

where $\Theta \in R^k$ is a set of dynamic parameters and $Y \in R^{n\times k}$ is a matrix of known functions of the generalized coordinates and their higher derivatives.

Property 3: Under an appropriate definition of the matrix C, the matrix $\dot{M} - 2C$ is skew symmetric.

Let $X \in R^m$ represent the position of end-effector in the task space. It is related to the joint space vector $q(t)$ as

$$X = h(q) \quad , \quad \dot{X} = J(q)\dot{q}, \tag{3}$$

where $h(\cdot): R^n \to R^m$ denotes the relation between joint space and task space, and $J(q) = \partial h(q) / \partial q \in R^{m\times n}$ is the Jacobian matrix mapping from joint space to task space. In this chapter we assume that the Jacobian is known, and future work will incorporate adaption schemes as proposed in [17, 18].

In semi-autonomous manipulation, agents first autonomously follow a desired trajectory, where the tracking performance is enhanced by coupled synchronization between the agents. In addition, when operated by a human operator, synchronization between the agents is used as a mechanism to possibly deviate from the pre-planned trajectory. In the subsequent sections, both the non-redundant and redundant robots will be discussed, and further, the effect of uncertain dynamics of heterogeneous robots will be considered in design of the control algorithms.

10.3 Semi-Autonomous Manipulation

10.3.1 Passivity property of a task space control algorithm

In this section, we discuss the passivity property of a task space trajectory tracking algorithm that is used in the subsequent control design. The individual systems are required to track a time-varying trajectory $X^d(t)$, which is assumed to be twice differentiable. Thus, the signals $\dot{X}^d(t)$, $\ddot{X}^d(t)$ are well defined and are additionally assumed to be bounded.

The dynamic uncertainty in the robot dynamics is represented by the uncertain parameter Θ. It is also assumed that the position of end-effector $X(t)$ is known from vision systems, position sensors or laser systems. The robot is operated in a finite task space where the Jacobian matrix has full rank.

Consider the dynamical system (2) with $F = 0$ and let the control input according to [19, 20] be given as

$$\begin{aligned} u(t) = \hat{M}(q)a(t) + \hat{C}(q,\dot{q})v(t) + \hat{g}(q) \\ - K_t s(t) - J^T K_J^T \tilde{X}(t) + J^T \tau(t), \end{aligned} \tag{4}$$

where $\hat{}$ denotes the estimate of the enclosed signal and τ is the synchronizing control that will be subsequently defined. The quantities $a(t)$, $v(t)$, and $s(t)$ are given as below (for the non-redundant case where $n = m$),

$$\begin{aligned} v(t) &= J^{-1}(\dot{X}^d - \Lambda(X - X^d)), \\ a(t) &= \dot{v}(t) = J^{-1}(\ddot{X}^d - \Lambda(\dot{X} - \dot{X}^d)) + \dot{J}^{-1}(\dot{X}^d - \Lambda(X - X^d)), \\ s(t) &= J^{-1}(-\dot{X}^d + \Lambda(X - X^d)) + \dot{q}, \end{aligned} \tag{5}$$

where J^{-1} denotes the inverse of J. The matrices K_t, K_J and Λ are positive definite diagonal matrices. Let $\tilde{X} = X - X^d$ and define $r(t) = Js(t)$, it becomes

$$r(t) = (\dot{X} - \dot{X}^d) + \Lambda(X - X^d) = \dot{\tilde{X}} + \Lambda\tilde{X}.$$

Using Property 2, the linear parametrization property for Lagrangian systems, the control input becomes

$$\begin{aligned} u(t) = Y(q,\dot{q},X,X^d,\dot{X}^d,\ddot{X}^d)\hat{\Theta} - K_t s(t) \\ - J^T(q)K_J^T\tilde{X}(t) + J^T(q)\tau(t), \end{aligned} \tag{6}$$

where $\hat{\Theta}$ is the estimate of the inertial parameters. The estimated dynamic parameter vector Θ is updated by

$$\dot{\hat{\Theta}} = -\Gamma^{-1}Y^T s, \tag{7}$$

where Γ is a positive definite matrix. Substituting (6) into (2), the closed-loop system can be written as

$$M\dot{s} + Cs + K_t s = Y\tilde{\Theta} - J^T K_J^T \tilde{X} + J^T \tau, \tag{8}$$

where $\tilde{\Theta} = \hat{\Theta} - \Theta$.

Lemma 10.1. The dynamical system (5), (7), and (8) is passive with (τ, r) as the input-output pair.

Proof. Consider the positive definite storage function V as

$$V(s,\tilde{X},\tilde{\Theta}) = \frac{1}{2}\left(s^T M s + \tilde{X}^T K_J \tilde{X} + \tilde{\Theta}^T \Gamma \tilde{\Theta}\right). \tag{9}$$

Differentiating the storage function along the system trajectory and using Property 3 ($\dot{M} - 2C$ is a skew symmetric matrix), the derivative reduces to

$$\begin{aligned} \dot{V} &= s^T J^T \tau - s^T K_t s - \tilde{X}^T K_J \Lambda \tilde{X} + \tilde{X}^T K_J J s - s^T J^T K_J^T \tilde{X} \\ &= r^T \tau - s^T K_t s - \tilde{X}^T K_J \Lambda \tilde{X}. \end{aligned} \tag{10}$$

Hence, the dynamical system (5), (7), and (8) is passive with (τ, r) as the input-output pair respectively. □

When only trajectory tracking control of individual systems is required, the synchronizing control τ equals zero. In this case, the zero solution of (5), (7), and (8) is globally stable and all signals are bounded. Integrating (10) from $[0,t]$, it is easy to see that $\tilde{X}$, $s \in \mathcal{L}_2$. As all signals are bounded, $\dot{\tilde{X}}$, $\ddot{\tilde{X}} \in \mathcal{L}_\infty$. It is well known that a square integrable signal with a bounded derivative converges to the origin. Hence, $\lim_{t\to\infty}\tilde{X}(t) = \lim_{t\to\infty}\dot{\tilde{X}}(t) = 0$, and both global stability of the system and convergence of the tracking error are guaranteed.

If the robotic manipulators are redundant, i.e. $n > m$, the null space of Jacobian matrix has a minimum dimension of $n-m$. Therefore, the task space velocity will not be influenced by the link velocity in the null space. This fact can be utilized in several sub-tasks, such as singularity avoidance and obstacle avoidance, to improve the performance of trajectory tracking.

Following [20, 21], the control scheme can be modified as

$$\begin{aligned} a(t) &= J^+(\ddot{X}^d - \Lambda(\dot{X} - \dot{X}^d)) + \dot{J}^+(\dot{X}^d - \Lambda(X - X^d)) + \frac{d}{dt}[(I - J^+J)\psi], \\ v(t) &= J^+(\dot{X}^d - \Lambda(X - X^d)) + (I_n - J^+J)\psi, \\ s(t) &= J^+(-\dot{X}^d + \Lambda(X - X^d)) - (I_n - J^+J)\psi + \dot{q}, \end{aligned} \tag{11}$$

where $\psi \in R^n$ is a negative gradient of the convex function for the sub-task to be optimized, I_n is $n \times n$ identity matrix, and $J^+ \in R^{n\times m}$ is pseudo-inverse of J, which is defined by $J^+ = J^T(JJ^T)^{-1}$ and satisfies $JJ^+ = I_m$.

Since pseudo-inverse J^+ has the following properties [20],

$J(I_n - J^+J) = 0$, $(I_n - J^+J)J^+ = 0$, $(I_n - J^+J)(I_n - J^+J) = I_n - J^+J$

the definition of $r(t)$ is the same as non-redundant robotic manipulators.

According to [22], the sub-task tracking error is defined as $e_N(t) = (I_n - J^+J)(\dot{q} - \psi)$. Pre-multiplying $s(t)$ in (11) by $(I_n - J^+J)$ and using the properties above, we can obtain the relation between the sub-task tracking error $e_N(t)$ and $s(t)$ as.

$$\begin{aligned}(I_n - J^+J)s(t) &= (I_n - J^+J)J^+(-\dot{X}^d + \Lambda(X - X^d)) \\ &\quad -(I_n - J^+J)(I_n - J^+J)\psi + (I_n - J^+J)\dot{q} \\ &= (I_n - J^+J)(\dot{q} - \psi) = e_N(t).\end{aligned}$$

Then, if $\lim_{t\to\infty} s(t) = 0$, then the sub-task tracking error also approaches the origin.

As the matrix $(I_n - J^+J)$ satisfies the property that $J(I_n - J^+J) = 0$, for redundant robots, the modified signals $a(t)$, $v(t)$, and $s(t)$ in (11) are employed for the control input (4) in the control task. Then following the proof discussed previously, the convergence of task-space tracking error and the sub-task tracking error is guaranteed by the control scheme.

Corollary 10.2. *Consider the dynamical system constituted by the redundant manipulator (7), (8) and (11). If the synchronizing control equals zero, then the manipulator asymptotically follows the desired trajectory, and the error of sub-task converges to the origin.*

10.3.2 Task space controlled synchronization

Lemma 10.1 essentially implies that the output synchronization results of [9] are applicable to the dynamical system (5), (7), and (8). Assuming Lagrangian dynamics (2) with $F = 0$, the closed loop dynamics for the individual N agent systems can be rewritten as

$$\begin{aligned}\dot{\tilde{\Theta}}_i &= -\Gamma_i^{-1} Y_i^T s_i, \\ \dot{\tilde{X}}_i &= J_i s_i(t) - \Lambda \tilde{X}_i, \\ \dot{s}_i &= M_i^{-1}(-C_i s_i - K_{ti} s_i + Y_i \tilde{\Theta}_i - J_i^T K_{Ji}^T \tilde{X}_i + J_i^T \tau_i) \quad i = 1, \ldots, N.\end{aligned} \tag{12}$$

The agents communicate the signals $r_i(t) = J_i^T s_i(t)$ with their neighbors and are said to output synchronize if

$$\lim_{t\to\infty} \left\| r_i(t) - r_j(t) \right\| = 0 \quad \forall i, j.$$

Define $z_i = [\tilde{\Theta}_i \ \tilde{X}_i \ s_i]^T$ as the state of the individual agent and the state of the interconnected multiagent system is denoted by $Z = [z_1 \dots z_n]^T$. Let the synchronizing control be given as

$$\tau_i(t) = \sum_{j\in\mathcal{N}_i} K_s(r_j(t) - r_i(t)) \quad i = 1, \dots, N. \tag{13}$$

where the synchronizing gain K_s is a positive constant. We next present the main result of the paper.

Theorem 10.3. Consider the dynamical system, described by (12) and (13), where the robotic systems are assumed to be non-redundant. If the Jacobian matrix has full rank, and the interconnected communication graph is balanced and strongly connected, then the agents output synchronize and asymptotically follow the desired trajectory.

Proof. Consider a positive definite storage function for the N agents system as

$$V(Z) = V_1(z_1) + \dots + V_N(z_n) = \sum_{i=1}^{N} V_i(z_i),$$

where $V_i(z_i)$ is the storage function in (14) for i_{th} agent. Following the proof of Lemma 10.1 (15) and the property of balanced graph, the derivative of this storage function along the trajectories of the system is given by

$$\dot{V}(Z) = -\frac{1}{2}\sum_{i=1}^{\mathcal{N}} \sum_{j\in\mathcal{N}_i} K_s(r_j - r_i)^T (r_j - r_i) - \sum_{i=1}^{\mathcal{N}} \left(s_i^T K_{ti} s_i + \tilde{X}_i^T K_{Ji} \Lambda \tilde{X}_i \right) \le 0 \ .$$

Thus, the zero solution of (12) and (13) is globally stable and all signals are bounded. Integrating the above equation from $[0, t]$, it is easy to obtain that $\tilde{X}_i$, s_i, and $(r_j - r_i) \in \mathcal{L}_2$, where $j \in \mathcal{N}_i$, $\forall i$. Following the arguments in proof of Lemma 10.1, the signals $\dot{\tilde{X}}_i$, $\ddot{\tilde{X}}_i$, and $(\dot{r}_j - \dot{r}_i) \in \mathcal{L}_\infty$. Consequently, $\lim_{t\to\infty} \tilde{X}_i(t) = \lim_{t\to\infty} \dot{\tilde{X}}_i(t) = 0$, $\lim_{t\to\infty}(r_j(t) - r_i(t)) = 0 \quad j \in \mathcal{N}_i, \forall i$, and all the agents of the interconnected system follow the desired trajectory in the task-space. Furthermore, the

individual systems output synchronize independent of the heterogeneous dynamic and kinematic structure. □

Based on the previous discussion for redundant robots, the next result follows.

Corollary 10.4. *Consider the dynamical system described by (12) and (13), where one or more redundant manipulators may cooperate with other robots. If the interconnected communication graph is balanced and strongly connected, then the agents output synchronize and asymptotically follow the desired trajectory. In addition, the convergence of sub-task tracking errors of redundant manipulators is guaranteed.*

It is possible to have delays in communication between the agents. The delays are assumed to be constant and bounded. As there can be multiple paths between two agents, T_{ij}^{k} denotes the delay along the k^{th} path from the i_{th} agent to the j_{th} agent, and we henceforth denote it as the path delay. We impose only the restriction that delays along all paths of length one are unique, i.e., the transmission delay from one agent to the other is uniquely defined.

Definition: In the presence of delays, the agents are said to delay-output synchronize if

$$\lim_{t\to\infty} \left\| r_j(t - T_{ji}^{k}) - r_i(t) \right\| = 0 \quad \forall i, j, k.$$

Let the delay-synchronizing control be given by

$$\tau_i(t) = \sum_{j\in\mathcal{N}_i} K_s(r_j(t - T_{ji}) - r_i(t)) \quad i = 1, \ldots, N. \qquad (14)$$

The result on controlled synchronization with communication delays follows

Theorem 10.5. Consider the dynamical system, described by (12) and (14), composed of nonredundant manipulators. If the Jacobian matrix has full rank, and the interconnected communication graph is balanced and strongly connected, then the agents delay-output synchronize and asymptotically follow the desired trajectory.

Proof. Consider a positive definite storage functional for the delayed system as

$$V(Z_t) = V_1(z_1) + \ldots + V_N(z_n) + \frac{K_s}{2}\sum_{i=1}^{N}\sum_{j\in\mathcal{N}_i}\int_{t-T_{ji}}^{t} r_j^T(\sigma) r_j(\sigma) d\sigma,$$

where the storage function $V_i(z_i)$ is given by (9) for i_{th} agent. Taking derivative along the trajectories of the system and exploiting the balanced graph assumption yields

$$\dot{V} = -\frac{K_s}{2}\sum_{i=1}^{\mathcal{N}}\sum_{j\in\mathcal{N}_i}(r_j(t-T_{ji}) - r_i)^T(r_j(t-T_{ji}) - r_i)$$
$$-\sum_{i=1}^{\mathcal{N}}\left(s_i^T K_{ti} s_i + \tilde{X}_i^T K_{Ji}\Lambda\tilde{X}_i\right) \le 0.$$

Hence, all signals in the dynamical system (12) and (14) are bounded. Following the arguments as in Theorem 10.3, it can be shown that $\lim_{t\to\infty}\tilde{X}_i(t) = \lim_{t\to\infty}\dot{\tilde{X}}_i(t) = 0$ and $\lim_{t\to\infty}(r_j(t-T_{ji}) - r_i(t)) = 0 \quad j\in\mathcal{N}_i, \forall i$. Strong connectivity of the communication graph guarantees delay-output synchronization in the presence of time delays in communication.

□

Corollary 10.6. *Consider the dynamical system, described by (12) and (14), where one or more redundant manipulators may cooperate with other robots. If the interconnected communication graph is balanced and strongly connected in the presence of constant and bounded communication delays, then the agents delay-output synchronize and asymptotically follow the desired trajectory. In addition, the sub-task tracking errors of the redundant manipulators converge to the origin.*

The next claim addresses the case when a human operator is included in the control loop. In the following analysis, we assume that there is no uncertainty ($\tilde{\Theta}_i \equiv 0$) in the system and take the communication delays to equal zero. The system dynamics based on the control law (4) with human operator, $F \neq 0$ in (2), can now be written as

$$\dot{\tilde{X}}_i = J_i s_i(t) - \Lambda\tilde{X}_i,$$
$$\dot{s}_i = M_i^{-1}(-C_i s_i - K_{ti} s_i - J_i^T K_{Ji}^T \tilde{X}_i + J_i^T \tau_i + J_i^T F_i), \qquad (15)$$

where $F_i(t) \in \mathcal{L}_\infty$ is the force applied by human operator on the end-effector of the i_{th} manipulator. It is to be noted that only one manipulator

is influenced by the human operator. Define $E_i = \{e_{ij} \mid j \in \mathcal{N}_i\}$ as the synchronization state of the i_{th} agent. Let $Z_{hi}(t) = [s_i(t)\ \tilde{X}_i(t)\ E_i(t)]^T$ denote the state of the i_{th} agent and $Z_h(t) = [Z_{h1}(t) \ldots Z_{hN}(t)]^T$. The final result demonstrates ultimate boundedness of all signals when the human operator is included in the control loop.

Theorem 10.7. *Given* $0 < \gamma < 1$ *, consider the interconnected manipulator systems described by (13) and (15). In the case that one of the agents is operated by a human operator, if all Jacobian matrices have full rank, and the interconnected communication graph is balanced and strongly connected, then all signals in the system are uniformly ultimately bounded.*

Proof. Consider a positive definite storage function for the N agent system as

$$V(Z_h) = \sum_{i=1}^{N} \frac{1}{2}(s_i^T M_i s_i + K_s \sum_{j \in \mathcal{N}_i} e_{ij}^T \Lambda e_{ij} + \tilde{X}_i^T K_{Ji} \tilde{X}_i).$$

Using equation (15), Property 3, and the property of balanced graph, the derivative of the storage function becomes

$$\dot{V} \leq -\sum_{i=1}^{N} \alpha_i \left\| Z_h \right\|^2 + s_h^T J_h^T F_h, \tag{16}$$

where $\alpha_i = \lambda_{min}(Q_i)$ with

$$Q_i = \begin{bmatrix} K_{ti} & \varnothing_{m\times m} & \cdots & \cdots \\ \varnothing_{m\times m} & K_{Ji}\Lambda & \varnothing_{m\times m} & \cdots \\ \vdots & \varnothing_{m\times m} & \frac{1}{2}\Lambda^T K_s \Lambda & \varnothing_{m\times m} \\ \vdots & \vdots & \varnothing_{m\times m} & \ddots \\ & & & \end{bmatrix}$$

Let $K_\alpha := min(\alpha_i), i = 1, \ldots, N$, and using the Cauchy-Schwartz inequality, the inequality (16) can be rewritten as

$$\dot{V}(Z_h) \leq -(1-\gamma)K_\alpha \left\| Z_h \right\|^2 \qquad \forall \left\| Z_h(t) \right\| \geq \beta,$$

where $\beta := \frac{\left\| J_h^T F_h \right\|}{\gamma K_\alpha}$. As K_α is bounded away from zero, therefore $\dot{V}(Z_h) \leq 0 \ \forall \ \left\| Z_h(t) \right\| \geq \beta$.

Hence, using Theorem 4.18 [24], the trajectories of this interconnected system are uniformly ultimately bounded. Additionally, as the graph is strongly connected, the synchronization errors between the agents are bounded.

10.4 Numerical Example

In this section, the semi-autonomous control scheme is validated through simulations in Simulink® on a group of robotic systems consisting of two two-link planar manipulators and two three-link planar manipulators. As shown in Figure 10.1, these manipulators are distributed along the Z-axis. The control goal is to synchronize the end-effectors in the X-Y plane while ensuring that they follow the desired trajectory. The agents are interconnected using a ring topology as shown in Figure 10.2, in which agents 2 and 3 are two-link manipulators, and agent 1 and 4 are the three-link manipulators, which are also redundant.

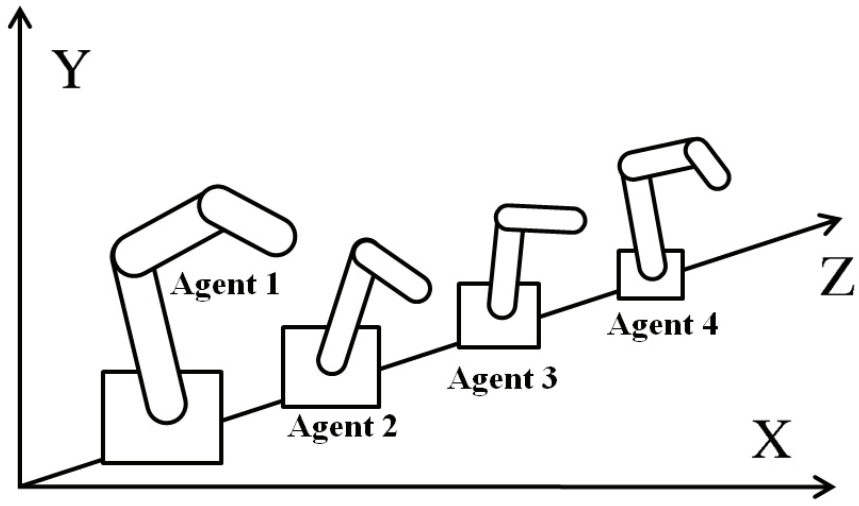

Figure 10.1: The diagram of the four planar robots.

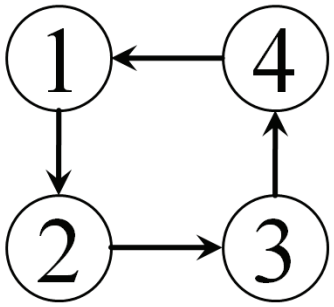

Figure 10.2: The agents interconnected in a balanced ring topology.

We consider the dynamics of planar manipulators as in [16]. The lengths of manipulators are defined as $L_1 = [1.2, 0.9, 0.8]$, $L_2 = [1.5, 1.4]$, $L_3 = [1.5, 0.6]$ and $L_4 = [1.3, 1.2, 0.8]$, and the initial angles of joints are assigned as $q_{10} = [1.1, 1.5, 0.4]$, $q_{20} = [0, 0.8]$, $q_{30} = [1.7, 1.8]$ and $q_{40} = [0, 0.5, 0.8]$. The desired trajectory for the end-effectors is given as $X = 1.2 + 0.5 \times \sin(t)$, and $Y = 1 + 0.3 \times \cos(t)$. In the simulation, the sub-task function for redundant manipulator agent 1 is selected as $\psi_1 = -20(q_{11} - 1)$, which is the negative gradient of $(10(q_{11} - 1))^2$, where q_{11} is the first joint angle of agent 1. This sub-task tracking function forces the first joint of agent 1 towards $q_{11} = 1$ rad. In the case of agent 4, $\psi_4 = \frac{\partial}{\partial q}(\det(J_4 J_4^T))$ is selected as in [20] for increasing the manipulability of the robot manipulators so as to avoid singularities.

We consider the case of trajectory tracking in task space with the proposed synchronizing control in the presence of communication delays. Agents communicate the signal $r_i(t)$ to their neighbors with communication delays, $T_{12} = 0.4$ sec, $T_{23} = 0.2$ sec, $T_{34} = 0.7$ sec, and $T_{41} = 0.5$ sec. These coupled agents achieve good tracking performance as shown in Figure 10.3. The solid line represents the desired trajectory and the dashed lines represent the trajectory of all agents. Figure 10.4 demonstrates the agents' joint angles as their end-effectors synchronize with each other and follow the desired trajectory. Moreover, the sub-task tracking control for both agent 1 and 4 ensures that the sub-task errors, $e_N(t)$, converge to the origin as shown in Figure 10.5.

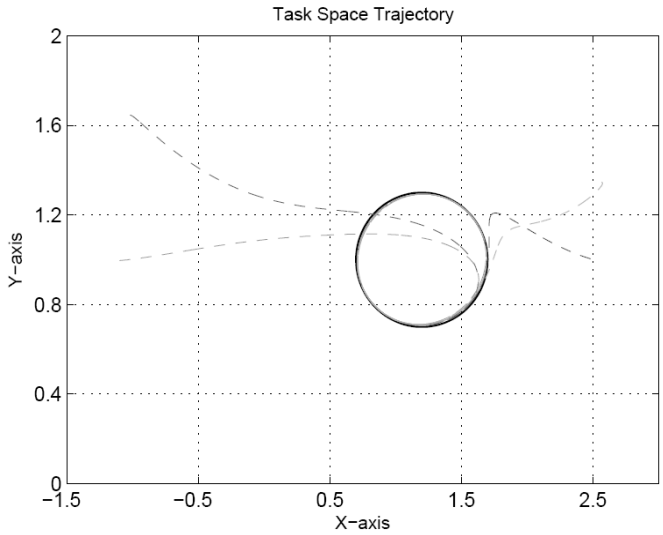

Figure 10.3: Trajectory of the end-effectors using task space tracking control with synchronization and time delays.

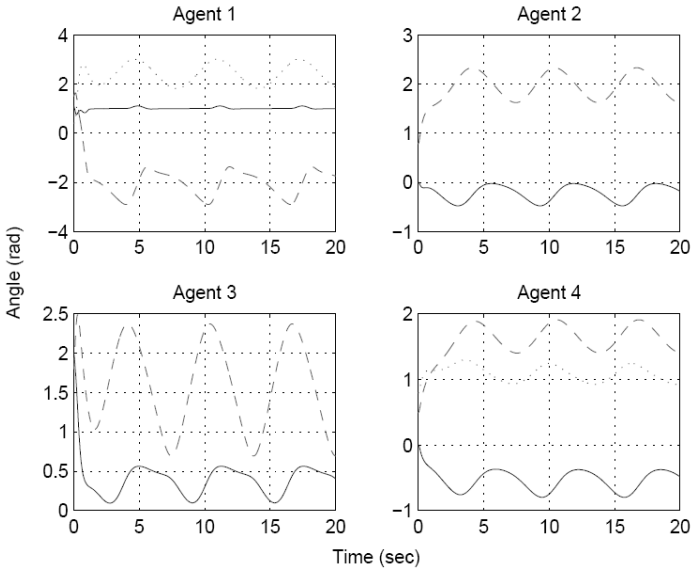

Figure 10.4: Joint angles of each agent using task space tracking control with synchronization and time delays.

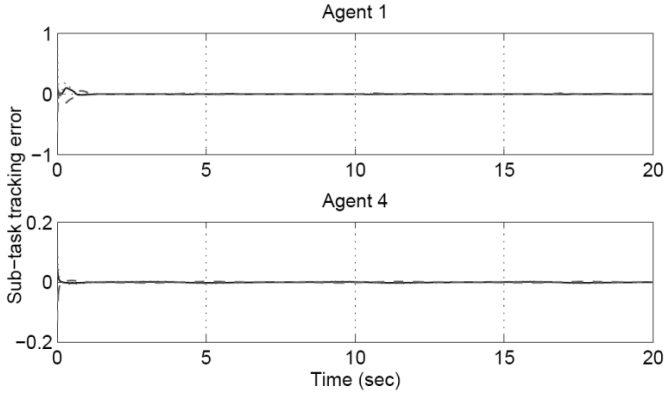

Figure 10.5: Sub-task tracking errors of redundant manipulators with synchronization and time delays.

10.5 Experimental Results

The proposed semi-autonomous control scheme was experimentally verified on four PHANToM Omni haptic devices in this section. The figure of a PHANToM Omni is shown in Figure 10.6, and more information can be obtained from [25]. Since all PHANToM Omnis are endowed with the same kinematics and dynamics, in order to achieve the implementation of controlled synchronization between heterogeneous manipulators, the individual systems are modified based on the model of PHANToM Omni in [23] as Figure 10.6 (b). Using the kinematic and dynamic model, the position of end-effector and Jacobian can be obtained for different links lengths, and hence the velocity of end-effector can be computed by (3). Further details of the experiment setups and the PHANToM Omni model are provided in [23].

(a) **(b)**

Figure 10.6: The appearance of PHANToM Omni and its modification for the experiments.

In the experiments, as shown in Figure 10.7, three different communication topologies were utilized to implement the proposed control scheme. In the subsequent discussion, the agents are labeled as shown in Figure 10.7. The experiments were conducted using two desktops communicating with another (using TCP/IP) over the wireless network on the campus of University of Maryland. Each of the computers provided sensing and control information to two PHANToM Omnis, as shown in Figure 10.7. The data collection and control input rate in the experiments was 1kHz. Moreover, in addition to the inherent communication delays and possible packet loss due to the wireless network, artificial time delays were added to the communication path and were given as $T_{12} = 0.45sec$, $T_{23} = 0.1sec$, $T_{34} = 0.3sec$, and $T_{41} = 0.2sec$. In the following experiment, the lengths of manipulators were defined as $L_1 = [150mm, 120mm]$, $L_2 = [133mm, 133mm]$, $L_3 = [140mm, 140mm]$, and $L_4 = [130mm, 150mm]$, where L_2 is the actual link length of a PHANToM Omni. Due to workspace limitations, the desired trajectory for the end-effectors was chosen as $X(t) = 60 \times sin(0.2\pi t)\, mm$, $Y(t) = 150 + 40 \times cos(0.2\pi t)\, mm$, and $Z(t) = 80\, mm$.

In the first experiment, task-space controlled synchronization without the human operator was conducted using topology 2. We define diag(d_1 , d_2 , d_3) to indicate a 3×3 diagonal matrix whose diagonal entries starting in the upper left corner are d_1 , d_2 , d_3 . Then, the control parameters are given as Λ = diag (2 , 2 , 2) , K_{ti} = diag (0.1 , 0.1 , 0.1) , K_{Ji} = diag (0.1 , 0.1 , 0.1) , and $K_{si} = 0.003$, where $i = 1, 2, 3, 4$. Figure 10.8 and Figure 10.9 demonstrate trajectory tracking in task space with controlled synchronization and time delays. As seen in the experimental results and expected from Theorem 10.5, heterogeneous agents follow the desired trajectory with good tracking performance. The joint angles of various agents are demonstrated in Figure 10.10.

In the next experiment, and as detailed in Theorem 10.7, a human operator can cause a manipulator to deviate from the pre-planned desired trajectory. The human operator influences the motion of agent 1 in the sequel. Due to the actions of the human operator, the increasing tracking errors increase, resulting in a higher tracking torque. As the torque provided by PHANToM Omni is limited, the tracking gains were reduced to avoid damage to the devices.

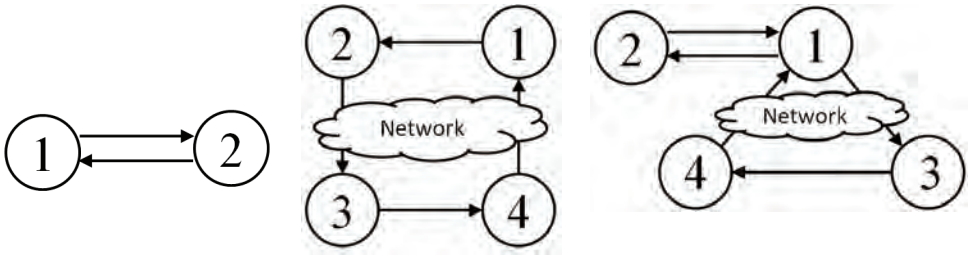

(a) Topology 1 **(b) Topology 2** **(c) Topology 3**

Figure 10.7: Balanced and strongly connected topology used for experiments.

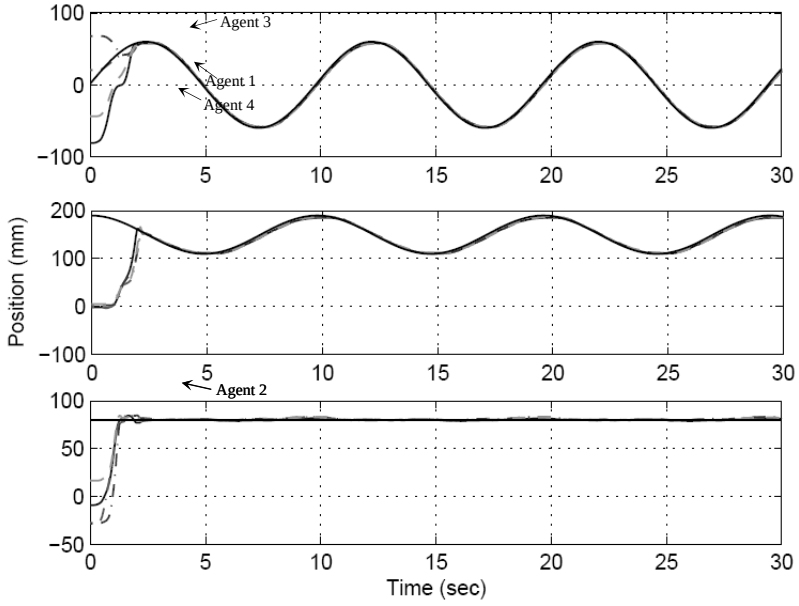

Figure 10.8: Tracking in task space in the presence of controlled synchronization and time delays

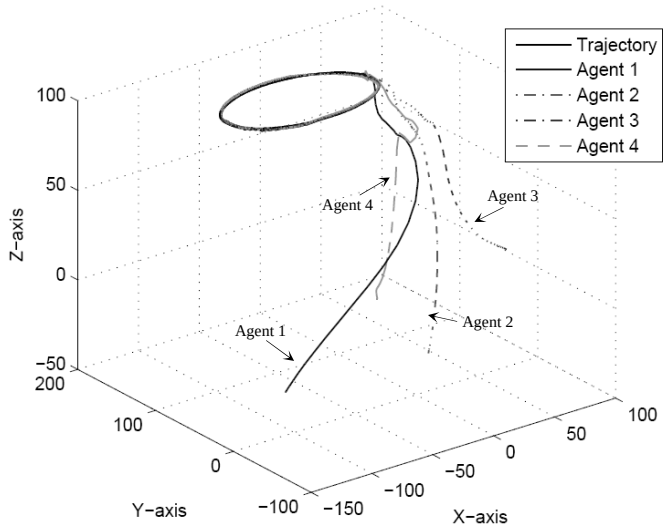

Figure 10.9: Tracking trajectory of the end-effectors in 3-D.

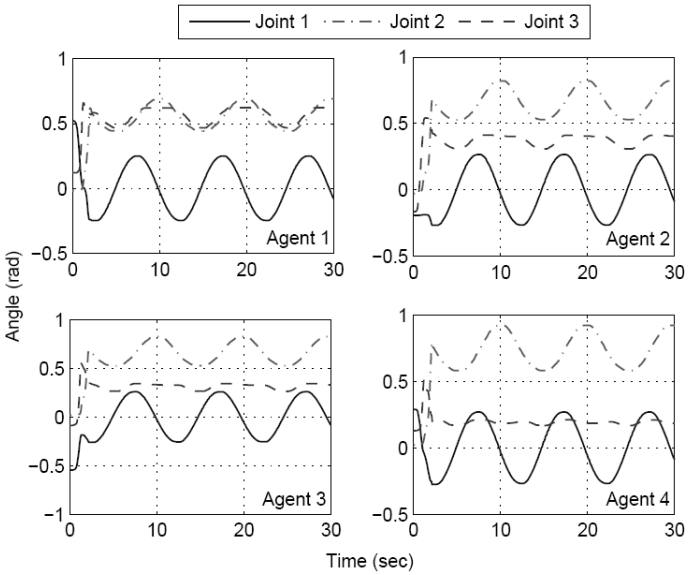

Figure 10.10: Joint angles of each manipulator using task space tracking control with synchronization.

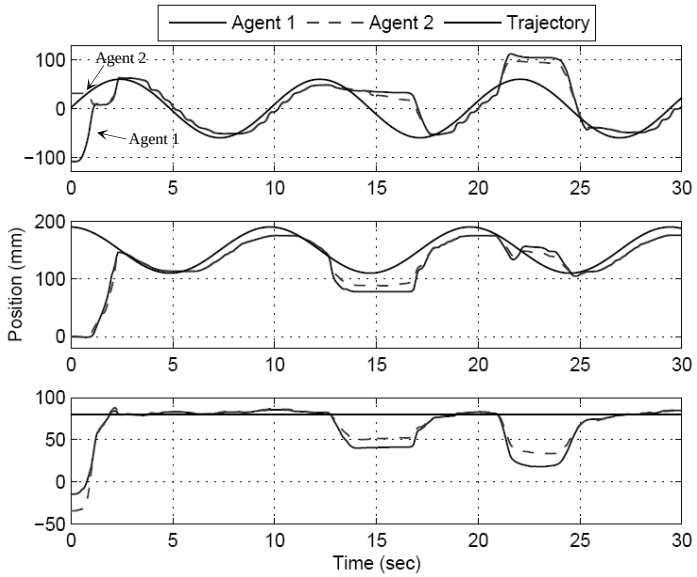

Figure 10.11: Task space tracking when the human operator influences the motion of agent 1.

The first experiment was based on topology 1 where the two agents were interconnected with a bidirectional graph. Control parameters for this case were defined as $\Lambda = \text{diag}(20, 20, 20)$, $K_{ti} = \text{diag}(0.016, 0.032, 0.016)$, $K_{Ji} = \text{diag}(0.016, 0.032, 0.016)$, and $K_{si} = 0.0032$, where $i = 1, 2$. The trajectories of end-effectors in the task space are shown in Figure 10.11. Agents follow the desired trajectory in the task space until the human operator forces the motion of agent 1 to deviate from the desired trajectory. Due to the coupling between the agents, agent 2 follows the first agent and the synchronization errors are bounded as seen in Figure 10.11. Subsequently, when the operator no longer influences the motion of agent 1, both agents track the desired trajectory. Figure 10.12 illustrates that the joint angles of the heterogeneous agents.

Next, we present experimental results for four agents with topology 2 and 3. In the case of topology 2, the control parameters are defined as $\Lambda = \text{diag}(6, 6, 6)$, $K_{ti} = \text{diag}(0.04, 0.04, 0.04)$, $K_{Ji} = \text{diag}(0.02, 0.02, 0.02)$, and $K_{si} = 0.0032$, where $i = 1, 2, 3, 4$. The trajectories in the task space and joint angles of the agents are shown in Figure 10.13 and Figure 10.14. It is evident that the synchronization performance

decreases with four agents when only one agent is being controlled directly by the human operator. When the topology is changed to topology 3, where agent 1 communicates its output $r_1(t)$ to agent 2 and agent 3 with control parameters $\Lambda = \text{diag}(8, 8, 8)$, $K_{ti} = \text{diag}(0.04, 0.04, 0.04)$, $K_{Ji} = \text{diag}(0.02, 0.02, 0.02)$, and $K_{si} = 0.0032$, $i = 1,2,3,4$. The synchrony between agent 2, agent 3 and agent 1 is better as compared to that with agent 4. The experimental results for topology 3 are shown in Figures 10.15 and 10.16.

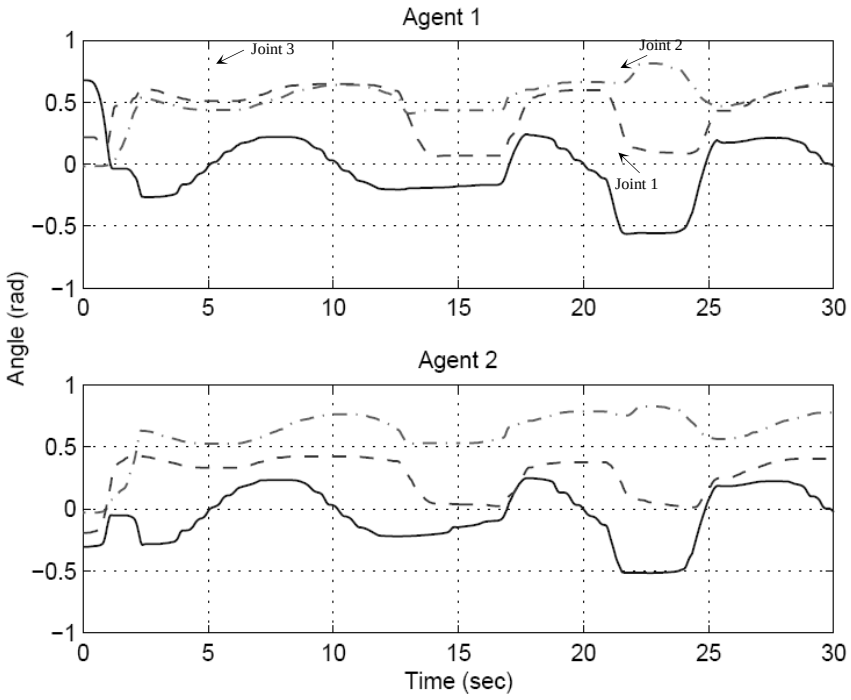

Figure 10.12: Joint angles of the agents under semi-autonomous control.

In the previous experiments, every agent was driven by task space tracking and synchronization control simultaneously. For semi-autonomous manipulation, the ability to track a desired trajectory or synchronize was significantly influenced by the assigned control parameters. If higher values were chosen for the tracking gains, K_{ti} and

K_{Ji}, such as in the case without the human operator, then the agents converge to the desired trajectory faster with smaller tracking errors. However, due to higher control torques resulting from higher gains, it is difficult for the human operator to manipulate any robotic system. Hence, semi-autonomous is difficult to achieve with higher tracking gains.

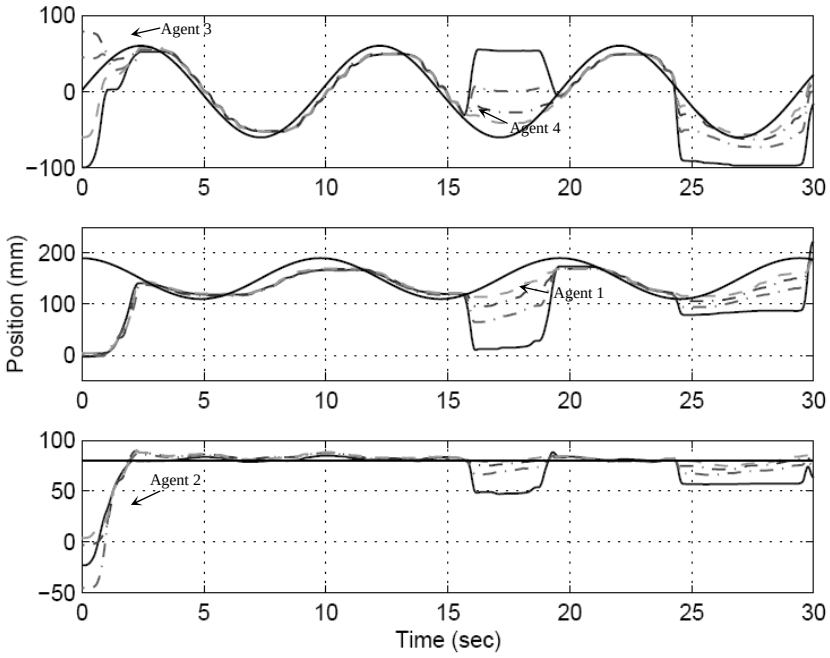

Figure 10.13: Task space tracking when the human operator influences the motion of agent 1.

From the experiments above, it is evident that semi-autonomous can be accomplished with lower tracking gains in the presence of controlled synchronization. When the gains are selected appropriately, as seen in Figure 10.13 and Figure 10.15, the agents initially synchronize to each other and then follow the desired trajectory. The trade-off between the synchronizing gain, K_{si}, and tracking gains K_{ti} and K_{Ji}, critically influence the semi-autonomous behavior of the system. It can also be inferred from the experiments that different interconnection topologies lead to different results under semi-autonomous control. For example, in

the experiments with topology 2 and topology 3, the agents that received output signals directly from the agent operated by the human operator were in better synchrony with each other.

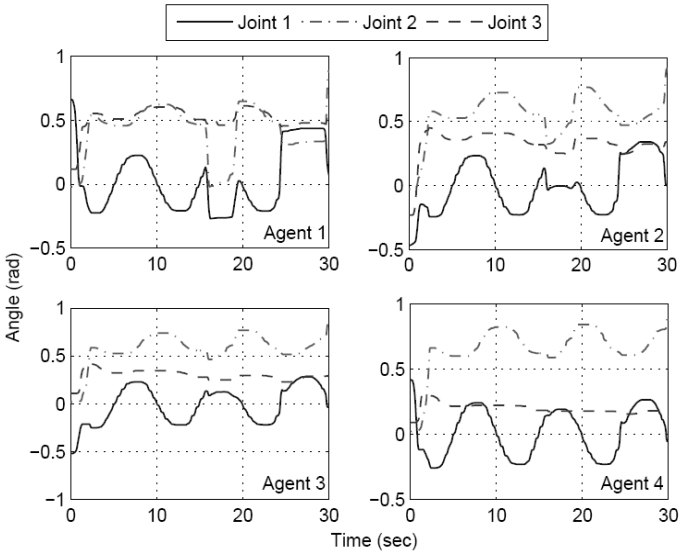

Figure 10.14: Joint angles of the agents under semi-autonomous control.

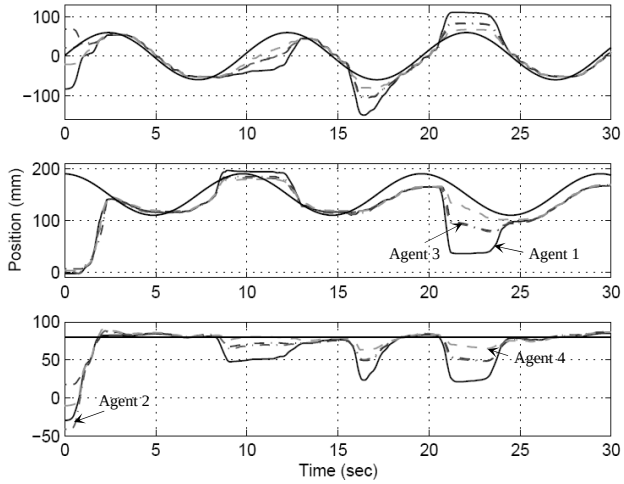

Figure 10.15: Task space tracking when the human operator influences the motion of agent 1.

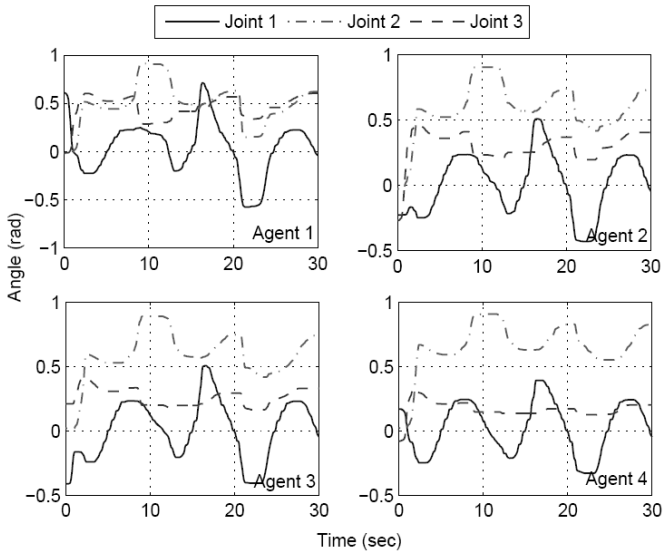

Figure 10.16: Joint angles of the agents under semi-autonomous control.

10.6 Conclusions

Semi-autonomous task space manipulation for heterogeneous robotic manipulators was proposed in this paper. We demonstrated that a group of robotic manipulators systems can be synchronized in the task space when following a nominal trajectory. The robustness of the proposed algorithm to time delays in communication was also demonstrated. The task space synchronization was first constructed assuming that the manipulators are non-redundant. Moreover, if one or more of the agents are redundant, an additional sub-task control was also utilized to avoid the singularity or obstacles in the workspace. In the presence of a human operator in the loop, we showed that the states of the semi-autonomous system are uniformly ultimately bounded.

The efficacy of the proposed algorithm was first demonstrated by simulations using two nonredundant and two redundant manipulators in the presence of communication delays. Furthermore, experiments were conducted on four PHANToM Omnis to verify the proposed schemes both with and without the presence of the human operator. Future work involves extension of the proposed approach to the problem of time-varying communication delays, multiple human operators, and kinematic uncertainties.

10.7 References

1. Quigley, M., Goodrich, M. A., and Beard, R. W., 2004, "Semi-autonomous human-UAV interfaces for fixed wing mini-UAVs," *IEEE/RSJ International Conference on Intelligent Robots and Systems.*
2. Ettelt, E., Furtwängler, R., Hanebeck, U. D., and Schmidt, G., 1998, "Design issue of a semi-autonomous robotic assistant for the health care environment," *Journal of Intelligent and Robotic Systems*, 22(3), pp. 191–209.
3. Lee, D. and Spong, M. W., 2006, "Semi-autonomous teleoperation of multiple cooperative robots of human-robot lunar exploration," *AAAI 2006 Spring Symposium.*
4. Rodriguez-Angeles, A. and Nijmeijer, H., July 2004, "Mutual synchronization of robots via estimated state feedback: a cooperative approach," *IEEE Transactions on Control Systems Technology*, 12(4), pp. 542–554.
5. Chung, S.-J. and Slotine, J.-J. E., 2009, "Cooperative robot control and concurrent synchronization of Lagrangian systems," *IEEE Transactions on Robotics*, 25(3), pp. 686–700.
6. Pogromsky, A. Y., 1998, "Passivity based design of synchronizing systems," *International Journal of Bifurcation and Chaos*, 8(2), pp. 295–319.
7. Pogromsky, A. and Nijmeijer, H., 2001, "Cooperative oscillatory behavior of mutually coupled dynamical systems," *IEEE Transactions on Circuits and Systems I*, 48(2), pp. 152–162.
8. Stan, G.-B. and Sepulchre, R., 2007, "Analysis of interconnected oscillators by dissipativity theory," *IEEE Transactions on Automatic Control*, 52(2), pp. 256–270.
9. Chopra, N. and Spong, M., 2006, "Passivity-based control of multi-agent systems," *Advances in Robot Control: From Everyday Physics to Human-Like Movements*, S. Kawamura and M. Svinin, eds., Springer Verlag, pp. 107–134.
10. Chopra, N. and Spong, M.W., 2006, "Output synchronization of nonlinear systems with time delay in communication," *IEEE Conference on Decision and Control*.
11. Chopra, N., Spong, M. W., and Lozano, R., 2008, "Synchronization of bilateral teleoperators with time delay," *Automatica*, 44(8), pp. 2142–2148.

12. Kawada, H., Yoshida, K., and Namerikawa, T., 2007, "Synchronized control for teleoperation with different configurations and communication delay," *IEEE Conference on Decision and Control*.
13. Nath, N., Tatlicioglu, E., and Dawson, D. M., 2009, "Teleoperation with kinematically redundant robot manipulators with sub-task objectives," *Robotica*, 24, pp. 1027-1038.
14. Chopra, N. and Liu, Y.-C., 2008, "Controlled synchronization of mechanical systems," *ASME Dynamic Systems and Control Conference.*
15. Godsil, C. and Royle, G., 2001, "*Algebraic graph theory*," Springer Graduate Texts in Mathematics No. 207, Springer.
16. Spong, M.W., Hutchinson, S., and Vidyasagar, M., 2006, *Robot Modeling and Control*, John Wiley & Sons, Inc., New York.
17. Dixon, W. E., 2007, "Adaptive regulation of amplitude limited robot manipulators with uncertain kinematics and dynamics," *IEEE Transactions Automatic Control*, 52(3), pp. 488–493.
18. Cheah, C. C., Liu, C., and Slotine, J. J. E., 2006, "Adaptive tracking control for robots with unknown kinematic and dynamic properties," *International Journal of Robotics Research*, 25(3), pp. 283–296.
19. Slotine, J.-J. and Li, W. P., 1988, "Adaptive manipulator control: A case study," *IEEE Transactions on Automatic Control*, 33(11), pp. 995–1003.
20. Zergeroglu, E., Dawson, D. M., Walker, I., and Behal, A., 2000, "Nonlinear tracking control of kinematically redundant robot manipulators," *American Control Conference*.
21. Yoshikawa, T., 1984, "Analysis and control of robot manipulators with redundancy," *The First International Symposium on Robotics Research.*
22. Hsu, P., Hauser, J., and Sastry, S., 1989, "Dynamic control of redundant manipulators," *Journal of Robotic Systems*, 6, pp. 133–148.
23. Liu, Y.-C. and Chopra, N., 2011, "Synchronization of multiple mechanical systems with dynamic uncertainty and communication delays," *ASME Journal of Dynamic Systems, Measurement and Control,* submitted.
24. Khalil, H. K., 2002, *Nonlinear systems*, Upper Saddle River, Prentice Hall, New Jersey.
25. SensAble Technologies, http://www.sensable.com.